Understanding how low energy electrons control the variability of the Earth's electron radiation belts

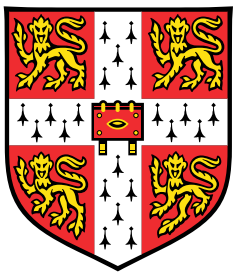

Hayley Jane Allison

Department of Applied Mathematics and Theoretical Physics
University of Cambridge
with
British Antarctic Survey
Space Weather and Atmosphere Group

This thesis is submitted for the degree of
Doctor of Philosophy

Darwin College

March 2019

Declaration

I hereby declare that, except where specific reference is made to the work of others, the contents of this dissertation are original and have not been submitted in whole or in part for consideration for any other degree, diploma, or qualification in this, or any other university. This dissertation is my own work and contains nothing which is the outcome of work done in collaboration with others, except as specified in the text and Acknowledgements. This dissertation is submitted for the degree of Doctor of Philosophy. It does not exceed the prescribed word limit for the relevant Degree Committee.

Hayley Jane Allison
March 2019

Abstract

Understanding how low energy electrons control the variability of the Earth's electron radiation belts

Hayley Jane Allison

The electron radiation belts are regions of geomagnetically trapped electrons, surrounding the Earth, presenting hazards to operational satellites. On the timeframe of hours, both the energy and particle flux of the radiation belts can change by orders of magnitude. Variations in the high energy relativistic electron flux depend on transport, acceleration, loss processes, and importantly, on the lower energy seed (10s – 100s keV) population. Seed population electrons are supplied to the radiation belt region during geomagnetically active periods and can be accelerated to higher energies via a range of processes. Unlike the higher energy, $>$1 MeV electrons, the azimuthal drift of the seed population is strongly affected by the convection electric field.

Using fourteen years of electron flux data from low Earth orbit (LEO) satellites, a statistical study was performed on the magnetic local time distribution of three seed population energies, across a range of activity levels, defined by the geomagnetic indices AE, AE*, Kp, the solar wind velocity, and $V_{sw}B_z$. During periods of high activity, dawn-dusk flux asymmetries of over an order of magnitude were observed for $>$30 and $>$100 keV electrons, due to increased flux in the dawn sector. For $>$300 keV electrons, magnetic local time asymmetries were also present, but arose primarily due to a decrease in the average dusk-side flux beyond L^* $\sim$4.5.

A novel method was developed that utilizes measurements from low altitude, polar orbiting POES and MetOp satellites to retrieve the seed population at a pitch angle of 90^o. The resulting dataset offers a high time resolution, across multiple magnetic local time planes, and was used to formulate event-specific low energy boundary conditions for the British Antarctic Survey Radiation Belt Model (BAS-RBM). This new low energy boundary

condition from LEO data has a higher spatial and temporal resolution, and a broader L^* coverage, than previous work.

The impact of variations in the seed population on the 1 MeV flux level was explored using the 3-D BAS-RBM to solve a diffusion equation for the electron phase space density. For some periods, an enhancement in the seed population was vital to recreate observed 1 MeV flux enhancements. A series of idealised experiments with the 2-D BAS-RBM were performed which highlight a careful balance between losses and acceleration from chorus waves. Our results show that seed population enhancements alter this balance by increasing the phase space density gradient, and consequently, the rate of energy diffusion, allowing acceleration to surpass loss. Additionally, pre-existing energy gradients in the phase space density and the duration of chorus wave activity determine whether $>$500 keV electrons were enhanced due to local acceleration.

Acknowledgements

To my three excellent and kind supervisors: Richard Horne, Sarah Glauert, and Giulio Del Zanna, thank you for all your guidance, help, and encouragement. You nurtured my passion for radiation belt physics and have each taught me so much. It has been an absolute pleasure to work with you and I could not have asked for better mentors. I have thoroughly enjoyed our many discussions over the years - thank you so much for your constant patience and for making this PhD such an enjoyable experience.

Additionally, I would like to thank the whole of the Space Weather and Atmospheres group at the British Antarctic Survey, as well as the Astrophysics group at DAMTP. I have always felt welcomed and encouraged by you all. In particular, thank you to Alex and John for many an insightful and interesting Journal Club hour, I have learnt a lot from both of you.

Thank you to wonderful PhD students with whom I shared an office. I have very much enjoyed spending the last few years with you.

Roger, I can not thank you enough for your unwavering reassurance. Undertaking this journey together has been a privilege.

I am exceedingly fortunate to have very supportive and encouraging parents. Thank you both for everything. Also, I am incredibly grateful to my wonderful grandparents. Thank you for taking the time to read my papers and for your constant interest. Thankfully, I have always remembered to tell people who my grandfather is.

The results of this thesis were funded by the Cambridge University Earth System Science NERC Doctoral Training Partnership (ESS DTP, grant number NE/L002507/1). The ESS DTP has been a fantastic source of training and support for which I am exceptionally grateful.

Table of contents

List of figures

List of tables

Chapter 1

Introduction

Discovered at the start of the space age, the Earth's electron radiation belts are large-scale regions of geomagnetically trapped particles, presenting hazards to satellites, and humans, in space. The formation and dynamics of this region have presented a fascinating field of study that has expanded and evolved in the past 60 years.

In this chapter we start by discussing the discovery of the Van Allen radiation belts before detailing charged particle motion and plasma populations in Earth's magnetosphere. Finally, we conclude by considering some of the mechanisms responsible for changes in the radiation belt regions.

1.1 The Discovery of the Van Allen Belts

The existence of the radiation belts was first hinted at in 1953 following the launch of rocket-carrying balloons - "rockoons" - near the north magnetic pole. A balloon was used to lift a small rocket up to an altitude of 20 to 25 km, at which point the rocket deployed and continued to a height of 100 - 110 km. The original objective of these experiments was to study cosmic ray intensities at high altitudes and latitudes. While previous rockoon launches had encountered radiation in accordance with the profile expected from cosmic rays, two balloons launched near Newfoundland measured a zone of radiation, extending out from 50 km altitude, that was considerably stronger than anticipated; a finding dubbed auroral soft radiation (Van Allen, 1957).

To better examine auroral soft radiation, James Van Allen and his group at the University of Iowa proposed a mission to place a satellite in a nearly pole-to-pole orbit. However, it was concluded that, at the time, such an orbit might not be technically feasible. Instead, a satellite orbiting over the lower latitudes of the Earth was adopted with the intention to better

survey cosmic ray intensities around the equatorial regions. Van Allen and the Iowa group prepared a Geiger counter for deployment on-board the United States' first artificial satellite and, on 31st January 1958, Explorer I was launched carrying this instrument.

Surprisingly, Explorer I measurements suggested that at high altitudes over the equatorial region, the count rate was extremely low, dropping to zero during some passes. This finding did not fit the expected profile from cosmic rays, and it was considered that the counter may have malfunctioned. Explorer II unfortunately failed on launch, but Explorer III, also carrying a Geiger counter, was later successfully placed into orbit on 26th March 1958 and confirmed the unexpected results of Explorer I. At altitudes of 320 - 480 km the particle count rate measured was low, however, as the satellite advanced out to 880 - 970 km the counts ascended rapidly before abruptly dropping to almost zero. It was Carl McIlwain who first suggested that the peculiar readings may be a result of instrument saturation and that the Explorer satellites were actually measuring an extremely high level of radiation, as opposed to a lack of it (Van Allen, 1957, 1958, 1959b).

Different, more discriminating, Geiger tubes were designed as part of the payload of Explorer IV, launched into orbit on 26th July 1958. The new data confirmed the suggestion that the instruments on board Explorer I and III had saturated, showing very high levels of radiation at $\sim$900 km and above (Van Allen et al., 1959). It was proposed that the radiation measured by the Explorer satellites consisted of electrons and protons trapped by the Earth's magnetic field, an idea first discussed theoretically years earlier by Carl Störmer who calculated the trajectories such particles might be expected to follow (Störmer, 1955). Data from Explorer I, III, and IV had supplied the first observational evidence of the geomagnetic trapping of charged particles.

In addition to carrying better refined particle detectors, Explorer IV also extended the observations to more than 50^{o} north and south of the magnetic equator and allowed intensity contours to be constructed. The contours suggested that previous missions had only sampled the lower portion of the radiation region, which likely extended out to much larger distances. Two possible structures for the full region of trapped radiation were proposed, one being a single torus of radiation encompassing the Earth, and another showing two belts: an outer region with a banana shaped cross-section and an inner region with a bean shaped cross-section (Van Allen, 1959a,b; Van Allen et al., 1959).

To determine which of the proposed structures best described the form of the trapped radiation, a Geiger tube was carried aboard the lunar probes Pioneer I and III. The new data confirmed that the radiation indeed extended outwards for many thousands of miles and showed a double peak in intensity, establishing the proposed two belt structure (Rosen et al.,

1959; Van Allen and Frank, 1959a,b). The radiation belts are now also known as the Van Allen belts in honour of the scientist who was instrumental in their discovery.

In the following section, we explore how charged particles are trapped by the Earth's magnetic field, forming the radiation belts first observed at the start of the space age.

1.2 Particle Motion

Earth is a magnetised planet, and the geomagnetic field exerts a force on moving charged particles. The motion of a charged particle through magnetic field **B** and electric field **E** can be described in terms of the Lorentz equation:

$$\frac{d\mathbf{p}}{dt} = q(\mathbf{v} \times \mathbf{B} + \mathbf{E}) \tag{1.1}$$

where q denotes the particle charge, **p** its momentum, and **v** its velocity. Simple examination of equation 1.1 demonstrates that an electric field acts to accelerate a charged particle parallel to the field direction (or antiparallel, depending on the particle charge), while the presence of a magnetic field results in a acceleration that is perpendicular to both the magnetic field and the velocity of the particle (Walt, 1994).

1.2.1 Gyromotion

In the scenario that no electric fields are present ($\mathbf{E} = 0$), equation 1.1 reduces to just the Lorentz force:

$$\frac{d\mathbf{p}}{dt} = q(\mathbf{v} \times \mathbf{B}). \tag{1.2}$$

As the resulting force on the particles acts perpendicularly to both the magnetic field direction and their velocity vector, gyration is evident. In the simple case that **B** is uniform in both time and space, and separating the velocity vector into components parallel ($\mathbf{v}_{\parallel}$) and perpendicular ($\mathbf{v}_{\perp}$) to the magnetic field yields

$$m\frac{d\mathbf{v}_{\parallel}}{dt} = 0 \tag{1.3}$$

and

$$m\frac{d\mathbf{v}_{\perp}}{dt} = q(\mathbf{v}_{\perp} \times \mathbf{B}). \tag{1.4}$$

The solution of equation 1.3 is $\mathbf{v}_{\parallel}$ = constant, indicating that the particle will move parallel to **B** with a constant speed. Equation 1.4 demonstrates that the velocity change resulting from the Lorentz force is perpendicular to $\mathbf{v}_{\perp}$, and so $\mathbf{v}_{\perp}$ remains constant in magnitude and the

particle follows a circular trajectory in the $\mathbf{v}_\perp - \mathbf{B}$ plane. The change in $\mathbf{v}_\perp$ is dependent on the charge of the particle and, as such, positively and negatively charged particles will gyrate in opposite directions (Cravens, 1997).

The Lorentz force exerted on a particle moving in a circular trajectory of radius r_{gyro} must be balanced by the centrifugal force

$$\frac{mv_\perp^2}{r_{gyro}} = qv_\perp B \tag{1.5}$$

where $v_\perp$ and B are the magnitudes of the perpendicular particle velocity and magnetic field, respectively. The radius of the circular trajectory followed is known as the gyroradius and is given by

$$r_{gyro} = \frac{mv_\perp}{B|q|}. \tag{1.6}$$

The gyroradius (or cyclotron radius) is directly proportional to the perpendicular velocity of the particle and therefore increases with increasing particle energy. In a 3,400 nT magnetic field (approximately equivalent to the equatorial geomagnetic field at a distance of 3 R_E, assuming a dipole field model) a 10 keV electron would have a gyroradius of $\sim$100 m, while for a 1 MeV electron this extends to $\sim$1.4 km.

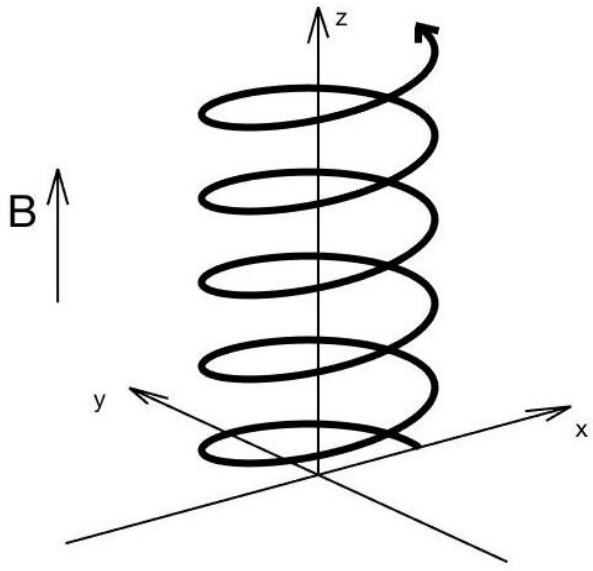

Figure 1.1 – The helical motion of a negatively charged particle in a uniform magnetic field ($\mathbf{E} = 0$).

The gyroperiod is the time taken for a particle to complete one rotation,

$$T_{gyro} = 2\pi \frac{m}{|q|B}, \tag{1.7}$$

and the angular gyrofrequency is

$$\Omega = \frac{2\pi}{T_{gyro}} = \frac{|q|B}{m}. \tag{1.8}$$

In the non-relativistic case where $m = constant$, the gyroperiod is independent of particle energy (Walt, 1994).

In a uniform magnetic field with no electric field, the combination of a constant drift parallel to the magnetic field and a circular gyration perpendicular to the magnetic field causes particles to travel in a helical motion. A helical trajectory of a negatively charged particle is shown in Figure 1.1. The relative ratio between the magnitude of the parallel and perpendicular components of the magnetic field prescribe the openness of the helix.

1.2.2 Bounce Motion

When a magnetic field is not uniform, but rather converges, charged particles display a phenomenon known as magnetic mirroring. As the particle spirals along the field, it experiences an increased field strength. If the change in the magnetic field is small over one gyroradius in one gyroperiod then the field can be approximated as being static, doing no work on the particle. By Faraday's law, this implies that the magnetic flux through the particle's orbit is constant, given by

$$\Phi = B\pi r_g^2 = \frac{\pi}{q^2}\frac{p_\perp^2}{B} = constant \tag{1.9}$$

where $p_\perp$ denotes the particle momentum perpendicular to the magnetic field. As π and q are constants, equation 1.9 shows that if the B experienced by the particle increases, i.e. as it moves into the converging field, $p_\perp$ must also increase. The values $p_\perp$ and B at two locations in a converging magnetic field (1 and 2) are therefore related by:

$$\frac{p_{\perp 1}^2}{B_1} = \frac{p_{\perp 2}^2}{B_2} \tag{1.10}$$

where the subscripts 1 and 2 denote two different locations. The perpendicular momentum can be expressed in terms of the total momentum,

$$p_{\perp}^2 = |p|^2 \sin^2 \alpha, \tag{1.11}$$

where α is the angle between the particle's velocity vector and the magnetic field direction, known as the particle pitch angle. Total momentum is conserved, therefore substituting equation 1.11 into 1.10 and cancelling constants yields

$$\frac{\sin^2 \alpha_1}{B_1} = \frac{\sin^2 \alpha_2}{B_2}. \tag{1.12}$$

As the particle moves into a converging field, B increases and α increases accordingly, up to a value of $\pi/2$, after which the particle reverses its motion parallel to the magnetic field and spirals back along the field line in the direction it came. The charged particle has been 'reflected' from a region of increased field strength due to the force exerted by the magnetic gradient.

The geomagnetic field converges in each hemisphere (discussed later in section 1.4.2.1) and, as a result, causes a phenomena known as magnetic trapping. As charged particles travel along the field, away from the equator, they enter into regions of stronger magnetic field and undergo magnetic 'mirroring'. The particle is then reflected back along the field before mirroring again in the opposite hemisphere. This back and forth between conjugate mirror points in the northern and southern hemispheres is known as the particle's bounce motion. The bounce period is the time taken for the particle for travel from the mirror point, to the opposite hemisphere and back again (Lyons and Williams, 1984).

Throughout each bounce period, the particle's pitch angle changes, ranging between a minimum value at the point of the weakest field strength and $\pi/2$ at each mirror point. At any specific point along the bounce motion, the pitch angle is known as the particle's local pitch angle. Another useful variable is the equatorial pitch angle which is defined as the pitch angle the particle has at the geomagnetic equator. Generally in the Earth's magnetic field, B is at its lowest value in the magnetic equatorial plane and so the equatorial pitch angle is the lowest pitch angle reached during a bounce period.

1.2.3 Drift Motion

In addition to both the gyration and hemisphere-to-hemisphere bounce motion, the charged particles in the geomagnetic field drift around the Earth. The origin of this drift motion stems

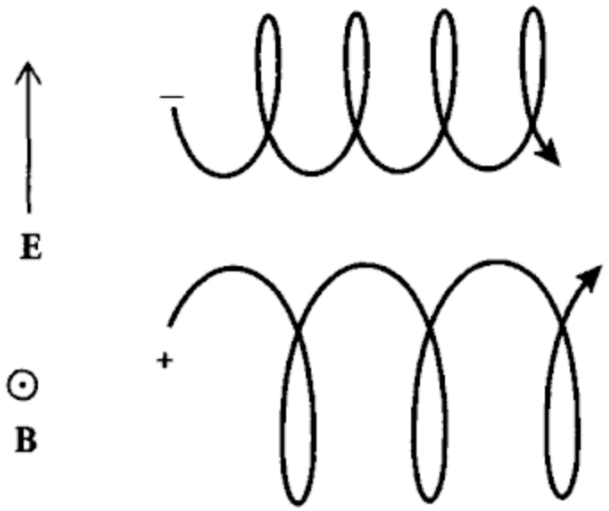

Figure 1.2 – Trajectories of an electron and ion in uniform **E** and **B** fields (Cravens, 1997).

primarily from large scale magnetospheric electric fields and the non-uniform structure of the geomagnetic field.

1.2.3.1 E × B Drift

The presence of non-zero electrostatic fields ($\mathbf{E} \neq 0$) can add additional components to the charged particle motion. In the case of an electrostatic field parallel to the magnetic field direction, charged particles are uniformly accelerated along a field line. Positively charged particles are accelerated in the direction of $\mathbf{E}_{\parallel}$ and negatively charged particles in the opposite direction. The relative charge separation can produce an additional electrostatic field which acts to cancel out the original parallel electric field (Kivelson and Russell, 1995). As such, parallel electrostatic fields are rarely found in the trapping region of the magnetosphere, but are important in accelerating particles in the aurora (Walt, 1994).

Electrostatic fields perpendicular to **B** result in a drift motion perpendicular to both **B** and $\mathbf{E}_{\perp}$. Figure 1.2 shows schematically how an electron and ion would be expected to move in the case of perpendicular time invariant electric and magnetic fields. If a charged particle has no component of its velocity parallel to the magnetic field, then in the case of a uniform magnetic field and no electrostatic field, it would undergo circular motion. A non-zero electric field acts to accelerate the particle through part of its orbit and decelerate it for the other part, resulting in a distorted circle. Over several gyrations this orbit distortion causes a net displacement, or a drift, in a direction perpendicular to both $\mathbf{E}_{\perp}$ and **B**.

To find the drift velocity in terms of **E** and **B** we move to a reference frame moving at velocity $\mathbf{V_d}$ perpendicular to **B**. The electric field in the moving system is

$$\mathbf{E}' = \mathbf{E} + \mathbf{V_d} \times \mathbf{B} \tag{1.13}$$

as given by balancing the force of a charged particle (equation 1.1) and the Coulomb force ($\mathbf{F_C} = q\mathbf{E}'$). The value $\mathbf{V_d}$ is chosen so that $\mathbf{E}' = 0$. Taking the cross product between **B** and equation 1.13 yields

$$\mathbf{B} \times \mathbf{E}' = \mathbf{B} \times (\mathbf{E} + \mathbf{V_d} \times \mathbf{B}). \tag{1.14}$$

Setting $\mathbf{E}' = 0$ and making use of the vector triple product rule gives

$$0 = \mathbf{B} \times \mathbf{E} + \mathbf{B} \times (\mathbf{V_d} \times \mathbf{B}) = \mathbf{B} \times \mathbf{E} + (\mathbf{B} \cdot \mathbf{B})\mathbf{V_d} - (\mathbf{B} \cdot \mathbf{V_d})\mathbf{B}, \tag{1.15}$$

where $\mathbf{B} \cdot \mathbf{B} = B^2$ and, as **B** and $\mathbf{V_d}$ are perpendicular, $\mathbf{B} \cdot \mathbf{V_d} = 0$:

$$0 = \mathbf{B} \times \mathbf{E} + B^2 \mathbf{V_d}. \tag{1.16}$$

Rearranging for $\mathbf{V_d}$ gives

$$\mathbf{V_d} = \frac{\mathbf{E} \times \mathbf{B}}{B^2}. \tag{1.17}$$

Equation 1.17 is independent of charge and so ions and electrons both drift in the same direction.

An electric field perpendicular to the geomagnetic field arises due to the rotation of the Earth. Angular momentum is transferred to the ionosphere (an ionised layer of the atmosphere) causing it to corotate with the planet. The corotating charges migrate into the mid-latitude region of closed field lines and the resulting corotation of the charged particles can be described in terms of an electric field (Davis, 1947; Maus, 2017). In the non-rotating frame of reference, the corotation electric field is given by $\mathbf{E_R} = -\mathbf{V_R} \times \mathbf{B}$, where $\mathbf{V_R} = \omega_E r \hat{\phi}$. The parameter ω_E is the angular velocity of the Earth's rotation and r is the radial distance from the center of the Earth. This electric field is directed radially inwards at the equator and results in a drift that causes charged particles to corotate with the Earth. Equipotential contours for the corotation electric field are shown in the top right panel of Figure 1.3.

In addition to the corotation electric field, a large scale electric field exists in the magnetosphere that originates from solar wind flowing across open polar cap field lines. This is known as the convection electric field and, in the equatorial plane, points in the dawn-to-dusk

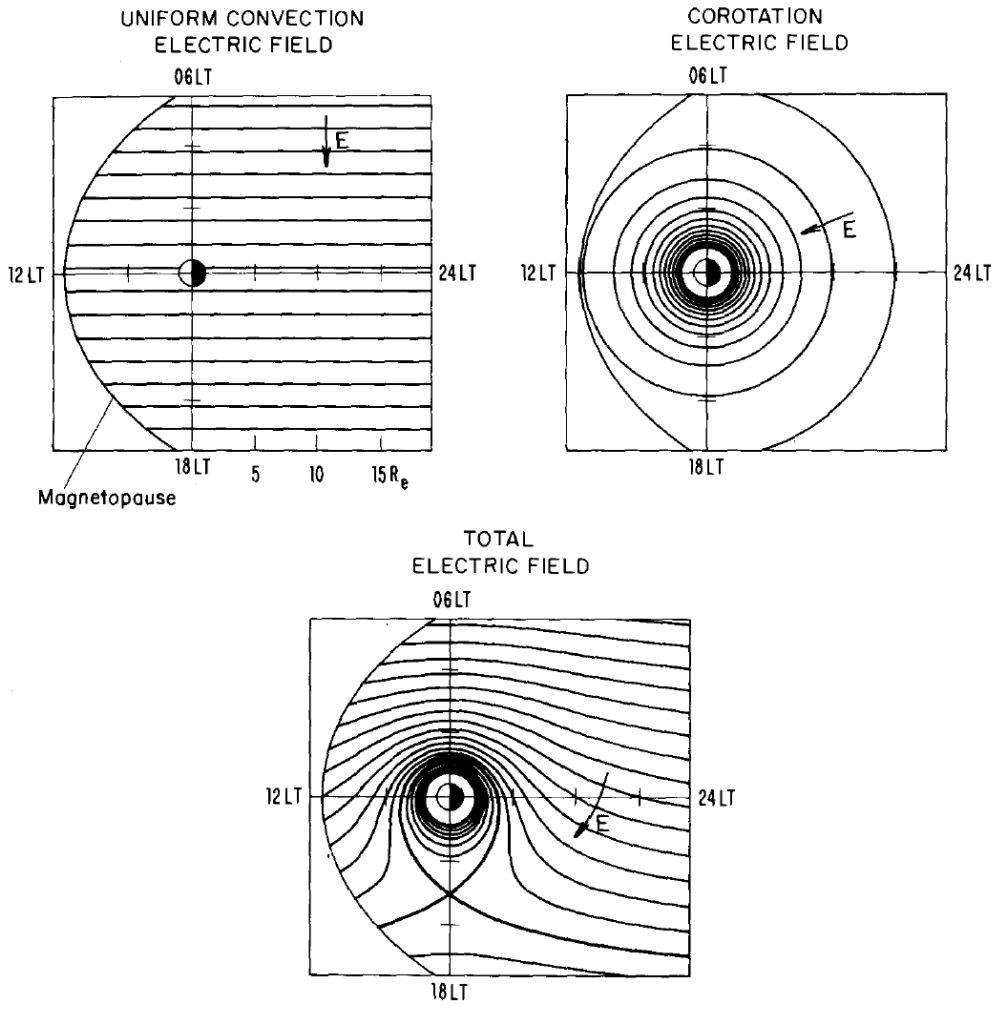

Figure 1.3 – Equipotential contours for magnetospheric electric fields in the equatorial plane (Lyons and Williams, 1984).

direction, producing a $\mathbf{E} \times \mathbf{B}$ anti-sunward drift of charged particles. The top left panel of Figure 1.3 shows the equipotentials of a uniform convection electric field in the equatorial plane, as presented by Lyons and Williams (1984).

The combination of the corotation electric field and the convection electric field potentials in the equatorial plane is shown in the bottom panel of Figure 1.3 where the convection electric field had a an assumed strength of $2.5 \times 10^{-4} Vm^{-1}$. In this electric field configuration (and ignoring the magnetic drifts described in the following two sections) charged particles close to the Earth will corotate under the influence of the corotation electric field, moving on closed drift paths around the Earth. Far from the Earth, the convection electric field will dominate the drift motion and the particles will drift from the night-side out through the

magnetopause on open drift paths. The separatrix between the region where the corotation electric field dominates, and particles are on closed drift paths, and the region where the convection electric field dominates, causing open drift paths, is called the Alfvén layer (Lyons and Williams, 1984).

1.2.3.2 Gradient Drift

In addition to drifts caused by electric fields present in the magnetosphere, the shape of the geomagnetic field results in a drift motion. The geomagnetic field can be approximated as being dipole-like, changing direction and magnitude along and across the field. For much of the geomagnetic field, the field strength decreases with increasing radial distance from the Earth. A gradient in the field strength in the direction perpendicular to **B** causes the magnetic field strength experienced by a gyrating charged particle to vary in magnitude throughout the gyromotion. Half of the gyration is in a stronger magnetic field than the other half, therefore the instantaneous radius of curvature throughout the gyromotion varies according to equation 1.6. Over several gyroperiods, this changing radius results in the particle drifting in a direction perpendicular to both **B** and ∇**B** (Kivelson and Russell, 1995).

If the gradient in the magnetic field is such that the magnitude of **B** does not change appreciably on the scale of a particle's gyroradius then the particle velocity may be split into

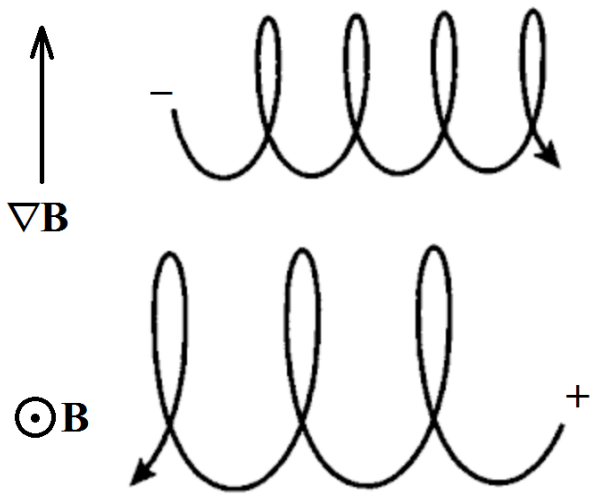

Figure 1.4 – The gradient drift motion for an ion and electron where the magnetic field gradient is directed towards regions of stronger B.

a gyration part, $\mathbf{v_g}$, and a small perturbation, $\mathbf{v_1}$:

$$\mathbf{v} = \mathbf{v_g} + \mathbf{v_1}. \tag{1.18}$$

Additionally, $\mathbf{B}$ can be approximated by the first two terms of a Taylor series expansion about $\mathbf{x} = 0$:

$$\mathbf{B} = \mathbf{B}(0) + \mathbf{x} \cdot \nabla \mathbf{B} \tag{1.19}$$

where $\mathbf{x}$ is the position vector. Assuming that $\mathbf{E} = 0$ and substituting equations 1.18 and 1.19 into the Lorentz equation (equation 1.1) gives

$$\frac{d(\mathbf{v_g} + \mathbf{v_1})}{dt} = \frac{q}{m}\left[(\mathbf{v_g} \times \mathbf{B}(0)) + (\mathbf{v_1} \times \mathbf{B}(0)) + (\mathbf{v_g} \times (\mathbf{x} \cdot \nabla \mathbf{B})) + (\mathbf{v_1} \times (\mathbf{x} \cdot \nabla \mathbf{B}))\right], \tag{1.20}$$

which in a uniform magnetic field becomes

$$\frac{d(\mathbf{v_g})}{dt} = \frac{q}{m}\mathbf{v_g} \times \mathbf{B}(0). \tag{1.21}$$

Subtracting equation 1.21 from 1.20 to isolate the perturbation velocity, and using $\mathbf{v_1} \times (\mathbf{x} \cdot \nabla \mathbf{B}) \sim 0$ as perturbations are small, results in

$$\frac{d\mathbf{v_1}}{dt} = \frac{q}{m}\left[(\mathbf{v_1} \times \mathbf{B}(0)) + (\mathbf{v_g} \times (\mathbf{x} \cdot \nabla \mathbf{B}))\right]. \tag{1.22}$$

The drift velocity is the time average of $\mathbf{v_1}$ over one gyroperiod,

$$\mathbf{v}_{\nabla B} = \langle \mathbf{v_1} \rangle = \frac{1}{T}\int_0^T \mathbf{v_1} \mathrm{d}t. \tag{1.23}$$

Taking the time average of equation 1.22 gives

$$\mathbf{v}_{\nabla B} \times \mathbf{B}(0) + \langle \mathbf{v_g} \times (\mathbf{x} \cdot \nabla \mathbf{B}) \rangle = 0 \tag{1.24}$$

where we have assumed a constant drift velocity. As the average is performed over a gyroperiod, $\mathbf{x}$ describes the gyromotion trajectory. If $\mathbf{B} = B(x,y)\hat{\mathbf{z}}$ the gyromotion can be expressed as

$$\mathbf{v_g} = v_g(\cos(\omega_c t + \phi)\hat{\mathbf{x}} - \frac{|q|}{q}\sin(\omega_c t + \phi)\hat{\mathbf{y}}) \tag{1.25}$$

and the position vector for the gyromotion trajectory as

$$\mathbf{x} = \frac{v_g}{\omega_c}(\sin(\omega_c t + \phi)\hat{\mathbf{x}} + \frac{|q|}{q}\cos(\omega_c t + \phi)\hat{\mathbf{y}}). \tag{1.26}$$

Substituting equations 1.25 and 1.26 into the second term of equation 1.24 and using $\langle \sin^2(\omega_c t + \phi)\rangle = \langle \cos^2(\omega_c t + \phi)\rangle = 1/2$ and $\langle \sin(\omega_c t + \phi)\cos(\omega_c t + \phi)\rangle = 0$ gives

$$\mathbf{v}_{\nabla B} \times \mathbf{B}(0) = \frac{|q|}{2q}\frac{v_g^2}{\omega_c}\frac{\partial B}{\partial x}\hat{\mathbf{x}} + \frac{|q|}{2q}\frac{v_g^2}{\omega_c}\frac{\partial B}{\partial y}\hat{\mathbf{y}} \tag{1.27}$$

and using equation 1.8 as the relationship for ω_c

$$\mathbf{v}_{\nabla B} \times \mathbf{B}(0) = \frac{m v_g^2}{2qB}(\frac{\partial B}{\partial x}\hat{\mathbf{x}} + \frac{\partial B}{\partial y}\hat{\mathbf{y}}) \tag{1.28}$$

which can also be expressed as

$$\mathbf{v}_{\nabla B} \times \mathbf{B}(0) = \frac{m v_g^2}{2qB}\nabla \mathbf{B}. \tag{1.29}$$

Taking the cross product of $\mathbf{B}(0)$ and equation 1.29 and implementing the vector triple product rule yields

$$\mathbf{v}_{\nabla B}B^2 - \mathbf{B}(0)(\mathbf{B}\cdot\mathbf{v}_{\nabla B}) = \frac{m v_g^2}{2qB}\mathbf{B}\times\nabla\mathbf{B}. \tag{1.30}$$

As the drift velocity is perpendicular to the field direction, $\mathbf{B}\cdot\mathbf{v}_{\nabla B} = 0$, and equation 1.30 can be rearranged to

$$\mathbf{v}_{\nabla B} = \frac{m v_g^2}{2qB^3}\mathbf{B}\times\nabla\mathbf{B}. \tag{1.31}$$

If $\mathbf{v}_{\nabla B}$ is significantly less than $\mathbf{v_g}$ then the component of the particle velocity perpendicular to the magnetic field ($v_\perp$) is approximately equal to the gyrovelocity, giving the standard relation for the gradient drift:

$$\mathbf{v}_{\nabla B} = \frac{m v_\perp^2}{2qB^3}\mathbf{B}\times\nabla\mathbf{B}. \tag{1.32}$$

The particle charge, q, in equation 1.32 dictates the direction of $\mathbf{v}_{\nabla B}$ and thus the ∇B drift motions of ions and electrons are oppositely directed, as shown in Figure 1.4.

1.2.3.3 Curvature drift

In the geomagnetic field the field lines curve in towards each hemisphere. The curvature of the field lines introduces an additional magnetic drift on the particle as a result of the centrifugal acceleration altering the gyroradius. A charged particle with a velocity component parallel to the magnetic field will experience a centrifugal force

$$\mathbf{F} = \frac{mv_{\parallel}^2}{R_c^2}\mathbf{R}_c \tag{1.33}$$

where $\mathbf{R}_c$ is the local radius of curvature of the magnetic field line. This force is equivalent to an electric field of magnitude $\mathbf{E}_c = mv_{\parallel}^2\mathbf{R}_c/qR_c^2$ and substituting this electric field into equation 1.17 gives a drift velocity equivalent to

$$\mathbf{v}_{curve} = \frac{mv_{\parallel}^2}{qR_c^2}\frac{\mathbf{R}_c \times \mathbf{B}}{B^2}. \tag{1.34}$$

As was the case for the ∇B drift, the sign of the particle charge determines the direction of curvature drift velocity and so electrons and ions drift in opposite directions.

The total drift velocity of a particle is the combination of the $\mathbf{E} \times \mathbf{B}$ drift, the gradient drift, and the curvature drift and is dependent on both the pitch angle and energy of the particle.

1.3 Adiabatic Invariants

Figure 1.5 summaries the gyration, bounce, and drift of charged particles experiencing both magnetic mirroring and gradient and curvature magnetic drifts in the geomagnetic field. Hamilton-Jacobi theory defines angle action variables for periodic motion which remain nearly constant for changes in the electromagnetic field when the rate of change is very slow in comparison with the period of the associated motion (Walt, 1994). If $\mathbf{p}$ is the particle momentum and $\mathbf{A}$ the electromagnetic vector potential, then the angle action variable associated with the motion is

$$\mathbf{J}_i = \oint_i [\mathbf{p} + q\mathbf{A}] \cdot d\mathbf{l} \tag{1.35}$$

where the path integral is performed over the periodic orbit. The three distinct periodicities associated with the gyration, bounce, and drift motions give rise to three angle action variables known as the adiabatic invariants.

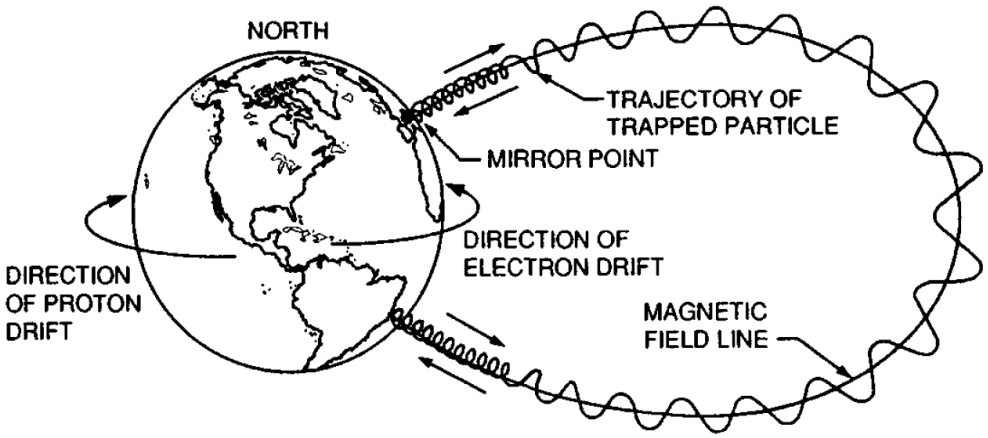

Figure 1.5 – Trajectories of trapped charged particles in the geomagnetic field, highlighting the gyration, bounce, and drift motion (Walt, 1994).

1.3.1 First Adiabatic invariant

The first adiabatic invariant is related to the particle's gyromotion described in section 1.2.1. Calculating the angle action variable for a particle gyration from equation 1.35 yields

$$J_1 = p_\perp (2\pi r_{gyro}) + q \oint \mathbf{A} \cdot d\mathbf{l}. \tag{1.36}$$

Substituting equation 1.6 for r_{gyro} and employing Stokes theorem gives

$$J_1 = \frac{2\pi p_\perp^2}{B|q|} + |q| \int \nabla \times \mathbf{A} \cdot d\mathbf{S} \tag{1.37}$$

where $d\mathbf{S}$ is an element of the area enclosed by the gyration. The curl of the vector potential is equal to the magnetic field, $\mathbf{B}$ and as $d\mathbf{S}$ points in the opposite direction to $\mathbf{B}$ equation 1.37 becomes

$$J_1 = \frac{2\pi p_\perp^2}{B|q|} - |q| B \pi r_{gyro}^2 = \frac{2\pi p_\perp^2}{B|q|} - \frac{\pi p_\perp^2}{B|q|} = \frac{\pi p_\perp^2}{B|q|}. \tag{1.38}$$

Rather than using J_1, the first invariant is taken to be

$$\mu = \frac{p_\perp^2}{2 m_0 B} \tag{1.39}$$

where m_0 defines the particle rest mass. Equation 1.39 is equal to J_1 except for constant factors and is known as the magnetic moment because, in the non-relativistic case, it is equal to the current round the particle orbit times the area of the loop. For the relativistic case, $p_\perp$

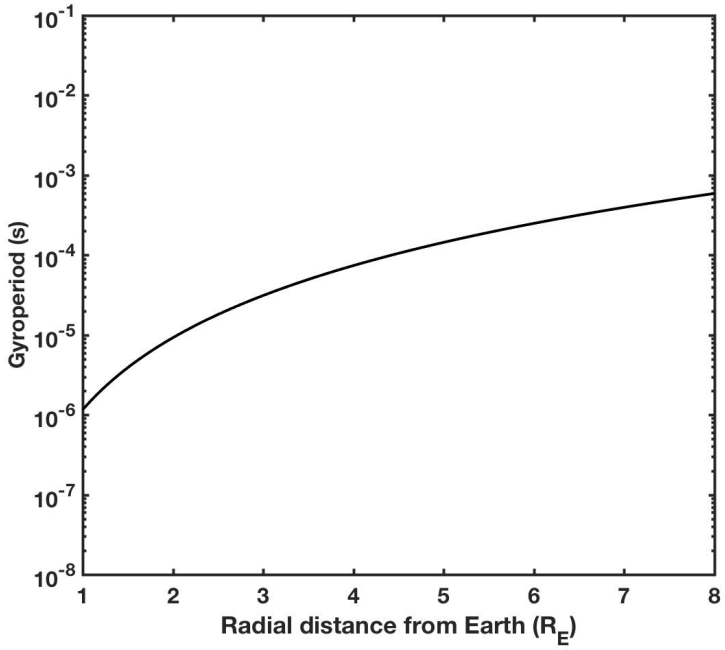

Figure 1.6 – Gyroperiods of an electron on the geomagnetic equator at various radial distances, calculated using equation 1.7 and assuming a dipole field.

is the relativistic momentum perpendicular to the magnetic field direction. For a particle of kinetic energy E the relativistic momentum is given by

$$p^2 = (E^2 + 2m_0c^2E)/c^2 \tag{1.40}$$

where c is the speed of light.

Figure 1.6 shows typical gyroperiods for an electron on the geomagnetic equator at various radial distances. The gyroperiods shown have been calculated using equation 1.7, assuming a dipole field. For the radial distances in Figure 1.6 the gyroperiods are less than a hundredth of a second. Provided that changes to the magnetic field occur on a time frame much longer than the period of gyration, μ is conserved.

1.3.2 Second Adiabatic invariant

The second adiabatic invariant is derived from the angle action variable associated with the bounce motion of a particle between mirror points and is given by

$$J_2 = \oint \mathbf{p} \cdot d\mathbf{l} + |q| \oint \mathbf{A} \cdot d\mathbf{l}. \tag{1.41}$$

Again using Stokes theorem and remembering that the curl of **A** is equal to the magnetic field,

$$J_2 = \oint \mathbf{p} \cdot d\mathbf{l} + |q| \int \mathbf{B} \cdot d\mathbf{S}. \tag{1.42}$$

Since integration along a magnetic field line encloses no area, the second term of equation 1.42 is zero and can be neglected. Therefore the second adiabatic invariant is

$$J_2 = \oint \mathbf{p} \cdot d\mathbf{l} = \oint p \cos\alpha dl = \oint p_{\parallel} dl \tag{1.43}$$

where again, in the relativistic limit, $p_{\parallel}$ defines the relativistic velocity in the direction parallel to the magnetic field.

The second invariant is often referred to as the integral invariant. A related quantity, I, can be derived from equation 1.43 in order to remove the particle momentum from the definition and express the invariant solely in terms of the magnetic field geometry. Considering equation 1.12 and setting B_2 to be the field strength at the mirror point, B_m, and hence $\alpha_2 = 90^o$ gives

$$\cos\alpha = \left[1 - \frac{B(l)}{B_m}\right]^{1/2}. \tag{1.44}$$

The quantity I is defined as

$$I = \frac{J_2}{2p} \tag{1.45}$$

and as such, substituting in equations 1.43 and 1.44 gives

$$I = \int_{l_m}^{l'_m} \left[1 - \frac{B(l)}{B_m}\right]^{1/2} dl \tag{1.46}$$

where l_m and l'_m are the locations of the mirror points in each hemisphere.

In an idealised dipole field, the magnetic field intensity is given by

$$\mathbf{B} = -B_0(2\hat{\mathbf{r}}\cos\theta + \hat{\theta}\sin\theta)(R_E/r)^3 \tag{1.47}$$

where r is the radial distance from the centre of the dipole and B_0 is the equatorial magnitude of B at $r = 1$. The radial distance from the centre of a dipole of a field line that crosses the magnetic equator at a radial distance, L, will obey the following relation with colatitude, θ:

$$r = LR_E \sin^2\theta. \tag{1.48}$$

The parameter L has units of R_E is known as McIlwain's L value (McIlwain, 1961). Substi-

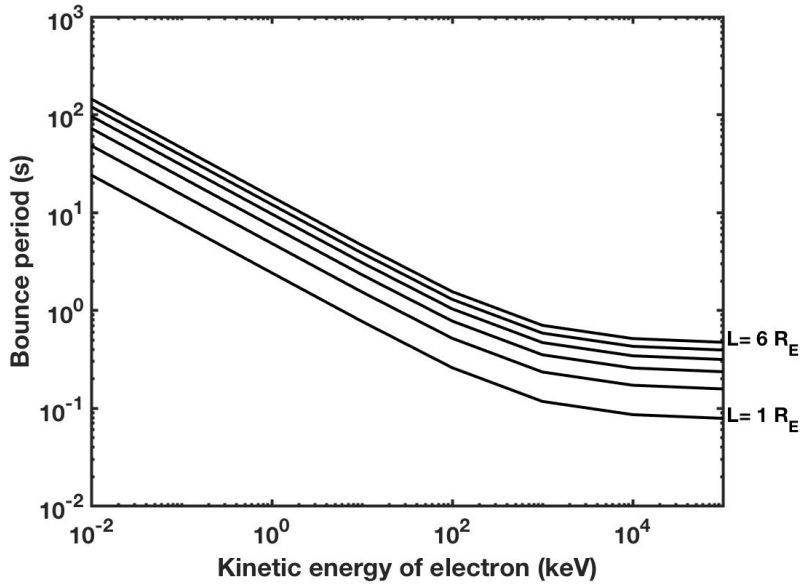

Figure 1.7 – Bounce periods of an electron with an equatorial pitch angle of 45° at various radial distances, calculated using equation 1.53 and assuming a dipole field.

tuting equation 1.48 into 1.47 and taking the magnitude of **B** gives the following expression for the magnetic field strength in a dipole field:

$$B = \frac{B_0}{L^3}(1+3\cos^2\theta)^{1/2}\csc^6\theta. \tag{1.49}$$

The bounce period of a particle in a dipole field is

$$T_{bounce} = 2\int_{l_m}^{l'_m}\frac{dl}{v_{\parallel}(l)} = \frac{2}{v}\int_{l_m}^{l'_m}\frac{dl}{\sqrt{[1-\frac{B(l)}{B_m}]}} = \frac{2}{v}\int_{l_m}^{l'_m}\frac{dl}{\sqrt{[1-\frac{B(l)}{B_{eq}}\sin^2\alpha_{eq}]}} \tag{1.50}$$

where B_{eq} and α_{eq} are the equatorial field strength and equatorial pitch angle respectively. A distance element dl of a field line in a dipole field is given by

$$dl = \sqrt{((dr)^2+(rd\theta)^2)} \tag{1.51}$$

and by differentiating equation 1.48, dr can be expressed in terms of $d\theta$. Equation 1.49 is then be substituted into equation 1.50 and the variable of integration changed from l to θ to give

$$T_{bounce} = \frac{4LR_E}{v}\int_{\theta_m}^{\pi/2}\frac{\sin\theta(1+3\cos^2\theta)^{1/2}}{\sqrt{1-\sin^2\alpha_{eq}\csc^6\theta(1+3\cos^2\theta)^{1/2}}}d\theta. \tag{1.52}$$

The integral in equation 1.52 cannot be evaluated exactly, however a good estimate is provided by Lenchek et al. (1961) for off-equatorial particles in a dipole magnetic field that differs from the numerically computed function by less than 1%. Therefore an approximate formula for the bounce time is given by

$$T_{bounce} = \frac{4R_E L}{v}(1.3802 - 0.3198(\sin\alpha_{eq} + \sin^{1/2}\alpha_{eq})). \tag{1.53}$$

Equation 1.53 has been used to calculate the bounce times shown in Figure 1.7 for electrons in a dipole field with an equatorial pitch angle of 45°. Provided that large scale changes in the magnetic field occur on time frames longer than the bounce time, J (and therefore I) may be treated as an invariant. Notice that equation 1.53 gives a finite bounce period for particles with an equatorial pitch angle of 90^o. As α_{eq} tends to 90^o, the denominator in the integral of equation 1.52 tends to zero and the integral cannot be evaluated.

1.3.3 Third Adiabatic Invariant

A final adiabatic invariant may be derived from the action angle variable associated with the drift motion of an electron. In the absence of electric fields, the geomagnetic field will cause charged particles to drift around the Earth due to the gradient and curvature drifts discussed in sections 1.2.3.2 and 1.2.3.3. Integrating equation 1.35 over the periodic drift motion gives the third adiabatic invariant

$$J_3 = \oint (\mathbf{p} + q\mathbf{A}) \cdot d\mathbf{l}. \tag{1.54}$$

The first term of equation 1.54 is neglected as $\mathbf{v}_d$ is generally orders of magnitude smaller than the total particle velocity $\mathbf{v}$ and thus the average momentum $\mathbf{p}$ in the drift direction is small. By employing Stoke's theorem and using $\nabla \times \mathbf{A} = \mathbf{B}$ the third invariant becomes

$$J_3 = q \oint \mathbf{B} \cdot d\mathbf{S}. \tag{1.55}$$

As the charge of the particle is constant, the quantity Φ can be extracted

$$\Phi = \oint \mathbf{B} \cdot d\mathbf{S} \tag{1.56}$$

which is the magnetic flux enclosed by the drift path. The third invariant therefore implies that the total flux enclosed within a particle drift shell is constant provided that large scale changes in the magnetic field occur on time scales longer than the particle drift period. For a perfect dipole field, this yields circular drift paths. Walt (1994) gives the following

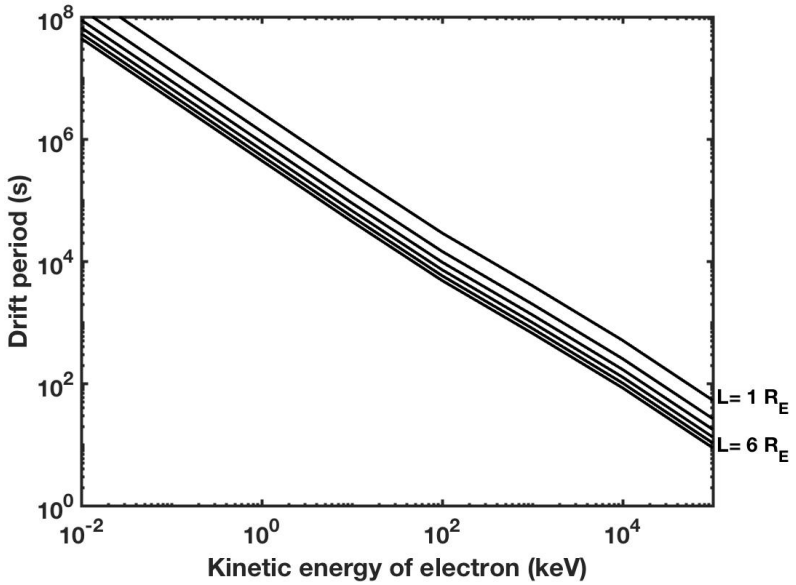

Figure 1.8 – Drift periods of an electron with an equatorial pitch angle of 90° at various radial distances, calculated using equation 1.57 and assuming a dipole field.

approximate expression for the drift time of electrons in a dipole field, assuming that no electric fields are present

$$T_{drift} = (1.557 \times 10^4)\frac{1}{L}\frac{1}{\gamma\beta^2}[1 - 0.3333(\sin\alpha_{eq})^{0.62}] \tag{1.57}$$

where $\beta = v/c$, $\gamma = (1/\sqrt{1-\frac{v^2}{c^2}})$, and c denotes the speed of light in a vacuum. Equation 1.57 has been used to calculate the drift periods shown in Figure 1.8 for an equatorially mirroring electron.

The pitch angle dependence of equation 1.57 can be used to examine the relative strengths of the gradient and curvature drifts in a perfect dipole field. An electron with a 90° equatorial pitch angle will experience a magnetic drift arising solely from the gradient in the field. However, an electron with very low equatorial pitch angle, e.g. 5°, will experience a much weaker $\nabla\mathbf{B}$ drift but will also have a drift velocity component originating from the curvature drift. Figure 1.9 shows the drift time for both a 90° and 5° equatorial pitch angle electron. The 90° electron showed shorter drift periods indicating that the gradient drift is moderately stronger than the curvature drift. As a result, electrons with equatorial pitch angles closer to 90° will drift around the Earth faster than electrons of low equatorial pitch angle.

It should be noted that for the drift times calculated from equation 1.57, shown in Figures 1.8 and 1.9, $\mathbf{E} \times \mathbf{B}$ drifts have been neglected. These drifts are particularly important for

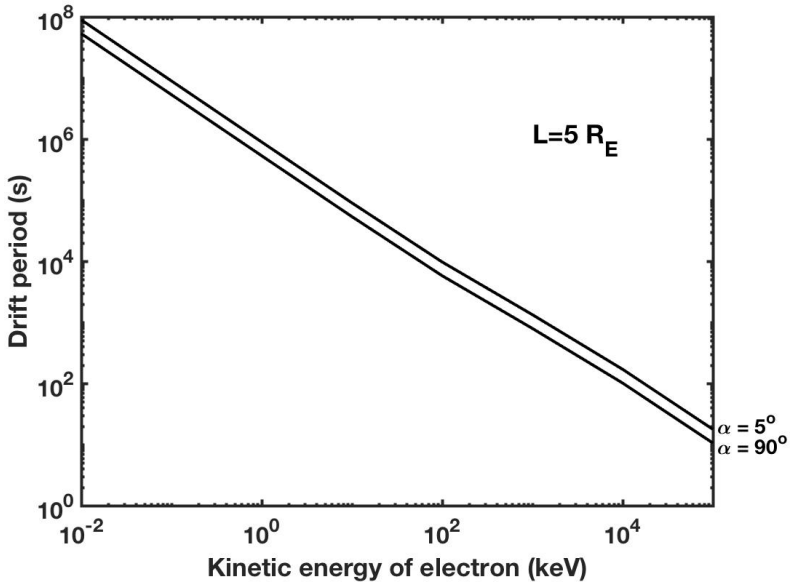

Figure 1.9 – Drift periods of an electron with an equatorial pitch angle of either 90° or 5°, calculated using equation 1.57 and assuming a dipole field.

electrons with energies less than several hundred keV and are likely to alter the drift times shown for these energies. However, to a first approximation, the presented time scales illustrate the periods for changes in the geomagnetic field below which the third adiabatic invariant can be assumed to be constant.

1.3.3.1 Roederer's L^* Parameter

A variation of the third adiabatic invariant is the Roederer L^* parameter, which in a perfect dipole field is equal to the McIlwain L parameter introduced by equation 1.48. L^* is defined as

$$L^* = \frac{2\pi B_0 R_E^2}{\Phi} \tag{1.58}$$

where B_0 is the magnetic field strength at the magnetic equator on the Earth's surface (Roederer and Zhang, 2014). For the geomagnetic field, considering the L^* parameter instead of the McIlwain L is advantageous as, at a constant value of L^*, changes in the plasma population resulting from adiabatic changes in the magnetic field can be filtered out. For a static or slowly changing magnetic field, an electron will follow constant L^* for the entirety of its drift path.

1.4 The Magnetosphere and the Sun-Earth System

Previous sections have introduced magnetic trapping of charged particles in the geomagnetic field as well as the motions of these trapped particles. Several trapped plasma populations exist in the geomagnetic field, of terrestrial or solar origin. These plasma populations can vary with time in response to changes in the Sun-Earth system.

1.4.1 The Sun and the Solar Wind

The Sun ejects plasma into interplanetary space at supersonic speeds, and this radially outflowing plasma is called the solar wind. Due to the high conductivity of the plasma, the solar magnetic field is transported outwards by the flow and is known as the interplanetary magnetic field (IMF).

The speed of solar wind originating from the Sun varies depending on the source region. Coronal holes are regions of open solar field lines and reduced coronal temperature and density that tend to emit solar wind with faster speeds than elsewhere. A coronal hole emitting fast solar wind ($\gtrsim$650 km s^{-1}), surrounded by regions of slower solar wind emission, results

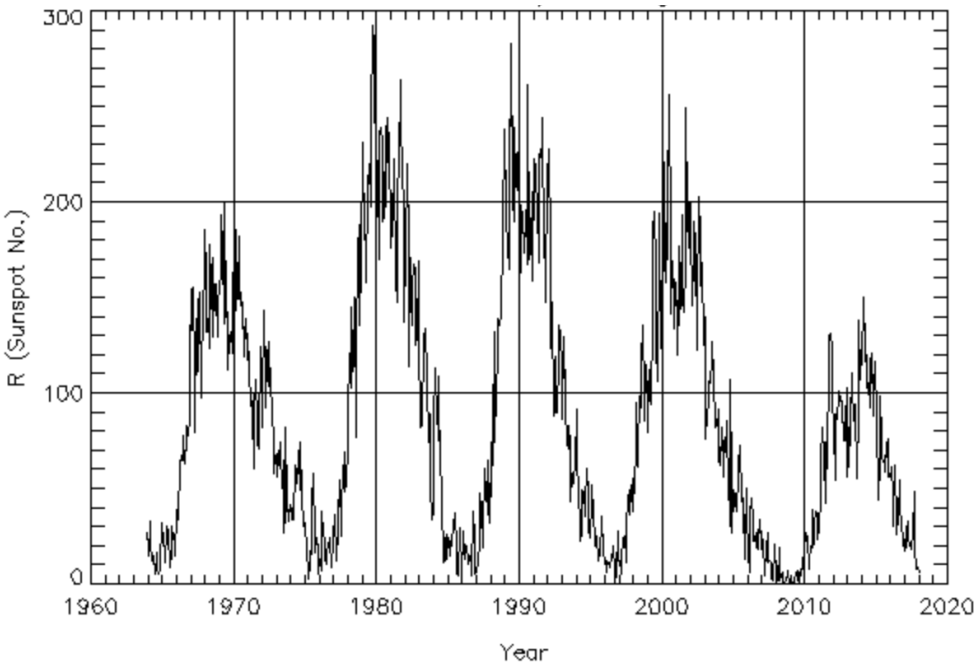

Figure 1.10 – Changing sunspot number from 28/11/1963 till 30/01/2018 showing the last five solar cycles.

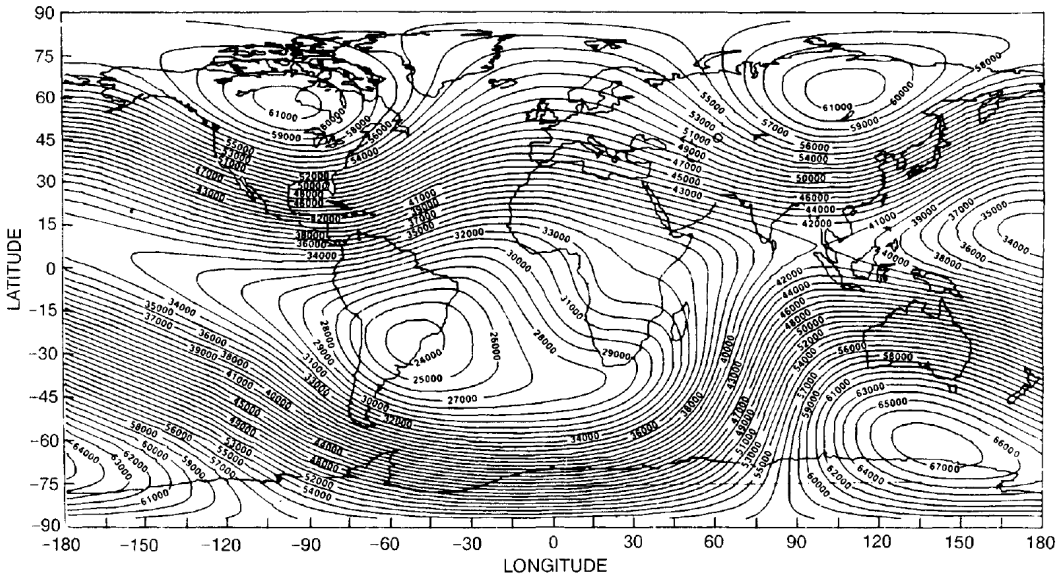

Figure 1.11 – Contours of constant geomagnetic field at the Earth's surface in the Mercator map projection. The magnetic field intensities are given in units of nT (Walt, 1994).

in a stream interface, with a compression of magnetic field lines and an elevated density. This structure is known as a co-rotating interaction region (CIR) or high speed stream (HSS).

Sometimes coronal structures become unstable and are "ejected" as a coronal mass ejection (CME). CMEs are highly energetic events that release large quantities of coronal matter into space. Some CMEs are associated with solar energetic particle (SEP) events which are highly energetic protons and electrons (keV to GeV energies) that originate from the sun (Pande et al., 2018). In some cases, SEP events can be largely dominated by protons and are referred to as solar proton events.

Observations of the sun have shown that the number of sunspots on its surface oscillates with a period of roughly 11 years, a variation known as the solar cycle (Figure 1.10). Geomagnetic activity reflects the solar cycle variations, with high magnetic activity correlated with solar maximum and the declining phase of the solar cycle (Chapman and Bartels, 1962).

1.4.2 The Magnetosphere

1.4.2.1 The Earth's Magnetic Field and the Dungey cycle

The primary component of the Earth's magnetic field originates from the convective motion of conductors, deep in the Earth's interior. The resulting geomagnetic field is somewhat dipole-like in configuration, with the magnetic axis offset from the rotation axis by approximately

11^{o}. As shown by the magnetic isocontours of Figure 1.11, the magnetic poles are located over northern Canada and southern Australia, with the northern hemisphere containing magnetic south and the southern hemisphere containing magnetic north. In addition to the magnetic poles, Figure 1.11 also shows a large region of reduced field located near the east coast of South America. This region is known as the South Atlantic Anomaly (SAA) and has the effect of causing charged particles to mirror at lower altitudes over these longitudes.

The dipole-like shape of the geomagnetic field is distorted by the solar wind and IMF. The solar wind undergoes an abrupt transition from supersonic to subsonic flow when reaching the magnetosphere, producing a bow shock. This interaction acts to compress the Earth's magnetic field on the day side, while the solar wind flow past the Earth elongates the field on the night side, forming the magnetotail. The dipole-like configuration may then be further deformed by a process known as magnetic reconnection. Earthwards of the bow shock and subsonic magnetosheath plasma is the boundary layer between the magnetosphere and the IMF, known as the magnetopause. When the IMF has a southward orientated component, the IMF and geomagnetic field have opposed components at the magnetopause, and reconnect in a diffusion region. In three dimensional space the reconnection location is known as the X-line. Once reconnected, magnetic field lines which previously were 'closed', with both ends connected to the Earth, become 'open', linking the geomagnetic field and the IMF. The newly opened magnetic flux is swept anti-sunwards by the solar wind, into the magnetotail. Continual loading of magnetic flux into the magnetotail increases the magnetic pressure, forcing open field lines attached to different hemispheres to again reconnect in a diffusion region located in the plasma sheet (see section 1.4.2.2), reforming closed field lines. The newly closed magnetic field then convects back to the day side where the process repeats. This large scale motion of the magnetic field and plasma is known as the Dungey cycle and is paramount to many of the processes and plasma populations in the magnetosphere (Dungey, 1961).

Figure 1.12 shows a schematic of the magnetosphere, illustrating the compressed field on the day side and the magnetic lobes in the extended magnetotail. The term 'polar cap' refers to the region in each hemisphere containing the footprints of the open field lines. When day side reconnection occurs at a faster rate than night side reconnection the polar cap area increases and the magnetopause distance will reduce as a result of the magnetic erosion. Likewise, when the night side reconnection rate surpasses the day side the polar cap area will reduce. The magnetopause boundary layer between the IMF and the geomagnetic field has also been labelled in Figure 1.12.

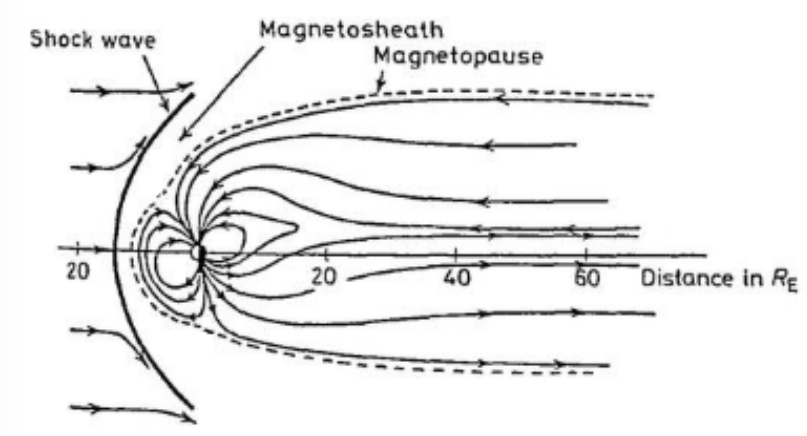

Figure 1.12 – Schematic of the non-midnight cross section of the magnetosphere, showing the shock wave or bow shock, magnetosheath, and magnetopause (Hargreaves, 1979).

The location of the magnetopause is dependent on the solar wind conditions and has important implications for the plasma populations within the magnetosphere. A widely used empirical relationship between solar wind parameters and the radial distance of the day side magnetopause location, $R_{magnetopause}$, was derived by Shue et al. (1998):

$$R_{magnetopause} = [10.22 + 1.29\tanh(0.184(B_z + 8.14))]D_p^{-\frac{1}{6.6}} \tag{1.59}$$

where B_z is the z-component of the IMF and D_p is the solar wind dynamic pressure. Later comparison between the Shue model and Cluster satellite observations of the magnetopause location showed an overestimation of 1 R_E and, as such, a 1 R_E correction is often applied to the Shue model value (Case and Wild, 2013).

1.4.2.2 The Plasma sheet

The reconnection process described in the previous section allows the formation of the plasma sheet. Following reconnection, magnetosheath plasma may enter the magnetosphere on open field lines and be swept anti-sunwards, into the night-side tail region. Additionally, terrestrial plasma can also populate the open field lines in the tail by the polar wind (outflow from the ionosphere in the polar cap regions). Tail side reconnection of open field lines then traps the plasma, from either terrestrial or solar origin, in the magnetosphere, forming a population known as the plasma sheet.

The plasma sheet consists of both ions and electrons with energies of a few keV and carries the electric current that separates the oppositely directed magnetic fields in the two

lobes of the magnetotail. In some form, the plasma sheet extends out to at least the lunar orbit ($\sim$60 R_E) reducing in thickness and number density with increasing distance from the Earth (Hill, 1974). At a distance of 18 R_E the plasma sheet has a thickness of approximately 6 R_E in the midnight sector, flaring out to twice this distance at the dawn and dusk sides of the magnetosphere.

As the plasma sheet lies between two oppositely directed magnetic lobes, the northern and southern lobes can reconnect, returning to a dipole form, and excess energy is communicated to the plasma. Material on newly the reconnected magnetic field can travel earthwards and a parcel of plasma and magnetic field, known as a plasmoid, is ejected down-tail.

1.4.2.3 Substorms

Section 1.4.2.1 introduced the cyclic motion of the magnetic field arising from dayside and nightside reconnection. If the opening of magnetic flux on the dayside is approximately equal to the closing of magnetic flux on the nightside for an extended period then the polar cap is relatively stable in size, as the amount of open flux is constant. When this balance arises while the IMF has a southwards component, a steady magnetospheric convection event occurs (Sergeev et al., 1996).

Conversely, substorms are the series of events associated with unbalanced reconnection rates. A substorm can be sectioned into three phases: the growth phase, expansion phase, and recovery phase. The first phase, the growth phase, is usually initiated by a southwards turning of the IMF. Enhanced dayside reconnection occurs, dominating nightside reconnection and open magnetic flux accumulates in the tail lobes, causing the polar cap to expand towards lower latitudes. The additional magnetic flux in the tail lobes leads to an intensification of the neutral sheet current by Ampère's law, stretching the field lines bisecting the plasma sheet into a more tail-like configuration. During the growth phase, the aurora appears in the form of auroral arcs.

The substorm onset, marking the start of the expansion phase, is observed as the sudden brightening of one of the auroral arcs in the midnight sector. At this point, the magnetic flux in the tail lobes has built up sufficiently to cause explosive nightside reconnection at 20 - 25 R_E (Hones, 1976). The enhanced nightside reconnection rate rapidly closes the open magnetic flux in the magnetotail and the stretched near-Earth magnetic field now becomes more dipole-like in structure. There is a reduction in the cross tail current at the near edge of the plasma sheet as current flow is diverted down towards the Earth along magnetic field lines, westwards through the auroral ionosphere, and back up the field, returning to the plasma sheet. This new current system is known as the substorm current wedge and is instrumental

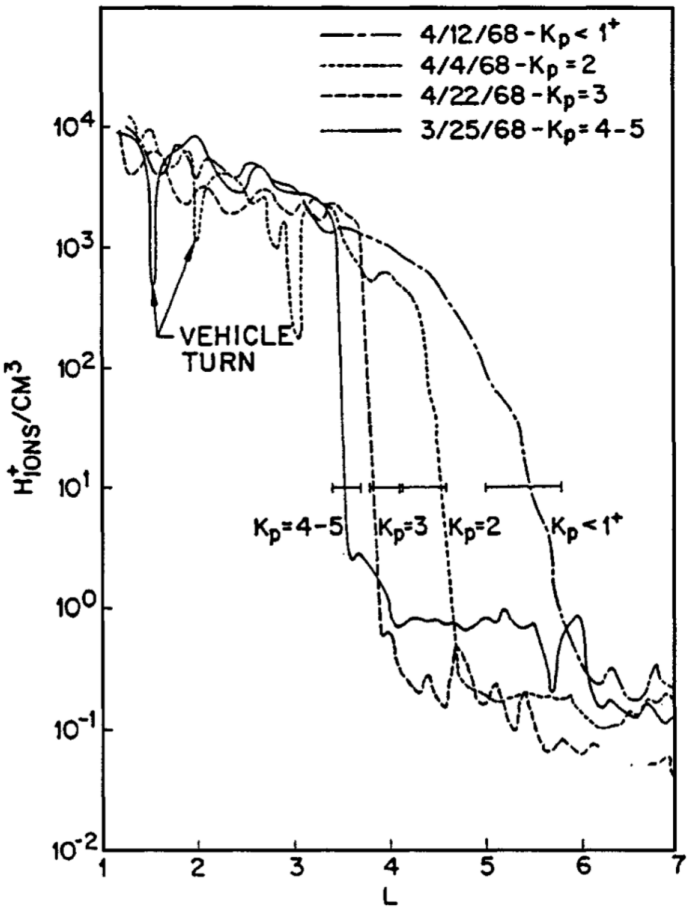

Figure 1.13 – Density in the equatorial plane of H+ at different L-shells as measured by OGO-5. Measurements taken during different geomagnetic conditions (different values of Kp) are shown (Cravens, 1997).

for the extreme auroral brightening and bulge expansion observed. During the substorm expansion phase ions and electrons are injected into the inner magnetosphere from the plasma sheet (Akasofu, 1964; McPherron et al., 1973).

In the recovery phase of a substorm, the polar cap contracts and the aurora fades. This phase typically lasts from 1 - 2 hours and ends when the magnetosphere has returned to a quiet state.

1.4.2.4 The Plasmasphere

Ionospheric plasma flows up the magnetic field and supplies the inner magnetosphere with a population of cold thermal ions and electrons that have energies less than 1-2 eV. Due to the low particle energies, $\mathbf{E} \times \mathbf{B}$ drift dominates over the gradient and curvature magnetic

drifts and the particles follow the equipotential contours shown in the third panel of figure 1.3. Inside the corotation - convection separatrix, ions and electrons co-rotate with the Earth, forming the plasmasphere, while outside, the low energy plasma is lost to the magnetopause. The plasma density in the plasmasphere significantly exceeds the density in the surrounding magnetosphere, owing to the closed particle drift paths. A sharp density gradient defines the edge of the plasmasphere, as shown in figure 1.13, a boundary known as the plasmapause.

As the convection electric field is not constant in time, instead varying with solar wind conditions, the location of the plasmapause is also activity dependent. When the convection electric field increases, the Alfvén layer (see section 1.2.3.1) moves closer to the Earth. If the timeframe for an increase in the convection electric field is faster than the drift period for a plasmaspheric particle ($\sim$24 hours) then the outermost plasma, previously on closed drift paths will instead follow an open drift trajectory. This part of the plasma is convected sunwards, forming a filament between the plasmasphere and magnetosphere known as a plasmaspheric plume.

Once the convection electric field subsides, the plasmasphere expands, slowly refilling. Refilling proceeds steadily until the plasmasphere reaches a density level where diffusive equilibrium with the ionosphere is achieved. Data has shown that the timescale for the plasmasphere to refill depends on the L value, $\sim$1 day at L = 2.5 and $\sim$8 days at L = 4 (Park, 1974).

1.4.2.5 The Ring Current

Both the gradient and curvature drifts, introduced in sections 1.2.3.2 and 1.2.3.3 respectively, are charge dependent (see Equations 1.32 and 1.34). The result is that, for ions at energies where the drift motion is dominated by the magnetic drifts, positive and negative charges travel azimuthally around the Earth in opposite directions. This differential motion of the ions and electrons creates a westward directed current flow known as the 'ring current' and generates a magnetic field, as prescribed by Ampère's law, which tends to oppose the basic geomagnetic field near the equator. Larger equatorial field depressions arise as the particle content, and total energy, of the ring current increases (Dessler and Parker, 1959; Sckopke, 1966).

Although all trapped particles in the inner magnetosphere contribute to the ring current, $\sim$10 keV to hundreds of keV ions contribute substantially to the total current density (Williams, 1987), while electrons supply a negligible portion of the energy (Baumjohann, 1993). The ring current is situated throughout the region where electrons and ions may

complete closed magnetic drifts around the Earth and thus extends over geocentric distances between $\sim$2 R_E and $\sim$9 R_E (Daglis et al., 1999).

1.4.2.6 Geomagnetic Storms

Geomagnetic storms are periods of intense solar wind - magnetosphere coupling, during which a large amount of energy is loaded into the magnetosphere, driving significant intensifications of the ring current. Primarily, magnetic storms are associated with conditions in the solar wind such as CMEs or CIRs (Hutchinson et al., 2011).

Geomagnetic storms typically exhibit three distinct phases. The initial phase is characterised by a positive magnetic field disturbance, associated with increased solar wind dynamic pressure compressing the magnetosphere and strengthening the day-side magnetic field.

The main phase corresponds to an enhancement of the ring current, and the total field at the Earth's surface is thus reduced. Generally, the main phase is initiated by a sustained period of southward IMF, allowing continual substorm activity to energise the ring current.

The third phase, known as the recovery phase, is often triggered by a weakening or a northwards turning of the IMF, resulting in ring current particles being lost faster than they are supplied. The depression of the geomagnetic field subsides as the ring current decays,

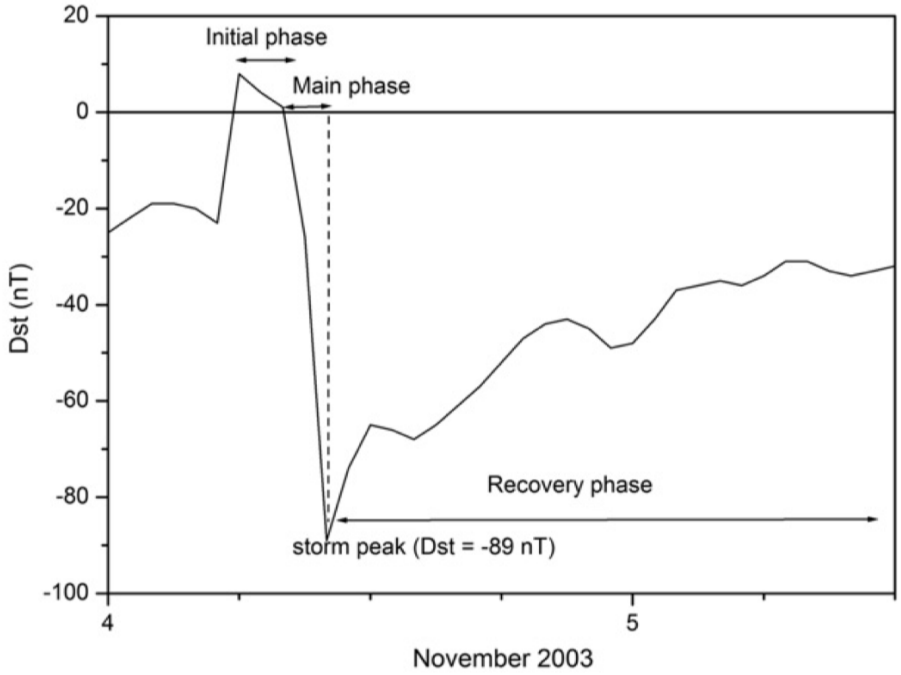

Figure 1.14 – Example of the Dst index for a geomagnetic storm on 4 - 5 November 2003, highlighting the initial phase, main phase, and recovery phase (Echer et al., 2011).

and geomagnetic conditions gradually return to the pre-storm state. The decay processes for the ring current include coulomb collisions within the plasmasphere, charge exchange with neutral hydrogen, and wave-particle interactions (Fok et al., 1995; Jordanova et al., 1996).

Global variations in the horizontal component of the magnetic field close to the magnetic equator can be represented by the disturbance storm time (Dst) index. Ground-based stations, between 20^o and 30^o from the magnetic equator, record the horizontal component of the Earth's field. Quiet time variation baselines are subtracted from these observations and correction factors for the latitude variations of the stations are applied. All data is then averaged to supply an hourly Dst index which is positive when the magnetic field is enhanced and negative when the field is depressed. Stations at low latitudes are used so as to eliminate possible disturbances originating from the auroral zones. Additionally, stations are not situated directly at the equator as an ionospheric current system know as the equatorial electrojet can also produce magnetic field perturbations (Baumjohann and Treumann, 1996; Sugiura, 1964; Sugiura and Poros, 1971).

1.4.2.7 The Radiation Belts

The Earth's radiation belts are a region of energetic charged particles trapped by the terrestrial magnetic field. Typically, these field-aligned populations exhibit a two belt structure, comprising of an inner belt and outer belt separated by a sparsely populated slot region. The inner radiation belt typically extends from $\sim$1.2 to $\sim$2.5 Earth radii and consists of energetic protons produced by cosmic ray albedo neutron decay (CRAND) and trapped solar protons (Selesnick et al., 2014, 2007). Electrons are also found in the inner radiation belt region, largely originating from injections, as the CRAND process is not thought to be a significant source of trapped electrons (Lenchek et al., 1961). Electron injections into the inner belt region occur fairly frequently for energies $<$600 keV, but only occasionally for higher $\gtrsim$1 MeV energies (Baker et al., 2007; Zhao and Li, 2013). As a result, for much of the 2012 - 2019 period observed by the twin Van Allen Probe mission, electrons with energies $>$900 keV were not observed in the inner zone (Fennell et al., 2015; Li et al., 2015).

The outer radiation belt extends from $\sim$3 to $\sim$8 Earth radii, for which electrons are the dominant energy carrier. The electron energies range from 1 keV to $\sim$10 MeV in this region. Compared to the inner belt, the outer radiation belt is a highly dynamic environment, affected by changing geomagnetic conditions and associated processes (Shprits et al., 2008a,b) discussed in the following section. A large number of satellites operate in the radiation belt region, and components such as solar cells, integrated circuits and sensors can be damaged or degraded by the charged particle populations (Horne et al., 2013). As a result, understanding

the formation, variability, and dynamics of the radiation environment is the subject of ongoing research.

1.5 Dynamics of the Electron Radiation Belts

Section 1.4.2.7 discussed a specific trapped particle population in the magnetosphere known as the radiation belts. Owing to the vast number of electrons which populate this region, the electron radiation belt content is generally discussed in terms of particle flux. If dA is an area element, $d\Omega$ an element of solid angle in the direction $\hat{\theta}$, then, at location $\mathbf{r}$, the number of electrons with energies between E and $E+dE$ passing through dA within $d\Omega$ of the direction $\hat{\theta}$ in a 1 second time interval is

$$dN(\mathbf{r},E,\theta) = j(E,\theta)dAdEd\Omega \tag{1.60}$$

where $j(E,\theta)$ is the differential, directional flux. The electron flux values are often presented in units of $cm^{-2}s^{-1}sr^{-1}keV^{-1}$ and the flux direction is usually given in terms of electron pitch angle (α).

The electron radiation belts are a highly variable environment where the flux can change by orders of magnitude on the time frame of hours. A number of processes are responsible for the variability and the relative importance of different mechanisms is the topic of ongoing research.

1.5.1 Wave-Particle interactions

Electromagnetic waves are generated both in the plasma region and externally (by lightning and man-made sources) and can interact with the trapped electron populations, potentially altering their energy, pitch angle and drift path. Wave-particle interactions violate one, or more, of the adiabatic invariants associated with particle motion (Schulz and Lanzerotti, 1974).

A number of electromagnetic waves exist in the magnetosphere; of particular interest for radiation belt particles are very low frequency (VLF) waves and ultra long frequency (ULF) waves.

1.5.1.1 ULF Waves and Radial Diffusion

Time-varying electromagnetic fields may be introduced to the magnetosphere by ULF waves, excited by solar wind velocity shear and pressure fluctuations at the magnetopause boundary (Bentley et al., 2018; Claudepierre et al., 2008, 2009; Ukhorskiy et al., 2006). ULF waves have frequencies of the order of a few millihertz and are sometimes referred to as Pc4 and Pc5 waves (Jacobs et al., 1964). Trapped particles can be scattered in L^* by these time-varying electromagnetic fields, a process known as radial diffusion (Elkington et al., 1999).

If the electromagnetic variations are asymmetric along a drift shell, particles can experience a cumulative displacement (Lejosne et al., 2012) and the associated change in L^* alters the values of the third invariant, Φ, while the values of μ and J remain constant. As a result, inward radial diffusion energises particles and increases the equatorial pitch angle, while outward radial diffusion leads to de-energisation, a reduction in pitch angle, and, ultimately, loss to the magnetopause. The direction of diffusion (inwards or outwards) depends on the L^* gradients of the electron populations, discussed further in section 2.1. Under suitable conditions, radial diffusion may significantly enhance or deplete the radiation belt flux.

1.5.1.2 VLF Waves

Plasma is a dispersive medium, therefore electromagnetic waves with different frequencies travel at different velocities as the refractive index, η, is frequency dependent. The dispersion relation for small amplitude waves in a cold magnetised plasma is given by

$$D(\omega,k,\tan\psi) = (S\tan^2\psi + P)\eta^4 - (RL\tan^2\psi + PS(2+\tan^2\psi))\eta^2 + PRL(1+\tan^2\psi) = 0 \tag{1.61}$$

where R, L, S, and P are the Stix parameters (Stix, 1962) and ψ is the wave normal angle (angle between the wave vector, **k**, and the background magnetic field).

$$R = 1 - \sum_\sigma \frac{\omega_{p\sigma}^2}{\omega^2}\frac{\omega(1+\Omega_\sigma)}{(\omega^2-\Omega_\sigma^2)} \tag{1.62}$$

$$L = 1 - \sum_\sigma \frac{\omega_{p\sigma}^2}{\omega^2}\frac{\omega(1-\Omega_\sigma)}{(\omega^2-\Omega_\sigma^2)} \tag{1.63}$$

$$P = 1 - \sum_\sigma \frac{\omega_{p\sigma}^2}{\omega^2} \tag{1.64}$$

$$S = 1 - \sum_\sigma \frac{\omega_{p\sigma}^2}{\omega^2}\frac{\omega^2}{(\omega^2-\Omega_\sigma^2)} \tag{1.65}$$

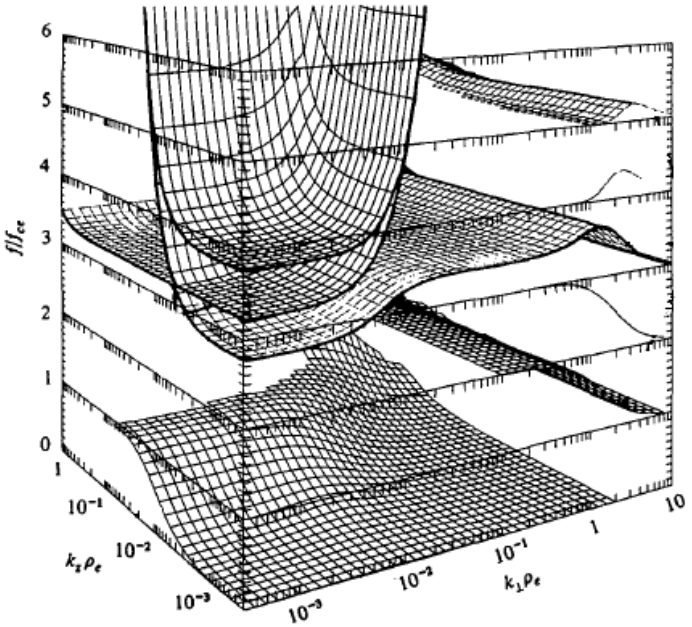

Figure 1.15 – Dispersion surfaces for an electron only plasma, showing the ratio between the wave frequency and the electron gyrofrequency on a linear scale versus wave vector components on a logarithmic scale. Adapted from Andre (1985).

Subscripts, σ, denote the particle species. The particle gyrofrequency, Ω_σ, was given previously by equation 1.8. The angular plasma frequency, $\omega_{p,\sigma}$, describes the oscillation of charged particles about their equilibrium position, and for particle species σ is defined as

$$\omega_{p,\sigma}^2 = \frac{n_\sigma q_\sigma^2}{\varepsilon_0 m_\sigma} \tag{1.66}$$

where n_σ is the number density, q_σ the charge, m_σ the particle mass, and ε_0 the vacuum permittivity.

The dispersion relation is a quadratic equation in η^2 and therefore, as $\eta = ck/\omega$, solutions relate the wave number, k, and frequency, ω, of waves that can exist in a plasma. Where $\eta^2 < 0$, solutions are imaginary and correspond to non-propagating evanescent waves which are purely damped. Analytical solutions of equation 1.61 can be given for parallel propagating waves ($\psi = 0^o$) and in cases when $\mathbf{k}$ and $\mathbf{E}$ lie in the same direction ($\psi = 90^o$). For all other wave normal angles, the dispersion relation must be solved numerically.

Dispersion surfaces, given by equation 1.61 for an electron only plasma are shown in figure 1.15 for ψ values from 0^o ($k_z\rho_e$ plane) to 90^o ($k_\perp\rho_e$ plane). Note that at each wave normal angle there are usually several 'branches' given by the dispersion relation. These

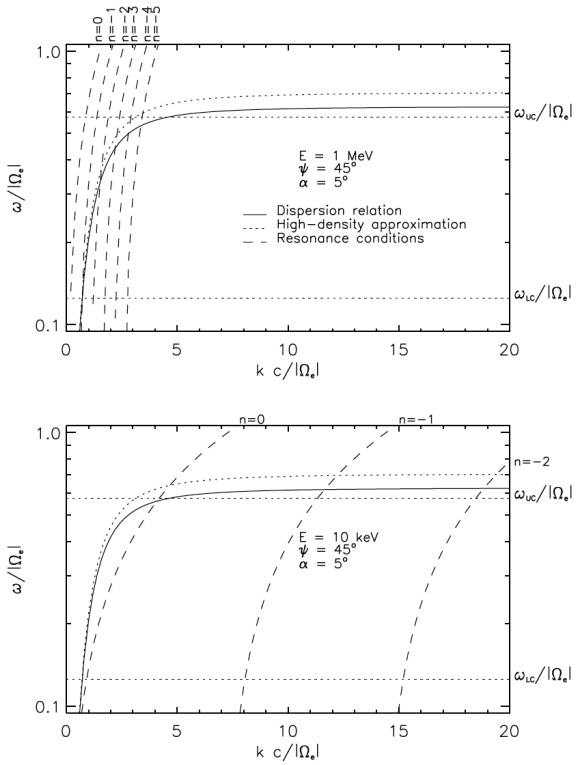

Figure 1.16 – The dispersion curves (solid lines) for $\omega_{p,e}/\Omega_e = 1.5$, and a wave normal angle of 45^o. Dashed lines are the resonance conditions for a various values of n for a 1 MeV electron (top panel) and a 10 keV electron (bottom panel). (Glauert and Horne, 2005).

branches can be further divided by the polarisation of the wave. Right-hand polarised waves rotate clockwise when looking along B_0 in the same sense as electron gyration, while left-hand polarised waves in the same direction as ion gyration. A dispersion surface of particular note describes whistler mode waves. These are right-hand polarised waves that occur at frequencies below the electron gyrofrequency.

For efficient energy transfer between a specific particle and wave, a resonant interaction is required, meaning that the particle and wave must maintain the same phase relation for a sufficient period of time. Resonance is achieved when a particle and wave have the same angular frequency i.e. $\omega = \Omega_\sigma$. However, it was shown that resonance is still possible when $\omega < |\Omega_\sigma|$ (as is the case for whistler mode waves) if the wave frequency is Doppler shifted up to the cyclotron frequency of the particle (Kennel and Petschek, 1966). The resonance condition defines the frequency, ω, at which an n^{th} order resonance occurs for a given wave vector and particle velocity

$$\omega - k_\parallel v_\parallel = \frac{n\Omega_\sigma}{\gamma} \tag{1.67}$$

where γ is the relativistic factor and introduces the component of the particle velocity perpendicular to the magnetic field, $v_\perp$. Frequencies where resonant wave-particle interactions occur are therefore the intersections between the resonance curves given by equation 1.67 and the dispersion relation. In other words, a resonance can occur when a given wave vector yields the same frequency value in both the resonance condition and dispersion relation. Figure 1.16 shows dispersion relations and resonance curves for a 1 MeV (top) and 10 keV (bottom) electron with an equatorial pitch angle of 5^o.

The Landau resonance is the specific case when $n = 0$ where waves with a parallel phase velocity $\sim \omega/k_{parallel}$ interact strongly with particles that have a similar parallel velocity, provided the wave has a parallel electric field. Whistler mode waves that propagate entirely along the background magnetic field have no parallel electric field component and therefore do not interact with particles via the Landau resonance.

Doppler shifted cyclotron resonance arises when the particle experiences the wave frequency Doppler shifted to a multiple of its gyrofrequency ($n \neq 0$). Under these conditions, the wave electric field rotates at n times the rate of the particle and depending on the initial phase of the wave, the particle can be accelerated or decelerated, altering the pitch angle and energy. For whistler mode waves propagating along the magnetic field, the frequency must

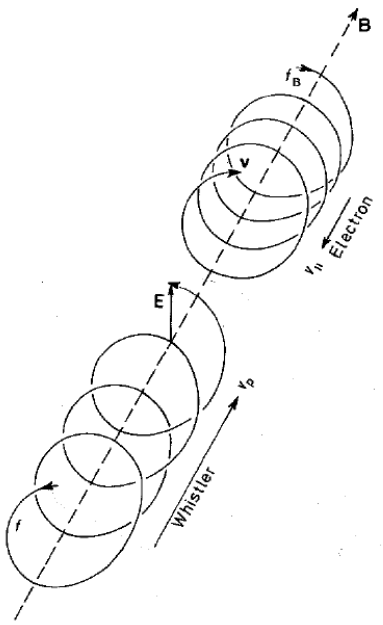

Figure 1.17 – Motion of an electron and the **E** field of a whistler mode wave about the geomagnetic field (Hargreaves, 1979).

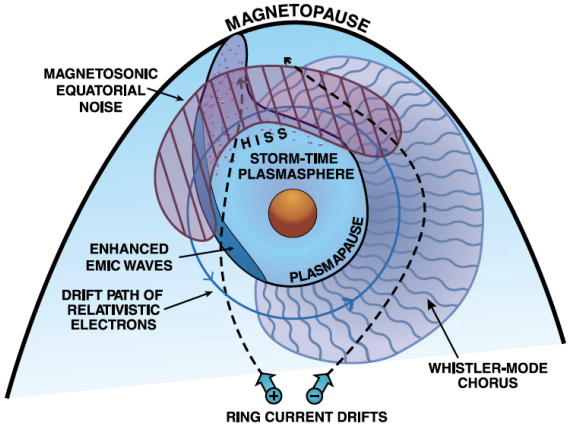

Figure 1.18 – Schematic of the spatial distribution of various waves in the inner magnetosphere in relation to the plasmasphere and the drifts of a 10 - 100 keV charged particle and a relativistic electron (Thorne, 2010).

be Doppler shifted up for resonance with electrons, and therefore the waves resonate with electrons travelling in the opposite direction as illustrated by figure 1.17.

A number of different wave modes can propagate in the inner magnetosphere. Of particular importance for radiation belt physics are the VLF waves illustrated in Figure 1.18. Note that waves tend to occur over a limited magnetic local time range and, therefore, electrons can encounter different waves during different parts of their azimuthal drift. Whistler mode chorus waves, plasmaspheric hiss, and electromagnetic ion cyclotron (EMIC) waves are known to be of particular importance for the Earth's electron radiation belts and are discussed below.

Chorus waves

Chorus waves are right-hand circularly polarised waves with frequencies below the local electron cyclotron frequency (f_{ce}), and therefore correspond to the whistler mode branch of the dispersion relation. Typical chorus wave frequencies range from a few hundred hertz to a few kilohertz. A banded structure is commonly observed, separating chorus waves into two distinct frequency ranges known as lower band, covering $0.1f_{ce}$ to $0.5f_{ce}$, and upper band chorus, $0.5f_{ce}$ to $0.9f_{ce}$ (Tsurutani and Smith, 1974). Chorus is generally observed outside of the plasmasphere, and are strongest in the dawn sector (Meredith et al., 2001).

Chorus waves are excited through cyclotron resonance with anisotropic $1\sim10$s keV electrons, injected from the plasma sheet into the inner magnetosphere during substorm activity (Hwang et al., 2007; Li et al., 2009). It is thought that the wave generation process

takes place near the equatorial plane, where chorus is near field aligned (Omura et al., 2007), and propagate away from this region, becoming more oblique at higher latitudes (Horne and Thorne, 2003). Additionally, due to Landau damping by superthermal electrons, chorus displays small propagation lengths on the nightside which increase with increasing MLT and maximise on the dayside (Bortnik et al., 2007).

Pitch-angle scattering during cyclotron and Landau resonance with chorus emissions provides a major mechanism for scattering electrons into the loss cone for a broad range of electron energies (Hikishima et al., 2009; Lam et al., 2010). This pitch angle scattering is the dominant scattering process leading to diffuse auroral precipitation (Ni et al., 2008; Nishimura et al., 2010). Chorus waves also cause local acceleration of the trapped radiation belt particles, transferring energy from the substorm injected low-energy (few keV) populations to the trapped high energy radiation belt electrons (Horne and Thorne, 2003). Studies have shown that chorus waves are important for flux enhancement events, especially in regions with a low plasma density (Horne et al., 2003, 2005a; Meredith et al., 2002).

Plasmaspheric hiss

Plasmaspheric hiss is a broadband and structureless whistler mode emission that occurs primarily inside the dense plasmasphere and in dayside plasmaspheric plumes. Hiss has typical frequencies between tens of hertz and several kilohertz (Li et al., 2015) and demonstrates a day-night asymmetry, with strongest emissions observed between noon and dusk (Meredith et al., 2004). Near the equatorial plane, hiss waves are nearly field-aligned, but become more oblique at higher latitudes (Ni et al., 2013). Ray tracing modelling has shown that hiss largely originates from a subset of chorus waves which avoid Landau damping during propagation and travel into the plasmasphere, becoming trapped by the high density plasma. Inside the plasmasphere, the discrete chorus emissions merge together to form plasmaspheric hiss (Bortnik et al., 2008). Formation from chorus alone is not sufficient to fully explain typical hiss wave powers (Chen et al., 2012a) suggesting that, in part, hiss also originates from in situ wave growth inside the plasmasphere (Chen et al., 2012b; Thorne et al., 1973).

Inside the plasmapause, hiss waves are an important scattering mechanism for radiation belt electrons, leading to atmospheric loss (Meredith et al., 2006a; Summers et al., 2008). Furthermore, hiss waves significantly impact the structure of Earth's electron radiation belts and are primarily responsible for the formation of the quiet time slot region (Lyons and Thorne, 1973; Meredith et al., 2007, 2006b).

EMIC waves

EMIC waves are left-hand polarised waves that typically have frequencies of a few hertz, separated into distinct frequency bands. Hydrogen band EMIC waves occur at frequencies between the proton cyclotron frequency and the helium ion cyclotron frequency, while helium band EMIC waves range between the helium ion cyclotron frequency and the oxygen ion cyclotron frequency. Generally, hydrogen band EMIC waves are observed outside the plasmasphere, while helium band EMIC waves are observed at locations inside and outside of the plasmasphere (Fraser and Nguyen, 2001). EMIC waves are excited by the temperature anisotropy of ring current ions with energies in the 10-100 keV range (Cornwall et al., 1970) and are generally found in the dusk sector, as shown by Figure 1.18 (Bossen et al., 1976; Meredith et al., 2014).

Due to the opposite polarisation, resonance with EMIC waves is not possible for all electron energies. Relativistic electrons are thought to 'overtake' EMIC waves and, as such, in the frame of reference of the particle, the wave polarisation is reversed and cyclotron resonance can occur. Therefore, EMIC waves generally resonate with $>$2 MeV electrons (Albert, 2003; Summers and Thorne, 2003), however this minimum resonant energy can reduce in regions of localised high magnetic field strength or high plasma density (Meredith et al., 2003b). Additionally, resonant EMIC wave interactions are typically limited to electrons that have pitch angles $\lesssim 60^o$. At these pitch angles, EMIC waves are an efficient mechanism for pitch angle scattering (Kersten et al., 2014; Usanova et al., 2014), resulting in losses to the atmosphere (discussed in section 1.5.3.1). EMIC waves are thought to significantly contribute to the decay of the radiation belts (Horne and Thorne, 1998; Qin et al., 2018) and the thinning of pitch angle distributions (Usanova et al., 2014).

1.5.2 Radial Transport

Radial transport leads to motion of the plasma across the magnetic field. Section 1.5.1.1 introduced radial diffusion, whereby electrons gradually diffuse in L^* due to small perturbations in the field, such as those introduced by ULF waves. While radial diffusion is a form of radial transport, radial transport is not always a diffusive process. Large scale changes in the convection electric field, or rapid magnetic field compressions can alter electron drift paths non-diffusively. As electrons with energies $<$500 keV are most affected by the $\mathbf{E} \times \mathbf{B}$ drift and have the longest drift periods, radial transport is particularly important for lower energy electrons.

1.5.3 Loss processes

Electrons leave the radiation belt region by being lost to either the atmosphere or the magnetopause. Both processes violate the adiabatic invariants discussed in section 1.3.

1.5.3.1 Losses to the Atmosphere

As described in section 1.2.2, electrons spiral along the terrestrial field and undergo magnetic mirroring in each hemisphere. The magnetic field strength required for an electron with an equatorial pitch angle of α_{eq} to undergo magnetic mirroring is $B_m = B_{eq}/\sin^2 \alpha_{eq}$, where B_{eq} is the strength of the magnetic field in the equatorial plane of the bounce motion. For equatorial pitch angles less than $\alpha_{LC} = \sin^{-1} \sqrt{(B_{eq}/B_a}$, where B_a is the field intensity at the top of the atmosphere ($\sim$100 km), B_m occurs at altitudes inside the Earth's atmosphere. Electrons with $\alpha_{eq} < \alpha_{LC}$ therefore enter the atmosphere during each bounce, where the overall density of particles becomes large enough for loss due collisions, and are rapidly removed from the trapping region.

As the geomagnetic field has some north-south asymmetries, B_a may differ between the two hemispheres. In such instances, the bounce loss cone angle, α_{LC}, is defined by the lower value of B_a.

Furthermore, primarily due to the South Atlantic Anomaly (SAA), the mirroring altitude of a drifting electron will depend on longitude, and will be lowest over the anomaly region. Electrons that were outside of the bounce loss cone away from the SAA may be inside the loss cone over the SAA. For a drift shell, the smallest equatorial pitch angle that allows an electron to drift entirely around the Earth without being lost to the atmosphere defines the *drift loss cone*. The drift loss cone will only contain trapped particles that have been scattered into the associated pitch angle range in their most recent drift period. By altering the pitch angle, wave particle interactions are responsible for diffusing particles into the drift or bounce loss cone and can enhance atmospheric losses.

1.5.3.2 Magnetopause shadowing

Particles can be lost in their drift around the Earth by crossing the magnetopause, a process named magnetopause shadowing. Magnetopause shadowing is believed to be particularly important for causing radiation belt dropouts at $L^* > 5$, where the relativistic electron flux can decrease by several orders of magnitude in just a few hours (Turner et al., 2012; Xiang et al., 2018). As the magnetopause moves inwards, electrons previously on closed drift paths can be diverted out to the magnetopause. This forms steep radial gradients at the edge of

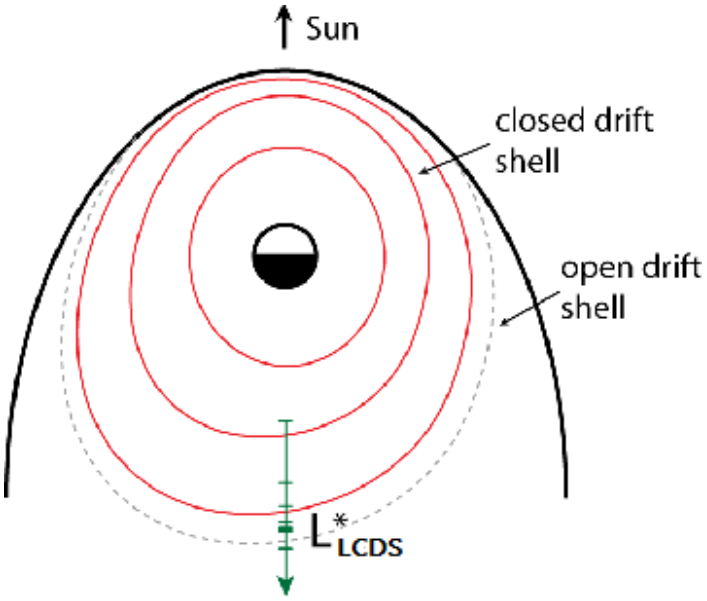

Figure 1.19 – An illustration of the last closed drift shell and associated L^*_{LCDS} (Koller et al., 2009).

the outer belt which, in turn, results in further loss though outwards radial diffusion (Shprits et al., 2006a).

As discussed previously, electrons with different initial pitch angles will follow different drift trajectories. In general, starting from the same location on the night side, a near perpendicular electron will drift to a greater radial distance at noon than an electron with more parallel propagation. As a result, the near perpendicular population is more likely to encounter the magnetopause on the dayside and be lost from the radiation belts. Near the outer edge of the outer radiation belt, the electron pitch angle distributions display a minimum centred around 90^o. This mechanism is known as *drift shell splitting*.

The last closed drift shell is the outermost drift path which entirely encircles the Earth without touching the magnetopause. It is an important concept for radiation belt particles as it defines the furthest extent of the outer radiation belt. As the definition of L^* requires a closed drift path, the last closed drift shell also corresponds to the maximum L^* value, L^*_{LCDS} for a particular magnetic field configuration. A schematic of L^*_{LCDS} is shown in Figure 1.19. As the magnetic topology varies, particularly the magnetopause location, the last closed drift shell will also change. Note that, as drift paths are pitch angle dependent, L^*_{LCDS} of the last closed drift shell will also depend on the particle pitch angle.

Chapter 2

Modelling the Earth's Electron Radiation Belts

2.1 Phase Space Density

In the previous chapter the various cyclic motions of a single electron in a static magnetic field were discussed. However, a great number of electrons reside in the radiation belt region and particles are generally considered in terms of flux values. How the particle flux varies over a specific drift or bounce path is of particular interest in order to understand, and ultimately model, the dynamics of the radiation belts.

Phase space is defined by the usual spatial coordinates $\mathbf{r} = (x, y, z)$ and their conjugate momenta, $\mathbf{p}$. Liouville's theorem (Walt, 1994) describes the density of electrons in phase space, a quantity called phase space density (PSD). For adiabatic motion along a dynamical path, the PSD remains constant, even when the particles change momentum as well as position.

A particularly useful relationship exists which links the PSD, $F(\mathbf{r}, \mathbf{p})$, to flux

$$F(\mathbf{r}, \mathbf{p}) = \frac{j(\alpha_{eq}, E)}{p^2} \tag{2.1}$$

where $j(\alpha_{eq}, E)$ is the electron flux at equatorial pitch angle α_{eq} and energy E. An important result can be inferred from equation 2.1. Where p^2 is constant, the electron flux does not vary along a dynamical path of a bounce or drift trajectory.

Another highly useful property of electron PSD is that it provides a diagnostic tool to determine the mechanism responsible for radiation belt enhancements. Acceleration mechanisms for radiation belt electrons follow two main themes: acceleration by inward

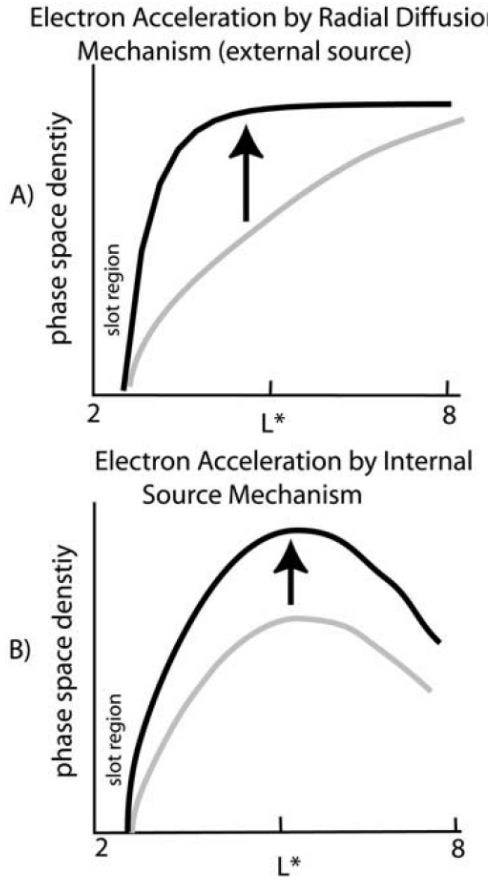

Figure 2.1 – Schematic demonstrating the different PSD gradients expected from (a) acceleration by radial diffusion and (b) local acceleration (Green and Kivelson, 2004).

radial diffusion of a source population, and in situ acceleration by wave particle interactions. The process of radial diffusion breaks the third invariant, conserving the other two, while local acceleration violates both the first and second invariant. The two types of acceleration mechanisms therefore result in different radial gradients in the electron PSD, calculated as a function of the three adiabatic invariants.

If a positive gradient exists in the L^* profile of the PSD given at constant μ and J then electrons can radially diffuse inwards from an external source. The PSD then increases at L^* values Earthwards of the source region and shows a characteristic change in the radial profile similar to that in Figure 2.1a. Acceleration by radial diffusion cannot produce growing peaks in the PSD profile as negative gradients result in outwards radial diffusion, acting to reduce peaks. On the other hand, Figure 2.1b shows how the PSD distribution at fixed μ and J would evolve under local acceleration. A localised PSD peak has formed which will continue to grow as electrons are energised. One can therefore differentiate between the two acceleration

mechanisms by considering the form of the PSD distribution (Boyd et al., 2018; Green and Kivelson, 2004).

Unlike the PSD profile at constant μ and J, the electron flux at a specific energy can show growing peaks in L^* due to inward radial diffusion. As electrons diffuse to lower L^*, the electron energy increases in order to conserve the first and second invariant. Considering a single energy, for example 1 MeV, electrons radially diffusing from an external source may not reach an energy of 1 MeV until $L^* < 4$. This would then manifest as a growing peak in the L^* profile of the electron flux inside $L^* = 4$.

2.2 Quasilinear Theory and Diffusion

Each of the three adiabatic invariants described in section 1.3 are associated with a periodic particle motion and an action integral that has a canonically conjugate phase. The phase of a particle signifies the angle through the associated cyclic motion, be that gyration, bounce, or drift. An adiabatic invariant is violated when particles with the same values for the three invariants, but different phases, respond differently to a stimulus. This requires the application of a force on spatial or temporal scales comparable to the particle motion associated with the invariant.

Particle collisions act on a scale both temporally and spatially abrupt with respect to gyration and are therefore a candidate process for violating adiabatic invariants. However, outside of the loss cone in the radiation belts, the plasma is rarefied and particle energies high, therefore Coulomb collisions are completely negligible (Schulz and Lanzerotti, 1974).

Interactions with electrostatic and electromagnetic plasma cyclotron waves also distinguish between particles having different gyration, bounce, and drift phases and therefore can violate the invariants. Particles interact with large numbers of small amplitude waves that have random phases. An electron resonantly interacts with one wave and is scattered in adiabatic invariant space to a state where it can resonantly interact with another wave in the spectrum. The overlap of particle populations at resonance with adjacent harmonics of wave spectra results in the stochasticity of particle motion. In the space of adiabatic invariants, particles exhibit a random walk motion analogous to the Brownian motion of particles due to collisions. The random walk motion results in net diffusion down PSD gradients as more electrons randomly move into regions of lower density than randomly move out of regions of lower density.

If the wave fields are small in amplitude, the resulting departure from adiabatic motion is also small and can be considered as a perturbation. Changes in the action integral, J_i,

are a function of the particle's phase, but appear random after phase-averaging the particle distribution. The particle distribution function is then handled perturbatively in an approach called quasi-linear theory and changes in the phase-averaged PSD distribution are expressed in terms of μ, J, Φ, and time, t, as a diffusive process (Ukhorskiy and Sitnov, 2013).

Schulz and Lanzerotti (1974) give the diffusion equation for radiation belt particles as

$$\frac{\partial f}{\partial t} = \sum_{ij} \frac{\partial}{\partial J_i} \left[D_{ij} \frac{\partial f}{\partial J_j} \right] \tag{2.2}$$

where f is the phase-averaged phase space density, D_{ij} is the diffusion coefficient, and J_i is one of the three action integrals that relate to the adiabatic invariants ($J_1 = 2\pi m_e \mu/|q|$, $J_2 = J$, and $J_3 = (q/c)\Phi$). The cyclotron frequency and drift frequency interactions are generally considered to be uncoupled and so terms involving D_{13} or D_{23} are neglected (Albert et al., 2009). Equation 2.2 is then written as

$$\frac{\partial f}{\partial t} = \frac{\partial}{\partial J_1} \left(D_{11} \frac{\partial f}{\partial J_1} + D_{12} \frac{\partial f}{J_2} \right) + \frac{\partial}{\partial J_2} \left(D_{12} \frac{\partial f}{\partial J_1} + D_{22} \frac{\partial f}{\partial J_2} \right) + \frac{\partial}{\partial J_3} D_{33} \frac{\partial f}{\partial J_3}. \tag{2.3}$$

It is common to change variables from (J_1, J_2, J_3) to (α_{eq}, E, L^*) and, for a dipole field, Glauert et al. (2014b) gives

$$\begin{aligned} \frac{\partial f}{\partial t} = \frac{1}{g(\alpha_{eq})} \frac{\partial}{\partial \alpha_{eq}} \left[g(\alpha_{eq}) \left(D_{\alpha_{eq}\alpha_{eq}} \frac{\partial f}{\partial \alpha_{eq}}\bigg|_{E,L^*} + D_{\alpha_{eq}E} \frac{\partial f}{\partial E}\bigg|_{\alpha_{eq},L^*} \right) \right]_{E,L^*} + \\ \frac{1}{A(E)} \frac{\partial}{\partial E} \left[A(E) \left(D_{EE} \frac{\partial f}{\partial E}\bigg|_{\alpha_{eq},L^*} + D_{E\alpha_{eq}} \frac{\partial f}{\partial \alpha_{eq}}\bigg|_{E,L^*} \right) \right]_{\alpha_{eq},L^*} + \\ L^{*2} \frac{\partial}{\partial L^*} \left[\frac{D_{L^*L^*}}{L^{*2}} \frac{\partial f}{\partial L^*}\bigg|_{\mu,J} \right]_{\mu,J} \end{aligned} \tag{2.4}$$

where

$$g(\alpha_{eq}) = T(\alpha_{eq}) \sin 2\alpha_{eq} \tag{2.5}$$

and

$$A(E) = (E + E_0)\sqrt{E^2 + 2E_0 E}. \tag{2.6}$$

Here, E_0 is the electron rest mass energy and $T(\alpha_{eq})$ is approximated by $T(\alpha_{eq}) \approx (1.3802 - 0.3198(\sin\alpha_{eq} + \sin^{1/2}\alpha_{eq}))$ (Lenchek et al., 1961).

2.3 Diffusion Coefficients

The diffusion coefficients in equation 2.4 are drift and bounce averaged so as to describe the evolution of the phase-averaged PSD.

2.3.1 Radial Diffusion Coefficients

Radial diffusion of the electron population is included in equation 2.4 via the term containing $D_{L^*L^*}$, the drift and bounce averaged radial diffusion coefficient. The stochastic effects of electric and magnetic field fluctuations are embedded in $D_{L^*L^*}$ which governs the diffusion rate of the PSD.

The first radial diffusion coefficients were developed by Fälthammar (1965) who considered the dynamics of trapped equatorial particles as they gradually diffused to a relaxed configuration. Subsequent measurements of the magnetospheric electric and magnetic fields showed that the power spectra exhibited a Kp dependence (Mozer, 1971), and $D_{L^*L^*}$ values parametrised by Kp were developed (Brautigam and Albert, 2000). These radial diffusion coefficients are defined for $1 \leq \text{Kp} \leq 6$ and take the form

$$D_{L^*L^*} = D^M_{L^*L^*} + D^E_{L^*L^*} \tag{2.7}$$

where $D^M_{L^*L^*}$ and $D^E_{L^*L^*}$ represent radial diffusion due to electromagnetic and electrostatic field fluctuations, respectively. The electrostatic field component originates from the substorm convection electric field fluctuations that rise sharply and decay slowly relative to the electron drift timescale (Cornwall, 1968).

In units of per day, $D^M_{L^*L^*}$ is based on data derived at L* = 4 and L* = 6.6 and is given by

$$D^M_{L^*L^*} = 10^{0.506Kp-9.325} L^{*10}. \tag{2.8}$$

The electrostatic component is also given in units of per day as

$$D^E_{L^*L^*} = \frac{1}{4}\left(\frac{cE_{rms}}{R_E B_0}\right)^2 \left[\frac{T}{1+(\omega_D T/2)^2}\right] L^{*6} \tag{2.9}$$

for an electron drift frequency, ω_D, given by

$$\omega_D = \left(\frac{3\mu c}{qL^{*2}R_E^2}\right)\left(1+\frac{2\mu B}{E_0}\right)^{-1/2} \tag{2.10}$$

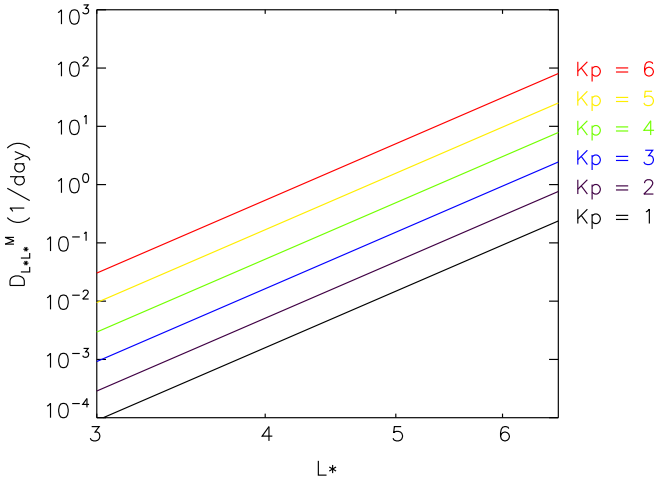

Figure 2.2 – Electromagnetic radial diffusion coefficients for a 90^o electron as given by Brautigam and Albert (2000).

where c is the speed of light, E_{rms} is the root mean square of the electric field amplitude, T is the exponential decay time (2700 seconds), B_0 is the Earth's dipole moment, and E_0 is the electron rest mass energy. E_{rms} is defined empirically for $1 \leq \text{Kp} \leq 6$ as

$$E_{rms} = 0.26(Kp-1)+0.1 \;\; mV/m. \tag{2.11}$$

Figure 2.2 shows the $D^M_{L^*L^*}$ component of the Brautigam and Albert (2000) $D_{L^*L^*}$ values for the $3.0 \leq \text{L}^* \leq 6.6$ range. The radial diffusion coefficient increases with Kp, resulting in faster diffusion during times of disturbed geomagnetic conditions. Owing to the the L^{*10} dependence, $D^M_{L^*L^*}$ is most significant at the largest L* values and as a result radial diffusion is important primarily in the outer radiation belt region.

2.3.2 Pitch Angle and Energy Diffusion Coefficients

In equation 2.4, $D_{\alpha_{eq}\alpha_{eq}}$, $D_{\alpha_{eq}E} = D_{E\alpha_{eq}}$, and D_{EE} are the drift and bounce averaged pitch angle, mixed pitch angle energy, and energy diffusion coefficients respectively. The bounce averaged pitch angle and energy diffusion rates are defined by

$$\left\langle D_{\alpha_{eq}\alpha_{eq}} \right\rangle = \left\langle \frac{(\Delta\alpha_{eq})^2}{2\Delta t} \right\rangle, \tag{2.12}$$

$$\left\langle D_{\alpha_{eq}E} \right\rangle = \left\langle \frac{\Delta\alpha_{eq}\Delta E}{2\Delta t} \right\rangle, \tag{2.13}$$

and

$$\langle D_{EE} \rangle = \left\langle \frac{(\Delta E)^2}{2\Delta t} \right\rangle \tag{2.14}$$

with units of s^{-1}, J s^{-1}, and J^2 s^{-1} (Glauert et al., 2014b), and give the expected diffusion rate of the electron PSD across the associated physical property. Here, the bounce averaged diffusion coefficients have been marked with angled brackets. Energy and pitch angle diffusion of radiation belt electron populations are thought to primarily arise from resonant interactions with various wave modes in the magnetosphere in the manner discussed in section 2.2.

The power spectral density, $B^2(\omega)$ of waves resulting in energy and pitch angle diffusion is assumed to have a Gaussian frequency distribution for frequencies in the $\omega_{LC} \leq \omega \leq \omega_{UC}$ range (where ω_{LC} and ω_{UC} are the lower and upper cut off frequency) and be zero otherwise. Likewise, $X = \tan(\psi)$ of the the wave normal angle, ψ, is also assumed to follow a Gaussian distribution between X_{min} and X_{max}.

Glauert and Horne (2005) derive the local diffusion coefficients, which are marked with a tilde below, describing the changes in the PSD resulting from resonant interactions with waves normally distributed in both $B^2(\omega)$ and X:

$$\widetilde{D_{\alpha\alpha}} = \sum_{n=n_l}^{n_h} \int_{X_{min}}^{X_{max}} X\, dX D_{\alpha\alpha}^{nX} \tag{2.15}$$

$$\widetilde{D_{p\alpha}} = \sum_{n=n_l}^{n_h} \int_{X_{min}}^{X_{max}} X\, dX D_{\alpha p}^{nX} \tag{2.16}$$

$$\widetilde{D_{pp}} = \sum_{n=n_l}^{n_h} \int_{X_{min}}^{X_{max}} X\, dX D_{pp}^{nX}, \tag{2.17}$$

where the summation is over the n-harmonic resonances ($n_l \leq n \leq n_h$) and

$$D_{\alpha\alpha}^{nX} = \sum_i \frac{q_\sigma^2 \omega_i^2}{4\pi(1+X^2)N(\omega_i)} \left[\frac{n\Omega_\sigma/(\gamma\omega_i) - \sin^2\alpha}{\cos\alpha} \right]^2 B^2(\omega_i) g(X) \frac{|\Phi_{n,k}|^2}{\left| v_\parallel - \frac{\partial\omega}{\partial k_\parallel} \right|_{k_{\parallel i}}} \tag{2.18}$$

$$D_{\alpha p}^{nX} = D_{\alpha\alpha}^{nX} \left[\frac{\sin\alpha\cos\alpha}{n\Omega_\sigma/(\gamma\omega_i) - \sin^2\alpha} \right]_{k_{\parallel i}} \tag{2.19}$$

$$D_{\alpha p}^{nX} = D_{\alpha\alpha}^{nX} \left[\frac{\sin\alpha\cos\alpha}{n\Omega_\sigma/(\gamma\omega_i) - \sin^2\alpha} \right]_{k_{\parallel i}}^2. \tag{2.20}$$

The integrals in equations 2.15 - 2.17 are evaluated at the parallel wave number, $k_{\|}$, and wave frequency, ω, that satisfy both the dispersion relation (equation 1.61) and the resonance condition (equation 1.67). For a given energy, n value, and wave normal angle, there may be more than one resonant frequency, hence a summation over i is included in equation 2.18. The charge of particle species σ is given by q_σ and $g(X)$ defines the variation of the wave magnetic field energy with wave normal angle as specified by the assumed Gaussian distribution. $|\Phi_{n,k}|^2$ depends on the wave refractive index and $N(\omega)$ is a normalisation factor that insures the wave energy per unit frequency is given by $B^2(\omega)$. Both are fully defined in Glauert and Horne (2005).

As a particle bounces between hemispheres, the pitch angle, α, varies. Other properties such as the wave normal angle distribution, the plasma density, and the magnetic field strength also change with latitude. The local diffusion coefficients are therefore averaged over the bounce path to obtain the bounce-averaged diffusion coefficients $\langle D_{p\alpha_{eq}} \rangle$, $\langle D_{\alpha_{eq}\alpha_{eq}} \rangle$, and $\langle D_{pp} \rangle$. Lyons et al. (1972) give the bounce averaged diffusion coefficients as

$$\langle D_{\alpha_{eq}\alpha_{eq}} \rangle = \frac{1}{\tau_B} \int_0^{\tau_B} \widetilde{D_{\alpha\alpha}} \left(\frac{\partial \alpha_{eq}}{\partial \alpha} \right)^2 dt \tag{2.21}$$

$$\langle D_{p\alpha_{eq}} \rangle = \frac{1}{\tau_B} \int_0^{\tau_B} \widetilde{D_{p\alpha}} \left(\frac{\partial \alpha_{eq}}{\partial \alpha} \right) dt \tag{2.22}$$

$$\langle D_{pp} \rangle = \frac{1}{\tau_B} \int_0^{\tau_B} \widetilde{D_{pp}} \, dt, \tag{2.23}$$

where τ_B is the bounce period of a particle. Changing from p to E to match the coordinates of equation 2.4 requires the following relations

$$\langle D_{EE} \rangle = \frac{c^2 E(E+2E_0)}{(E+E_0)^2} \langle D_{pp} \rangle \tag{2.24}$$

and

$$\langle D_{\alpha_{eq}E} \rangle = \frac{c^2 E}{(E+E_0)} \langle D_{p\alpha_{eq}} \rangle . \tag{2.25}$$

Using the equations given throughout this section, the Pitch Angle and Energy Diffusion of Ions and Electrons (PADIE) code calculates the fully relativistic pitch angle, energy, and mixed diffusion coefficients for resonant wave particle interactions. PADIE uses the full electromagnetic dispersion relation for a predominately cold plasma (Glauert and Horne, 2005) and is valid for any linear electromagnetic wave mode and for any ratio of plasma frequency to gyrofrequency.

Bounce averaged diffusion coefficients describing the rate of changes in the electron PSD distribution resulting from various wave modes are calculated using the PADIE code (e.g. Glauert et al., 2014b; Horne et al., 2013; Kersten et al., 2014). For a specific wave mode of interest, Gaussian distributions are fitted to the observed power spectral density profile and wave normal angle distributions. Measurements of wave and plasma properties are used to supply various coefficients to PADIE in order to determine the diffusion coefficients relating to the selected wave mode.

Notice that the diffusion coefficients in equation 2.4 are drift averaged as well as bounce averaged. Drift averaging is achieved by sectioning observed wave properties into MLT sectors then using the PADIE code to form bounce averaged diffusion coefficients for the wave and plasma properties in each specified sector. The resulting $\langle D_{E\alpha} \rangle$, $\langle D_{\alpha\alpha} \rangle$, and $\langle D_{EE} \rangle$ values are then averaged over all the MLT sectors to obtain the drift and bounce averaged diffusion coefficients ($D_{E\alpha}$, $D_{\alpha\alpha}$, and D_{EE}) for equation 2.4.

2.4 The British Antarctic Survey Radiation Belt Model

The electron radiation belts can be modelled by solving the 3-D diffusion equation given in section 2.2. In this thesis, the British Antarctic Survey Radiation Belt Model (BAS-RBM) was used to model the radiation belt region (Glauert et al., 2014b). The equation used in the BAS-RBM differs from equation 2.4 slightly as cross diffusion terms, $D_{\alpha_{eq}E}$ and $D_{E\alpha_{eq}}$, are neglected. Albert and Young (2005) and Subbotin et al. (2010) show that mixed pitch angle energy diffusion has little effect on equatorially mirroring electron populations. However, other studies have shown a significant effect on $>$2 MeV electron populations with equatorial pitch angles $<60^o$ (Tao et al., 2009, 2008).

While collisions between radiation belt particles can be ignored, for electrons in the loss cone, Coulomb collisions with the atmosphere constitute an important loss process (see section 1.5.3.1). A loss term f/τ_C is therefore included in the model equation where τ_C is a quarter of the electron bounce time inside the loss cone, and infinite elsewhere. Additionally, a similar term f/τ_M is included to account for losses to the magnetopause. τ_M is only finite outside of the last closed drift shell where it is set so that the flux is reduced by three orders of magnitude in one drift period. Including loss terms and neglecting cross diffusion yields

the following equation

$$\frac{\partial f}{\partial t} = \frac{1}{g(\alpha_{eq})}\frac{\partial}{\partial \alpha_{eq}}\left[g(\alpha_{eq})\left(D_{\alpha_{eq}\alpha_{eq}}\frac{\partial f}{\partial \alpha_{eq}}\bigg|_{E,L^*}\right)\right]_{E,L^*} + \frac{1}{A(E)}\frac{\partial}{\partial E}\left[A(E)\left(D_{EE}\frac{\partial f}{\partial E}\bigg|_{\alpha_{eq},L^*}\right)\right]_{\alpha_{eq},L^*} + L^{*2}\frac{\partial}{\partial L^*}\left[\frac{D_{L^*L^*}}{L^{*2}}\frac{\partial f}{\partial L^*}\bigg|_{\mu,J}\right]_{\mu,J} - \frac{f}{\tau_C} - \frac{f}{\tau_M} \tag{2.26}$$

which is solved by the BAS-RBM.

The radial diffusion coefficients used in the BAS-RBM are those given by Brautigam and Albert (2000). However, as Kim et al. (2011) suggest that the electrostatic component of the radial diffusion coefficient, $D^E_{L^*L^*}$, results in unrealistically high flux values in the slot region, the approach of Miyoshi et al. (2006) is used and $D_{L^*L^*}$ is taken as $D_{L^*L^*} = D^M_{L^*L^*}$, given by equation 2.8.

Pitch angle and energy diffusion coefficients describing interactions with chorus waves, plasmaspheric hiss, EMIC waves, and lightning generated whistlers are used in the model. Additionally, pitch-angle diffusion due to collisions with atmospheric atoms are incorporated following Abel and Thorne (1998) and provide a significant contribution inside, or very near to, the loss cone. The $D_{\alpha_{eq}\alpha_{eq}}$ and D_{EE} values from each of the listed processes are added together to form diffusion coefficients for equation 2.26. These coefficients are functions of α_{eq}, energy, and L*, and, by considering activity dependent wave data, are parameterised by either the Kp or AE (described in chapter 4) indices.

The last closed drift shell, L^*_{LCDS}, used in the model is given by an estimate from Glauert et al. (2014a)

$$L^*_{LCDS}(\alpha_{eq}) = (L_m - 1)(1.6375 - 0.00975\alpha_{eq}) + 0.05387\alpha_{eq} - 4.8937 \tag{2.27}$$

where L_m is the magnetopause standoff distance in units of Earth Radii. The Shue et al. (1998) model, given by equation 1.59, is used to define L_m, and hence the last closed drift shell in the model.

Using time dependent geomagnetic indices to drive the diffusion coefficients and solar wind parameters to set the last closed drift shell, the BAS-RBM solves equation 2.26.

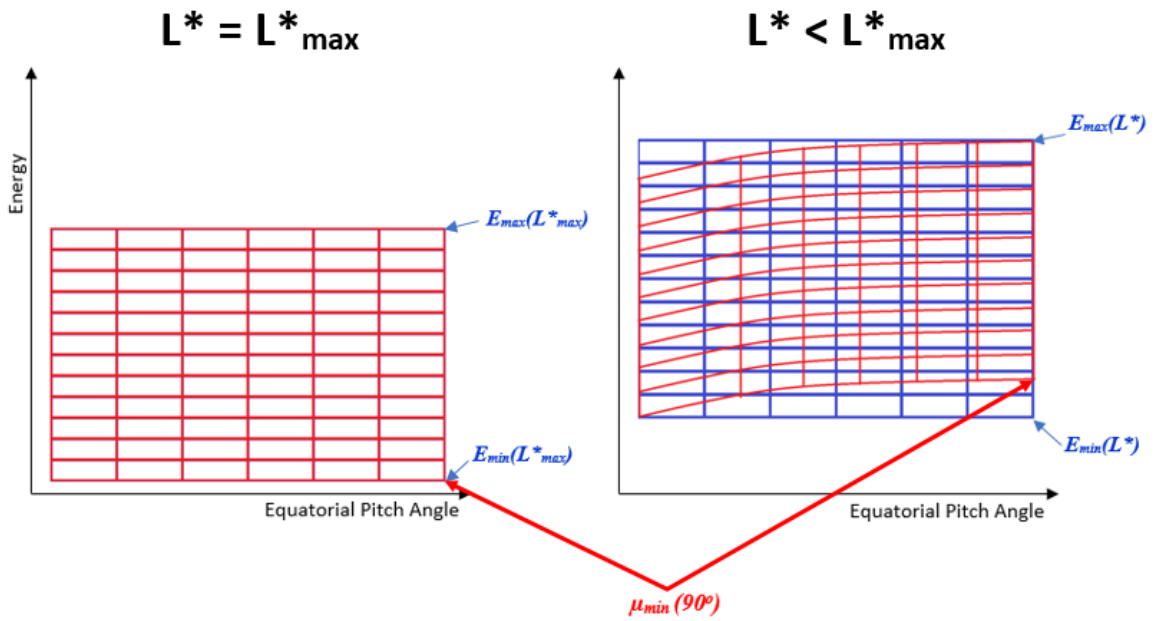

Figure 2.3 – Schematic of the BAS-RBM μ - J grid (red) and the $\ln(E)$-α_{eq} grid (blue) at L^*_{max} and $L^* < L^*_{max}$.

2.4.1 Calculation Procedure

A regularly spaced grid in L^* is used for the BAS-RBM calculation, covering values in $L^*_{min} \leq L* \leq L^*_{max}$ range. At each value of L^*, the model uses two computational grids to take account of the different constant quantities in equation 2.26 (subscripted values on the partial derivatives). One grid has points at the same μ and J for all L^* and is used to determine the radial diffusion. The other grid is regularly spaced in equatorial pitch angle and ln(energy), and has a different maximum and minimum energy at each L^*. This grid is used for the pitch angle and energy diffusion in the calculation.

At L^*_{max}, electron energies between the selected minimum and maximum energy values ($E_{min}(L^*_{max})$ and $E_{max}(L^*_{max})$, respectively), and equatorial pitch angles $0^o \leq \alpha_{eq} \leq 90^o$, are used to define the values of the μ-J grid following equations given by Schulz and Lanzerotti (1974), that assume a dipole magnetic field

$$\mu = \frac{p^2 L^{*3} \sin^2 \alpha_{eq}}{2 m_e B_0} \tag{2.28}$$

$$J = 2 p R_E L^* Y(\sin \alpha_{eq}). \tag{2.29}$$

Here p is the electron's momentum, B_0 the Earth's dipole moment, and $Y(\sin\alpha_{eq})$ is a function given in Schulz and Lanzerotti (1974).

For each L^* value lower than L^*_{max}, the regularly spaced $\ln(E)$-α grid has a minimum energy, $E_{min}(L^*)$, given by the J value that corresponds to $E = E_{min}$, $\alpha_{eq} = 0^o$ at L^*_{max}. The maximum energy, $E_{max}(L^*_{max})$, is then given by the μ value corresponding to $E = E_{max}$, $\alpha_{eq} = 90^o$ at L^*_{max}. The two grids at $L^* = L^*_{max}$ and $L^* < L^*_{max}$ are illustrated in Figure 2.3.

Equation 2.26 is solved using an implicit finite difference scheme, in four steps, employing an operator splitting technique. The first step calculates the loss as a non-discretised exponential expression. Following this, the next two steps solve for pitch angle and energy diffusion, performed on the $\ln(E)$ - α_{eq} grids at each L^*. The solution is then interpolated onto the μ - J grid where radial diffusion was computed. For the next time step, the process is reversed, with radial diffusion solved first and the PSD then interpolated back onto the $\ln(E)$ - α_{eq} grids at each L^* to compute pitch angle and energy diffusion (Glauert et al., 2014b).

2.4.2 Boundary Conditions

Equation 2.26 is solved for L^* values $L^*_{min} \leq L^* \leq L^*_{max}$, equatorial pitch angles $0^o \leq \alpha_{eq} \leq 90^o$, and a range of energies that depend on L^*. A schematic of the calculation box is shown in Figure 2.4a. Boundary conditions are required to define the PSD at the edges of the calculation domain. These correspond to the maximum and minimum values of each of the model coordinates, E, α_{eq}, and L^* and are illustrated in Figure 2.4b - d. At $\alpha_{eq} = 0^o$ and $\alpha_{eq} = 90^o$ the change in the phase-averaged PSD with respect to α_{eq} is set to zero (i.e. $\frac{\partial f}{\partial \alpha_{eq}} = 0$). For the E_{max} boundary, the condition $f = 0$ is used as the PSD for very high energy electrons is likely to be negligible. The remaining three boundary conditions (f at L^*_{min}, L^*_{max}, and E_{min}), are supplied by observations. An overview of the boundary conditions is given in table 2.1.

The data driven L^*_{max} and E_{min} boundaries are of particular importance as these introduce time variations in the PSD flowing into the calculation region and capture enhancements in the low energy content from non-diffusive processes.

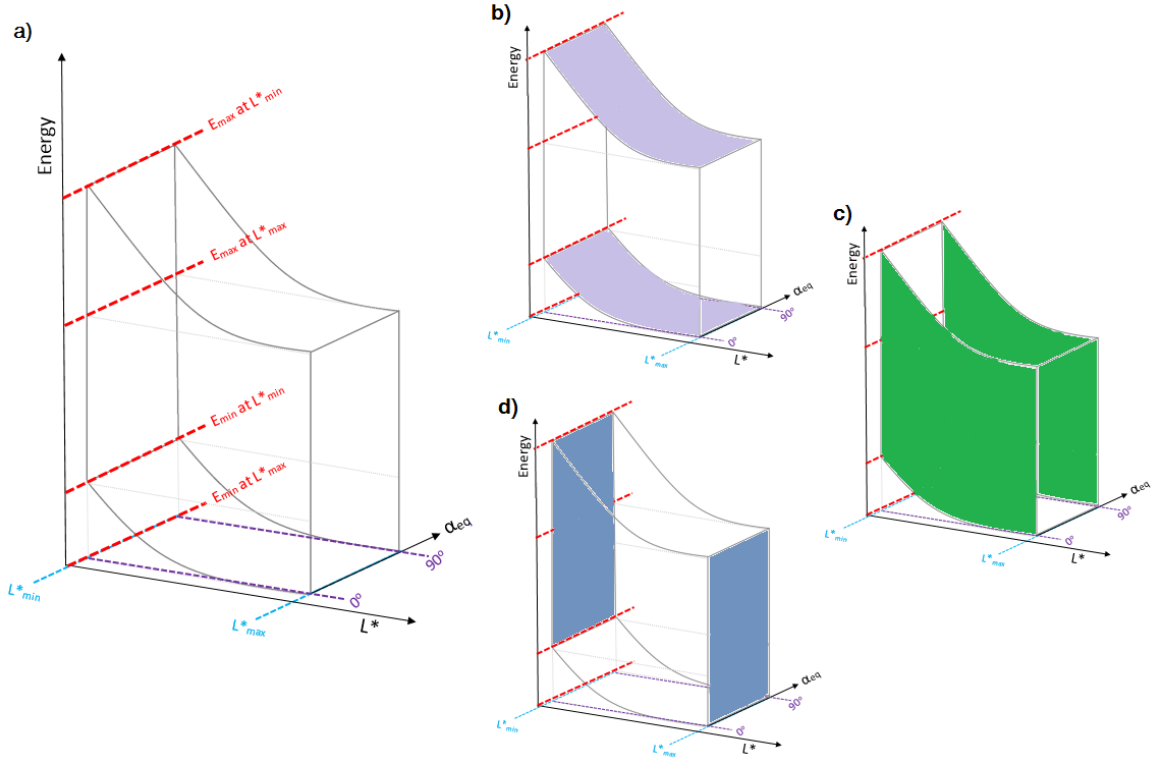

Figure 2.4 – Schematic of the BAS-RBM calculation box with an L* dependent energy range (a). E_{min} and E_{max} boundaries are shown by the purple surfaces (b), $\alpha_{eq} = 0^o$ and $\alpha_{eq} = 90^o$ boundaries by the green surfaces (c), and the L^*_{min} and L^*_{max} boundaries by the blue surfaces (d).

Boundary	Location	Boundary condition
Minimum equatorial pitch angle	$\alpha_{eq} = 0^o$	$\frac{\partial f}{\partial \alpha_{eq}} = 0$
Maximum equatorial pitch angle	$\alpha_{eq} = 90^o$	$\frac{\partial f}{\partial \alpha_{eq}} = 0$
Maximum Energy	E_{max} at L^*_{max}	$f = 0$
Minimum Energy	E_{min} at L^*_{max}	PSD set by data
Maximum L*	L^*_{max}	PSD set by data
Minimum L*	L^*_{min}	PSD set by data

Table 2.1 – Boundary conditions used in the BAS-RBM

Chapter 3

Literature Review

3.1 Observations of the Electron Radiation Belts

Satellite observations of the electron flux in the radiation belt region show considerable variability. Rapid flux depletions result from dropout events (Borovsky and Denton, 2009; Freeman Jr., 1964; Morley et al., 2010; Onsager et al., 2002; Xiang et al., 2017, 2018) and more gradual reductions arise due to pitch angle scattering, losses to the atmosphere, and outward radial diffusion (Lyons et al., 1972; Meredith et al., 2006b; Pfitzer and Winckler,

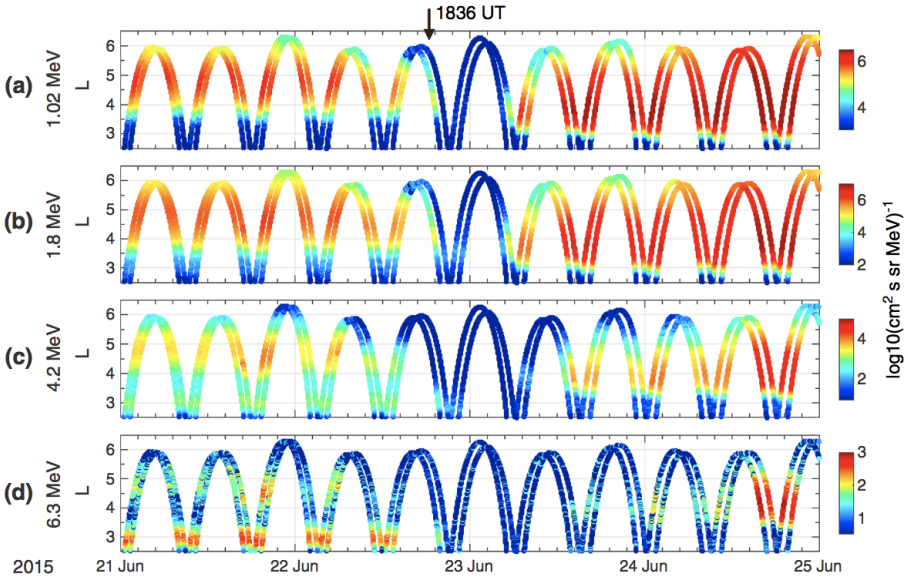

Figure 3.1 – Van Allen Probes electron flux measurements for energies (a) 1.02 MeV, (b) 1.8 MeV, (c) 4.2 MeV, and (d) 6.3 MeV during the 21-24 June 2015. Figure from (Xiang et al., 2017).

1968; Shprits et al., 2006a). Energisation processes lead to relativistic flux enhancements (Boyd et al., 2018; Glauert et al., 2014a; O'Brien et al., 2001), which can occur fairly rapidly ($\sim$hours) (Liu et al., 2018; Reeves et al., 2013). Figure 3.1, from Xiang et al. (2017), presents a flux dropout event that occurred on the 22 June 2015, and shows subsequent energy-dependent flux enhancements. The flux reduced by more than two orders of magnitude over a period of several hours, remained low for $\sim$8 hours and, at 1 MeV (Figure 3.1a), returned to pre-dropout levels in $\sim$5 hours. The 1.02 - 6.3 MeV flux then continued to increase, and by the 25 June, was higher at L = 4 than at the start of the period.

Electron enhancements are not solely an adiabatic response to the changing magnetic field (Kim and Chan, 1997) as, in an adiabatic process, there is no net energy gain or loss. When the magnetic field relaxes back to its previous state, the particles also revert. McAdams and Reeves (2001) subtracted adiabatic variations from electron flux observations and showed a residual flux increase for relativistic electrons. Additionally, observations of the radiation belt region show enhancements that persist after a magnetic disturbance has subsided, and likewise flux depletions that do not later return. Non-adiabatic acceleration and loss processes, that violate at least one of the three invariants, are therefore responsible for these changes.

Radiation belt relativistic flux enhancements are associated with increased geomagnetic activity, and often occur during periods of reduced Dst ($<$-30 nT), signifying a geomagnetic storm (Dessler and Karplus, 1961; Li et al., 2001; Reeves, 1998). However, nonstorm time enhancement events are also observed (Schiller et al., 2014). Owing to the complex balance between acceleration and loss processes, a statistical survey of the radiation belt response to moderate (Dst $<$-50 nT) and intense (Dst $<$-100 nT) geomagnetic storms showed that about half of all events increased the relativistic flux level, one fifth decreased the flux, and the remaining $\sim$30% of events produced no significant change (Reeves et al., 2003). Studying the various mechanisms responsible for enhancements and losses, as well as the relative balance between them, is crucial to understand, and ultimately predict changes in the flux of the radiation belts (Baker et al., 2014).

3.2 Leading Theories for Radiation Belt Enhancements

A number of acceleration mechanisms have been proposed to explain the replenishment of the relativistic electron content in the radiation belts. Baker et al. (1986, 1979) suggested Jovian particles may be a source for MeV electrons during periods when the interplanetary magnetic field connects Jupiter and Earth. Sheldon et al. (1998) considered the possibility of diffusive filling of the radiation belts from trapped electron populations in the cusp. Fujimoto

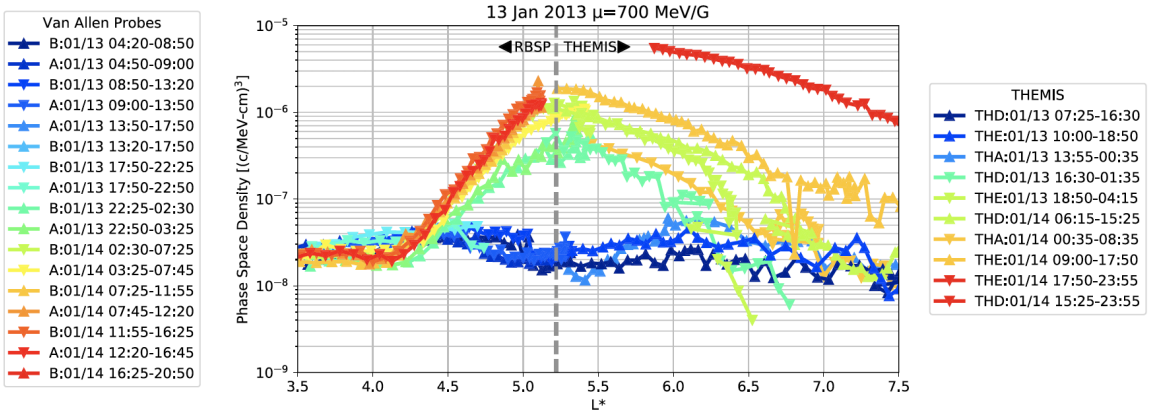

Figure 3.2 – Van Allen Probes and THEMIS PSD data for the 13 Jan 2013 showing a growing peak. Figure from Boyd et al. (2018).

and Nishida (1990) suggested that the repeated combination of radial diffusion and cross-L diffusion at low altitudes, known as large-scale recirculation, could lead to significant particle acceleration. However, it has since been noted that processes for low altitude cross-L diffusion are unclear (Friedel et al., 2002). Borovsky (1986) discuss acceleration by 'magnetic pumping'; the combination of cyclic magnetic compressions and pitch angle scattering. While suggested to be an important mechanism for the radiation belts of Jupiter (Borovsky et al., 1981; Goertz, 1978), further work has shown that magnetic pumping only has a minor effect at Earth (Borovsky et al., 2017).

The two most prevalent theories are broadly referred to as radial transport and local acceleration. Radial transport moves a source population at large radial distances inwards, violating the third invariant. Particle energisation occurs via betatron acceleration as electrons move into regions of stronger magnetic field, conserving their first two invariants (see sections 1.3.1 and 1.3.2). Radial transport may act diffusively (Barker et al., 2005; Schulz and Lanzerotti, 1974; Su et al., 2015; Walt, 1994), driven by ULF wave activity (Elkington et al., 1999; Liu et al., 1999; Ozeke et al., 2014, 2012), or non-diffusively by rapid cross field transport, such as during a strong interplanetary shock (Foster et al., 2015; Hudson et al., 2017; Li et al., 1993). Simulations using a 1-D radial diffusion equation have shown relativistic electron flux enhancements in agreement with observations for a number of storm events (Liu et al., 2018; Miyoshi et al., 2003; Ozeke et al., 2019; Shprits et al., 2005). Features such as the three belt structure occasionally observed during the Van Allen Probes mission (Baker et al., 2013b; Shprits et al., 2013; Thorne et al., 2013a) have also been achieved using radial diffusion models (Mann et al., 2016).

Local acceleration involves accelerating electrons *at* a particular L^* by violating their first and second adiabatic invariants via resonant wave-particle interactions. By computing diffusion curves, this type of acceleration has been shown to be primarily associated with whistler mode chorus waves (Summers et al., 1998) which can act to stochastically accelerate electrons between 100 keV and a few MeV (Horne and Thorne, 1998, 2003). Experiments using a 1-D energy diffusion equation later showed that, in 24 hours, chorus waves could cause the flux of >0.8 MeV electrons to increase by more than an order of magnitude (Horne et al., 2005a). For the Halloween storm of 2003, an event where the outer radiation belt was depleted and reformed closer to the Earth, Horne et al. (2005b) demonstrated that electron interactions with chorus waves were able to explain the observed relativistic flux enhancements. Moreover, during this event, acceleration by radial diffusion was not sufficient to increase the relativistic flux level in accordance with observations (Horne et al., 2005b; Shprits et al., 2006b). Later studies showed that efficient electron acceleration by whistler mode chorus waves was able to recreate flux enhancements seen in Van Allen Probes data (Li et al., 2014; Thorne et al., 2013b).

By examining the radial profiles of PSD data, a technique presented by Green and Kivelson (2004) (see section 2.1), a number of studies have considered whether radial diffusion or local acceleration is the dominant mechanism for >1 MeV enhancements. Analysis of PSD radial profiles, at constant μ and J, has largely focused on specific events (Green and Kivelson, 2004; Iles et al., 2006; Reeves et al., 2013; Selesnick and Blake, 2000; Turner et al., 2014, 2013) and have all found growing peaks in PSD which could not be explained by inward radial diffusion alone. Chen et al. (2007) performed a longer term study, using data from GPS constellations, Polar, and LANL-GEO satellites to conduct a superposed epoch analysis of PSD as a function of L*, for the 2001-2002 time period. They found PSD peaks at $L^* \sim$ 5-6 that persisted throughout geomagnetic storms, as well as during non storm times, for μ = 2083 MeV/G, K = 0.03 $G^{1/2}R_E$ electrons, indicative of local acceleration. Boyd et al. (2018) also conducted a survey, examining the radial profiles of PSD data from Van Allen Probes and THEMIS during 80 outer belt enhancement events. Local acceleration was found to be the dominant mechanism for creating near equatorial >1 MeV electrons in the outer belt. Growing PSD peaks, similar to that shown in Figure 3.2, were observed for 87% of enhancement events during the Van Allen Probes era, and the L* value of the growing peak was well correlated with the plasmapause location.

3.3 Low Energy and High Energy Electron Populations

Creating relativistic flux enhancements by chorus wave acceleration is however only half of the story; a population that can be accelerated to relativistic energies is also required.

Electrons are supplied to the radiation belt region from the night-side plasmasheet (Friedel et al., 2001; Ganushkina et al., 2014; Korth et al., 1999). Energetic electron flux increases in the magnetosphere usually correspond to periods of substorm activity and are associated with substorm injections (DeForest and McIlwain, 1971; Kronberg et al., 2017). Observationally, these appear as simultaneous flux enhancements across a range of energies, known as dispersionless injections (Ingraham et al., 2001; Liu et al., 2009; Sergeev et al., 1998). Away from the injection region, flux enhancements at various energies are dispersed in time as a result of the differing drift velocities (Sergeev et al., 1992; Turner et al., 2017). Simulations have shown that dispersionless injection signatures can be understood as a consequence of changes in the electric and magnetic fields resulting from the dipolarization process during substorm onset (Li et al., 1998; Sarris et al., 2002; Zaharia et al., 2000). Ganushkina et al. (2013) modelled the transport and acceleration of 50 - 250 keV electrons from the plasma sheet to geostationary orbit and found that substorm-associated impulsive fields and large-scale convection are the drivers of energetic electron flux increases during storm times. Likewise, by examining the dynamics of three enhancement events measured by Van Allen Probes, Tang et al. (2018) drew similar conclusions.

Analysing SAMPEX and THEMIS data, Kissinger et al. (2014) showed that electrons with energies less than a few hundred keV were supplied to the radiation belt region during steady magnetospheric convection events, in the absence of substorm activity. This suggests that plasma sheet electrons enter the radiation belts during times of enhanced convection electric field (Friedel et al., 2001), as well as by substorm injections. Additionally, Califf et al. (2017) showed that enhancements in the convection electric field can perturb the drift paths of dusk-side 10s - 300 keV electrons, already in the radiation belt region, causing them to move earthwards as they propagate round to the dawn-side. The inward motion increases the energy of the electrons, further bolstering the 130 - 500 keV flux level in the dawn-side slot region. In this instance, radial transport has increased the seed population in the chorus acceleration region without additional electrons being added to the belts.

Plasma sheet electrons supplied to the radiation belts generally have energies up to a few hundred keV (Baker et al., 1989; Cayton et al., 1989) and are categorised into source (1 - 10s keV) and seed (10s - 100s keV) populations. Jaynes et al. (2015) analysed Van Allen Probes and GOES data between August - September 2014 and found that both increased

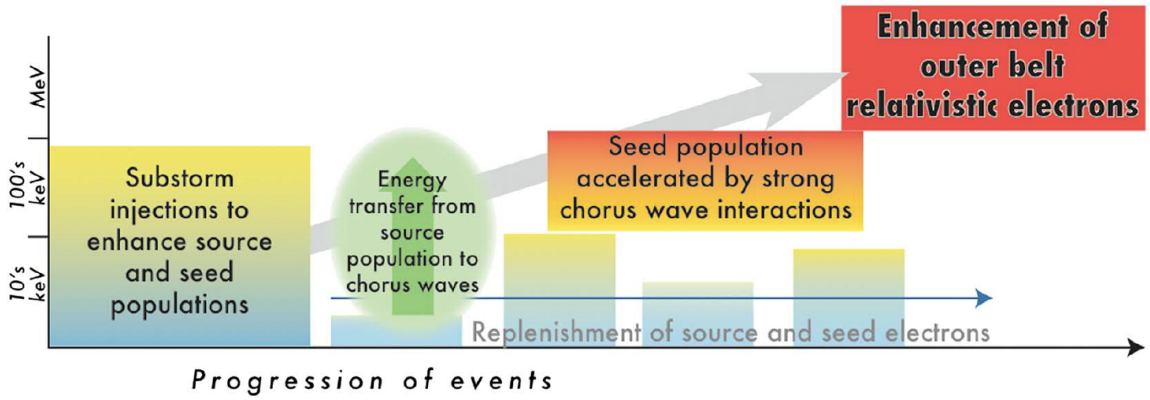

Figure 3.3 – Schematic illustrating the seed-source mechanism for relativistic flux enhancements. Figure from Jaynes et al. (2015).

seed *and* source populations were required for enhancements in the MeV flux. They suggest that the source population gives rise to chorus wave growth (Tsurutani and Smith, 1974), accelerating the accompanying seed population to MeV energies. If either population is absent, a relativistic radiation belt enhancement does not occur. The source-seed mechanism is summarised in the schematic shown in Figure 3.3, taken from Jaynes et al. (2015).

Further observational studies, considering specific events, have also linked increases in the energetic electron flux to subsequent radiation belt enhancements at higher energies. Using data from both Akebono and NOAA satellites to study a geomagnetic storm in November 1993, Obara et al. (2000) showed that the enhanced 30 - 100 keV electron flux seeded the subsequent increase in the >1 MeV electrons. Foster et al. (2013) presented Van Allen Probes observations of the March 2013 event, concluding that an increase in the 100 keV flux and chorus wave activity led to prompt energisation of highly relativistic electrons observed outside the plasmapause. Boyd et al. (2014) analysed PSD profiles from the same event, also finding that chorus acceleration of an enhanced seed population caused the increase in the >1 MeV flux, eventually resulting in enhancements in the multi-MeV electron population.

In addition to studies of particular events, surveys have also shown that enhancements in the seed population are an important consideration for energisation of >1 MeV (core) electrons. Data from all geomagnetically disturbed periods during the CRRES mission showed that the most significant relativistic electron flux enhancements were associated with enhanced seed electron flux and enhanced lower band chorus wave power (Meredith et al., 2003a). Boyd et al. (2016) performed a statistical analysis of PSD data from the first 26 months of the Van Allen Probes mission, considering three values of μ representing the seed population, μ = 150 MeV/G ($\sim$200 keV at $L^* = 5$); the core population, μ = 1000 MeV/G

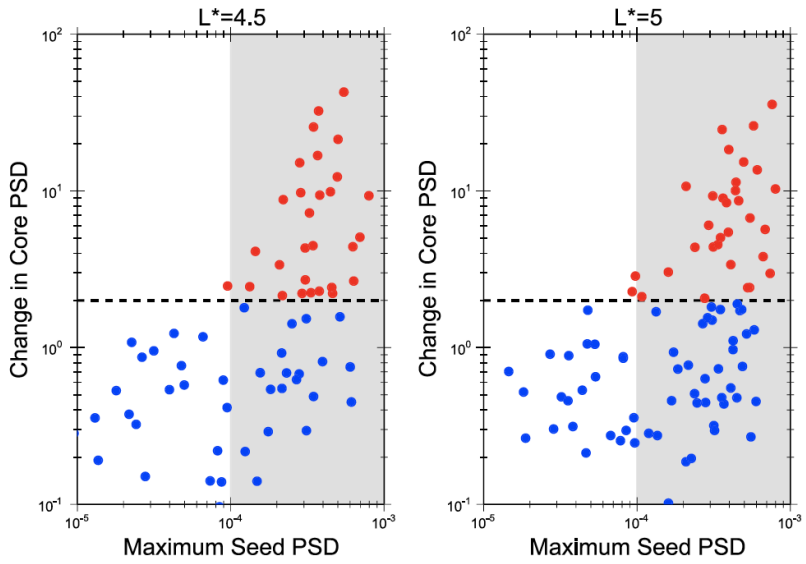

Figure 3.4 – Comparison of the maximum seed PSD value and the fractional change in the core PSD in the following 48 hours after each seed population enhancement for (left) L* = 4.5 and (right) L* = 5. The dashed line shows where the core population increased by a factor of 2 and points above this value are plotted in red. Figure from Boyd et al. (2016).

(∼1 MeV at L^* = 5); and the ultra-relativistic population, μ = 2000 MeV/G (∼2.5 MeV at L^* = 5). A cross correlation analysis showed the seed and core populations to be well correlated at each L^* value in the outer radiation belt, with a correlation coefficient of 0.73 and a time lag of 10 - 15 hours. The seed population showed a poorer correlation with the ultra-relativistic PSD at the same L^* value, perhaps indicating that electrons locally accelerated by chorus waves are also redistributed by radial diffusion in order to reach multi-MeV energies. Additionally, correlations between >1 MeV electrons and lower energy flux values have also been shown using measurements taken at geostationary orbit (Li et al., 2005; Turner and Li, 2008). Boyd et al. (2016) also find evidence of a seed population threshold that is necessary for subsequent acceleration. Figure 3.4, taken from the paper, shows the maximum seed PSD during an event compared to the fractional change in the core PSD in the following 48 hours, for two different values of L^*. Maxmimum seed PSD values above the threshold are shaded in grey. The reason for this threshold value is still unclear, but is suggested to be associated with the Kennel-Petschek limit (Kennel and Petschek, 1966) where the flux at these electron energies approaches a limiting value due to pitch angle scattering.

Observations from a number of satellite missions have therefore strongly suggested that enhancements in the seed population are related to increases in the core electron flux. Horne et al. (2005a) show that, for electrons with energies less than ∼300 keV, interactions with

chorus waves result in a competition between acceleration and loss, while above ∼300 keV, electrons are accelerated faster than they are lost from the system. As the injected seed population is thought to primarily cover the energy range ∼30 to ∼ 300 keV, this suggests a delicate interplay between both acceleration and loss from chorus waves. As such, changes in the level of the seed population may notably affect the enhancement of >1 MeV populations. Understanding temporal and spatial changes in the seed population, and how these changes impact >1 MeV enhancements in the radiation belt region, is thus an important area of research to ultimately understand the variability of the region.

3.4 Open Questions Highlighted by Modelling the Radiation Belt Region

As discussed in section 2.4.2, changes in the seed population can be introduced to radiation belt models via the data-driven low energy boundary condition. As a result, radiation belt models provide an excellent test-bed to examine links between energetic electron populations and the >1 MeV flux.

A study by Glauert et al. (2014a) used the BAS-RBM to model an initially empty radiation belt region, and set the PSD on the outer boundary to zero, so that electrons on the low energy boundary were the only source for the outer radiation belt. In the experiment shown in Figure 3.5, they demonstrated that an enhanced 3 MeV population could be achieved by acceleration of the ∼150 keV flux. An increase in the 700 keV flux was seen after ∼16 hours while an increase in the 1.5 MeV flux was observed ∼1 day later. After a number of days, 3 MeV electrons appear. As the radial diffusion coefficients used in this study were not energy dependent, the energy dependent delay is due to the time taken to accelerate electrons to higher energies by chorus.

For specific events, use of numerical models to explore the effect of changes in the seed population has been limited to two studies (excluding those in chapter 7 of this thesis) that provide conflicting results. Subbotin et al. (2011a) used the Versatile Electron Radiation Belt (VERB) code to model a storm occurring on 21 - 24 April 2001. The low energy boundary condition and outer boundary condition were supplied by the Rice Convection Model (Toffoletto et al., 2003) and the VERB results compared to the output using time-invariant boundary conditions. As shown in Figure 3.6, Subbotin et al. (2011a) observed little variation between results using the two different low energy boundary conditions, but the same condition for the outer boundary. They concluded that MeV flux values are relatively

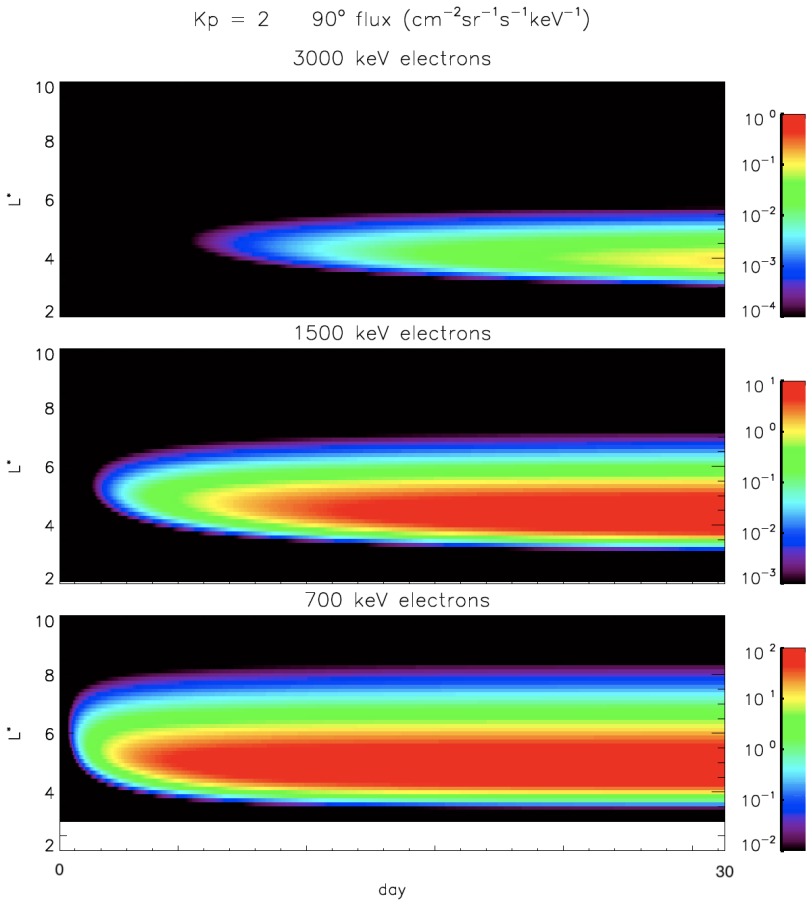

Figure 3.5 – Equatorially mirroring electron flux through a 30 day period with Kp = 3 starting with an empty outer radiation belt. The flux for three different energies are shown. Figure from Glauert et al. (2014a).

insensitive to the flux at low values of μ, and are more readily influenced by the outer boundary condition.

Conversely, when a realistic seed population was used for the low energy boundary condition of DREAM 3D and event specific diffusion coefficients were employed, Tu et al. (2014) obtained model results that were much closer to observations for the October 2012 "double-dip" storm than otherwise. As shown in Figure 3.7, they initially ran DREAM 3D with no chorus, hiss, or EMIC waves, solely exploring the effect of radial diffusion (panel c). The model PSD exhibits the observed dropout, but the subsequent enhancement is absent. When acceleration by chorus waves was also included, but the increased seed population absent (panel d), the PSD following the storm was much smaller than observed. Finally, including chorus wave acceleration, with a low energy boundary condition set by Van Allen Probes observations (panel e), the enhancement at μ = 1279 MeV/G was much closer to the

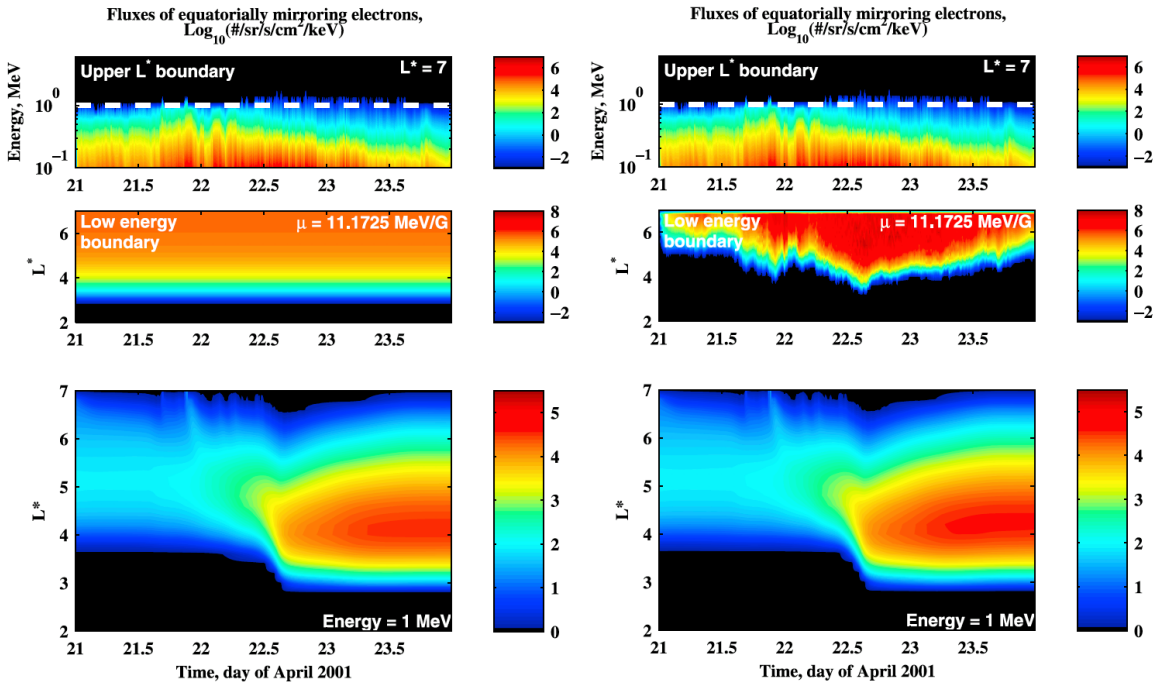

Figure 3.6 – VERB 1 MeV Electron flux (bottom panels) using a constant low energy boundary condition (left) and variable low energy boundary condition (right). The outer boundary condition (top panels) used was the same in both simulations. Figure from Subbotin et al. (2011a).

measured values. Tu et al. (2014) therefore demonstrate that an increased seed population was vital for the observed enhancement in the μ = 1279 MeV/G PSD, in direct contrast with the conclusions of Subbotin et al. (2011a).

Aside from exploring the impact changes in the seed population can have on radiation belt core populations, radiation belt models show little consensus on how to generally set the low energy boundary condition. Some models determine the low energy boundary condition directly from data (Albert et al., 2009; Glauert et al., 2014b). Others assume that there is a value of the first invariant, where the low energy boundary condition is set, where the PSD is constant with L* (Varotsou et al., 2005, 2008) or time (Su et al., 2010; Subbotin and Shprits, 2009; Subbotin et al., 2011a). Models using a time invariant low energy boundary condition do so under the assumption of a balance between convective source and losses at low values of μ.

Since the launch of the Van Allen Probes, data-driven low energy boundary conditions often make use of this dataset (Li et al., 2014; Ma et al., 2015; Ripoll et al., 2018; Tu et al., 2014). However, as the Van Allen Probes are a fixed lifetime mission, this begs the question of what data can be used beforehand and afterwards; a problem tackled in chapter 6.

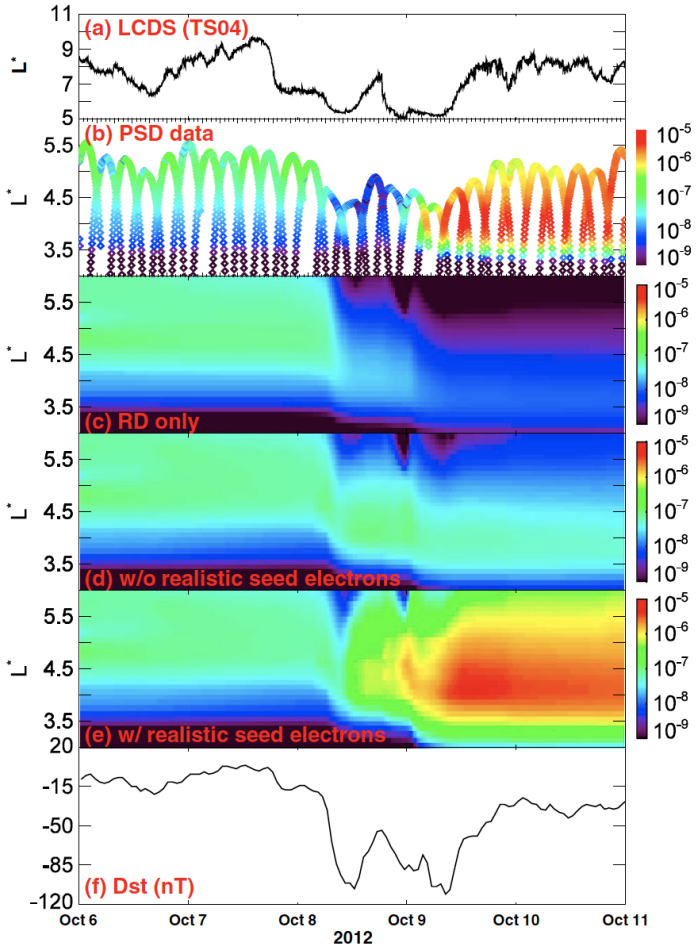

Figure 3.7 – Electron PSD data (in units of $(c/MeV/cm)^3$) from the Van Allen Probes (b) and simulation results (c-e) at μ =1279 MeV/G and K=0.115 $G^{1/2}R_E$ for the October 2012 storm. The last closed drift shell for the period is shown in panel (a) and the Dst index in panel (f). Figure from Tu et al. (2014).

As well as differing on how the low energy boundary condition is set, various models use different minimum energies for the calculation. The Versatile Electron Radiation Belt-3D typically sets the minimum energy at 10 keV (Kim and Shprits, 2013; Shprits et al., 2011; Subbotin and Shprits, 2009), the Salammbô model at 10 keV (Varotsou et al., 2005, 2008), the British Antarctic Survey Radiation Belt Model (BAS-RBM) at 153 keV (Glauert et al., 2014b), Ma et al. (2015) at 180 keV, and Albert et al. (2009) at 200 keV. As discussed in chapter 1, electron drift paths are energy dependent, owing to the energy dependence of the gradient and curvature magnetic drifts. The suitability of different minimum energies for drift-averaged 3-D models is explored chapter 5.

Chapter 4

Instrumentation and Geomagnetic Indices

The research presented in this thesis utilises data from two satellite missions, the Polar Operational Environmental Satellites (POES) and the dual Van Allen Probes. Additionally, the AE and Kp activity metrics are used to interpret observations, as well as to drive the BAS Radiation Belt Model, described in chapter 2. Here we introduce the Van Allen Probes and POES datasets and describe the activity metrics.

4.1 Van Allen Probes

The Van Allen Probes, formerly the Radiation Belt Storm Probes, are two satellites in near-equatorial geostationary transfer orbit. The orbital trajectories for the probes are shown in Figure 4.1 in Geocentric Solar Ecliptic[1] (GSE) coordinates. The satellites are often referred to by their prelaunch designators, Radiation Belt Storm Probe (RBSP)-A and RBSP-B, and are shown as red and blue tracks, respectively. Notice how the eccentric orbit of one probe essentially follows the other. The two orbits are nearly identical, with a $\sim$9 hour period, however apogees differ by $\sim$100 km, allowing one satellite to overtake the other every $\sim$75 days.

The orbit of the Van Allen Probes precesses around the Earth at a rate of 210^o per year. It therefore takes more than a year and a half to complete a full revolution in MLT. The eccentric orbit allows for measurements of the radiation belt environment throughout the inner belt and slot region as well as most of the outer radiation belt. Apogee is at a radial

[1]The GSE coordinate system has its X axis pointed towards the Sun and its Z axis perpendicular to the plane of the Earth's orbit around the Sun

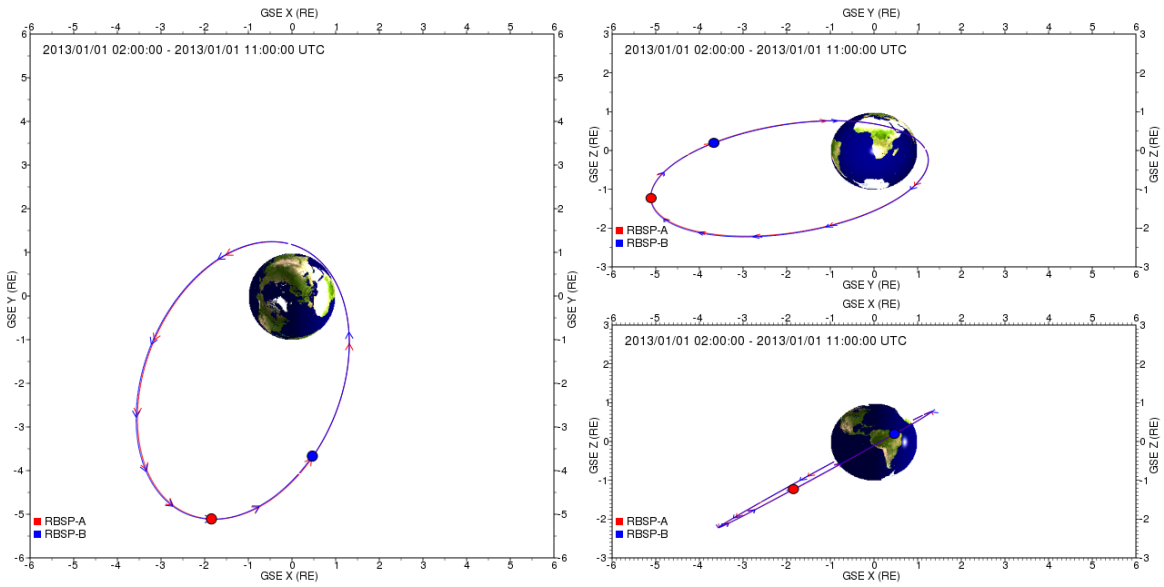

Figure 4.1 – Van Allen Probes orbits between 02:00:00 and 11:00:00 on 1 January 2013 in GSE coordinates in the x-y plane (left), the y-z plane (top right), and the x-z plane (bottom right). The trajectory of RBSP-A is shown in red and RBSP-B in blue.

distance of ≈ 5.8 R_E whilst perigee is at an altitude of ≈ 600 km. The orbits show a 10^o inclination and are therefore close to the magnetic equatorial plane.

Initially launched on 23 August 2012 from Cape Canaveral Air Force Station, the instrument suites on-board the Van Allen Probes have provided data on the radiation belt region for the past $\sim$6.5 years.

4.1.1 MagEIS

The Magnetic Electron Ion Spectrometer (MagEIS) is part of the Energetic Particle, Composition, and Thermal Plasma (ECT) suite (Spence et al., 2013). The MagEIS instruments were powered up on 6 September 2012 and measure the differential flux and angular distributions of electrons with energies ranging from $\sim$20 keV to $\sim$4.8 MeV. There are four magnetic spectrometers on-board each of the two spacecrafts: one low-energy unit ($\sim$20 to $\sim$240 keV), two mid-energy units ($\sim$80 to $\sim$1200 keV), and one high-energy unit ($\sim$800 keV to $\sim$4800 keV). The low- and high-energy units, as well as one of the mid-energy units, are mounted 75^o with respect to the spin axis. The final mid-energy unit is set 35^o to the spin axis, the data from which has not been publicly released.

Electrons enter the detector through a collimator with a 20^o aperture, into a uniform magnetic field. The magnetic field then focuses the charged particles onto a linear strip

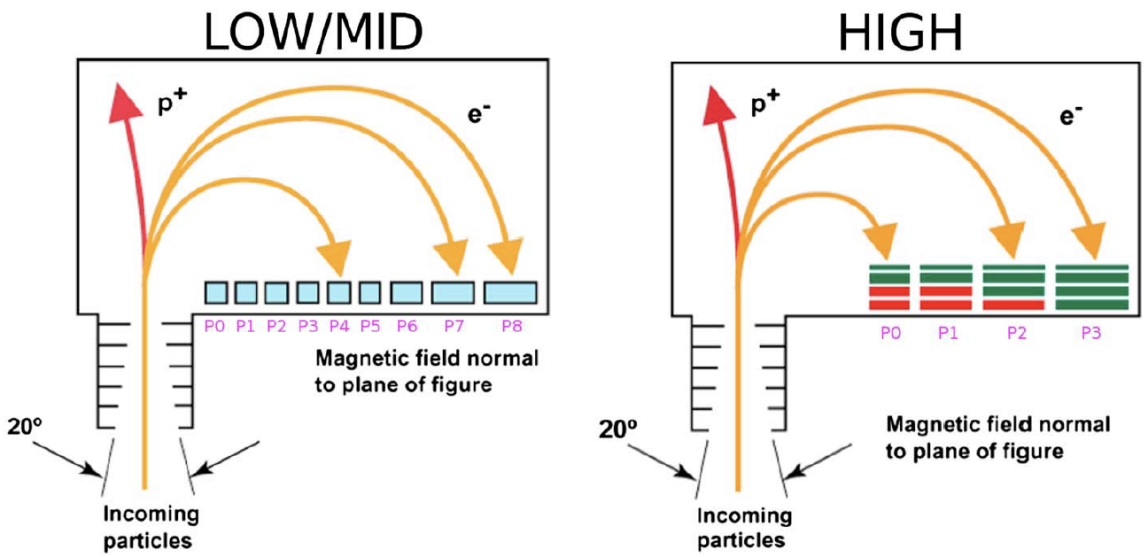

Figure 4.2 – Schematic of the MagEIS low- and mid-energy units (left) and the high-energy unit (right). Inside the detector box, the uniform magnetic field is directed normally into the plane of the figure. For the high-energy unit, unused rear detector pairs are coloured in red. Figure from Claudepierre et al. (2015).

of detectors. Ions that enter through the collimator cannot strike the detectors due to their oppositely directed sense of gyration (Blake et al., 2013), as shown by the red arrows in Figure 4.2. The low- and mid-energy units are very similar in design, differing only in the thickness of the silicon detectors and the internal magnetic field strength. The detector plane consists of nine solid state detectors or 'pixels' (labelled P0 - P8 on the left side of Figure 4.2). The high-energy unit has four stacks of silicon solid-state detectors, each stack forming a pixel (labelled P0 - P3 on the right side of Figure 4.2). Unlike the low- and mid-energy units, each pixel of the high-energy unit consists of a front and rear detector. Using two detectors for each pixel enables a coincidence measurement to reduce background response. The front detector is a single silicon detector, while the rear detector consists of three pairs of silicon detectors sandwiched together (6 silicon detectors in total). The rear detector is designed to stop the maximum energy electrons that can reach a given pixel. As the gyroradius increases with electron energy, pixels 0 and 1 only use one of the rear detector pairs, pixel 2 uses two, and pixel 3 uses all three. The front detector and the active pairs of the rear detector are shaded green in Figure 4.2. The front detector is smaller in area than the rear detector, to reduce the percentage of electrons which would make a valid coincidence, but instead exit out of a side of the thick rear detector.

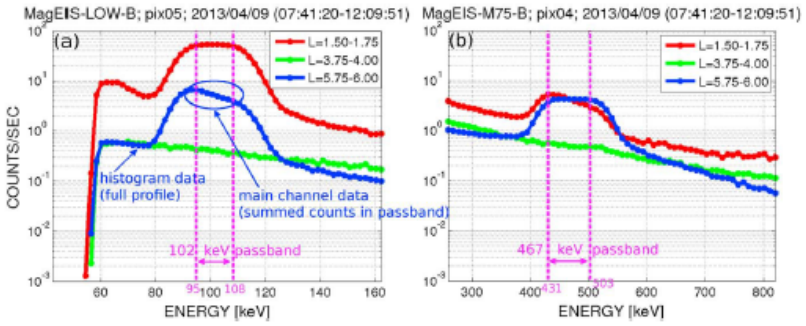

Figure 4.3 – Examples of the histogram data product from the MagEIS (a) low- and (b) mid-energy units on-board RBSP-B for three ranges of L. The channel pass-bands are marked in pink and the main channel data labelled. Figure from Claudepierre et al. (2015).

In total, there are 22 pixels across the low-, mid-, and high-energy units of the MagEIS detector. MagEIS therefore records measurements of the electron radiation belt environment in 22 energy channels. Each MagEIS pixel can provide electron count rate as a function of energy, produced by pulse height analysis of each electron strike, called the histogram data product. An example of the histogram data is shown in Figure 4.3. A peak in the count rate distribution arises corresponding to the energy range of electrons preferentially steered towards the pixel by the internal magnetic field of the detector. The energy 'pass-band' for each pixel (the electron energy range steered towards the pixel) was determined prior to launch by exposing the flight units to radiative sources. The electron counts within the energy pass-band are summed on-board to produce the main channel data. To give a background corrected data product, the count rate away from the peak in the histogram data is used to estimate the background counts. The background estimate is then subtracted from the main channel data to give the background corrected measurement for the energy channel (Claudepierre et al., 2015). Main channel count rates are converted to differential electron flux by dividing the measurement by the detection efficiency and geometric factor of the instrument as well as by the energy width of the pass-band and the accumulation time.

The Van Allen Probes are spinning spacecraft with a spin period of $\sim$11 s and a spin axis roughly pointing towards the Sun. Particle pitch angle distributions can be calculated over each spin by sectoring the measurements into an integer number of angular partitions. The number of sectors in a spin can be adjusted by ground command and has not remained constant throughout the mission. However, the MagEIS pitch angle resolved data is supplied to the user in 11 pitch angle bins. The data accumulation time for the main channel data is one spin period, which is subdivided by the different angular sectors. MagEIS data is provided simultaneously for all pitch angle bins with a time resolution of $\sim$11 seconds.

The low- and mid-energy detectors have an alternative mode of operation called high rate mode where additional angular data is recorded. To stay within the telemetry allocation, the high rate mode data cannot be collected simultaneously with histogram data, and therefore background correction is not possible. High rate mode is run occasionally for $L^* > 3$ and background-corrected MagEIS data will return missing data values for these intervals (Claudepierre et al., 2015).

4.1.2 REPT

Relativistic Electron-Proton Telescope (REPT) is another instrument in the ECT suite on-board both Van Allen Probes satellites that was powered on during the 1 and 2 September 2012. Unlike MagEIS, there is only one REPT detector on each probe, which measures $\sim$1 - 20 MeV electrons in 11 energy channels.

REPT consists of a stack of high-performance silicon solid state detectors, in thick casing, with a 32^o collimation aperture. A schematic of the REPT instrument design is shown in Figure 4.4. The silicon detectors are outlined in blue, in front of which a beryllium window (white outline) is located to exclude low energy electrons and protons. The telescopes are mounted nearly perpendicularly to the spin axis of the probes and sample particles from all local pitch angles during most magnetic field orientations. As with the MagEIS data, the spacecraft spin is sectored to give pitch angle resolved measurements.

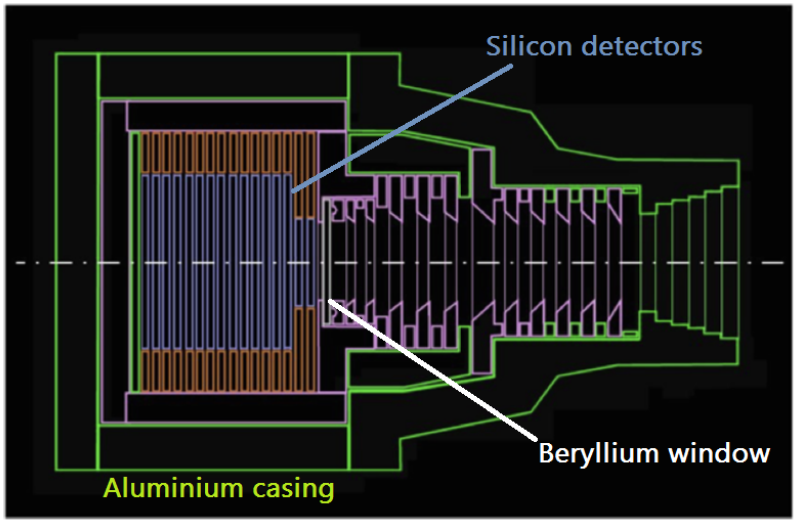

Figure 4.4 – Cross section of the REPT instrument. Blue outlined region shows the silicon detectors. Figure from Baker et al. (2013a).

When one or more of the silicon detectors in the stack exceeds a threshold within a coincidence window, a particle is recorded. The detector electronics then compare the pulse height analysis values against twenty logic statements to qualify the particle species and energy range. The measured count rates are corrected for background and dead time effects before being converted to physical flux units to provide pitch angle resolved differential flux values for each of the energy channels (Baker et al., 2013a). REPT data is provided to the user in 17 pitch angle bins, with an ∼11 second cadence.

Some of the lower REPT energy channels overlap with energies measured by the MagEIS instrument. However there is some discrepancy between the datasets, which is shown in chapter 7, Figure 7.9. In this thesis, no attempt has been made to resolve any differences between the MagEIS and REPT data products. Additionally, while MagEIS can measure electron energies up to ∼4.8 MeV, in the MagEIS data files, electron flux values are seldom provided for the energy channels >1.5 MeV.

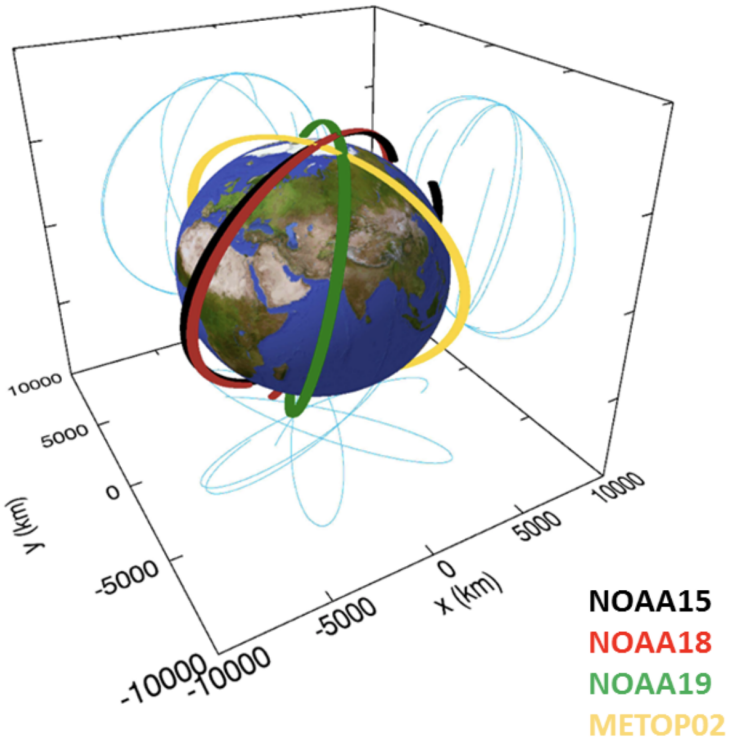

Figure 4.5 – Trajectories of a selection of POES and MetOp satellites from 2014-06-22 23:00:00 to 2014-06-23 00:40:00.

4.2 POES and MetOp Satellites

The polar orbiting POES constellation operates at an altitude of ∼850 km with ∼98.5^o inclination and are owned by the National Oceanic and Atmospheric Administration (NOAA). Each satellite has an orbital period of ∼100 minutes and transits the Earth ∼14 times a day. As a result of the high inclination orbit, an L^* range spanning from $L^* < 1.3$ to $L^* > 8.5$ can be sampled, dependent on activity. Additionally, each spacecraft is Sun-synchronous and operates over a limited range of MLT. Combining data from multiple POES satellites yields rapid observations of the radiation belt region across multiple MLT planes.

Since the launch of NOAA15 in 1998 (see Table 4.1) all POES satellites have carried the second generation of the Space Environment Monitor (SEM-2). The final POES satellite to be deployed was NOAA19, launched in 2009. The POES fleet was succeeded by the Meteorological Operational (MetOp) satellites, owned by the European Space Agency and operated by the European Organisation for the Exploitation of Meteorological Satellites (EUMETSAT). The MetOp satellites operate at a similar altitude and orbital inclination to the original POES spacecrafts and, for data continuity, also carry SEM-2. NOAA16 and NOAA17 were decommissioned in 2014 and 2013, respectively, but the SEM-2 units on-board NOAA15, NOAA18, NOAA19, MetOp01, MetOp02, and MetOp03 are, to date, still operational. As a result, the POES and MetOp dataset provides information on the radiation belt environment for the past ∼20 years and, as MetOp03 was only launched in November 2018, is likely to continue for years to come. For the remainder of this thesis, no distinction is made between POES and MetOp satellites, and the term *POES satellites* may refer to either.

Satellite	Start	End
NOAA15	1 July 1998	Ongoing
NOAA16	10 October 2001	9 June 2014
NOAA17	12 July 2002	10 April 2013
NOAA18	7 June 2005	Ongoing
NOAA19	2 June 2009	Ongoing
MetOp01	19 October 2006	Ongoing
MetOp02	17 September 2012	Ongoing
MetOp03	7 November 2018	Ongoing

Table 4.1 – POES and MetOp satellites data availability

4.2.1 SEM-2

Electron count data are collected by the Medium Energy Proton and Electron Detector (MEPED) as part of SEM-2 on-board the POES and MetOp satellites. The MEPED instrument includes two solid state silicon detector telescopes that measure electrons with energies in the 30 - 2500 keV range. Each detector has three integral electron channels, sampling 30 - 2500 keV (>30 keV), 100 - 2500 keV (>100 keV), and 300 - 2500 keV (>300 keV) electrons. The two telescopes are mounted perpendicular to one another, where one telescope, T0, is aligned so that the centre of the field of view is rotated 9^o from the local zenith. The field of view centre axis of the second telescope, T90, is rotated 9^o from the direction anti-parallel to the spacecraft velocity. Data from each detector are accumulated for 1 s, and since the electronics are shared between the two telescopes, supplied at a 2 s time resolution. T0 primarily samples the magnetic field aligned direction, observing electrons in the loss cone (Rodger et al., 2010b). T90, on the other hand, mostly measures perpendicular to the local magnetic field direction and mainly samples trapped electrons or those in the drift loss cone (Rodger et al., 2010a). Electron populations observed by T0 and T90 are discussed further in appendix A of this thesis. Both T0 and T90 have a detector opening angle of 30^o.

The MEPED instruments on each satellite were built at the same time and cross-calibrated before being deployed. Furthermore, the instruments undergo a weekly in-flight calibration

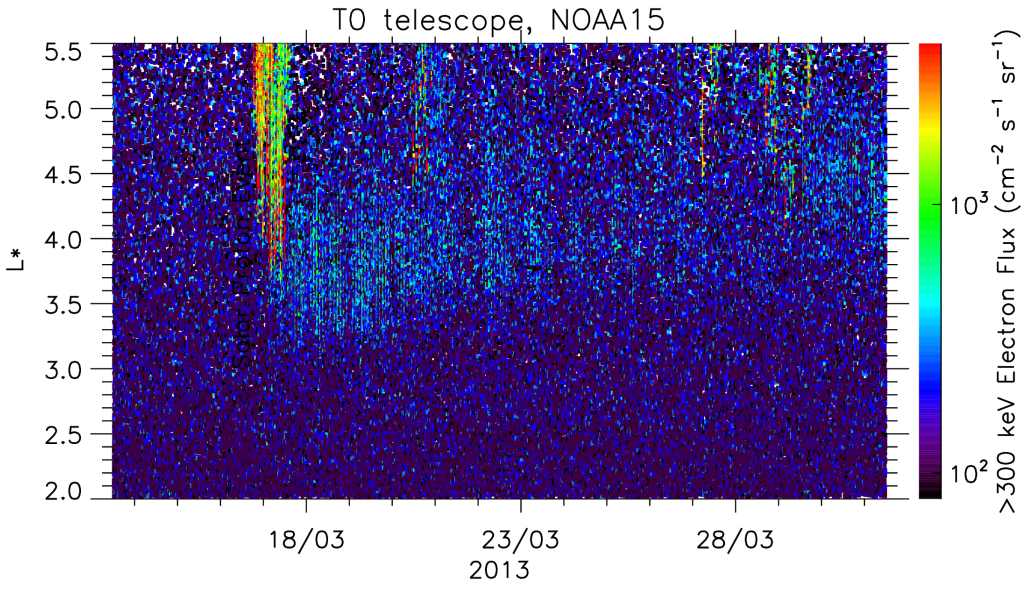

Figure 4.6 – An example of a solar proton event occurring on 17 March 2013 observed by the >300 keV channel of the T0 telescope of NOAA15. All flux values shown relate to the bounce loss cone.

procedure, detailed in Evans and Greer (2004). Count rates are converted to integral electron flux by dividing by the instrument geometric factor. In the British Antarctic Survey database, all electron flux values measured by SEM-2 have been corrected for contamination from ring current protons using the bow tie method described by Lam et al. (2010). However, the electron flux values can still be contaminated by protons during solar proton events (SPEs). Figure 4.6 shows proton contamination in the >300 keV flux channel of the T0 detector on-board NOAA15 during 17 March 2013 (green/red spike for $L^* > 3.5$). The contaminated values are significantly higher than the surrounding measurements. Note that the lighter blue region, centred at $L^* \sim 3.75$, for the week following the SPE is a result of enhanced precipitation during the magnetic storm that occurred at the same time. Smaller green spikes following the SPE (e.g. on the 21, 27, and 29 March) are likely the result of substorm activity.

We excluded SPEs by adopting the definition given by the NOAA Space Weather Prediction Center. Any data collected during periods when the level of the >10 MeV proton flux measured by the Energetic Particle Sensor on-board the primary Geostationary Operational Environmental Satellite (GOES) exceeded 10 cm^{-2} s^{-1} sr^{-1} were omitted from the dataset.

4.3 Geomagnetic Indices

4.3.1 AE

The Auroral Electrojet (AE) index was first introduced by Davis and Sugiura (1966) and is related to ionospheric currents in the auroral region that become enhanced due to increased conductivity during substorm activity. These currents cause deviations in the geomagnetic field that can be observed by ground-based magnetometers in the auroral zone. Data from 12 observatories in the northern auroral region are used to construct the AE index. The average intensity during the five geomagnetically quietest days of the previous month is subtracted from the measurements at each station as a baseline correction. The largest (AU) and smallest (AL) deviations in the horizontal component of the geomagnetic field during a minute time interval are selected and the difference (AU - AL) defined as the AE value for the time window.

A useful activity index which can be derived from AE is AE*. The AE* index was first introduced by Meredith et al. (2004) and is defined as the highest value of AE in the previous 3 hours. AE* is useful when considering wave and particle measurements in relation to activity as it allows for the transit time of supplied source and seed populations to travel away from the night side of the planet.

4.3.2 Kp

The K-index is a number related to maximum fluctuations of the horizontal component of the geomagnetic field as measured by a mid-latitude ground-based magnetometer during a 3 hour interval, relative to a quiet day. The maximum positive and negative deviations during the 3 hour period are added together to determine the total maximum fluctuation. Look-up tables specific to each observatory are used to convert the maximum fluctuation in nanoteslas to a K-index on a 9-point semi-logarithmic scale. The conversion varies for each observatory so that the rate of occurrence of a certain level of K is approximately the same for each magnetometer. In practice this results in observatories at higher geomagnetic latitudes recording higher magnetic fluctuations for a given K-index (Bartels et al., 1939). The label 'K' comes from the German word 'Kennziffer', meaning character digit.

The planetary K-index, or Kp index, was first introduced by Bartels and Veldkamp (1949) with the aim of expressing the world-wide features in geomagnetic disturbances. It is the mean of the standardised K-indices from 13 observatories between 44^o and 60^o northern or southern geomagnetic latitude and is updated every 3 hours. A typical magnetic storm corresponds to Kp $\gtrsim 3$.

Chapter 5

The Magnetic Local Time Distribution of Energetic Electrons in the Radiation Belt Region

The results of this chapter have been published in the *Journal of Geophysical Research: Space Physics* as:

Allison, H. J., Horne, R. B., Glauert, S. A., and Del Zanna, G., (2017), *The Magnetic Local Time Distribution of Energetic Electrons in the Radiation Belt Region*, *J. Geophys. Res. Space Physics*, 122, 8108–8123, doi:10.1002/2017JA024084

The presented analysis is the outcome of the author's own work, with R. B. Horne, S. A. Glauert, and G. Del Zanna providing advice and supervision. The results from this chapter were presented at Autumn MIST 2016, held at the Royal Astronomical Society in London, and also at the Fall AGU Meeting 2017 in New Orleans, Louisiana. For the latter, the author received an AGU Outstanding Student Paper Award.

5.1 Introduction

Electrons in the energy range of a few keV to a few hundred keV are transported into the inner magnetosphere from the night-side plasma sheet by substorm injections and enhanced convection (Arnoldy and Chan, 1969; Birn et al., 1998; Cayton et al., 1989). The $>$1 MeV populations of the radiation belts are thought to be formed by the subsequent acceleration of

these injected electrons (Boyd et al., 2016; Horne et al., 2003, 2005a). Potential energisation mechanisms include inward radial diffusion (Mann et al., 2004; O'Brien et al., 2001) and local acceleration via wave-particle interactions (Horne, 2007; Horne et al., 2005a; Reeves et al., 2013; Thorne, 2010).

Since particle drift paths vary with energy (described in section 1.2.3), electron populations can exhibit energy dependent variations in magnetic local time (MLT). For relativistic electrons (e.g. 1 MeV), gradient and curvature magnetic drifts dominate the drift velocity, resulting in closed drift paths throughout the radiation belt region. At lower electron energies (e.g. 1 keV), the energy-dependent magnetic drifts are weaker and the $\mathbf{E} \times \mathbf{B}$ drift can become influential to the particle motion. The large scale electric fields, $\mathbf{E}$, in the magnetosphere are the corotation and convection fields, introduced in section 1.2.3.1. As the convective drift is in a sunward direction, the combination of this motion, magnetic drifts, and corotation can result in open drift paths that transit the dawn-side of the earth before reaching the magnetopause (Chen and Schulz, 2001; Kavanagh et al., 1968). With increasing convective electric field strength, the region of open drift paths can penetrate to lower L-shells. However, even for electrons of a few eV (where magnetic drifts are of little consequence), the convection electric field cannot dominate the drift motion below the Alfvén layer (as discussed in sections 1.2.3.1 and 1.4.2.4).

Present 3-D global models of the radiation belts use a drift-averaged approximation, essentially assuming that the electron flux and diffusion coefficients can be averaged over an L^* and the calculation performed using the drift-averaged values (e.g. Albert et al., 2009; Glauert et al., 2014b; Shprits et al., 2011; Tu et al., 2014; Varotsou et al., 2005). When the electron flux is mostly uniform in MLT, the drift-average approximation is a useful simplification to the calculation, removing the MLT dimension. Whilst wave power and properties exhibit an MLT dependence (Kersten et al., 2014; Meredith et al., 2012, 2004; Sigsbee et al., 2010), the time scale of the azimuthal drift for the MeV energy electrons is short in comparison with the time scale for acceleration or scattering. The electrons rapidly move through regions where wave-particle interactions occur and then, as they are on closed drift paths, shortly return. The net result is that changes in the electron flux at MeV energies are mostly uniform in MLT.

However, lower energy electrons, which drift more slowly and may be on open drift paths, are more likely to exhibit a higher flux in the dawn sector, where chorus waves are typically observed (Horne et al., 2013), and a lower flux elsewhere. To account for this, 3-D radiation belt models can attempt to exclude electron energies which may demonstrate significant MLT variations when selecting the minimum energy of the calculation region. As

discussed in chapter 3, currently various global models use a range of values for the lower bound of the energy. The Versatile Electron Radiation Belt-3D typically sets the minimum energy at 10 keV (Kim and Shprits, 2013; Shprits et al., 2011; Subbotin and Shprits, 2009), the Salammbô model at 10 keV (Varotsou et al., 2005, 2008), the British Antarctic Survey Radiation Belt Model (BAS-RBM) at 153 keV (Glauert et al., 2014b), Ma et al. (2015) at 180 keV, and Albert et al. (2009) at 200 keV.

Statistical studies of the global distribution of precipitating $\leq$ 12 keV electrons (Hardy et al., 1985) and trapped suprathermal (0.1 - 16.5 keV) electrons (Bortnik et al., 2007; Li et al., 2010; Meredith et al., 2004) have demonstrated an enhanced electron flux in the dawn sector during periods of high activity. For higher energy electrons, such statistical studies are less extensive. Meredith et al. (2016) presented the global distribution of seed population ($\sim$30 keV - $\sim$300 keV) electrons observed for AE $>$ 300 nT, while Thorne et al. (2007) used more than a year of data from multiple passes of a *single satellite* to construct the statistical distribution of 153 keV and 340 keV electron flux for three levels of activity, defined by AE*. In both studies, an MLT variation was observed for electrons with energies exceeding 100 keV but were unclear for energies greater than 300 keV.

In this chapter, the $>$30, $>$100, and $>$300 keV electron flux observed by the Polar Operational Environmental Satellites (POES) are investigated to quantify at what energies MLT variations can be observed, and hence the minimum electron energy which may be included in 3-D (i.e. drift-averaged) radiation belt calculations. The MLT distribution of the electron flux is evaluated at several activity levels to account for changes in the convection electric field with activity (Kivelson, 1976) and the occurrence of substorm injections. Such a survey is possible as the POES constellation provides high time resolution multipoint electron flux measurements, covering several MLTs, across a broad range of L^*. Previous work has considered the energy-dependent radial structure of the radiation belts using data from the Van Allen Probes satellites (Reeves et al., 2016). Here we study a wider L^* range than is possible with the Van Allen Probes and additionally consider the energy-dependent MLT structure.

5.2 Instrumentation and Dataset

Fourteen years of data from the POES satellites are used, from 1 January 2000 to 31 December 2013. As shown in Figure 5.1, this date range covers a little more than one solar cycle, including the declining phase of cycle 23 along with the rising phase of 24. The electron flux for a wide range of geomagnetic activity is therefore included in our analysis.

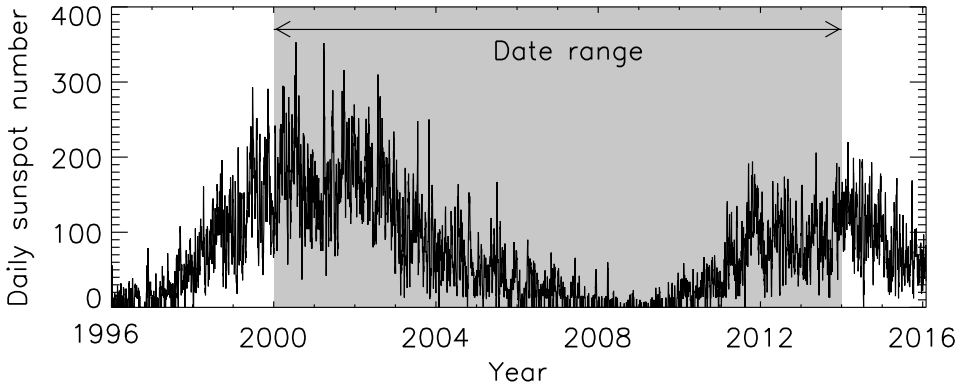

Figure 5.1 – Date range investigated in relation to the solar cycle

5.2.1 NOAA POES Satellites

As discussed in chapter 4, the orbital period of POES is ∼100 minutes and the data sampling rate 2 seconds. The high inclination orbit provides a cross-section through the radiation belts every quarter period, with a resolution of ∼25 minutes. During the time period examined, data from up to six POES satellites are used, providing observations from multiple MLT planes. Coupled with the L^* range covered during an orbit, the POES constellation provides very rapid, multipoint observations of the radiation belt region and is particularly equipped to study the changing MLT structure.

Since the MEPED instruments on-board each POES satellite were built at the same time, cross-calibrated before being deployed, and undergo a weekly in-flight calibration procedure, no further cross-calibration has been applied to the data. MEPED measures electron flux data in three energy channels, >30, >100, and >300 keV (Evans and Greer, 2004). The upper limit of each energy range is 2.5 MeV; however, as electron energy distribution functions show strong negative gradients with increasing energy (Cayton et al., 1989; Sergeev et al., 1992), the flux measurements tend to be dominated by electrons with energies just above the lower cut off.

The MEPED instrument has two solid-state detector telescopes, T0 and T90, mounted such that each measures electrons at different pitch angles. As discussed in the previous chapter, generally T90 observes stably trapped electrons or those in the drift or bounce loss cone (Rodger et al., 2010a), while T0 measures precipitating flux, primarily in the bounce loss cone (Rodger et al., 2010b). At low L^*, the populations measured by the two telescopes can reverse. A selection procedure, detailed in appendix A, has been applied to ensure that only data taken outside the drift and bounce loss cone were included in the study. For a

measurement to be used in the following analysis, the centre of the detector field-of-view must have been outside the drift and bounce loss cone. T0 only observes trapped flux for some magnetic longitudes in the equatorial region, relating to $L^* \lesssim 1.5$. T90 on the other hand observes trapped flux down to $L^* \approx 2$ over the South Atlantic Anomaly. For $1.5 < L^* < 2$, neither telescope field-of-view centre axis lay outside the drift and bounce loss cones.

During solar proton events, high energy protons can penetrate the magnetosphere and reach lower altitudes where POES operates, especially at high latitudes (Richard et al., 2002). As a result, contamination of the measured electron flux may occur. To avoid this, periods when the level of $>$10 MeV protons, measured by the Energetic Particle Sensor of the Geostationary Operational Environmental Satellites GOES-10 and GOES-13, exceeded 10 cm^{-2} s^{-1} sr^{-1} were omitted from the study. This is the NOAA Space Weather Prediction Center's definition of a solar proton event and has been adopted by previous authors when handling POES data (e.g. Lam et al. (2010); Meredith et al. (2016)). Additionally, POES electron flux values stored in the British Antarctic Survey database have been corrected for ring current proton contamination using the bow tie method described by Lam et al. (2010).

5.2.2 Cumulative Distribution Functions of Activity Measures

Activity data spanning the selected date range was used to produce the cumulative distribution functions (CDFs) of AE, AE*, Kp, solar wind speed (V_{sw}), and $V_{sw}B_z$ (the solar wind speed multiplied by the z component of the interplanetary magnetic field). The AE* index, first introduced by Meredith et al. (2004), is defined as the highest value of the AE index in the preceding three hours. This helps account for the travel time of injected electrons to transit away from the night-side of the planet. The activity and solar wind data were taken from NASA's OMNIWeb data explorer, with the exception of Kp, which originated from the British Antarctic Survey's database, and is available from the Polar Data Centre.

From the CDFs, shown in Figure 5.2, the activity values corresponding to the 40^{th}, 60^{th}, 80^{th}, 95^{th}, and 98^{th} percentiles were calculated. These values were then used to bound six activity levels for each of the five activity measures and are listed in table 5.1. By assigning levels of activity based on probability, statistical consistency was ensured across different parameters. The above percentiles were selected as these adequately captured low to extreme activity, giving a notable change between each level. For $V_{sw}B_z$, the axis has been reversed so that periods of very negative $V_{sw}B_z$ were assigned as high activity.

The CDFs for AE, AE*, and Kp all display a similar shape, skewed towards lower values. In contrast, the shape of the V_{sw} curve indicates that it is distributed about a central speed,

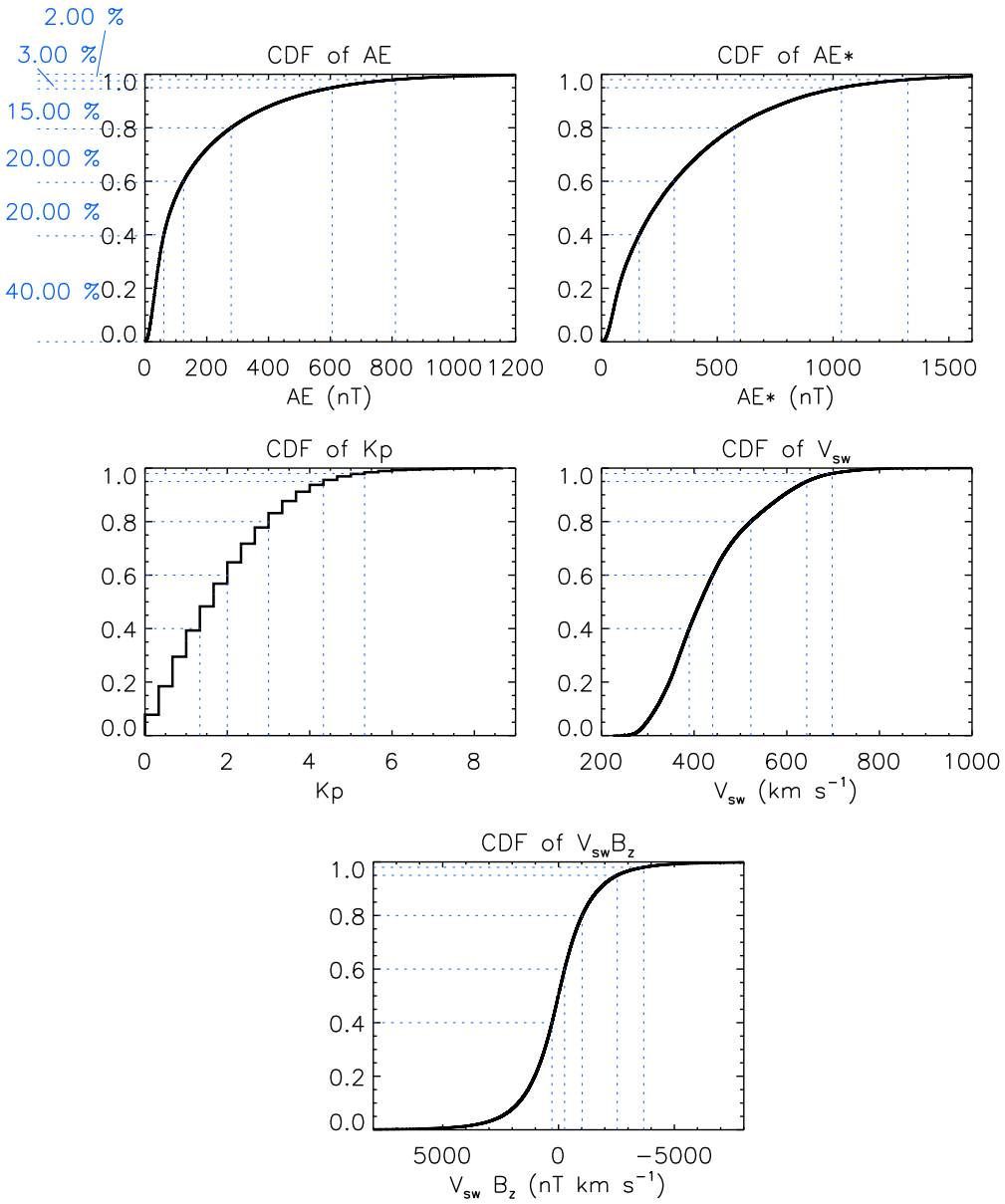

Figure 5.2 – The cumulative distribution functions for AE, AE*, Kp, V_{sw}, and $V_{sw}B_z$ activity measures from 1st January 2000 to 31st December 2013. Dotted lines correspond to the 40th, 60th, 80th, 95th, and 98th percentiles chosen to bound the six activity levels. The percentage of activity data contained within each level is marked on the left-hand-side of the panel.

with exceedingly low values being a rare occurrence. Interestingly, whilst speeds above 550 km s^{-1} are sometimes regarded at a fast solar wind speed (Denton and Borovsky, 2012), Kp $\sim$3 or AE $\sim$300 nT, are generally considered only moderate, but all correspond to the 80th percentile. The CDF for $V_{sw}B_z$ is almost centered on zero, implying that periods of positive and negative $V_{sw}B_z$ have near equal rates of occurance.

Table 5.1 – Activity level boundaries for AE, AE*, Kp, V_{sw}, and $V_{sw}B_z$.

	AE (nT)	AE* (nT)	Kp	V_{sw} (km s^{-1})	$V_{sw}B_z$ (nT km s^{-1})
A1	< 61	< 163	< 1.33	< 389.5	> 282
A2	61 – 125	163 – 314	1.33 - 2	389.5 – 440	282 – (-263)
A3	125 – 279	314 – 573	2 – 3	440 – 522.4	(-263) – (-1018)
A4	279 – 606	573 – 1036	3 – 4.33	522.4 – 643.1	(-1018) – (-2535)
A5	606 – 811	1036 – 1323	4.33 – 5.33	643.1 – 698	(-2535) – (-3679)
A6	$\geq$ 811	$\geq$ 1323	$\geq$ 5.33	$\geq$ 698	$\leq$ (-3679)

5.3 Magnetic Local Time Variation of Electron Flux

To form a statistical average of the global distribution of the electron population, measurements of the electron flux from each of the POES satellites during the 14 year date range were collated and binned by both MLT and L^*. Physically, the L^* parameter is another form of the third adiabatic invariant, Φ, (Roederer, 1970) and was described in section 1.3.3.1 (see equation 1.58). L^* was calculated with the UNILIB software library using the International Geomagnetic Reference Field and the Tsyganenko 96 (T96) model (Tsyganenko, 1995). T96 was chosen as this model has an explicitly defined realistic magnetopause and applies to both storms and quiet times. Enough data on the solar wind and geomagnetic indices were available to apply the model to the whole 14 year dataset. MLT values for the POES data were also calculated using this field model.

Each MLT bin covered one hour, centred on the hour, and L^* spanned from 1 to 8, divided into 28 groups of width $L^* = 0.25$. To investigate the evolution of the electron flux distribution with changing activity, the flux data was further sorted into the six activity levels, defined by either AE, AE*, Kp, V_{sw}, or $V_{sw}B_z$, listed in table 5.1. These levels have been determined by the percentiles stated in section 5.2.2. By using AE, AE*, Kp, V_{sw}, and $V_{sw}B_z$ to individually bin the flux readings, a more complete picture of the changes to the global distribution with increasing activity can be obtained.

For each of the five activity metrics listed above, the >30, >100, and >300 keV measurements were sorted into one of the 4032 L^*-MLT-activity bins. Figure 5.3 shows the mean of each L^*-MLT bin, spatially arranged to give the average electron flux distribution for each of the six activity levels defined by AE. Each row corresponds to >30, >100, or >300 keV electrons and the mini dial beneath each map displays the number of values sampled in each MLT-L^* bin. In some regions, electron flux measurements with the centre axis of the detector field-of-view outside of the drift and bounce loss cones were not taken by either telescope of the MEPED instrument. One such region forms a clear ring of missing data between L^*

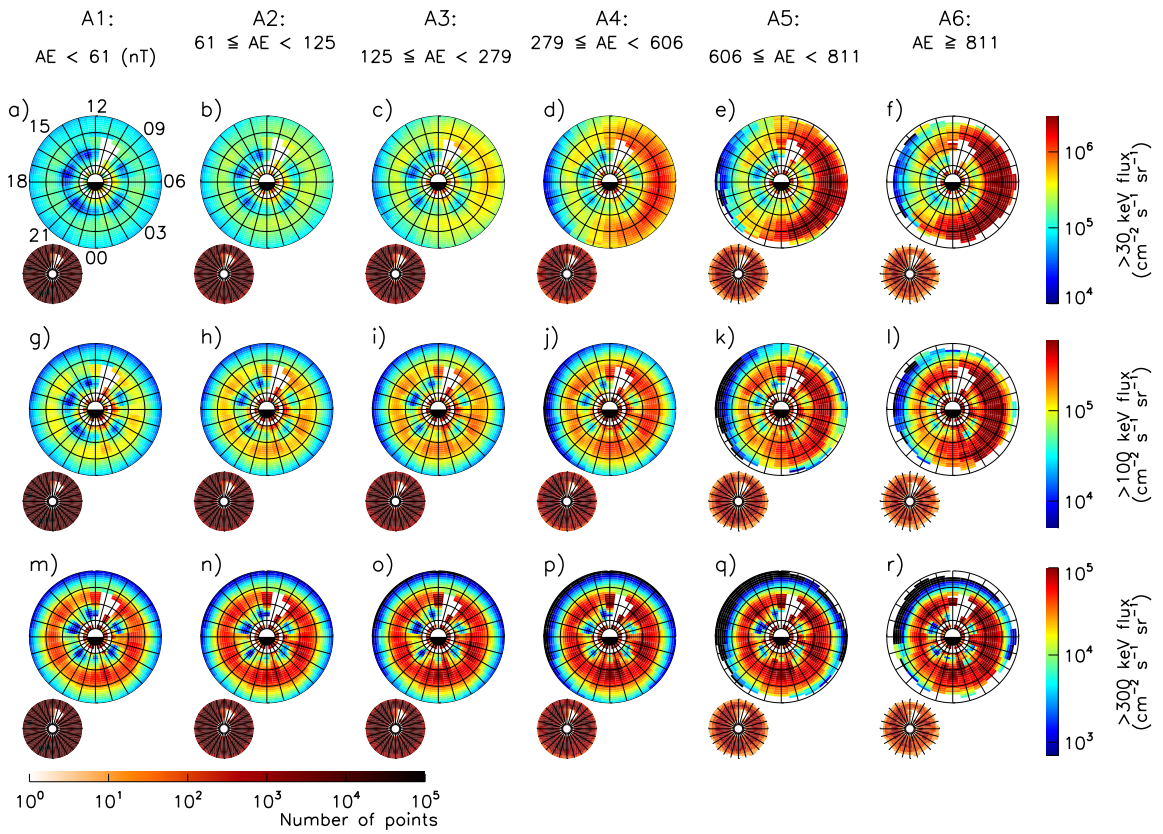

Figure 5.3 – Average flux distributions for >30 keV, >100 keV, and >300 keV electrons observed by the POES satellites over the stated date range, ordered by six AE levels. The plots are orientated in the equatorial plane with noon at the top and dawn to the right. The plots extend out to L^* = 8 and markers denote the L^* = 2, 4, and 6 positions.

= 1.5 - 2, separating where T0 measured trapped flux from where T90 measured trapped flux. Excluding isolated regions, there are generally ∼10,000 values in each L^*-MLT bin, giving a good statistical significance to the average. At the lower activities considered, this can be much higher, up to ∼100,000 readings. Averages calculated from 10 or fewer flux measurements were not shown in Figure 5.3.

Figure 5.3 shows that, with increasing activity, the flux level rises, particularly for the >30 keV electron flux (panels a - f). At this energy, the flux increase is mostly localised to the dawn-side of the earth, resulting in a notable MLT asymmetry in the electron flux distribution. For >100 keV electrons (panels g - l), as activity rises, the flux increase is again largest in the dawn sector. Even the >300 keV flux distributions (panels m - r) show a dawn-side increase in electron flux that is moderately higher than on the dusk-side. At the lowest activity level (panels a, g, and m), no notable MLT variation in the flux is seen for any

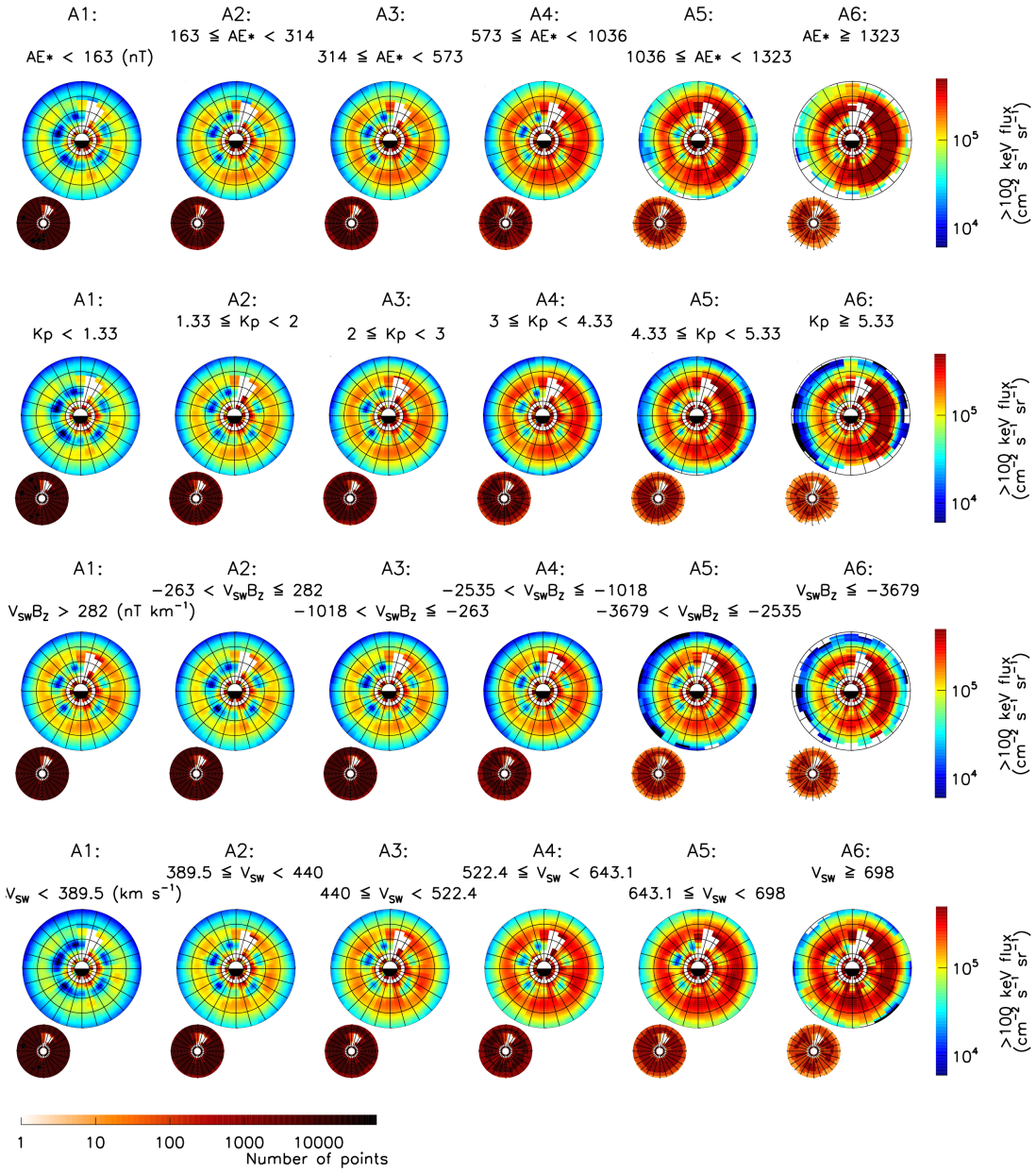

Figure 5.4 – Average >100 keV electron flux distributions observed by the POES satellites over six ranges of AE*, Kp, $V_{sw}B_z$, and V_{sw}. As for Figure 5.3 the plots extend out to $L^* = 8$.

of the electron energies studied, implying that 40% of the time (from Figure 5.2) the flux at these energies is fairly symmetric in MLT throughout the radiation belt region.

Figure 5.4 shows the >100 keV electron flux distribution, ordered by the six activity levels of AE*, Kp, $V_{sw}B_z$, and V_{sw}. While differences can be observed between flux sorted

by the different activity measures, for all activity measures considered, the >100 keV flux showed an increase with rising activity level that was highest on the dawn-side.

Two belts, an inner belt $\lesssim 2.5$ and an outer belt $\gtrsim 4$, separated by a region of lower flux, can be observed in the >30 keV and >100 keV global electron flux distributions shown in Figures 5.3 and 5.4. There is some suggestion of this structure at >300 keV, but it is less apparent as the majority of the inner zone flux at this energy seems to lie in the L^* range where neither T0 or T90 observe electrons outside of the loss cone. With increasing AE, for the >30, >100, and >300 keV electron flux in Figure 5.3, the inner edge of the outer ring moves earthwards and the two belts become less defined. A similar observation is shown in Figure 5.4 for the >100 keV flux AE*, Kp, and V_{sw} increase and $V_{sw}B_z$ decreases. A model by Liu et al. (2003) has shown that electrons below 150 keV can be injected into $L^* = 3$ during times of high activity. Thorne et al. (2007) then showed that chorus waves could act to accelerate these 'slot region' electrons to higher energies, resulting in slot region filling for electrons up to around 800 keV. Other processes, such as radial diffusion, may also be important for slot filling. A further study by Reeves et al. (2016), examining Van Allen Probes data, concluded that slot region filling is common at energies below a few 100 keV. The reduction of the two belt structure with increasing activity shown in Figure 5.3 supports this conclusion.

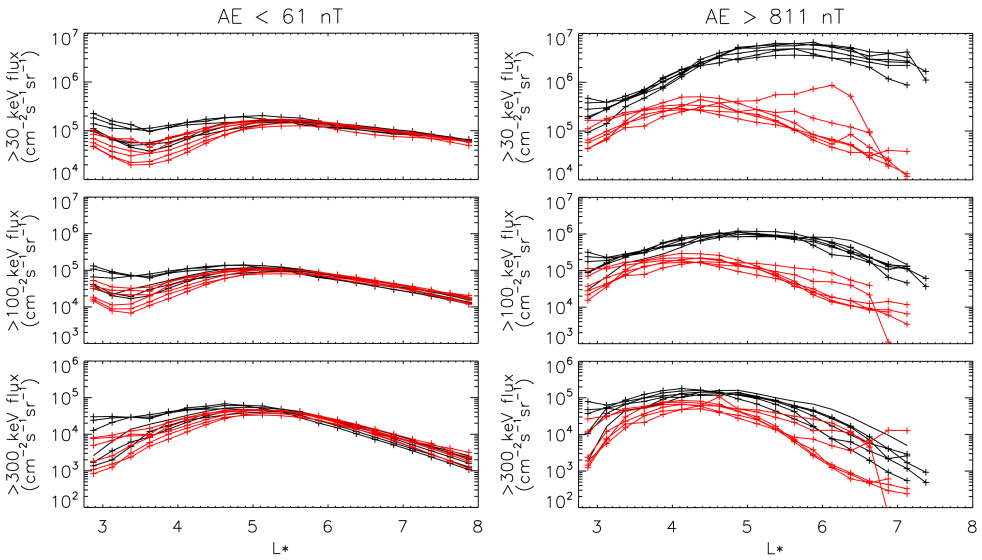

Figure 5.5 – The average >30, >100, and >300 keV electron flux at each L^* for the lowest (AE < 61 nT) and highest (AE > 811 nT) levels of AE. Red lines show dusk sector MLTs (16 - 21 MLT) and black lines show dawn sector MLTs (04 - 09 MLT).

5.4 Quantifying the Extent of MLT Variations

Figure 5.5 shows the >30, >100, >300 keV flux at each L^* for each of the 16 to 21 MLT bins (dusk sector) as red lines and the 04 to 09 MLT bins (dawn sector) as black lines. At the lowest level of AE (left panels) the dawn and dusk sector flux values are very similar for much of the outer radiation belt region. At the highest level of activity (right panels) differences

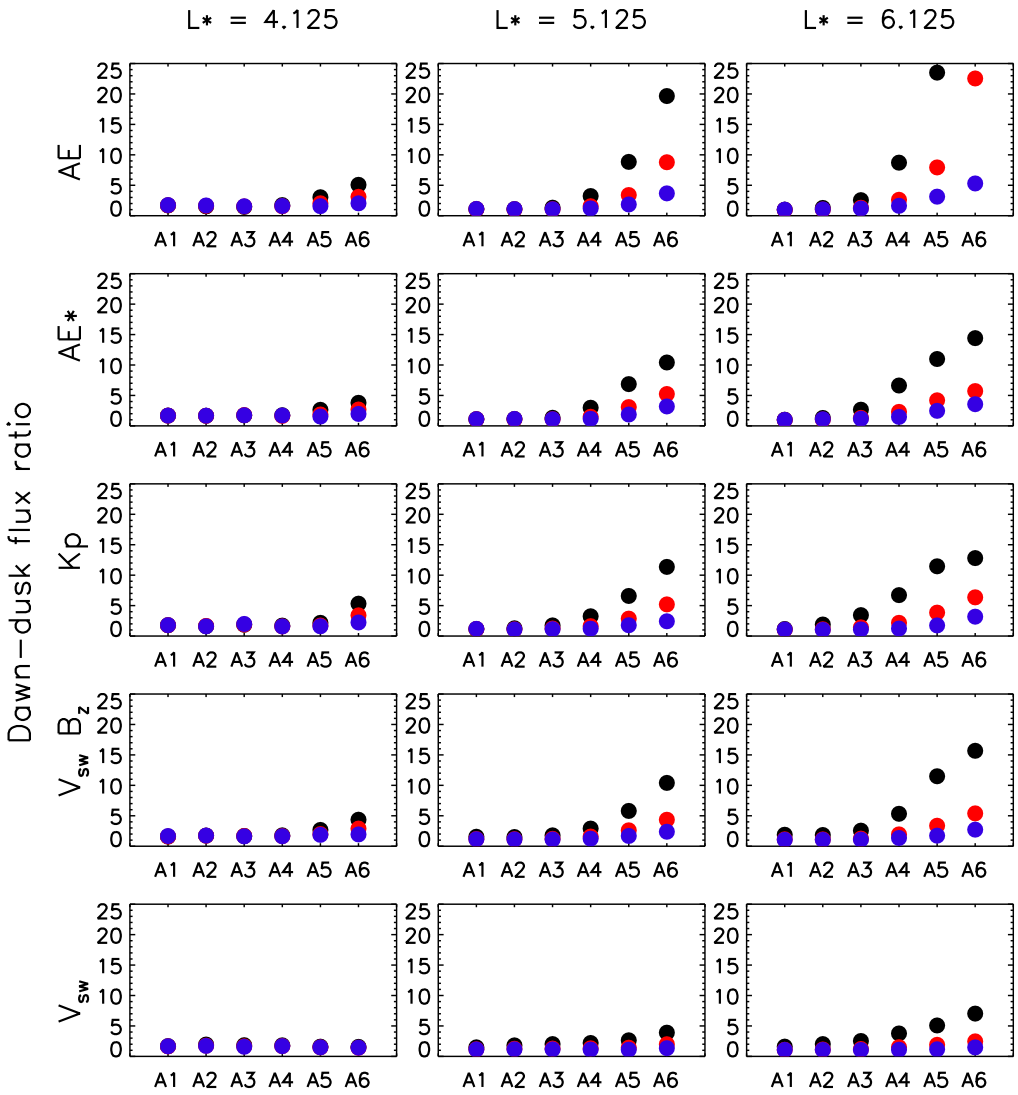

Figure 5.6 – Ratio of the average electron flux in the dawn sector to average flux in the dusk sector at each activity level defined by AE, AE*, Kp, $V_{sw}B_z$, and V_{sw} for three L^* values. Ratios for the >30 keV flux are in black, the >100 keV flux in red, and the >300 keV flux in blue. Note that the ratio of the dawn and dusk sector >30 keV flux exceeds the range of the y-axis in the top right panel with a value of 39.48 (L^*=6.125, AE defined activity levels).

can be observed between the two populations. To quantify the extent of the variation of the electron flux in MLT at a particular L^* distance, flux measurements taken between 04 and 09 MLT (the dawn sector) were collated and a mean calculated. An average flux for the MLT range 16 to 21 (the dusk sector) was determined in the same manner. The ratio was then taken between these dawn and dusk averages; henceforth referred to as the dawn-dusk flux ratio. Three L* bins were studied in this way, L^* = 4.125, 5.125, and 6.125, covering the outer radiation belt region. At each L^* value the dawn-dusk flux ratio was plotted against the activity level. This was repeated for each of the five activity metrics included in this study and is shown in Figure 5.6.

It should be noted that L^* is dependent on the magnetic configuration and it is possible that for very active periods $L^* > 5$ may not always exist. Here we simply present the dawn-dusk flux ratios according to POES satellite readings and L^* calculated using T96 as the external field model. Regardless of the activity metric used to define the activity levels, the ratios presented in Figure 4 are calculated from more than a thousand flux measurements.

It is apparent from Figure 5.6 that the dawn-dusk flux ratio can be much greater than one, and can exceed a factor of 20. The largest dawn-dusk ratios are for the >30 keV flux (black circles), but the >100 keV and >300 keV flux ratios (red and blue circles) also suggest a dawn-dusk flux asymmetry with values which can be larger than 20 and 5, respectively. The dawn-dusk flux variation tends to increase with activity level for all five activity metrics.

Additionally, for a given activity level, the ratios increase with L^*. At a fixed MLT and time, electrons drifting at a larger L^* will cross the equator further from the earth than those drifting at a smaller L^*. For a particular MLT, the equatorial magnetic field strength tends to be weaker the further you are from the Earth, reducing the magnetic drifts and increasing the convective drift velocity. Consequently, at the same MLT, electrons at larger L^* are more likely to be affected by an enhanced convection electric field than those at smaller L^*.

What is perhaps surprising is that the dawn-dusk flux ratio for >300 keV electrons also rises with increasing activity and L^* for all activity metrics considered, except solar wind velocity. This is a much higher energy than that used as a low energy boundary in most drift averaged radiation belt models (e.g. Glauert et al., 2014b; Shprits et al., 2013; Varotsou et al., 2008).

Dawn-dusk flux asymmetries were largest for A5 and A6 at L^* = 6.125 when the activity levels were defined by AE. This is likely due to the AE index being related to substorm injections and not subjected to the same time-blurring as AE* (which is the highest level of AE over the previous 3 hours). For a given level of activity, e.g. A5, the dawn-dusk flux ratios for AE*, Kp, and $V_{sw}B_z$ are similar. However, the corresponding level for V_{sw} is

consistently lower. At no V_{sw} defined activity level does any dawn-dusk ratio exceed 10. AE and AE* are both direct measures of currents associated with substorms and Kp is a direct measure of the magnetic field variation caused by a geomagnetic disturbance. The solar wind velocity is not a direct measure of geomagnetic activity, it is one factor along with the B_z component of the interplanetary magnetic field that drives substorms and electron injections. During periods of fast solar wind and fluctuating interplanetary magnetic field, more energy is loaded into the system which then results in periods of overall enhanced convection and substorms. As a result, the combination of V_{sw} and B_z gives dawn-dusk flux ratios that are more consistent with AE, AE*, and Kp. Kellerman and Shprits (2012) showed that tens of keV to MeV electron fluxes measured at geostationary orbit correlated well with V_{sw} once a suitable time delay had been applied. Here, the flux in each of the three energy channels does increase with increasing V_{sw} but this flux increase is more uniform in MLT.

Figure 5.6 shows a range of dawn-dusk ratios, extending from below 1 to more than 20. The question is then at what level does an MLT variation become problematic for radiation belt models which use a drift-average approximation? As the low energy flux is larger at dawn than the drift average, models applying an acceleration process to the average flux are likely to result in flux levels for higher energy electrons that are lower than observed. We suggest that to obtain a result to a factor of three agreement with data, a dawn-dusk ratio exceeding three is significant. Regardless of the activity measure used to define the levels, below activity level A3, a dawn-dusk ratio exceeding three is not observed. This indicates that a minimum electron energy (E_{min}) of 30 keV would be valid in 3-D radiation belt models that do not extend beyond L^* = 6.125 provided that during the time frame considered AE, AE*, Kp, and V_{sw} do not exceed 125 nT, 314 nT, 2, and 440 km s^{-1} respectively and $V_{sw}B_z$ is above -263 nT km s^{-1}. From Figure 5.2, this condition could be fulfilled 60% of the time. Radiation belt models are however mainly used to study periods of high activity to understand the physical processes involved (Albert et al., 2009; Glauert et al., 2014a; Li et al., 2014; Shprits et al., 2013). Figure 5.6 shows that during the higher levels of activity defined by AE (A4, A5, and A6) the >30 keV dawn-dusk ratios can exceed 20 or, when activity is defined by AE*, Kp, or V_{sw}, ratios can exceed an order of magnitude. In this case, a higher value of E_{min} could be required. Whilst the dawn-dusk ratios for the >100 and >300 keV flux are lower than those for the >30 keV flux, ratios exceeding 3 are still observed at A5 and A6. The implication is that an E_{min} of 100 or 300 keV may only be suitable 95% or 98% of the time respectively.

The average >30, >100, and >300 keV dawn and dusk side flux at each L^* is shown in Figure 5.7 for the six levels of activity defined by AE (coloured lines). Figure 5.7 shows that

the mean dawn-side >30 keV flux increases with AE throughout the radiation belt region. The mean dusk-side >30 keV flux (panel b) also increases comparably below $L^* \sim 4$ but, for $L^* \gtrsim 5$, the rise in the average dusk-side flux from activity levels A1 to A3 was less than on the dawn-side. Beyond A3 the average dusk-side flux actually drops with increasing activity.

For >100 keV electrons, the average dawn-side flux (panel c) again increased throughout the radiation belt region between activity levels A1 and A6. However, on the dusk-side the average flux (panel d) only increased with activity for $L^* \lesssim 5$. At larger L^*, the average dusk-side flux again falls with rising activity and the peak in the flux-L^* profile shifts from $L^* \sim 5$ to $L^* \sim 4$. This is a particularly interesting feature and is discussed further in the following section.

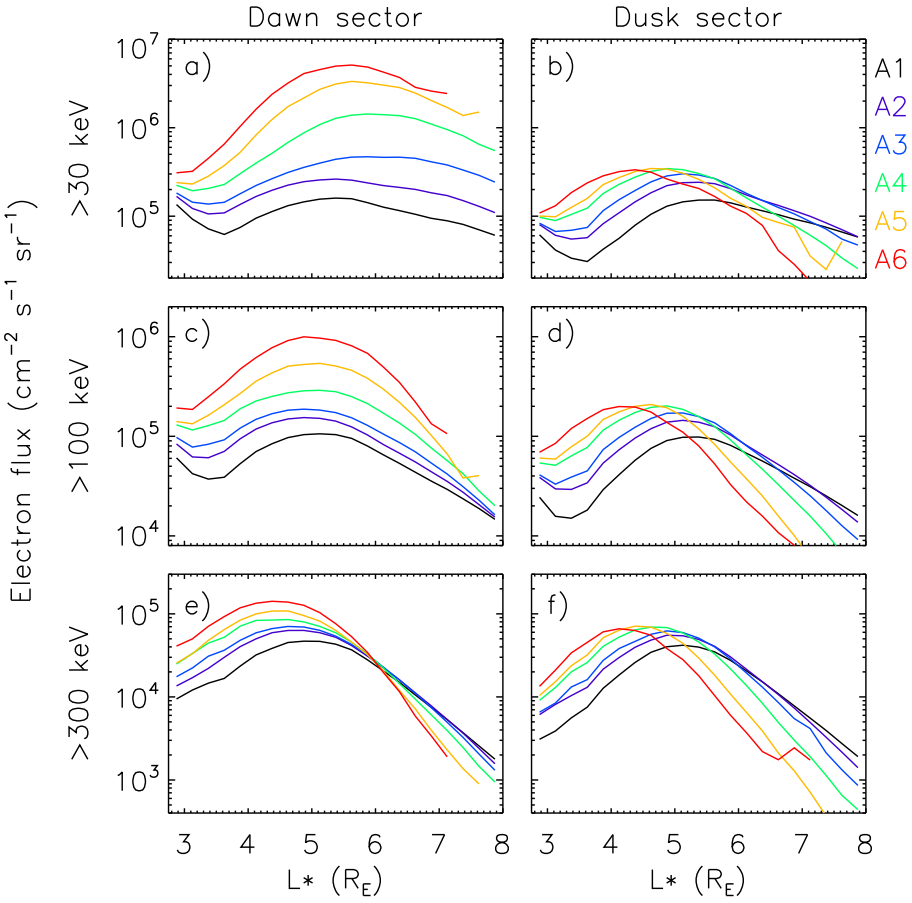

Figure 5.7 – Average dawn sector and dusk sector electron flux - L^* profiles for >30, >100, >300 keV electrons. The profiles for each of the six activity levels defined by AE index are shown here, each in a different colour.

Perhaps the most intriguing dawn-dusk average flux variation is that observed for the >300 keV electrons. At this energy, the average dawn-side flux (Figure 5.7e) rises with increasing AE for $L^* \lesssim 5.5$ but remains approximately constant with increasing activity between $L^* \gtrsim 5.5$ and $L^* \sim 6.2$. For $L^* > 6.2$ the dawn side flux decreases with increasing activity. The average dusk-side flux at >300 keV (panel f) shows similar behaviour to the dusk-side >30 keV and >100 keV flux (panels b and d). For dusk sector MLTs, the >300 keV flux rises with activity out to $L^* \sim 4.5$ and, at larger L^*, falls as activity increases. In the dusk sector, the peak in the flux-L^* profile moves from $L^* \sim 5$ to $L^* \sim 4$ with rising AE. As a result, the >300 keV dawn-dusk ratios greater than 3 observed at $L^* = 6.125$ in Figure 5.6 arise due to a dusk-side depletion rather than a dawn side enhancement.

Figure 5.7 only shows the average dawn and dusk-side flux-L^* profiles for the six activity levels defined by AE. However, the average dawn and dusk-side flux distributions displayed similar trends when the activity levels were defined by AE*, Kp, and $V_{sw}B_z$, as shown for the >100 keV and >300 keV flux in Figure 5.8. Note however, that when the Kp index was used to set the six activity levels, the dawn side flux was lower at A6 for $L^* > 6$ than for the other activity metrics. Figure 5.9 shows the mean dawn and dusk side flux-L^* profiles for activity levels defined by V_{sw}. Unlike in Figures 5.7 and 5.8, the average dawn and dusk side

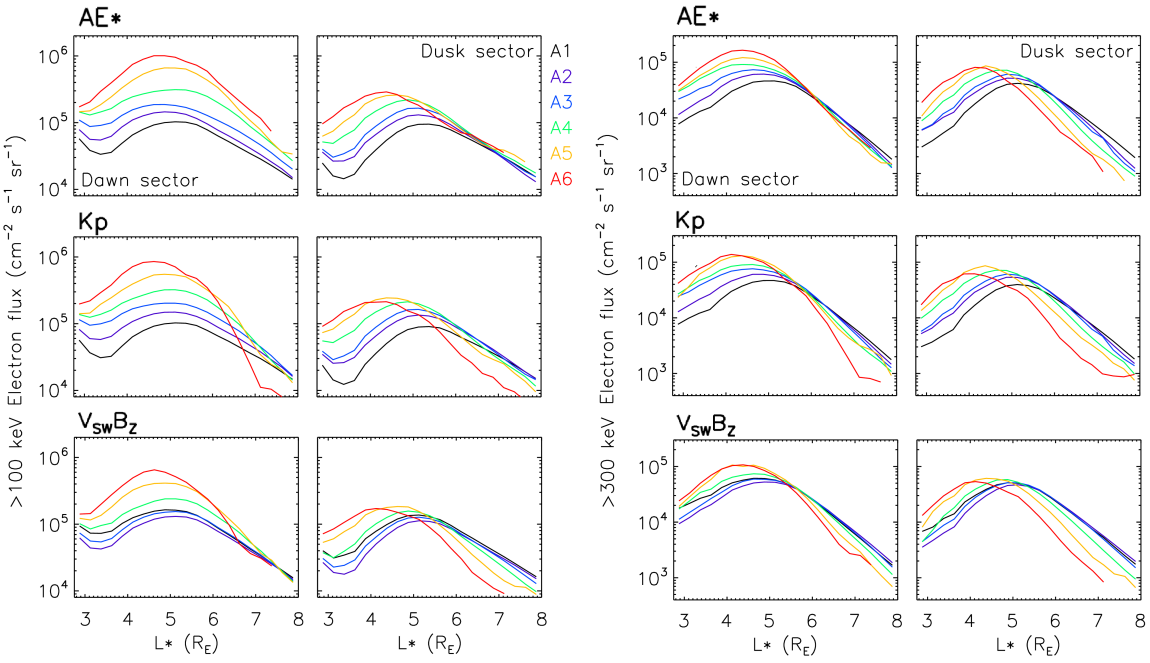

Figure 5.8 – Average dawn sector and dusk sector electron flux - L^* profiles for >100 keV and >300 keV electrons at the six activity levels defined by AE*, Kp, and $V_{sw}B_z$.

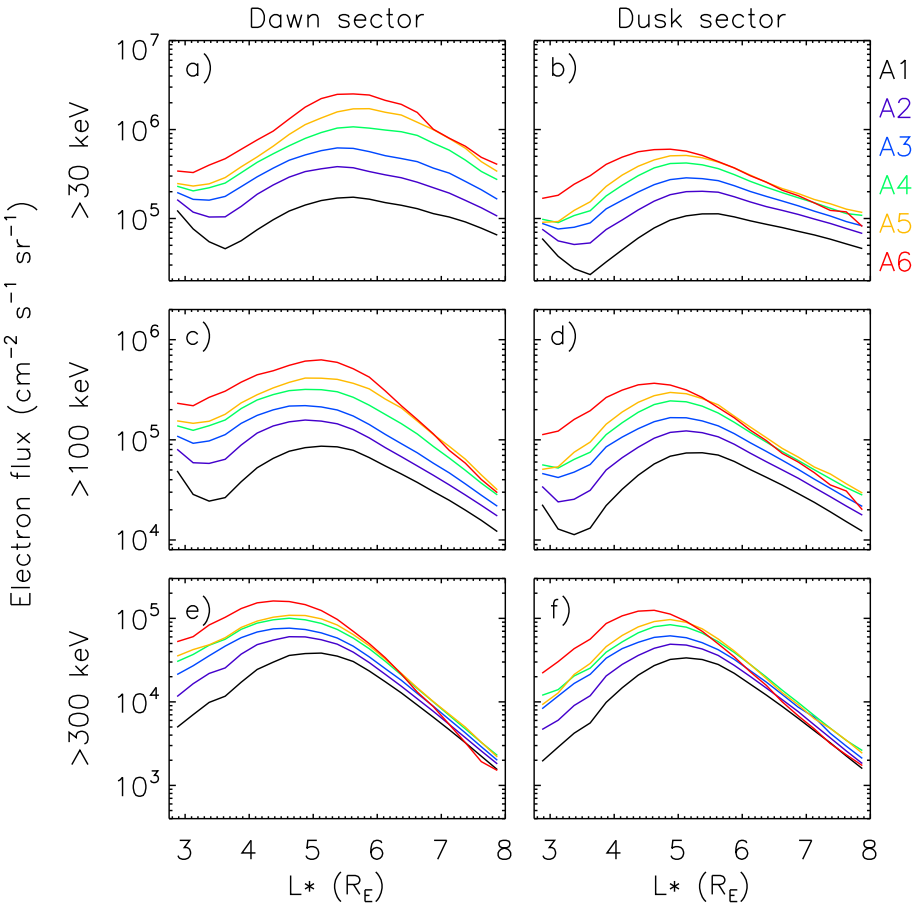

Figure 5.9 – Same as Figure 5.7 but for the six activity levels defined by V_{sw}, each in a different colour.

flux both rose with activity for $L^* > 6$. As discussed previously, this is perhaps due to solar wind speed being only one driver of geomagnetic activity.

As L^* is dependent on the magnetic field configuration, it is possible that during some active periods not all L^* values in the L^* = 3 - 8 range may exist. Dawn or dusk flux averages that were calculated from fewer than 100 measurements were not plotted on Figures 5.7, 5.8, or 5.9.

5.5 Causes of the Dusk Side Depletion

Trajectories of equatorially mirroring electrons, which have starting energies of 30, 100, and 300 keV on the dawn side of the Earth (at X = 0), are shown in Figure 5.10. Here a dipole magnetic field was used together with the Kp dependent Volland-Stern electric field

(Maynard and Chen, 1975) to calculate electron drift trajectories by solving the following equation for the guiding centre velocity ($\mathbf{v}_{gcd}$):

$$\mathbf{v}_{gcd} = \frac{\mathbf{E} \times \mathbf{B}}{B^2} + \frac{\mu}{qB^2}\mathbf{B} \times \nabla \mathbf{B}, \tag{5.1}$$

where $\mathbf{E}$ is the electric field, $\mathbf{B}$ is the magnetic field, q is the electron charge, and μ is the first adiabatic invariant. Equation 5.1 is the sum of the $\mathbf{E} \times \mathbf{B}$ drift given by equation 1.17 and the gradient drift given by equation 1.32. POES satellites observe electrons with much lower pitch angles than 90^o but, so that only the $\nabla \mathbf{B}$ magnetic drift need be considered, trajectories of equatorially mirroring electrons have been presented here. In chapter 1, Figure 1.9 showed that the gradient and curvature drift times are similar for a dipole field, suggesting that considering only 90^o electrons is a fairly good approximation which greatly simplifies the calculation.

Constant Kp = 5.33 has been used to set the Volland-Stern electric field for the trajectories shown in Figure 5.10a, corresponding to the lower bound of the A6 Kp activity level. A constant Kp = 7.00 was used for the drift paths in Figure 5.10b, chosen to be notably higher than the Kp lower bound of A6. The drift paths are calculated for several starting radial distances between 4 and 7.5 R_E for each electron energy.

In the previous section it was shown that the observed dawn-dusk asymmetry for >30 keV electrons measured by the POES satellites occurs due to an activity related increase in the dawn-side flux throughout the outer radiation belt region that was not reflected on the dusk-side. On the dusk-side, the average >30 keV electron flux for $L^* \gtrsim 5$ actually fell with rising activity. Figure 5.10 shows that this observation is consistent with the theoretical picture of 30 keV electrons on open drift paths due to an enhanced convection electric field, causing electrons to leave the magnetosphere on the day side before reaching the dusk-sector. The flux of >100 keV electrons measured by POES also increased with activity on the dawn side while decreasing on the dusk side. Figure 5.10a again shows that 100 keV electrons could be on open drift paths due to enhanced convection.

In Figure 5.10, for Kp = 5.33 (row a), 300 keV electrons that pass the dawn-side at a distance between 4 and 7.5 R_E are not on open drift paths unlike some, or all, of the corresponding drifts for 30 and 100 keV electrons. Even for a Volland-Stern electric field corresponding to Kp = 7.00 (row b), a higher Kp than the lower threshold of A6, the 300 keV electrons still showed closed drift paths. However, in Figure 5.7e and f the >300 keV flux observed by the POES satellites shows a dusk side depletion in the same manner as the >30 and >100 keV flux. Tracing 300 keV electrons demonstrates that, while on closed drift

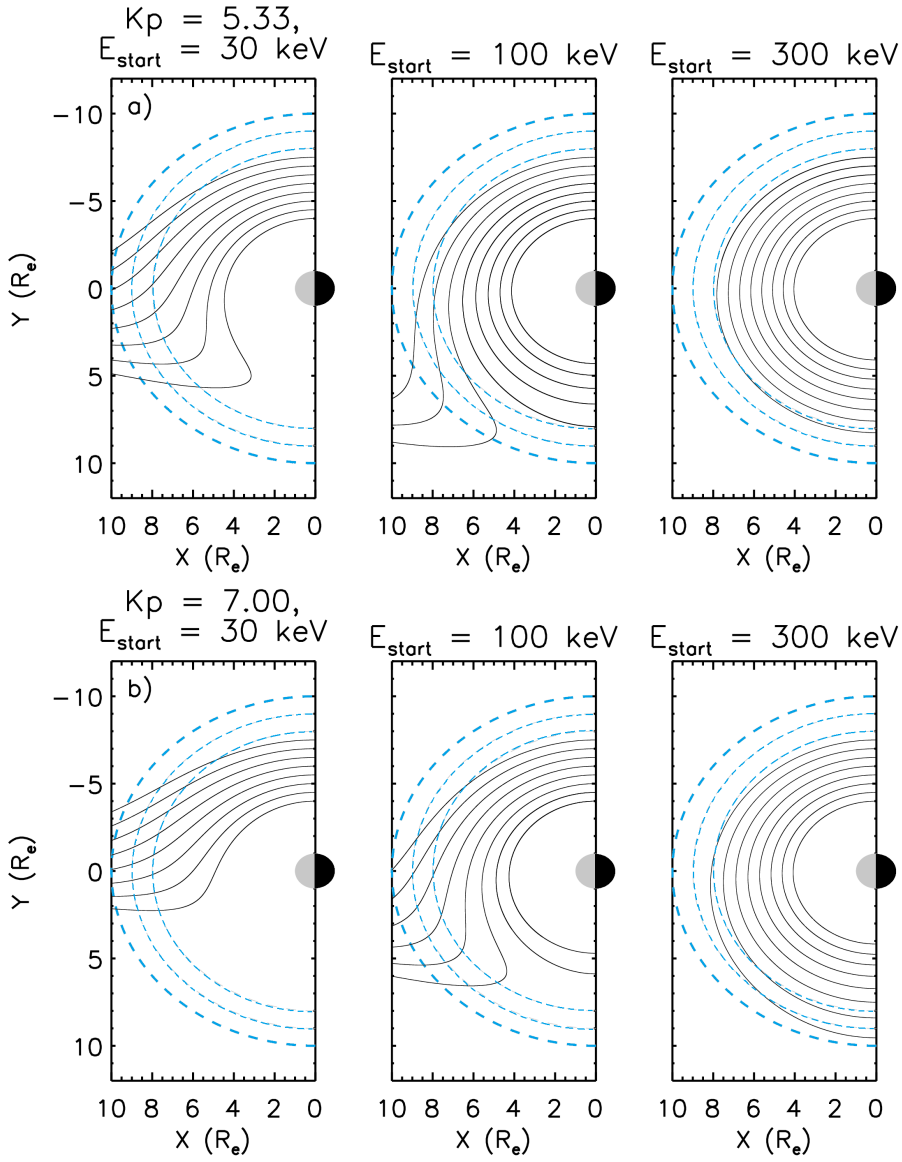

Figure 5.10 – Drift paths of equatorially mirroring electrons in a dipole magnetic field for a Volland-Stern electric field assuming a constant Kp of a) 5.33 and b) 7.00. These are shown as if looking down on the northern hemisphere, with the Sun to the left of the page. The drift paths shown start on the dawn-side of the Earth at radial distances between 4 and 7.5 R_E and relate to electrons with starting energies of 30, 100, and 300 keV. The blue dashed lines mark radial distances of 8, 9, and 10 R_E for reference.

paths, the trajectories *have* been perturbed by the convection electric field. In Figure 5.10a (far right panel), 300 keV electrons that started at 7.5 R_E at X = 0 on the dawn side are at $\sim$8.5 R_E at X = 0 on the dusk side. Depending on the location of the magnetopause, this

radial transport by the convection electric field could still result in electrons encountering the magnetopause before completing a full drift.

Other processes, such as electron scattering due to wave-particle interactions, could also cause a reduction in the dusk-side flux. On the dusk-side, interactions with hiss or electromagnetic ion cyclotron (EMIC) waves can scatter electrons into the loss cone, removing them from the region (Kersten et al., 2014; Meredith et al., 2004). Meredith et al. (2004) showed that while equatorial hiss is not typically significant beyond a Mcllwain L value of L = 5, midlatitude hiss is observed beyond L = 6 in the MLT range 12 - 15. EMIC waves have been shown to be strong where the ring current overlaps the plasmasphere (Kersten et al., 2014) and act on electrons with pitch angles below $\sim 45^{o}$ (Usanova et al., 2014). Due to the low altitude orbit of the POES satellites, the pitch angles of the electron flux at L^{*} = 5 - 6 are below 45^{o}. However, EMIC waves generally resonate with >500 keV electrons (Albert, 2003; Meredith et al., 2003b; Summers and Thorne, 2003) so would likely only account for a small portion of the dusk-side loss. Furthermore, the reduction of the dusk-side flux is most pronounced during the highest level of activity, for which $\sim$99.995% of AE measurements greater than 811 nT are accompanied by the magnetopause moving below L = 8 in the preceding hour. For this illustrative calculation the magnetopause location was calculated using the widely used Shue Model (Shue et al., 1998) with the 1 R_E correction applied (Case and Wild, 2013). We therefore suggest that the largest contribution to the reduction in the average dusk-side >300 keV electron flux during periods of high activity was the combination of magnetopause shadowing effects and radial transport by an enhanced convection electric field.

5.6 Causes of the Dawn Side Enhancement

In Figures 5.3 and 5.7 the average dawn-sector >30 and >100 keV flux increased with activity. A study by Kissinger et al. (2014) found that electrons with energies less than a few hundred keV were supplied to the radiation belt region in the absence of substorms, during steady magnetospheric convection events. The increased convection electric field strength causes plasma sheet electrons on open drift paths to enter the radiation belt region (Friedel et al., 2001). The particle tracing calculation in Figure 5.10 shows 30 and 100 keV electrons on open drift paths due to an enhanced convection electric field. Therefore, it is likely that the >30 keV and >100 keV flux can increase in the dawn-sector due to enhanced convection of plasma sheet particles. Additionally, the >30 and >100 keV flux will likely be further increased by substorm injections (Cayton et al., 1989; Tang et al., 2018).

In Figure 5.7f, the average >300 keV dawn side flux also increased with activity between $L^* \sim 4.5$ and $L^* \sim 6$, an L^* range where the corresponding dusk side flux decreased. While the >30 and >100 keV dawn sector flux may be enhanced from convective plasma sheet inflow, Figure 5.10 shows that >300 keV electrons are unlikely to be on open drift paths, even at activities significantly higher than the lower limit of A6. Without a rapid supply of >300 keV electrons, the combination of magnetopause shadowing and radial transport from an enhanced convection electric field would cause a decrease in flux that rapidly affects all MLT. As a result, the loss mechanism for >300 keV electrons suggested in the previous section cannot alone explain the observed asymmetries in the >300 keV flux.

A very similar result to Figure 5.7 was obtained when AE* was used to define the activity levels, shown in Figure 5.8. As using AE* helps account for electron drift time (Meredith et al., 2004), the variations between the dawn and dusk side >300 keV flux-L^* profiles are unlikely due to the transit time of electrons.

Outside of the last closed drift shell (the maximum value of L^*), the magnetic topology is such that the electron drift trajectory will result in loss to the magnetopause. As electrons are lost within a drift period, regardless of the electric field strength, the flux observed outside of the last defined L^* value is transient. Considering this, in the northern hemisphere, for the ascending phase of the satellite orbit, the POES electron flux measurements for the 5^o of magnetic latitude (Lat_{mag}) following the first undefined L^* value were binned by the magnetic latitude change ($\Delta\text{Lat}_{\text{mag}}$) and MLT. For the descending phase of the orbit, in this hemisphere, the electron flux measurements for the 5^o of Lat_{mag} prior to the last undefined L^* value were binned by $\Delta\text{Lat}_{\text{mag}}$. The situation described above was reversed when the satellite was in the southern hemisphere.

Calculating the mean of flux measurements in each MLT-$\Delta\text{Lat}_{\text{mag}}$ bin gave the average electron flux distribution outside the last L^* value in terms of the magnetic latitude change. Figure 5.11 shows the result of this analysis for the six activity levels defined by AE*. Using AE* should help mitigate the effect of the electron drift time from the average. The average flux for >30, >100, and >300 keV electrons, not on a closed magnetic drift paths due to the magnetic topology, rose with activity on the dawn side (to the left of the dashed white line). Average electron flux increases with AE* are not evident for many of the dusk sector MLT bins and it would appear that the increase in electron flux occurs mostly for the midnight to dawn MLT range. Electrons encountering the magnetopause prevents the enhanced dawn-side population from propagating to the dusk flank. That this trend is observed for >300 keV electrons as well as for >30 and >100 keV electrons is consistent with rapid enhancements

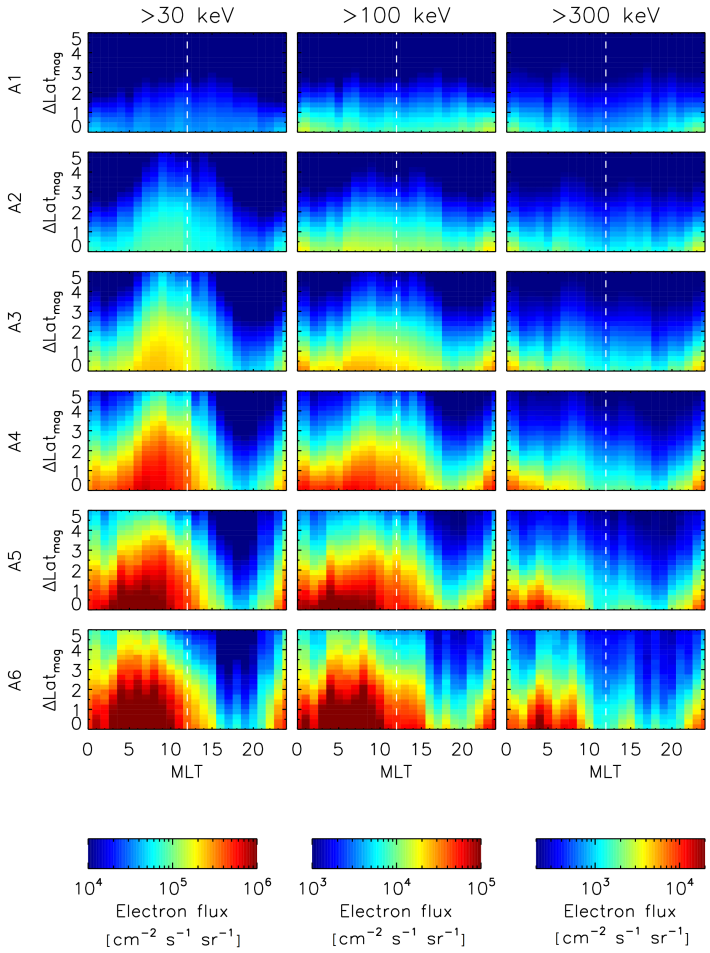

Figure 5.11 – >30, >100, and >300 keV electron flux measured by the POES satellites binned by AE*, MLT, and the magnetic latitude change from the magnetic latitude of the last defined L^* value.

of the >300 keV electron population supplying electrons to the dawn sector faster than they can be lost to the magnetosphere.

Chorus wave acceleration may help to sustain the dawn-side flux by acting on electrons of lower energy, accelerating them to 300 keV and beyond. However, the timescale for this acceleration is of the order of hours, longer than the drift time of ∼300 keV electrons (Horne et al., 2005a). Excluding electric drifts, a 300 keV electron takes ∼15 minutes to travel from midnight to noon at $L^* = 6$ (from equation 1.57).

Sergeev et al. (1992) suggest that an observed simultaneous enhancement of electron flux at energies extending from 200 keV to ∼1 MeV during the 7th May 1986 may be

a result of the dipolarization of field lines on the night-side. This is the reconfiguration of the magnetic field from a stretched tail-like structure to a quasi-dipole-like formation (Sauvaud and Winckler, 1980; Sugiura et al., 1968). Electrons undergo non-adiabatic local acceleration as a result of the induced electric field associated with the magnetic fluctuations. Additionally, the changing magnetic field can cause alterations to electron drift shells. Sergeev et al. (2014) also observed dispersionless injections at geostationary orbit across a range of energies extending from 10s of keV to more than 350 keV shortly after a dipolarization onset, covering the energy range of interest here. Further work considering changes in the O+ population has shown that nonadiabatic acceleration, likely due to dipolarization events, can occur in the inner magnetosphere at Mcllwain L $<$ 6.6 (Nosé et al., 2016). Similar enhancements have also been observed in the electron population at L $\sim$ 5.5 for energies up to 3 MeV, again linked to intense dipolarization electric fields (Dai et al., 2015).

The observed dawn sector $>$300 keV flux enhancement could therefore originate from electrons being injected into the radiation belts with energies $>$300 keV as a result of intense induced electric fields associated with dipolarization events. Coupled with drift paths which encounter the magnetopause, this effect would result in dawn-dusk $>$300 keV flux asymmetries, as observed in Figure 5.11.

5.7 Discussion

Electrons with energies of hundreds of keV and above injected into the radiation belt region as a result of intense dipolarization electric fields provide a population of higher energy electrons which can be accelerated by other processes such as wave-particle interactions and radial transport. In the absence of magnetopause shadowing and at lower L^* values, these electrons would likely be on closed drift paths. Chorus waves acting on this population may help explain the rapid occurrence of MeV electrons sometimes observed during storm time (Horne et al., 2005a; Reeves, 1998).

Chorus waves are observed mainly on the dawn-side of the earth (Meredith et al., 2012) and act to precipitate electrons of a few tens of keV. However, since the average $>$30 keV electron flux observed is higher at dawn than dusk, this suggests that injections and enhanced convection are efficient at supplying electrons at low equatorial pitch angles, operating at a faster rate than electrons can be lost by chorus precipitation.

The results presented in section 5.3 are based on measurements taken at low earth orbit and, as a result, are representative of low equatorial pitch angles. It is noted that chorus waves propagating primarily in the dawn sector are likely to diffuse electrons to lower pitch angles,

while on the dusk side, chorus waves are less intense (Horne et al., 2013). However, the change in equatorial pitch angle distributions caused by wave-particle interactions typically occurs over many drift orbits (Lyons et al., 1972) and therefore the pitch angle distributions on the dawn side are unlikely to be extensively different to those at dusk. Recent findings by Shi et al. (2016), using Van Allen Probes data, support this. They examined the anisotropy of electron pitch angle distributions for three levels of activity and did not find dawn-dusk variations in the pitch angle distributions of 100, 200, and 350 keV electrons for any of the three activity levels.

Statistical global electron flux distributions, similar to those in Figure 5.3, have been shown by Thorne et al. (2007) for 153 keV and 340 keV electrons measured by the Combined Release and Radiation Effects Satellite (CRRES), at three levels of AE*. In agreement with the >100 keV results in this chapter, Thorne et al. (2007) also found dawn-dusk asymmetries in the 153 keV flux that developed with increasing activity. A notable difference to the results presented here is the flux level of the inner belt. Thorne et al. (2007) showed that, at lower activities, the inner region contained the highest electron flux. This has been affirmed by Reeves et al. (2016) when considering the energy dependent radial distribution of the radiation belts. However, in Figure 5.3 the flux of the inner region is comparable to that of the outer belt. POES satellites generally observe flux with low equatorial pitch angles, approximately 11^{o} at $L^{*} \sim 3$. Pitch angle distributions (PADs) in the inner belt are highly anisotropic with a peak near 90^{o}, whilst at larger L^{*} values, distributions are significantly flatter (Shi et al., 2016). The electron flux measurements presented by Thorne et al. (2007) and Reeves et al. (2016) are representative of electrons near 90^{o} pitch angle. Considering the peaked PADs in the inner belt, we would expect the low pitch angle electron flux measured by the POES satellites to be smaller than the equatorially perpendicular flux presented by Thorne et al. (2007) and Reeves et al. (2016). Further out, as the PADs tend to be considerably flatter, the difference between flux at high and low pitch angles might not be so large.

The observation of a dawn-dusk flux ratio that increases with geomagnetic activity has important implications for modelling studies. Flux asymmetries along an electron drift shell may cause inconsistencies between 3-D model results and data. We suggest here that one way to address this issue is by careful selection of the energy of the low energy boundary. Current drift averaged 3-D models set the lowest energy value between 10 keV and ∼200 keV. Our results suggest that the boundary should be set at higher energy with increasing activity otherwise the models may under- or over-estimate acceleration and losses. However, the disadvantage of setting the boundary at a higher energy is that, since most models use a

co-ordinate system based on the first invariant (see chapter 2), it restricts simulations of the radiation belts at lower L^* to increasingly higher energies.

Recent work has highlighted the importance of seed population acceleration in the generation of relativistic and ultrarelativistic electrons (Jaynes et al., 2015; Thorne et al., 2013b) indicating that processes acting on lower energy electrons are crucial to understanding the radiation belt region as a whole. In order to include electrons influenced by the convection electric field in radiation belt calculations, a convection-diffusion model is needed. Examples of convection-diffusion models are the Versatile Electron Radiation Belt-4D model (Shprits et al., 2015), the Asymmetric Physical Radiation Belts model (Bourdarie et al., 1997), and the Comprehensive Inner Magnetosphere-Ionosphere Model (Fok et al., 2014). The MLT dependence of the >30 keV, >100 keV, and >300 keV electrons during active conditions shown in this chapter highlights the importance of the development of these MLT dependent models in order to better understand the region. Statistical studies such as that presented here could help provide boundary conditions for such models.

After an active period, the flux at each L^* returns to being mostly homogenous in MLT. This is indicated by the electron flux for activity levels below A3 which did not show notable MLT asymmetries. Dawn-dusk flux asymmetries set up during a period of high activity will likely degrade over several drift periods.

5.8 Summary and conclusions

A statistical study of the global distribution of the >30, >100, and >300 keV electron population has been presented using data spanning 14 years from the multi-satellite low earth orbit POES constellation. AE, AE*, Kp, V_{sw}, and $V_{sw}B_z$ have each been used to define six activity levels to study the change in the global electron flux distribution with increasing activity. Our principle results are the following:

1. With increasing activity the average >30 keV electron flux increased. This rise in flux was primarily localized to the dawn-sector, resulting in an MLT asymmetry in the electron flux distribution which can be more than a factor of 20. Asymmetrical >30 keV flux distributions may be due to electrons at this energy being on open drift paths.

2. As the average >30 keV flux was seen to be higher in the dawn sector than the dusk during periods of high activity and remain so throughout the dawn sector, this suggests that electron injections are more efficient at supplying $\sim$ 30 keV electrons than chorus precipitation is at removing them at the low pitch angles observed.

3. The average >100 keV flux for $L^* \lesssim 5$ rose with activity on both the dawn and dusk-sides of the earth. For $L^* > 5$, the average dawn-side flux continued to rise with activity while the average dusk-side flux decreased, resulting in flux asymmetries which can be of the order of a factor of 20 when AE was used to define activity.

4. As activity increased, the >300 keV average dawn-side flux rose for $L^* \lesssim 6$. On the dusk-side, the peak of the average flux-L^* distribution shifts inwards with rising activity and the flux increases for $L^* \lesssim 5$. Exterior to this L^* range, the flux decreases as activity rises. We suggest that the asymmetry observed in the >300 keV electron flux distribution is due to the combination of magnetopause shadowing, causing a dusk-side loss, and injections of >300 keV electrons, from some dipolarization fronts, sustaining the dawn-side flux level.

5. Below activity level A3 (corresponding to AE < 125 nT, AE* < 314 nT, Kp < 2, V_{sw} < 440 km s^{-1}, and $V_{sw}B_z$ > -263 nT km s^{-1}), no dawn-dusk asymmetry in the flux distribution greater than a factor of three was observed. We therefore suggest that drift-averaged radiation belt models could set a minimum energy of 30 keV at L^* ∼6 when modelling periods of low to moderate activity. For more active periods, a larger value of E_{min} is required otherwise the models may over- or underestimate the acceleration and loss processes. At activity level A3 and beyond, E_{min} should be larger than 100 keV and should be set to approximately 300 keV for very extreme activities.

In addition to being a useful indicator for the location of the minimum energy in 3-D radiation belt models, this study, has highlighted that, during times of high activity, measured electron fluxes at energies below ∼300 keV should only be considered representative of the MLT at which the values were recorded. Flux levels measured by low energy instruments, such as MagEIS on the Van Allen Probes, could vary depending on whether the spacecraft was on the dusk or dawn-side of the earth by more than an order of magnitude during geomagnetically active periods. This variation should be taken into account when analysing low energy electron flux data and highlights the importance of multiple satellites when investigating radiation belt electrons at energies below 300 keV.

Chapter 6

Determination of the Equatorial Electron Differential Flux From Observations at Low Earth Orbit

The results of this chapter have been published in the *Journal of Geophysical Research: Space Physics* as:

Allison, H. J., Horne, R. B., Glauert, S. A., and Del Zanna, G., (2018), *Determination of the Equatorial Electron Differential Flux From Observations at Low Earth Orbit*, *J. Geophys. Res. Space Physics*, 123, 9574–9596, doi:10.1029/2018JA025786

The presented analysis is the outcome of the author's own work, with R. B. Horne, S. A. Glauert, and G. Del Zanna providing advice and supervision. The results from this chapter were presented at the AGU Chapman conference on Particle Dynamics in the Radiation belts 2018 held in Cascais, Portugal and also at the Fall AGU meeting 2018 in Washington, DC.

6.1 Introduction

As discussed in chapter 3, a number of studies have highlighted observed links between increases in the seed population (30 - 500 keV electrons) and the generation of relativistic electrons in the Earth's radiation belts (e.g. Boyd et al., 2016; Jaynes et al., 2015, etc). Substorm injections can increase the seed population, providing additional electrons that can

be accelerated to relativistic energies, potentially resulting in larger relativistic flux levels (Obara et al., 2000).

Using the DREAM3D diffusion model, Tu et al. (2014) showed that model results were closer to observations for the October 2012 storm when a realistic seed population was used for the low energy boundary and event specific diffusion coefficients were employed. Tu et al. (2014) effectively demonstrated that knowledge of the seed population is important to fully understand the evolution of the radiation belts.

At present, the Van Allen Probes MagEIS instruments provide measurements of the energetic electron flux throughout the Earth's radiation belt region and were introduced in chapter 4. The twin Van Allen Probes operate in a highly elliptical near-equatorial orbit, with a period of $\sim$9 hours and an apogee of $\sim$5.8 R_E, inside geostationary orbit (Mauk et al., 2013). Level 3 data from MagEIS supplies the electron flux for energies in the range $\sim$30 keV - 4 MeV in 11 pitch angle bins (Blake et al., 2013). The MagEIS instruments were powered on in September 2012 and remain in operation (Spence et al., 2013), providing an excellent dataset with which to study the seed population (see chapter 4). For radiation belt models, the Van Allen Probes data can be used to create event specific low energy boundary conditions in order to examine periods after September 2012 and inside $L^* \approx 5.5$. However, before this period, seed population data tends to be limited in energy and pitch angle coverage.

Prior to 2012, the NOAA POES Satellites were operational and they will continue to be past the end of the Van Allen Probes mission (likely early 2020). POES measure $>$30, $>$100, and $>$300 keV electron data at a 2s resolution (Evans and Greer, 2004). Launched in May 1998, NOAA15 was the first POES satellite to carry SEM-2. Since then, additional POES satellites have been launched and, to date, six are still sampling data. POES MEPED measurements are therefore available for the last 20 years, providing a wealth of information on seed population electrons. Operating in a $\sim$98.5^o inclination low Earth orbit, these satellites sample the electron flux across a broad range of the magnetic coordinate L^*. During quiet conditions, POES coverage can extend from $L^* < 1.3$ to $L^* > 8.5$; a larger L^* range than possible with the Van Allen Probes. Due to the orbit, the POES satellites offer very rapid measurements of the radiation belts and provide data in multiple magnetic local time (MLT) planes. However, one of the major limitations of the POES dataset for studying the seed population is that the electron channels of MEPED only supply integral flux. Additionally, measurements are taken near the bottom of magnetic field lines, and the electron flux sampled is consequently of low equatorial pitch angle. If the POES MEPED dataset could be used to determine the differential flux at a number of seed population energies, for equatorial pitch angles close to 90^o, it could provide detailed information of the seed population prior to the

Van Allen Probes mission (September 2012) and form event specific low energy boundary conditions for radiation belt models when MagEIS data is unavailable.

In this chapter, a method is developed to determine the differential electron flux for energies mainly in the 100 - 600 keV range, at a 90^{o} equatorial pitch angle, from measurements taken by the integral electron channels of MEPED on-board the POES satellites at low Earth orbit. Such a task has two main challenges, the first of which involves inferring the state of the energetic electron component of the radiation belts using the low equatorial pitch angle data measured by the POES satellites. In section 6.3 we present a method to convert the electron flux from the POES satellites to omnidirectional flux, using statistical pitch angle distributions determined from Van Allen Probes measurements. The second main challenge involves using integral flux measurements to deduce the electron flux at a number of seed population energies. Two different methods are explored here, the first of which uses data from the AE9 model, discussed in section 6.4.1, and the second employs an iterative approach based on what is referred to as a 'Reverse Monte Carlo method' (McGreevy, 2001), discussed in section 6.4.2. The omnidirectional flux for a range of energy values are finally converted to directional 90^{o} flux, using the technique presented in section 6.5. In order to validate the results, we compare the outputs at various energies (100 - 600 keV) to observations from the Van Allen Probes, the results of which are given in section 6.6. It is suggested that the presented methods could be used to formulate event specific minimum energy boundary conditions for radiation belt models, using MEPED flux measurements, in order to better study times, or L^{*} values, outside the Van Allen Probes mission. We investigate this idea in sections 6.7 and 6.8. Finally successes and drawbacks of the method are discussed and conclusions presented in sections 6.9 and 6.10.

6.2 POES satellites

The polar orbiting POES constellation were first introduced in chapter 4 and also used for the analysis in chapter 5. Each POES satellite is Sun-synchronous and operates over a limited range of MLT. In this study, data from multiple POES spacecraft have been combined (an approach also taken in chapter 5), yielding rapid observations of the radiation belt region across multiple MLT planes; an important consideration for electrons at seed population energies (Allison et al., 2017).

As discussed in chapers 4 and 5, MEPED contains two solid-state detector telescopes, T0 and T90, mounted in perpendicular orientations, both with a $\pm 15^{o}$ viewing angle. The T0 telescope generally samples precipitating electrons in the bounce loss cone (Rodger et al.,

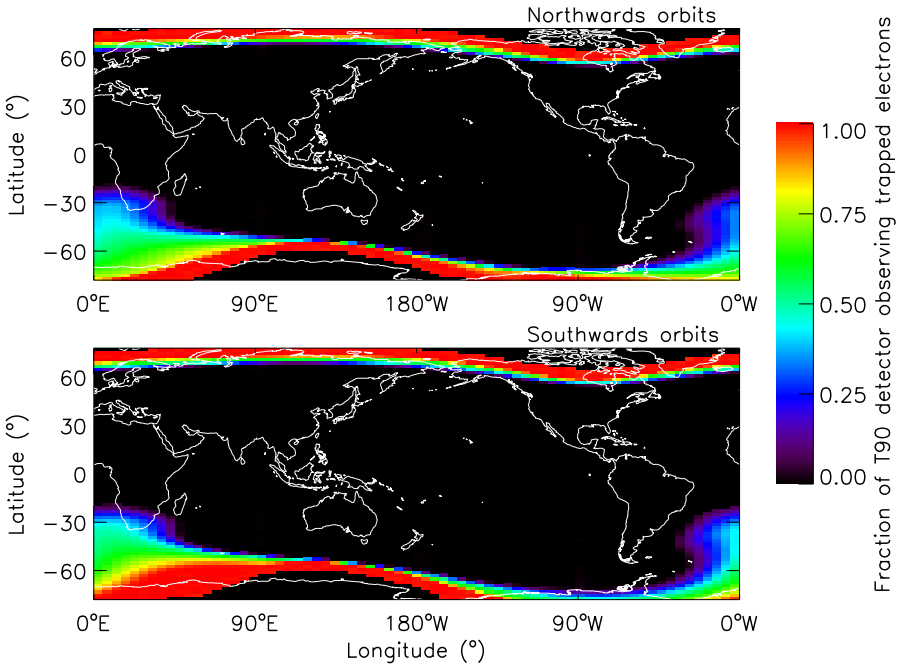

Figure 6.1 – World map showing the fraction of the T90 telescope $\pm 15^{o}$ viewing angle observing trapped electrons for 2011 NOAA15 data.

2010b) while T90 generally observes a mix of trapped, drift loss cone, and bounce loss cone electrons for much of the radiation belt region (Rodger et al., 2010a). For further details, see appendix A.

Following the approach outlined by Rodger et al. (2010a), we use the International Geomagnetic Reference Field (IGRF) model (Thébault et al., 2015) for mid 2011 to determine the angular width of the loss cone and hence the electron populations sampled by the T90 telescope of MEPED. By considering the $\pm 15^{o}$ of the telescope, Figure 6.1 shows the fraction of the T90 telescope field-of-view that sampled trapped electrons at each location for NOAA15 data from 2011. Due to significant difference in the pitch angles viewed, highlighted by Rodger et al. (2010a), northwards and southwards-going orbits have been considered separately.

Rodger et al. (2010a) suggested the flux of trapped electrons observed by T90 will likely be larger than the flux in the drift or bounce loss cone. Since the directionality is introduced to the measurement by assuming an isotropic incident flux (Yando et al., 2011), if the trapped population is observed for only a fraction of the look direction, and is larger than bounce or drift loss cone contributions, this assumption could result in an underestimation of the electron flux. Considering measurements when the T90 detector entirely viewed the trapped

electron population and measurements when no trapped electrons were observed showed that, the majority of the time, the two cases were within a factor of four of one another. This is likely because when no trapped electrons are observed, the measurement was dominated by the drift loss cone flux. Appendix A shows that T90 samples the drift loss cone for much of the outer radiation belt. Here we have ignored measurements where less than 20% of the field-of-view responded to trapped electron flux and used $f_{corrected} = f_{measured}/(0.75\tau + 0.25)$ to approximately correct for when only a fraction of the detector, τ, observed the trapped population.

The L^* values for the POES data used in this study have been calculated using IGRF and the T96 external field (Tsyganenko, 1995).

6.3 Convert to Omnidirectional Flux

The electron flux at a particular time and location in the magnetosphere typically depends on both energy and pitch angle (Gannon et al., 2007; Horne et al., 2003; Ni et al., 2015; Shi et al., 2016). We have assumed that the integral flux is conserved along the field line, so, the local $\sim 90^o$ flux measured by the POES satellites at low earth orbit are therefore equivalent to the flux of electrons at a smaller equatorial pitch angle given by conservation of the first adiabatic invariant. In effect, we have assumed that the POES integral flux measurement can be mapped up the field line to describe the electron flux at a small equatorial pitch angle. This assumption is an extension of Liouville's theorem, introduced in section 2.1. Equation 2.1 shows that if p^2 is constant then the differential flux does not vary along a bounce path. As the integral flux is the total of many differential flux values at different energies, we have extended the theorem to the integral flux here.

Following this, the omnidirectional flux can then be calculated from the POES measurement by considering an appropriate equatorial pitch angle distribution and integrating over all pitch angles. This is required particularly for the integral to differential flux conversion using the AE9 model flux-energy distributions, detailed in the following section, as the AE9 model returns omnidirectional flux (Ginet et al., 2013).

Previous work has sometimes assumed that the electron flux, j, at energy, E, has a pitch angle distribution of $j(E,\alpha) = j(E,90^o)\sin^{n(E)}\alpha$ (Gannon et al., 2007; Vampola, 1997). Typically, as electron flux distributions generally decrease with increasing energy (Cayton et al., 1989), integral flux measurements are dominated by electrons with energies just above the lower cut off. Assuming that at a particular location $n(E)$ changes relatively slowly with energy in comparison to the decrease in electron flux, then, for the electron energies that

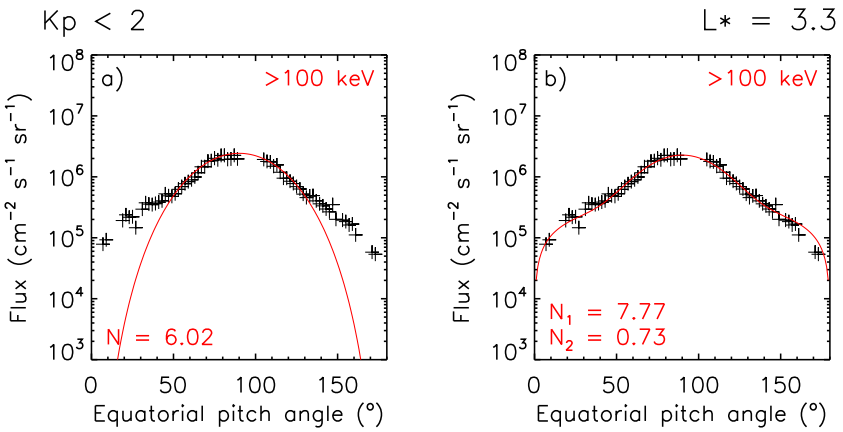

Figure 6.2 – A comparison of (a) fitting equation 6.1 (red line) to the MagEIS >100 keV pitch angle distribution at L^* = 3.3, Kp $<$ 2 (black plus symbols) and (b) instead fitting equation 6.4 (red line).

dominate the integral flux measurement, $n(E)$ is relatively constant. Hence, we have assumed that the integral electron flux greater than energy threshold E_T at equatorial pitch angle α can be approximated by

$$F(E > E_T, \alpha) = F(E > E_T, 90^o) \sin^{N(E_T)} \alpha. \tag{6.1}$$

where the energy dependent $n(E)$ parameter has been replaced with $N(E_T)$, a shape parameter for the integral flux that depends instead on the lower energy threshold, E_T. The variable $F(E > E_T, 90^o)$ is the integral flux of electrons with energies greater than E_T at an equatorial pitch angle of 90°. By integrating equation 6.1 over all solid angle, the omnidirectional integral electron flux can be obtained:

$$F(E > E_T) = 2\pi F(E > E_T, 90^o) \int_0^\pi \sin^{N(E_T)+1} \alpha \, d\alpha. \tag{6.2}$$

Evaluating the integral of equation 6.2 and substituting in equation 6.1 for $F(E > E_T, 90^o)$ we obtain an expression for the omnidirectional integral flux of electrons with energies greater than E_T, given the integral flux measurement at pitch angle α

$$F(E > E_T) = 2\pi \frac{F(E > E_T, \alpha)}{\sin^{N(E_T)} \alpha} \frac{\sqrt{\pi}\Gamma(1 + \frac{N(E_T)}{2})}{\Gamma(\frac{3+N(E_T)}{2})} \tag{6.3}$$

where Γ refers to the gamma function.

The MEPED instrument on board the POES satellites supplies >30, >100, and >300 keV electron flux measurements. To convert each of these three flux readings to omnidirectional flux using equation 6.3, the parameters N(>30 keV), N(>100 keV), and N(>300 keV) were required. Shi et al. (2016) had previously found the $n(E)$ values for the differential flux of electrons with energies varying from 100 keV to 1 MeV using MagEIS data. We instead require $N(E_T)$ values to describe the pitch angle distributions of the integral flux measured by the electron channels of the MEPED detector. The level 3 data from the MagEIS instruments on board the Van Allen Probes provide high resolution electron flux measurements over the energy range ∼30 keV - 4 MeV, in 11 pitch angle bins. For each pitch angle bin, we interpolated the MagEIS data to the lower energy threshold of each POES electron channel. The MagEIS electron flux measurements between the lower threshold energy and 2.5 MeV were then integrated to provide the >30, >100, and >300 keV electron flux for each pitch angle bin. The centroid of the pitch angle bins were mapped to the equator to give the equatorial pitch angle of the MagEIS integral flux.

Background corrected MagEIS data from 1 January 2013 till 31 May 2016 were used to calculate the >30, >100, and >300 keV flux for a range of equatorial pitch angles. The integral flux data was sorted into bins of width $0.2L^*$ with centroids between L^* = 1.5 to 5.7, by equatorial pitch angle with a resolution of 2°, and by three levels of activity defined by the Kp index (Kp $<$ 2, 2 $\leq$ Kp $<$ 4, and Kp $\geq$ 4). The parameter L^* for the MagEIS data was calculated using the International Geomagnetic Reference Field and the T89 external field (Tsyganenko, 1989). For each bin that contained more than 20 values, the mean was evaluated, giving the average equatorial pitch angle distribution of the electron flux for each activity and L^*. Equation 6.1 was then fitted to the data using a non-linear least squares fit.

At L^* values that generally relate to the outer edge of the inner belt, equation 6.1 did not always provide a good fit to the observations. Figure 6.2a shows how the average >100 keV flux (Kp $<$ 2 and L^* = 3.3 bin) changes with equatorial pitch angle (black plus symbols). Over plotted is the result of fitting equation 6.1 to the data (red line). It is clear that for pitch angles away from 90°, the fit may significantly underestimate the electron flux. For some activities and L^* values we instead assume the following form for the equatorial pitch angle distribution:

$$F(E > E_T, \alpha) = A_0 F(E > E_T, 90^o) \sin^{N_1(E_T)} \alpha + (1 - A_0) F(E > E_T, 90^o) \sin^{N_2(E_T)} \alpha \quad (6.4)$$

where A_0 is a parameter in the range $0 < A_0 \leq 1$ and we have two shape parameters, $N_1(E_T)$ and $N_2(E_T)$. Figure 6.2b shows the result of applying this new distribution to the average

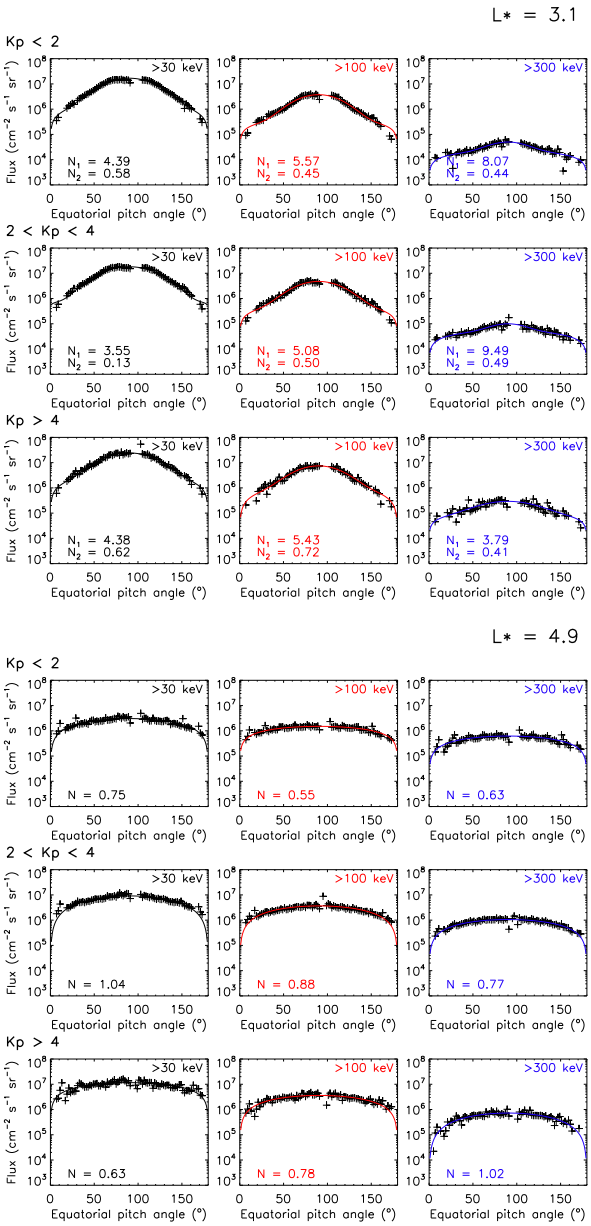

Figure 6.3 – Examples of fitting either equation 6.1 or 6.4 to the MagEIS data (black plus symbols) for $L^* = 3.1$ and $L^* = 4.9$.

$>$100 keV data. For $\alpha \leq 20^o$ and $\alpha \geq 160^o$ the fit is now closer to the observations, having reduced the difference by an order of magnitude or more.

The shape of the pitch angle distribution shown in Figure 6.2 is most likely due to the effect of hiss waves on the electrons. Lyons et al. (1972) showed that within the slot region, the pitch angle diffusion coefficient can show a minimum with respect to pitch angle as

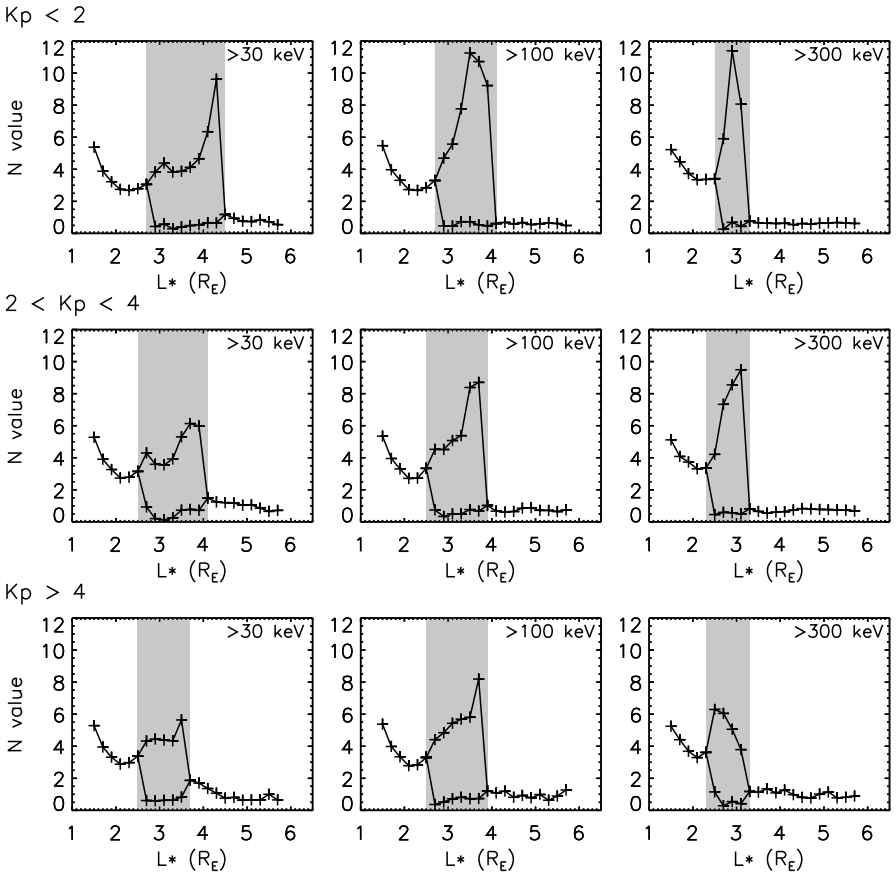

Figure 6.4 – N value parameters found from Van Allen Probes measurements across a range of L^* values for >30, >100, and >300 keV electrons at three levels of Kp. L^* values where Equation 6.4 was used in place of Equation 6.1 are shaded in grey.

regions of significant diffusion by cyclotron resonances and by the Landau resonance are separated in pitch angle. In the slot region, Meredith et al. (2009) also showed similar deep minima in the pitch angle diffusion coefficients calculated by the PADIE code (Pitch Angle and energy Diffusion of Ions and Electrons) (Glauert and Horne, 2005), using wave observations from two satellites. A significant reduction in the total diffusion rate for pitch angles between the effective range of the Landau and cyclotron resonances results in hiss waves primarily scattering electrons with pitch angles away from 90°. The population near 90° is scattered at a much slower rate, producing an equatorial pitch angle distribution that is mostly flat, with a sharp peak around 90°. Zhao et al. (2014a) has previously presented observations of the pitch angle distributions of 460 keV differential electron flux that showed a similar form to those seen in Figure 6.2. They referred to these pitch angle distributions as having a "cap" form.

Examples of the average equatorial pitch angle distributions derived from MagEIS data for two L^* bins, L^* = 3.1 and L^* = 4.9, are shown in figure 6.3. Depending on which best suited the observations, either equation 6.1 or 6.4 was fitted to the data (selected by eye). For all activity levels and energies in the L^* = 3.1 bin, equation 6.4 was fitted to the data. For L^* = 4.9, equation 6.1 was fitted to the data. The N shape parameters for each fit are given in the bottom left hand corner of each panel. When the single sine function was appropriate, these values can be used in equation 6.3 with the POES observations to give the omnidirectional flux. For pitch angle distributions where equation 6.4 was instead fitted to the MagEIS data, the omnidirectional flux is given by

$$F(E > E_0) = 2\pi F(E > E_0, 90^o) \left(A_0 \frac{\sqrt{\pi}\Gamma(\frac{N_1(E_0)}{2} + 1)}{\Gamma(\frac{3+N_1(E_0)}{2})} + (1 - A_0) \frac{\sqrt{\pi}\Gamma(\frac{N_2(E_0)}{2} + 1)}{\Gamma(\frac{3+N_2(E_0)}{2})} \right) \tag{6.5}$$

where all parameters are as previously defined and $F(E > E_0, 90^o)$ can be found from equation 6.4.

The N values obtained by fitting equation 6.1 to the average pitch angle distributions for >30, >100, >300 keV electrons are plotted against L^* in Figure 6.4. The grey regions highlight L^* values where the double $\sin^N \alpha$ distribution (equation 6.4) was used for the fitting in place of equation 6.1 and, for these L^* values, the two resulting N values are instead plotted. The $N(E_T)$ values decrease with L^* for $L^* \leq 2.5$, then follow a form best described using equation 6.4 out to $L^* \sim 4$, and finally flatten out at $N \sim 0.5$. The last L^* bin shown in Figure 6.4 is L^* = 5.7. Whilst MagEIS data was available at larger L^*, there were fewer flux measurements for these L^* values, particularly for Kp > 4. For this reason we did not use the MagEIS data to calculate the $N(E_T)$ values for $L^* > 5.7$. However, as the $N(E_T)$ values showed little variation with L^* beyond $L^* \sim 5$, one might expect the $N(E_T)$ parameters to also remain at a similar level for larger L^*.

By using either Equation 6.3 or 6.5 and the $N(E_T)$ values given in Figure 6.4 the POES integral flux measurements taken at low earth orbit, mapped to small equatorial pitch angles, were converted to omnidirectional flux.

6.4 Integral to Differential Flux Conversion

Previous work has made use of a variety of methods to infer the differential flux from integral measurements. Singular Value Decomposition (Höcker and Kartvelishvili, 1996) was used to calculate particle flux at a high energy resolution from the integral count

rates measured by the Standard Radiation Environment Monitor (SREM) (Sandberg et al., 2012). As part of a technique to remove proton contamination from the electron channels of MEPED, an inversion method was used to estimate the differential electron flux of the precipitating POES data (T0 detector) (Peck et al., 2015). The spectral shape used in the method presented by Peck et al. (2015) was calculated using a combination of exponential, power law, single relativistic Maxwellian, and a double relativistic Maxwellian. In addition, past work has also used integral flux to derive boundary conditions for radiation belt models. Geostationary Operational Environmental Satellites (GOES) integral electron flux data was used to formulate boundary conditions for the VERB-3D radiation belt model in order to study the September 2012 storm (Shprits et al., 2013). Here we present two novel methods to convert from integral electron flux to differential flux across a range of energies, with focus on 100 - 600 keV electrons.

6.4.1 Method One: Using Distributions from the AE9 Model

AE9 is a recently developed standard design model of radiation belt flux levels for the purposes of spacecraft engineering. The development and features of AE9 are detailed by Ginet et al. (2013). The AE9 model was formed using measurements made by particle detectors on-board 33 satellites in a variety of orbits, comprehensively cross-calibrated. AE9 uses the various datasets to compile the omnidirectional integral flux corresponding to a number of lower threshold energies (henceforth called integral flux distributions), as well as the omnidirectional differential flux *at* various energies (henceforth called differential flux distributions), for a chosen satellite orbit. These flux distributions are given for different percentiles, whereby the 40th percentile corresponds to the integral/differential flux-energy profile the measured flux would be expected to be below 40% of the time. The electron flux corresponding to various percentiles, ranging from the 2^{nd} to the 98^{th}, can be extracted from the AE9 model. As a result, AE9 provides a library of integral and differential flux distributions, where the changing levels of electron flux are captured by the different percentiles. Here we make use of this library to find a differential flux distribution which fits the integral flux observations made by POES.

Using version 1.3 of the AE9 model, we extracted the distribution of omnidirectional integral flux against lower threshold energy and the profile of omnidirectional differential flux against energy for percentiles ranging from the 2^{nd} to the 98^{th}, at each radii considered. Circular orbits at the equator were used, with radii ranging from 1.5 R_E to 8 R_E in steps of 0.25 R_E. An example of both the integral and differential flux distributions at a distance of 4

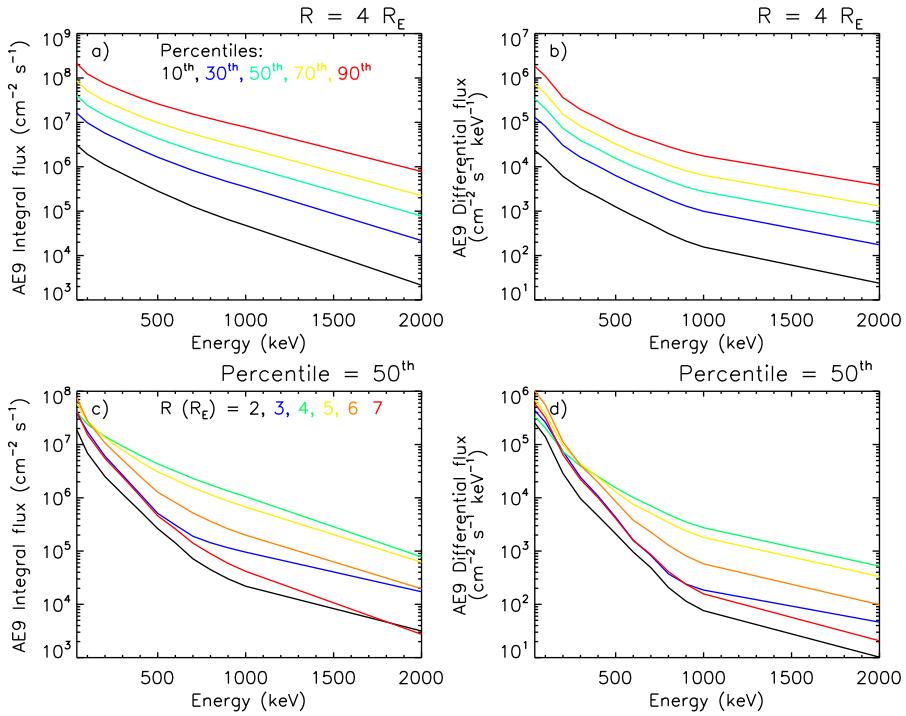

Figure 6.5 – Flux energy distributions from the AE9 model. The integral electron flux against the lower energy threshold (a) and differential flux against energy (b) are shown for a circular satellite orbit at the magnetic equator with a radius of 4 R_E. For panels (a) and (b) the black line shows the AE9 data equating to the 10th percentile, blue shows the 30th percentile, green shows the 50th, yellow the 70th, and red the 90th. The integral (c) and differential flux (d) relating to the 50th percentile are shown for circular orbits of various radii. In panels (c) and (d) the black line shows the AE9 data for an orbit radius of 2 R_E, blue for 3 R_E, green for 4 R_E, yellow for 5 R_E, orange for 6 R_E, and red for 7 R_E.

R_E are shown in Figure 6.5a and b respectively; various colours relate to different percentiles. Panels c and d show the AE9 model flux-energy profiles relating to the 50th percentile of the integral and differential flux for orbits of varying radii.

In the geomagnetic field, the L^* parameter does not directly relate to a radial distance at the magnetic equator. However, we assume that the flux-energy profile for a particular L^* value may be largely described by one of the distributions averaged over a circular orbit with a radius R in the range $(L^*\text{-}1) \leq R\ (R_E) \leq (L^*\text{+}1)$. For each POES electron flux measurement, we found AE9 average flux profiles relating to 9 distances in the $(L^*\text{-}1) \leq R\ (R_E) \leq (L^*\text{+}1)$ range, at intervals of 0.25 R_E. For each of the resulting 9 circular orbits, a flux-energy distribution was given for each integer percentile value spanning from the 2nd to the 98th. The omnidirectional >100 keV POES flux value was then compared to the >100 keV AE9 flux values to find the percentile at each of the nine distances closest to the >100 keV observation.

The percentiles with values for the >100 keV flux that lay immediately either side of the POES observation were interpolated to give an integral flux-energy distribution that passed through the omnidirectional value of the >100 keV POES flux. The same scaling was also applied to the equivalent differential flux distributions.

After comparing the >100 keV flux to the various AE9 flux-energy profiles, we are left with 9 integral flux-energy distributions, each passing through the POES value of the omnidirectional >100 keV flux, and 9 corresponding differential flux distributions. Each integral and differential flux-energy distribution pair relates to one of the distances in the specified range. By comparing the >300 keV omnidirectional flux obtained from the POES satellite measurement to the >300 keV flux from the remaining integral flux profiles, we identified the AE9 distribution closest to observations. This integral flux distribution was extracted, as was the corresponding differential flux profile. For integral flux values with a lower threshold energy greater than 300 keV, a scaling factor was applied to the final integral flux distribution so that the >300 keV flux passed through the observed value. The same scaling factor was applied to the extracted differential flux distribution for energies greater than 300 keV.

The final differential flux profile was assumed to describe the flux-energy distribution at the POES measurement time. Repeating the above process for all times where the POES satellite observed trapped flux returned an estimate of the omnidirectional differential flux for the period. The energy values for the differential electron flux equate to the energies requested from AE9 model, which can be as low as 40 keV.

6.4.2 Method Two: Using an Iterative Fit

Using the integral flux values, we applied a iterative approach, based on a 'Reverse Monte Carlo' (RMC) method (McGreevy and Pusztai, 1988), to recreate the differential flux distribution. The iterative method employs a simple basic process. An initial flux-energy distribution was set and χ^2 calculated:

$$\chi^2 = \sum_{n=1}^{3} \frac{(\log_{10}(f_{calc}(E > E_n)) - \log_{10}(f_{obs}(E > E_n)))^2}{\sigma_{err}^2} \tag{6.6}$$

where $f_{calc}(E > E_n)$ defines the integral flux values calculated from the initial flux-energy distribution for >30, >100, and >300 keV electrons and $f_{obs}(E > E_n)$ are the corresponding POES observations. As the flux at different energies may vary by several orders of magnitude, we perform the iterative calculation in log space. The parameter σ_{err} is the error margin

on the logarithm of the observed integral flux measurements. One of the flux values in the flux-energy distribution was then randomly selected and the logarithm of the flux moved up or down by a random value of up to 0.1. Following the move, χ^2 was recalculated, and if the value was smaller than the previous χ^2, the move was accepted. If the new χ^2 was larger than the previous value then the move was accepted with a probability randomly selected from the normal distribution. The process was repeated iteratively until the modulus of the total change in χ^2 in 2000 iterations was less than 0.02. The outcome is a differential flux-energy distribution which, when integrated, should reproduce the POES measurements to within the error margin.

Several distribution shapes may return the observed integral flux values. Ideally, we require additional measurements to direct the result towards the actual distribution. In the absence of extra measurements, we applied the constraint that the flux must fall with increasing energy. This assumption was also made in section 6.3 and is generally reasonable as electron flux distributions typically decrease with energy (Cayton et al., 1989). The energy spacing between flux values should be constant so that during the random selection stage, the flux at each energy has an equal probability of being selected. To avoid having too many flux values, which would act to slow the iterative progression down, whilst still retaining a fine energy resolution at the seed population energies of interest, we assumed that above 1.2 MeV, the electron flux contributed little to the integral flux measurements and could be negated without considerable impact to the result. Following this, we then considered the integral flux values to have an upper energy threshold of 1.2 MeV instead of the 2.5 MeV of the POES electron channels (Evans and Greer, 2004).

Initially, 118 flux values were set for energies ranging from 30 keV to 1.2 MeV, obeying the following form for 30 keV $\leq$ E $<$ 600 keV:

$$\log_{10}(f(E)) = A - \frac{(A-B)(E-30)}{(600-30)} \tag{6.7a}$$

for 600 keV $\leq$ E $<$ 1.2 MeV:

$$\log_{10}(f(E)) = B - \frac{(B-C)(E-600)}{(1200-600)} \tag{6.7b}$$

where $f(E)$ is the omnidirectional electron differential flux, E the electron energy in keV, $A = \log_{10}(f(30\text{ keV}))$, $B = \log_{10}(f(600\text{ keV}))$, and $C = \log_{10}(f(1.2\text{ MeV}))$. The electron flux at 30 keV was estimated using the POES $>$30 and $>$100 keV measurements, assuming a constant flux between 30 keV and 100 keV. Likewise, the electron flux at 600 keV was

estimated using the POES >300 keV measurement by assuming a constant flux from 300 keV to 1.2 MeV. As the electron flux at 1.2 MeV is likely significantly lower than the flux at 600 keV, we subtract 1.5 from the logarithm of the estimated 600 keV flux as a first estimate for C. The distribution resulting from equations 6.7a and 6.7b was then used as the initial flux-energy profile in the iterative Reverse Monte Carlo style method.

For the χ^2 calculation given by equation 6.6 we required a value for σ_{err}, the error value on the logarithm of the omnidirectional POES flux measurement. Sources of error include uncertainties in the instrument correction factors, Poisson noise in the count data, as well as errors incurred from the bow-tie correction (Lam et al., 2010). Further errors are also introduced when converting to omnidirectional flux: by the pitch angle distributions assumed and the parametrization by Kp. Considering the above, we adopted a 40% error in the POES measurement values, which yields a σ_{err} of approximately 0.2. It should be noted that assuming a larger measurement error of 50% (where $\sigma_{err} \sim 0.24$) did not notably impact the resulting spectra.

The described iterative method was applied to POES omnidirectional integral electron flux data for each measurement time. The result was an estimate of the omnidirectional differential flux, at energies between 30 keV and 1.2 MeV in 10 keV increments.

6.5 Conversion to 90^o Electron Flux

Following the application of one of the methods described in Sections 6.4.1 or 6.4.2, the POES electron flux data has been used to estimate the omnidirectional electron flux at a number of energy values. As a final step, the omnidirectional electron flux was converted back to directional flux by assuming a pitch angle distribution at each energy, E, that obeys either a

$$j(E,\alpha) = j(E,90^o)\sin^{n(E)}\alpha \tag{6.8}$$

or

$$j(E,\alpha) = A_0 j(E,90^o)\sin^{n_1(E)}\alpha + (1-A_0)j(E,90^o)\sin^{n_2(E)}\alpha \tag{6.9}$$

distribution in pitch angle. The shape parameter, $n(E)$, for the pitch angle distribution of differential flux (as opposed to $N(E_T)$ for integral flux) is dependent on both the electron energy and the L^* of the measurement.

Shi et al. (2016) had previously evaluated the $n(E)$ shape parameters for differential electron flux using the level 3 MagEIS data and assuming the distribution given by equation 6.8. Here, we have binned the electron flux data by L^* instead of the L used by Shi et al.

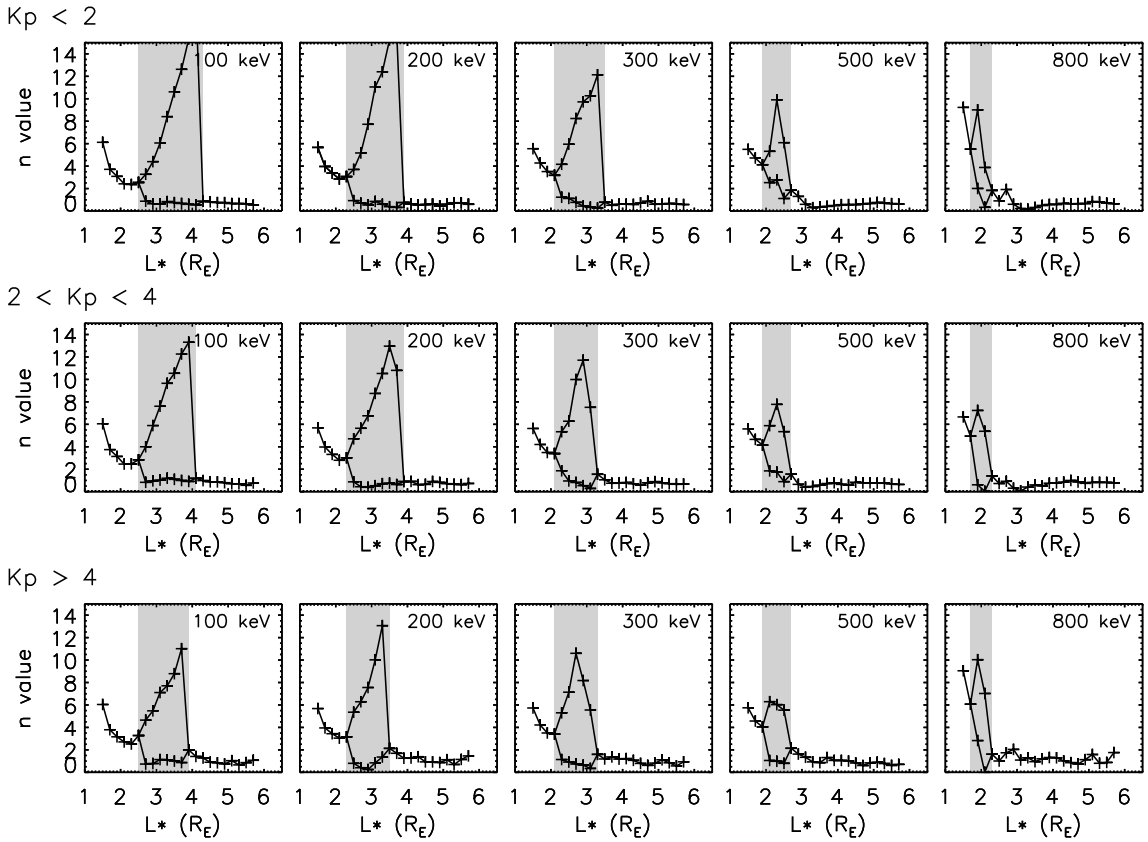

Figure 6.6 – The $n(E)$ value shape parameters found from MagEIS differential flux measurements across a range of L^* values for 100, 200, 300, 500, and 800 keV electrons at three levels of Kp. L^* values where a double sine function was fitted instead of a single sine function are shaped in grey.

(2016), making the conversion to directional flux consistent with the rest of the study. Additionally, when considering integral flux, we identified that a single sine distribution was not always an appropriate fit to the data (Figure 6.2). This was mirrored by the differential flux equatorial pitch angle distributions, again for L^* values relating to the outer edge of the inner belt. Zhao et al. (2014a) also found differential flux pitch distributions with a sharp peak near 90°, referred to as 'cap' pitch angle distributions in their study. In this work we build on the study by Shi et al. (2016) by forming L^* dependent $n(E)$ values and fitting equation 6.9, a double sine function, when the single sine form did not offer a good fit to the data.

Background corrected level 3 MagEIS data was interpolated to 100, 200, 300, 500, and 800 keV, then, as in section 6.3, binned by Kp, L^*, and equatorial pitch angle. The binned data was averaged to form statistical equatorial pitch angle distributions for the differential

flux at the listed five energies, for L^* bins with centroids ranging from L^* = 1.5 to 5.7 in steps of $0.2L^*$, and at three levels of the activity index Kp. A single or double sine distribution was then fitted to the average distributions to determine appropriate $n(E)$ parameters for each L^* bin, energy, and activity level.

By integrating equation 6.8 over all solid angle we obtain an expression similar to Equation 6.3, and rearranging for the 90° electron flux gives

$$j(E,90^o) = \frac{j(E)}{2\pi} \frac{\Gamma(\frac{3+n(E)}{2})}{\sqrt{\pi}\Gamma(1+\frac{n(E)}{2})} \tag{6.10}$$

where, as in Equation 6.3, Γ denotes the gamma function. Likewise, integrating equation 6.9 gives the following expression for the differential flux of 90° electrons:

$$j(E,90^o) = \frac{j(E)}{2\pi} \left[A_0 \frac{\sqrt{\pi}\Gamma(1+\frac{n_1(E)}{2})}{\Gamma(\frac{3+n_1(E)}{2})} + (1-A_0) \frac{\sqrt{\pi}\Gamma(1+\frac{n_2(E)}{2})}{\Gamma(\frac{3+n_2(E)}{2})} \right]^{-1} \tag{6.11}$$

The $n(E)$ values found from fitting either equation 6.8 or 6.9 to the average pitch angle distribution for differential flux are shown in Figure 6.6. The grey regions show where equation 6.9 has been fitted. For 100 and 200 keV electrons in particular, the n_1 values obtained from fitting equation 6.9 to the pitch angle distribution rose continually with increasing L^*. The rise in n_1 was paired with a reduction in the A_0 parameter with increasing L^*. This implies that as the peak around 90° narrowed with increasing L^* the height reduced. Eventually, the peak around 90° became indistinguishable from the rest of the pitch angle distribution, and a single sine form was again appropriate. The $n(E)$ values shown in Figure 6.6 were used in accordance with equation 6.10 or 6.11 to determine the electron-flux energy distribution at an equatorial pitch angle of 90°. Note that, with a slight alteration, equations 6.10 and 6.11 may also be used to convert the omnidirectional flux to equatorial pitch angles other than 90°, although for simplicity, only the results achieved for equatorial pitch angles of 90° are compared to Van Allen Probes data in the following validation section.

6.6 Validation

To test the methods presented in the previous sections, we compared the differential 90° flux obtained from POES data to background corrected electron flux measurements from the MagEIS instruments on board Van Allen Probe A. The Van Allen Probes operate near the magnetic equatorial plane, providing observations of the radiation belts. Figure 6.7 shows

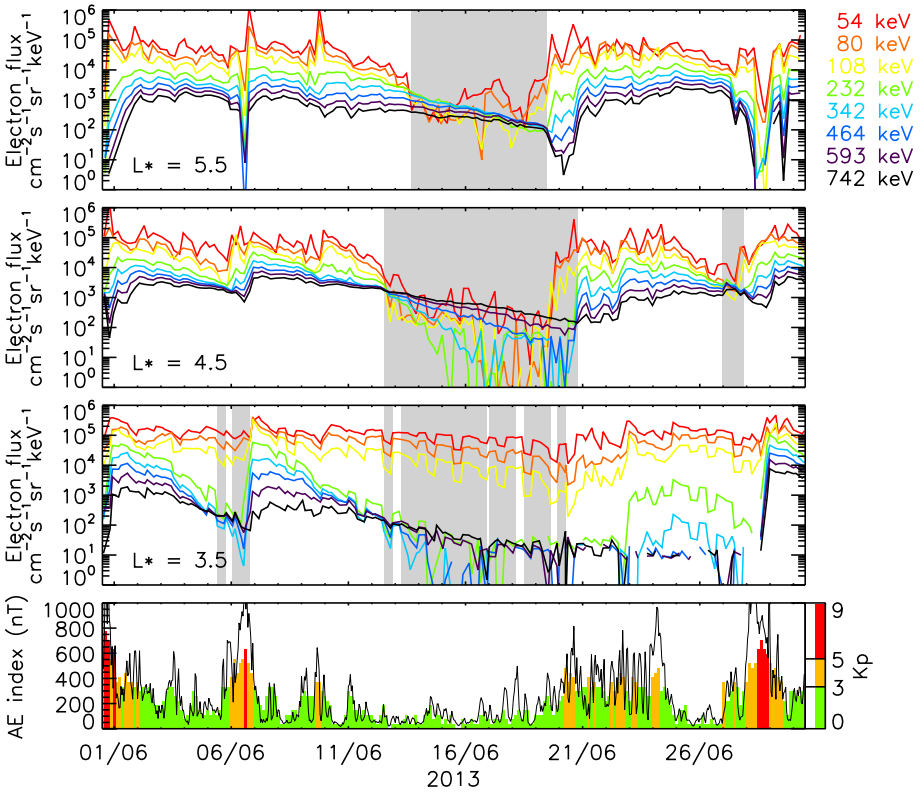

Figure 6.7 – Electron flux measured by the Van Allen Probes during June 2013 for L^* = 5.5, 4.5, and 3.5. The Kp and AE index for the period is also shown. Greyed sections indicate where the flux of higher energy electrons has exceeded that of lower energy electrons.

the measured 90° pitch angle electron flux for the month of June in 2013 from eight MagEIS energy channels, ranging between 54 and 742 keV. Data from Probe A were sorted into three L^* bins centred on L^* = 5.5, 4.5, and 3.5, each of width L^* = 0.1. For reference, both the AE and Kp index are also shown in the bottom panel of Figure 6.7. It is worth noting that although the Van Allen Probes operate near the magnetic equator, the 90° local pitch angle channel may not always relate to a 90° equatorial pitch angle. However, for the purpose of the following comparison, equivalence is assumed as differences are likely to be minor.

For several periods during June 2013, the electron flux at higher energies exceeded that at lower energies and the flux-energy distribution displayed a region of positive gradient. If the measured flux from two consecutive MagEIS energy channels showed an increase with energy then Figure 6.7 was shaded in grey. Reeves et al. (2016) first observed a minimum in flux as a function of energy, seen during March 2013, at the inner edge of the outer radiation belt. At this location, electron flux distributions showed a minimum at energies of a few hundred keV during quiet time conditions. Occurrences of the so-called ‘S-shaped’ energy

structure of the outer radiation belt have since been attributed to the combination of radial transport and wave-particle interactions with plasmaspheric hiss (Ripoll et al., 2016, 2017). Figure 6.7 shows that the 593 and 742 keV electron flux exceed the flux of lower energy electrons at all three L^* values shown, but most commonly at $L^* = 4.5$. In agreement with the findings of Reeves et al. (2016), this typically occurred during quiet periods.

Flux-energy distributions that do not fall with increasing energy violate the assumptions made in Sections 6.3 and 6.4.2. Additionally, electron flux distributions that display a minimum around several hundred keV are not returned by the AE9 model and so can not be obtained from the method presented in Section 6.4.1. As a result, during periods when the 'S-shaped' energy structure of the outer radiation belt arises, we would not expect either method presented in this chapter to produce realistic 90^o differential electron flux. We therefore have omitted these periods from the validation. The issue of the outer radiation belt 'S-shaped' energy structure is discussed further in the following section.

To compare the output of either method 1 or method 2 to the electron flux level observed by Van Allen Probe A, we have produced the scatter plots shown in Figure 6.8. Six months of data from 2013, ranging from 1 April to 30 September, covering the entire summer season has been used for the validation. During the six month period, four POES satellites and one MetOp satellite were operational: NOAA15, NOAA16, NOAA18, NOAA19, and METOP02. The integral electron flux data from each of these satellites was converted into differential flux, then sorted into six L^* bins centred on $L^* = 5.5$, 5.0, 4.5, 4.0, 3.5, and 3.0, each of width $L^* = 0.1$. Van Allen Probe A data shown in Figure 6.7 was sorted by L^* in the same manner. For each L^* value, the resulting differential flux from the five POES satellites were interleaved, providing the electron flux along an L^* cut at a much higher time resolution than can be obtained from the Van Allen Probes. As the intention is to ultimately compare the converted flux value to that observed by the MagEIS instrument, two hour averages were produced from the POES flux data and these averages interpolated to the Van Allen Probe data times. The MagEIS energy channels were interpolated to regular energies ranging from 100 to 600 keV in spacings of 100 keV. We then plotted the 90^o electron flux derived from the POES data against the MagEIS flux at the same L^*, energy, and time, as shown in Figure 6.8a and c, with points color coded by electron energy. Figure 6.8a compares the flux resulting from method 1 to MagEIS data while Figure 6.8b compares the flux from method 2.

A perfect recreation of the Van Allen Probes data would produce a straight line with a gradient of 1. Figure 6.8a and b show a clear positive correlation and a spread that is primarily confined within an order of magnitude of the Van Allen Probes observation. However, there

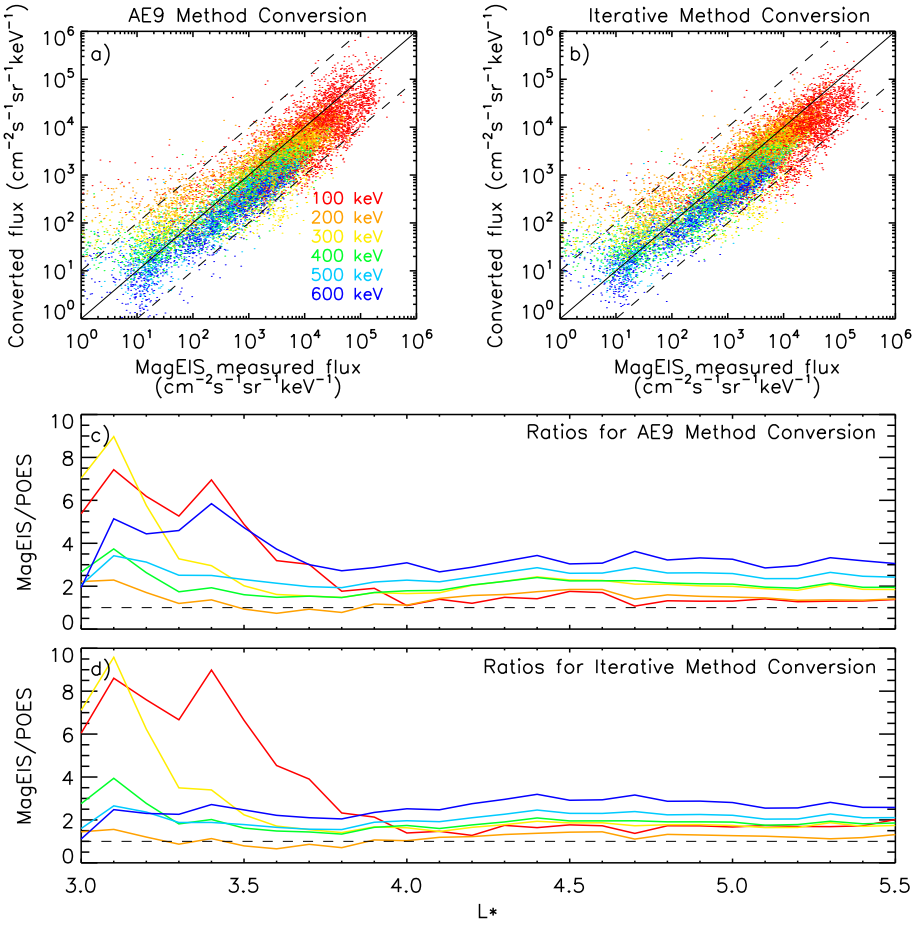

Figure 6.8 – Comparing both conversion methods to Van Allen Probes data. (Panel a) Scatter plot between the electron flux at various energies derived from the POES data using method 1 and that observed by the Van Allen Probes MagEIS instruments. (Panel b) Same as panel a but for POES flux values obtained using method 2. (Panel c) ratio of MagEIS flux to POES flux values from method 1 for a range of L^* values. (Panel d) Same as panel c but for method 2.

is a tendency for the differential 90° flux obtained from POES data, via either method, to be lower than the observed value, particularly for 500 and 600 keV electrons.

To further aid analysis, the average ratios between the Van Allen Probe A MagEIS observations and the 90° electron flux retrieved from POES measurements were calculated for L^* values ranging from 3.0 to 5.5. Figure 6.8c shows these ratios for the 90° electron flux formed by applying method 1 to the POES data. Different colored lines relate to the energies listed in panel a and a dashed line marks the ratio value of 1. For $L^* \gtrsim 3.7$, the average ratios resulting from method 1 were less than a factor of 4 for all energies in the 100 - 600 keV range. Additionally, the average ratios remained relatively constant with L^* for each electron

energy and typically increased with energy. For $L^* \lesssim 3.7$, larger differences between the MagEIS measurements and the POES method 1 converted flux were observed. The ratios displayed more variability with changing L^* and, in particular, the difference between the 100 keV MagEIS flux and the 100 keV converted POES flux increased notably. In this L^* range, the average ratio values no longer rose with increasing energy.

Figure 6.8d shows that, generally, differences between the output of method 1 and method 2 were minor. Again for $L^* \gtrsim 3.7$, the average ratios for the considered energies were less than a factor of 4 and remained fairly consistent with L^*. However, a notable variation between method 1 and 2 is that for $L^* \lesssim 3.7$ the average ratio values for the 600 keV flux from method 2 (blue line panel d) are lower than seen for method 1 (blue line panel c), suggesting the larger ratios for the 600 keV flux from method 1 in this L^* range originate from the form of the differential flux spectra assumed using the AE9 distributions. Conversely, the increased ratios for the 100 and 300 keV flux for $L^* \lesssim 3.7$ are seen in the results of method 2 as well as method 1, indicative that the differences between the POES and MagEIS observations here are unlikely to be a result of the integral to differential flux conversion and may stem from a greater variability in the pitch angle distributions for these energies than has been captured by the three levels of Kp, used in section 6.5.

In general, Figure 6.8 illustrates an agreement between the POES converted flux and Van Allen Probes observations that is typically within a factor of four for most energy and L^* values.

6.7 Using the POES Data to Form a Low Energy Boundary Condition

Previous work has shown the importance of a realistic seed population in accurately recreating radiation belt dynamics (Tu et al., 2014). However, in the absence of Van Allen Probes data, the level of the seed population throughout the radiation belt region is generally difficult to ascertain. Here we use the POES data to study the seed population for June 2013 and compare the time sequence of the flux to Van Allen Probe A observations.

Present 3-D radiation belt models generally either set the minimum energy to a constant value throughout the calculation region (e.g. Tu et al., 2013; Wang et al., 2017) or the minimum energy is defined by a line of constant first adiabatic invariant, μ (e.g. Albert et al., 2009; Glauert et al., 2014b). Here we formulate the 90^o electron flux at energies following a line of first adiabatic invariant to explore using the presented methods to generate low energy

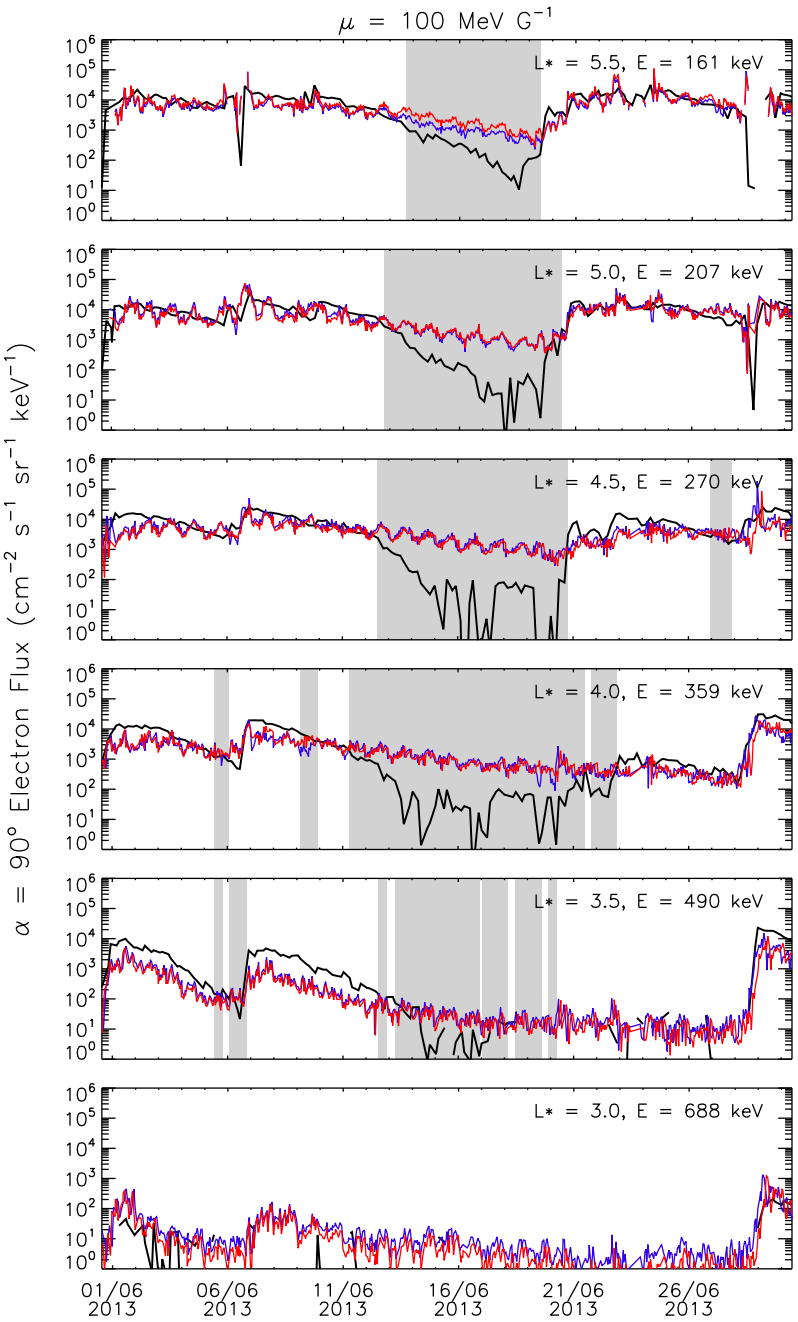

Figure 6.9 – Comparison of the Van Allen Probes MagEIS electron flux (black line) at six values of L^*, for energies following a line of constant μ = 100 MeV/G and the electron flux outputted by method 1 (red line) and method 2 (blue line). As in figure 6.7, greyed regions show periods when the assumption that electron flux falls with increasing energy is violated.

boundaries for models like the BAS Radiation Belt Model (Glauert et al., 2014b). Figure 6.9 shows both the Van Allen Probe A data (black line) and the output from applying method 1

(red line) and method 2 (blue line) to the POES data, at various L^* values covering the outer radiation region. The flux is given for electron energies defined by following a line of μ = 100 MeV/G, calculated assuming a dipole field for simplicity. The value of μ corresponds to an energy of $\sim$161 keV at L^* = 5.5 and is therefore a relatively reasonable value for the low energy boundary of a 3D Radiation Belt Model for June 2013 (Allison et al., 2017). One hour averages of the converted POES flux are shown. As with Figure 6.7, periods when more than two energy channels of MagEIS showed that the electron flux did not fall with increasing energy are shaded in grey. It is clear that during these greyed periods, when our underlying assumptions do not hold, the electron flux obtained from applying either method to the POES data typically overestimates the electron flux. However, for times outside of these grey regions, the converted flux displays a similar shape to the Van Allen Probe data and is mostly within a factor of $\sim$5 of the observations.

In general, throughout the outer radiation belt, we were able to use the POES low Earth orbit integral electron flux measurements to obtain a time sequence for the 90^o pitch angle flux at selected seed population energies, that mostly resembled the observations by the MagEIS instruments when the assumption made in both section 6.3 and 6.4.2 held. For smaller L^* values, differences between the MagEIS recorded value and the converted POES flux are more apparent, however, general trends in the MagEIS flux variation in time were mostly followed. Flux increases likely associated with the rise in activity on the 1, 7, and 29 of June are captured in the converted POES flux. Likewise, the sharp decreases in the flux seen at L^* = 5.5 and 5.0 on the 28 June 2013 are also reproduced. In agreement with the results shown in figure 6.8, figure 6.9 shows that the two methods return similar results. Thus, it is suggested that using either method described in this chapter would provide a realistic low energy boundary condition.

6.8 Using the Low Energy Boundary Condition from POES data in the BAS Radiation Belt Model

The low energy boundary condition formulated from POES data for June 2013, shown in section 6.7, has been used in the BAS Radiation Belt Model (Glauert et al., 2014b). To avoid starting the simulation during the high Kp period at the beginning of June 2013 (so electron enhancements are calculated by the model rather than being supplied by the initial condition), we run the BAS Radiation Belt model starting on the 3 June 2013. The diffusion coefficients used by Glauert et al. (2018) in the BAS Radiation Belt Model have also been

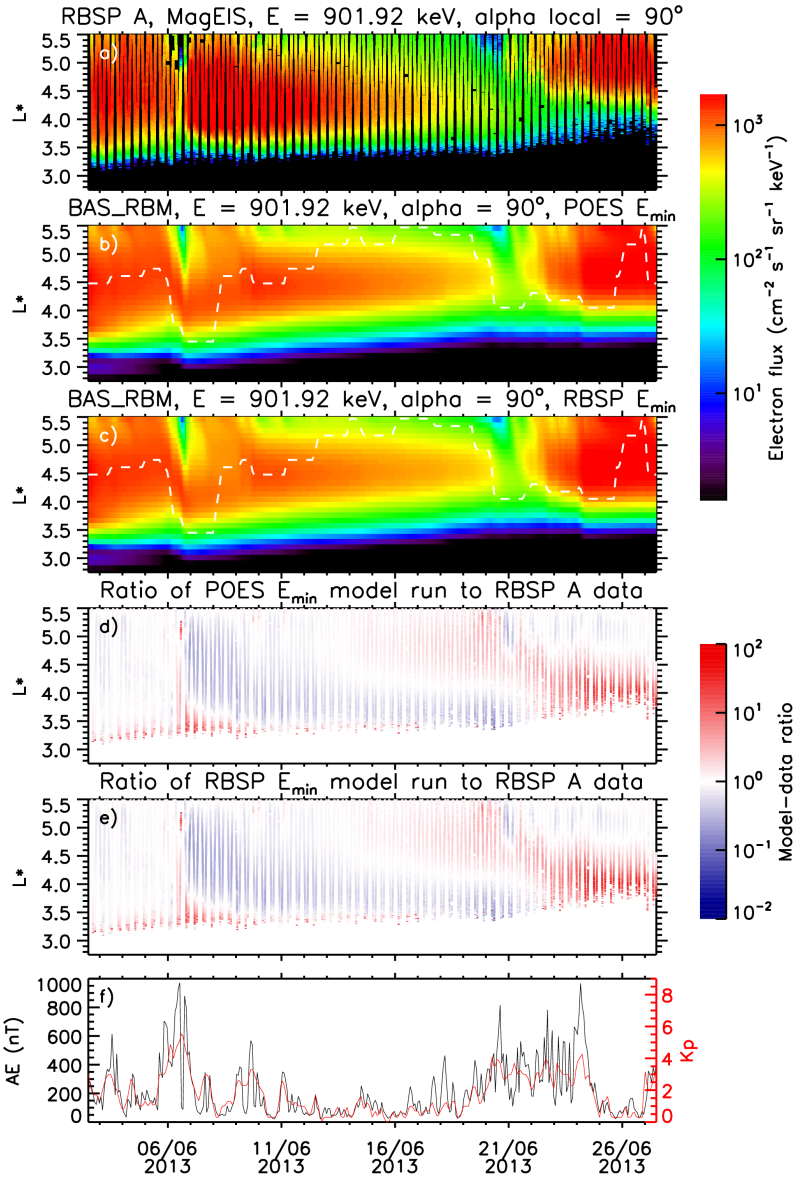

Figure 6.10 – Panel a): Van Allen Probe A MagEIS flux of 0.9 MeV electrons at a local pitch angle of 90°. Panel b): 0.9 MeV electron flux from BAS Radiation Belt Model using a low energy boundary condition supplied by POES data. Dashed white line marks the plasmapause location given by Carpenter and Anderson (1992). Panel c): same as panel b but using Van Allen Probe A data to supply the low energy boundary condition. Panel d): ratio of the 0.9 MeV model flux obtained using the POES low energy boundary condition to the MagEIS measured values. Panel e): same as panel d but for the model run using the Van Allen Probes low energy boundary condition. Panel f): the Kp and AE indices for the period.

used here. Radial diffusion coefficients are given by the electromagnetic component of the Kp dependent model from Brautigam and Albert (2000). Pitch angle and energy diffusion

coefficients have been calculated by the PADIE code (Glauert and Horne, 2005) and include contributions from whistler mode chorus waves (Horne et al., 2013), electromagnetic ion cyclotron (EMIC) waves (Kersten et al., 2014), plasmaspheric hiss and lightning generated whistlers (Glauert et al., 2014b). Losses due to magnetopause shadowing are included as described by Glauert et al. (2014a).

As discussed in chapter 2, the 3-D BAS Radiation Belt Model requires boundary conditions on six surfaces, corresponding to the maximum and minimum of each of the three coordinates: α, energy, and L^*. At the minimum and maximum α boundaries ($\alpha = 0^o$ and $\alpha = 90^o$) the change in the phase-averaged phase space density with respect to α is set to zero (i.e. $\frac{\partial f}{\partial \alpha} = 0$). At the maximum energy boundary, a phase space density of zero is used ($f = 0$). Van Allen Probes data from MagEIS and REPT have been used to formulate the initial condition and the minimum and maximum L^* boundaries. Further details on how these datasets were cleaned and used to construct the boundary conditions are given in chapter 7. The low energy boundary condition has been supplied by POES data following the techniques presented in this study. As performing the conversion from integral flux to differential flux by either method 1 and 2 returns largely similar results in Figure 6.9, we have used method 1 to generate the low energy boundary condition for the BAS Radiation Belt Model.

Figure 6.10b shows the model results for perpendicular 0.9 MeV electrons obtained using the POES low energy boundary condition. The $\sim$0.9 MeV flux measured by MagEIS is shown in panel a. Both the data and the model output exhibit a small drop-out on the 6 - 7 June 2013, during which both the AE and Kp indices increase. Van Allen Probe A then observed an enhanced electron flux which gradually decays over an extended period where Kp remains less than 2. As shown by Figure 6.7, this quiet period largely encompasses times where 'S-shaped' energy structure of the outer radiation belt was observed. The model (Figure 6.10b) also produces a flux enhancement following the drop-out, however, as evidenced by the ratio between the model output and observations in panel d, this flux increase is lower than observed and, for $L^* > 4$, exhibits a slower decay.

A second drop-out was observed on the 20 June where the AE and Kp indices both increased and remained high for several days. Again, a flux enhancement in both the model output and Van Allen Probe A data was observed following the drop-out. In the model output (panel b) this second enhancement extends down to $L^* = 4$, while the observations suggest the flux increase to have been mostly at $L^* > 4.5$. From the 22 June, for $L^* > 4.5$, the the model-data ratio in panel d suggests a very good agreement between the model and Van Allen probe measurements. Conversely, at lower L^*, the disparity in the inward extent of the enhancement produces the model's largest departure from the data.

As a comparison, the results from the BAS Radiation Belt Model, using a low energy boundary condition formulated from Van Allen Probe A MagEIS data, are shown in Figure 6.10c. The method used to form the Van Allen Probe low energy boundary is described in detail in the next chapter. Encouragingly, the model output using the POES low energy boundary condition (panel b) and the results from using the Van Allen Probes low energy boundary condition (panel c) are largely similar. This was expected as Figure 6.9 showed the two low energy boundary conditions to be fairly alike, generally showing the same features. The largest variations between the two low energy boundary conditions in Figure 6.9 mostly occurred during the shaded periods, marking times when 'S-shaped' energy structure of the outer radiation belt was observed. Comparing Figure 6.10b and c suggests that the overestimations of the seed population in the POES low energy boundary condition, during quiet times, as a result of the 'S-shaped' energy structure, has not had an adverse effect on the model output.

Although mostly similar, there are slight differences between the two model outputs. Following the initial enhancement starting on the 7 June, the model run using the POES low energy boundary condition produced a slightly higher 0.9 MeV electron flux than the model run using the Van Allen Probes low energy boundary condition. Additionally, the second enhancement starting around the 22 of June does not extend quite as low in L^* for the model run shown in panel b as that in panel c. These variations may be a result of the MLT coverage and rapid L^* sampling offered by the POES satellites.

The general agreement between Figure 6.10b and c suggests that the POES low energy boundary condition would provide a good event specific low energy boundary condition for periods outside of the Van Allen Probes mission. Furthermore, another use of the methods presented in this chapter would be to provide an alternative event specific low energy boundary conditions for events during the Van Allen Probes mission. Comparing the model output obtained from using the POES low energy boundary condition to the model output from using the Van Allen Probes low energy boundary condition for the same event would enable the relative importance of changes in the seed population on higher energy enhancements to be examined. The low energy boundary condition formulated from POES satellite data may include localised and short lived enhancements, unseen by the Van Allen Probes. As such, this could potentially lead to better understanding of how the dynamics of the seed population affect flux enhancements.

6.9 Discussion

Two methods were developed for retrieving the differential electron flux from the POES integral flux measurements. The first method, presented in section 6.4.1 requires less computation time than the iterative technique discussed in section 6.4.2. As Figure 6.9 shows that the two methods yield similar results, it is therefore recommended that method 1 is generally used. It is however encouraging that the results of the two entirely different methods for converting from integral to differential flux resulted in similar outputs.

In figure 6.7, several periods were identified in the MagEIS data where the electron flux increased with energy. As the MEPED detectors on board the POES satellites measure integral electron flux, solely using POES data, we were unable to determine occasions when this occurred. A deepening minimum around 300 keV tends to produce a peak at $\sim$800 keV. This peak is included in the integral measurement, but, as we assume that the electron flux falls with increasing energy, we attribute its contribution to an increased flux at the lower energy values. As a result, when the flux distribution showed this form, the methods presented typically return flux values for energetic electrons that are higher than observed, as shown by Figure 6.9. The minimum is thought to be be formed by the combination of losses due to hiss waves and gradual radial diffusion (Ripoll et al., 2017) and primarily occur during quiet times. For more active periods, when wave acceleration processes are affective (Meredith et al., 2012), we tend to see energetic electron injections and flux-energy distributions that do fall with increasing energy. As a result, when the seed population is likely to be an important component to accurately reproduce the $\sim$1 MeV electron flux in radiation belt models, the methods presented in this chapter for forming a low energy boundary condition are unlikely to be affected by S-shaped distributions. Overestimating the seed population during quiet times may cause the model flux at energies very close to the low energy boundary to be overestimated. However, in the absence of a significant acceleration mechanism, this is unlikely to extend to energies far from the boundary, as evidenced by the 0.9 MeV flux from the BAS Radiation Belt Model using the POES low energy boundary condition, shown in Figure 6.10b. During the quiet period from the 12 - 20 of June 2013, when 's-shaped' energy structure was observed over a range of L^* and the seed population overestimated by the POES low energy boundary condition, the model result obtained (Figure 6.10b) is largely similar to the model output where the low energy boundary condition was supplied by MagEIS observations (Figure 6.10c).

What is perhaps surprising is how regularly the electron flux rises with increasing energy as well as the L^* range over which this was observed (exhibits the 'S-shaped' energy structure).

During June 2013 the MagEIS data showed that the assumption was violated for L^* = 3.5 to 5.5. The integral flux observed by the POES satellites did not always decrease sharply when the Van Allen Probes MagEIS instrument recorded a sharp drop in the electron flux at energies close to the lower energy threshold of the integral channel. As the integral flux is the measurement over a broad energy range, this agrees with the observations of Reeves et al. (2016) and Ripoll et al. (2016), which suggest that during such periods the flux level at higher energies is maintained, forming minima in the flux-energy distributions.

Figure 6.9 shows that during the first half of June 2013, at L^* = 3.5, the 490 keV MagEIS flux rapidly increased twice (on the 1 and 7 of June). The converted POES flux from both methods 1 and 2 rose for these instances but did not show enhancements to the same extent as the observations. Figures 6.4 and 6.6 suggest that for $L^* > 4.5$, the shape parameter of the average pitch angle distribution does not vary notably with activity for any of the electron energies considered. Conversely, for L^* values in the 2 - 4.5 range, the $n(E)$ and $N(E)$ values showed a larger variation with Kp. If the pitch angle distributions for the integral flux during both enhancements in early June were better described by higher $N(E)$ than that of the average distribution for the activity level, the omnidirectional flux used in the conversion would also be higher and may account for the differences observed between the MagEIS flux and the converted values. Likewise if larger $n(E)$ better described the pitch angle distribution for the 490 keV electrons, the 90^o pitch angle flux would be underestimated. The pitch angle distributions can take forms which are not described by any of the functions presented in this chapter. Gannon et al. (2007) observed so-called butterfly distributions which show a double peak form with a minimum near 90^o. Whilst butterfly distributions were not considered when fitting to the average Van Allen Probes pitch angle data, these pitch angle distributions can exist in the radiation belt region (Albert et al., 2017; Zhao et al., 2014b). The occurrence rate of butterfly distributions for 510 keV electrons has been shown to exhibit a local time dependence, with butterfly distributions seen primarily on the night side at L $>$ 5.5 (Gannon et al., 2007). Ni et al. (2016) demonstrated a similar night side bias for butterfly distributions in MeV energy electron populations for L $\gtrsim$ 5.5, however pitch angle distributions have been shown to be largely energy dependent (Zhao et al., 2018) and the findings of Gannon et al. (2007) suggest butterfly distributions occur more readily at L $>$ 5.5 for higher energy electrons. This was also observed by Horne et al. (2003), with butterfly distributions seen at L = 6 for electrons greater than 340 keV whilst pancake distributions were observed at lower energies. Further work is required to better understand the occurrence of butterfly distributions for 100 - 300 keV electrons for $L^* > 4.5$ as previous studies have largely focused on electrons of higher energy. A fully MLT dependent, empirical pitch angle distribution

model is beyond the scope of the current study. However, a larger library of potential pitch angle distributions, including MLT variations, may be used to improve the results from the method in future work.

As ratios shown in Figure 6.8 are primarily greater than one, the methods presented in this chapter tend to produce electron flux values moderately less than those observed by MagEIS. It is possible that some of this variation originates in the average pitch angle distributions assumed, as discussed above. Additionally, disparities may arise from the L^* mapping of the data as the POES and Van Allen Probes L^* values have been calculated using different external field models (Tsyganenko (1995), i.e. T96, and Tsyganenko (1989), i.e. T89, respectively). The MagEIS and SEM-2 instruments have different designs and ways of operating and as such, the lower values for the electron flux given from the POES measurements may also arise from instrumentation differences. For $L^* \gtrapprox 3.7$ the average ratios between the MagEIS flux measurements and the electron flux retrieved from the POES measurements are fairly consistent in L^* for each energy. As such, the ratio values could potentially be used as a correction factor, which would encompass the aforementioned sources of error, to improve the agreement between the POES retrieved flux and the MagEIS observations, as has been applied in previous work (Meredith et al., 2017).

Figure 6.9 displays a curious feature of the POES data. A slight diurnal variation can be observed for each of the L^* cuts shown. This diurnal fluctuation has been reported by previous authors (Meredith et al., 2016) where it was attributed to sampling effects. The diurnal pattern has been reduced in part by considering only the trapped electron population and correcting measurement times where trapped electrons were only observed by part of the field-of-view (as described in section 6.2). However, despite this, some daily variation still persists in the POES data. All five POES satellites used in this study exhibit the diurnal fluctuation separately and further work is required to fully understand its origin.

Average pitch angle distributions, formulated using MagEIS data have been considered in this study to convert the POES data to omnidirectional flux, and to estimate the electron flux at a 90^o pitch angle. Where equation 6.8 was fitted to the average MagEIS equatorial pitch angle distributions, the resulting $n(E)$ values shown in Figure 6.6 are largely similar to those presented by Shi et al. (2016) (who also assumed the form given by equation 6.8). Additionally, the n values from the 100 keV electron differential flux pitch angle distributions are near to the $>$100 keV N parameters for L^* values where a single sine function was used. An agreement between the differential 100 keV n values and the N values for the integral $>$100 keV flux supports the assumption made in section 6.3 that allows the pitch angle distributions to be approximated by equation 6.1, and this is further reinforced by comparing

the 300 keV n values to the >300 keV N values. When Shi et al. (2016) considered how the $n(E)$ varied with L (as opposed to L^* used in this study), a notable peak in the $n(E)$ values can be observed in the region of L = 2 - 4, with the exact L of the peak depending on both electron energy and activity. This peak in $n(E)$ for L values relating to the slot region is likely associated with the cap distributions named by Zhao et al. (2014a), where a sharp peak in the flux can be seen around a pitch angle of 90^o for an otherwise mostly flat distribution. In sections 6.3 and 6.5, a second equation involving two sine functions was fitted to pitch angle distributions that displayed this form, and the corresponding L^* values where shaded grey in Figures 6.4 and 6.6. Generally, for equivalent electron energies and activity levels, the L range for the peak in $n(E)$ shown by Shi et al. (2016) are similar to the L^* values where the distribution consisting of two sine functions best fitted the pitch angle distribution. For both the integral and differential flux, the L^* values where cap pitch angle distributions were observed reduced with increasing electron energy. The energy dependence in the location of these cap pitch angle distributions agrees with the suggestion that the observed cap pitch angle distributions are formed by hiss waves Lyons et al. (1972).

There are four main benefits of using the methods put forth in this chapter to formulate the low energy boundary condition for radiation belt models from low Earth orbit POES data. First, it enables the low energy boundary to be calculated for 3D radiation belt models with a higher temporal resolution than can be achieved with the Van Allen Probes. As such, it enables the importance of short lived seed population enhancements to be examined. Second, with multiple satellites, a better MLT coverage is given by POES and, in addition to improving the drift average, the retrieved POES data could be used to formulate low energy boundary conditions for up-and-coming 4D models. Third, the POES and MetOp satellites present a wealth of data, with SEM-2 coverage spanning $\sim$19 years, enabling event specific low energy boundary conditions to be formed for events prior to the start of the Van Allen Probes mission, and likely afterwards. Using a realistic low energy boundary, derived from data, enables better understanding of the role of local acceleration during such events (Tu et al., 2014). Fourth, POES is able to measure the electron flux out to the last closed drift shell. Glauert et al. (2014a) presented a method where the phase space density was set to zero for the outer boundary condition, simulating losses to the magnetopause. By using the methods presented in the current chapter to formulate the low energy boundary condition for an event, and using an outer boundary condition such as that described by Glauert et al. (2014a), the entire radiation belt region could be studied using a radiation belt model. Other uses of the retrieved dataset include examining the evolution of the seed population across multiple MLTs. Once the POES data has been converted to differential

flux, it can be used to calculate the phase space density. Analysis of the phase space density evolution is a valuable tool to ascertain physical processes active in the radiation belt region (Green and Kivelson, 2004) and the coverage of multiple MLT planes may help to further identify processes affecting the seed population.

6.10 Summary and Conclusions

Here we have presented a novel method to convert the >30, >100, and >300 keV electron flux measurements from the POES satellites at low earth orbit to differential flux values across a range of energies, at 90^o pitch angle. The retrieval process consisted of the following steps:

1. Measurements where the POES satellites observed the trapped electron population were isolated and, when trapped electrons were only observed by part of the MEPED T90 field-of-view, a correction was applied.

2. The POES data was mapped the equatorial plane and converted to omnidirectional integral flux by assuming that the pitch angle distribution obeyed either a single or double sine form. The required parameters for the conversion to omnidirectional flux were determined by analysing Van Allen Probes data at a number of L^* values and at three levels of Kp.

3. The omnidirectional integral flux measurements were then converted to an omnidirectional differential flux spectrum. Two methods to convert the omnidirectional integral flux readings have been investigated. The first method employs a library of flux-energy distributions returned by the AE9 model and the second uses a Reverse Monte Carlo style iterative fitting approach.

4. Lastly, the omnidirectional flux at each energy was converted to 90^o directional flux by again assuming an energy-dependent pitch angle distribution that obeyed a single or double sine function, depending on L^*. The associated shape parameters were found using average pitch angle distributions from level 3 MagEIS data for 100, 200, 300, 500, and 800 keV electrons, at three levels of Kp and L^* = 1.5 - 5.7.

The results from both methods were compared to observations from the MagEIS instruments on board the Van Allen Probes. For $L^* \gtrsim 3.7$, the average difference between the converted POES flux and the MagEIS measurement was less than a factor of 4 for energies

100 - 600 keV. For $L^* \lesssim 3.7$, average differences tended to be larger, likely due to pitch angle distributions having a greater dependence on activity for this L^* range.

The 90^o equatorial pitch angle flux, at a number of L^* values, for electron energies following a line of constant μ = 100 MeV G^{-1} were computed using the POES data, and the time sequence of flux compared to the equivalent flux from MagEIS. Typically, both methods produce flux values close to the MagEIS measurements, particularly for L^* = 4.5 - 5.5. The POES data was also used to produce a low energy boundary condition for the BAS-RBM for the 3 - 27 June 2013. Using the POES low energy boundary in the model produced a very similar model output at 0.9 MeV to when MagEIS data was used for the low energy boundary condition. We therefore suggest that the methods presented here could be used to formulate event specific low energy boundary conditions for radiation belt models in order to better study events outside the time period covered by the Van Allen Probes mission (prior to 2012, and with MetOp data, potentially after the Van Allen Probes are no longer operational) or at L^* outside the Van Allen Probes Orbit.

The assumption that the electron flux falls with increasing energy did not always hold, resulting in the flux potentially being overestimated. However, the conditions leading to the breakdown of this assumption primarily occur during quiet times. If POES data was used to generate the low energy boundary condition for radiation belt models, an overestimation of the seed population during quiet periods is unlikely to dramatically alter model outputs at higher energies.

In conclusion, we have formulated the electron flux at 90^o equatorial pitch angle for a number of seed population energies, using integral electron flux measurements taken from POES satellites operating in low earth orbit. The resulting method can produce data that, for electron energies between 100 and 600 keV, are typically within a factor of 4 of the MagEIS observed levels. The method also enables the reconstruction of the electron differential flux at the equator for the entire period 1998 - 2018.

Chapter 7

On the Importance of Gradients in the Low Energy Electron Phase Space Density for Relativistic Electron Acceleration

The results of this chapter have been published in the *Journal of Geophysical Research: Space Physics* as:

Allison, H. J., Horne, R. B., Glauert, S. A., and Del Zanna, G., (2019), *On the Importance of Gradients in the Low Energy Electron Phase Space Density for Relativistic Electron Acceleration*, J. Geophys. Res. Space Physics, 124, 2628– 2642, doi:10.1029/2019JA026516,
.

The presented analysis is the outcome of the author's own work, with R. B. Horne, S. A. Glauert, and G. Del Zanna providing advice and supervision. The results from this chapter were presented at Autumn MIST 2018, held at the Geological Society in London, and at the Royal Astronomical Society Specialist Discussion Meeting on Storms and Substorms 2019.

7.1 Introduction

Whistler-mode chorus waves are an important acceleration and loss mechanism in Earth's electron radiation belts (e.g. Bortnik et al., 2007; Horne and Thorne, 1998; Horne et al.,

2005a,b; Lam et al., 2010; Summers et al., 1998; Thorne et al., 2005). A study by Jaynes et al. (2015), considering Van Allen Probes data, highlighted the interplay between the source electrons (1-10s keV), responsible for chorus wave generation, and seed electrons (30 - 100s keV), in the acceleration of relativistic populations. Substorm particle injections can supply both source and seed electrons to the inner magnetosphere, generating chorus waves and providing an increased low energy population that can be accelerated to higher energies (Boyd et al., 2014; DeForest and McIlwain, 1971; Ganushkina et al., 2013; Obara et al., 2000; Omura et al., 2008; Sergeev et al., 1998; Tang et al., 2016; Tsurutani and Smith, 1974; Zhang et al., 2009).

As detailed in chapter 3, a number of observational studies have shown strong correlations between increases in the seed population and subsequent enhancements in the core population ($>$1 MeV) (Boyd et al., 2016; Li et al., 2005; Tang et al., 2016; Turner and Li, 2008), with chorus waves as the likely acceleration mechanism (Boyd et al., 2014, 2018; Foster et al., 2013; Meredith et al., 2003b; Obara et al., 2000). However, Horne et al. (2005a) demonstrated that, for electrons with energies less than $\sim$300 keV, interactions with chorus waves result in a competition between acceleration and loss, while above $\sim$300 keV, electrons are accelerated faster than they are lost from the system. The seed population in the outer radiation belt primarily covers the energy range $\sim$30 to $\sim$ 300 keV, and therefore will likely experience both significant acceleration and loss from chorus wave interactions. As suggested by Boyd et al. (2016), the level of the seed population may affect this balance and, therefore, the occurrence of $>$1 MeV flux enhancements.

Numerical radiation belt models provide an excellent test-bed to explore links between the seed population and the core ($>$1 MeV) population. Changes in the seed population can be introduced to the calculation by the low energy boundary condition, allowing the impact on the $>$1 MeV flux arising from PSD variations at this boundary to be evaluated. Despite this, use of numerical models to explore the effect of changes in the seed population has thus far been limited to two published studies that provided conflicting results. Using the VERB 3D model, Subbotin et al. (2011a) found that the 1 MeV flux was relatively insensitive to the flux at the lowest value of the first adiabatic invariant, μ. However, conversely, Tu et al. (2014) obtained model results that were much closer to observations for the October 2012 "double-dip" storm when a realistic seed population was used for the low energy boundary condition of DREAM 3-D, and event-specific chorus diffusion coefficients were employed.

In this chapter, we investigate the effect of changes in the seed population on the 1 MeV electron flux using the British Antarctic Survey Radiation Belt Model (BAS-RBM) (Glauert et al., 2014b). In section 7.3, model results using a low energy boundary condition set by

Van Allen Probe observations are compared to those using time-constant flux values. The results of changing the energies of the low energy boundary are explored in section 7.5. We then further examine the impact of the seed population in idealised theoretical studies using the 2-D version of the BAS-RBM in sections 7.6 and 7.7.

7.2 BAS Radiation Belt Model

The BAS-RBM, described in chapter 2, is a 3-D diffusion model, that calculates the evolution of the phase-averaged phase space density, $f(p,r,t)$, by solving equation 2.26.

7.2.1 Diffusion Coefficients

The drift and bounce averaged pitch angle and energy diffusion coefficients used in the model calculations (D_{EE} and $D_{\alpha\alpha}$) had been previously calculated with the Pitch Angle Diffusion of Ions and Electrons (PADIE) code (Glauert and Horne, 2005) using statistical wave models for whistler mode chorus (Horne et al., 2013), Electromagnetic Ion Cyclotron (EMIC) waves (Kersten et al., 2014), and hiss waves (Meredith et al., 2018). Chorus waves are mainly observed outside the plasmasphere and hiss inside. To account for this, an activity dependent plasmapause model has been built into the drift and bounce averaged diffusion coefficients by considering wave and density observations from the datasets used to construct the statistical wave models (Horne et al., 2013; Meredith et al., 2018). The radial diffusion coefficient, $D_{L^*L^*}$, is taken to be the Kp dependent magnetic component given by Brautigam and Albert (2000) (defined for Kp values between 1 and 6). The Shue et al. (1998) model is used for the magnetopause location, from which, the last closed drift shell (LCDS) is estimated as described by Glauert et al. (2014a).

7.2.2 Boundary Conditions and Initial Conditions

For the following analysis, the BAS-RBM was used to solve equation 2.26 for L^* values $L^*_{min} \leq L^* \leq L^*_{max}$, equatorial pitch angles $0^o \leq \alpha \leq 90^o$, and a range of energies that depend on L^*. As radial diffusion acts at constant first and second adiabatic invariant, the high and low energy boundaries follow lines of constant μ and J, defined by selecting the minimum and maximum energies (E_{min} and E_{max}) at L^*_{max}.

As discussed in section 2.4.2, at each of the minimum and maximum values of L^*, α, and energy, boundary conditions are required to define the calculation domain. At $\alpha = 0^o$ and α

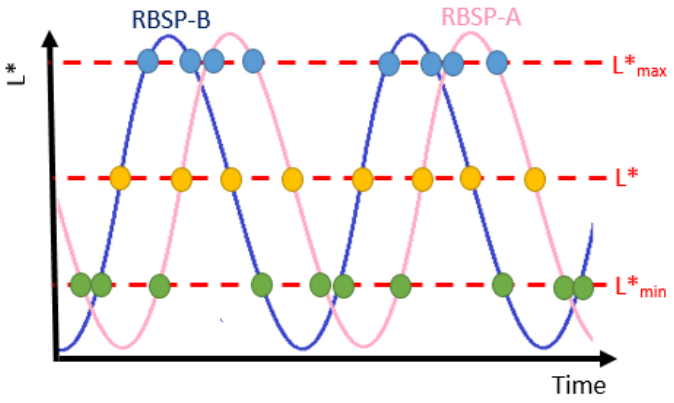

Figure 7.1 – Schematic of the Van Allen Probes L^* sampling, illustrating extracting measurements at particular L^* values (not to scale).

= 90^o the change in the phase-averaged phase space density with respect to α is set to zero (i.e. $\frac{\partial f}{\partial \alpha} = 0$). For the E_{max} boundary, $f = 0$ at the $E_{max} - \alpha$ surface.

The remaining three boundary conditions (f at L^*_{min}, L^*_{max}, and E_{min}) are supplied by the Van Allen Probes dataset, described in chapter 4. For the present study, the inner boundary, L^*_{min}, was set at $L^* = 2.5$ and the outer boundary, $L*_{max}$, at $L^* = 5.5$. An L^*_{max} value of $L^* = 5.5$ was selected as the Van Allen Probes sample $L^* = 5.5$ twice nearly every orbit, unlike for larger L^* values. An L^*_{max} of 6.0, for example, results in an outer boundary condition made from far fewer data points. Data from both MagEIS (Blake et al., 2013) and REPT (Baker et al., 2013b) instruments (see chapter 4) have been used to formulate $f(\alpha, E, L^*)$ at the L^*_{min} and $L*_{max}$ boundaries. The electron flux values for energies between 31.7 keV and 1.5 MeV have been taken from MagEIS data, while flux at energies $\geq$ 1.8 MeV are from REPT. MagEIS measurements were also used for the E_{min} boundary.

Flux data from the local 90^o pitch angle bin of the MagEIS and REPT instruments were utilised. In the data files, the energy centroid of each energy channel can vary with time, but energy values are typically centred around an average and tend to only deviate by a few keV. Measurements corresponding to energies that differed from the average energy centroid of the channel during the period by more than 5% were omitted. Additionally, the background correction algorithm can sometimes retain isolated very low flux values, in regions where all surrounding values were below the background level. If a measurement was more than an order of magnitude below the geometric mean of the flux for the energy channel, and the three preceding and three succeeding flux values had been removed by the background correction algorithm, then the measurement was also omitted.

For each energy channel, the energy of the measured electron flux may differ between RBSP-A and RBSP-B. If the average energy for a given channel of REPT or MagEIS (once >5% deviations had been omitted as discussed above) varied by more than 8 keV between the two probes, then the flux was interpolated to the energy of the probe that had the most valid data points for the energy channel. If the energy differed by less than 8 keV, then the central channel energy for both probes was set to the mid-point between the two energy values. As MagEIS and REPT data were supplied at different times, the flux values were binned into minute time intervals and the geometric mean for each minute computed. The resulting minute-averaged, cleaned datasets from both probes were used to formulate the boundary conditions.

For the inner and outer L^* boundaries, flux measurements corresponding to an L^* value within ± 0.05 of the selected L^*_{min} or L^*_{max} value were extracted from the dataset. It was assumed that inbound and outbound L^* crossings would likely be separated by more than 3 minutes, and if more than one flux measurement corresponded to the appropriate L^* range within the 3 minute time window then the measurements were averaged. L^* slices from the two probes were interleaved and, as a value is always required for the boundary condition, interpolation was performed to populate energy channels with missing data. For the inner boundary condition, the $\gtrsim$800 keV electron flux was below background level. As demonstrated by Fennell et al. (2015) and Li et al. (2015), >900 keV electrons are seldom observed in the inner belt and, as a result, at these energies, the flux was set to a fill value of $5\times10^{-3}\ cm^{-2}s^{-1}sr^{-1}keV^{-1}$. Finally, the 90^o flux at L^*_{min} and L^*_{max} was converted to phase space density (PSD) by calculating the relativistic momentum for each electron energy and employing Louiville's theorem via equation 2.1. The BAS-RBM then assumes a pitch angle distribution to use this 90^o PSD to populate the L^*-α_{eq} surface at L^*_{min} and L^*_{max}, which, for the version of the model used here, is a sine function.

The initial condition was also formulated from the cleaned, minute-averaged Van Allen Probes data. PSD values were required at the start of the model run, for each L^*, Energy, and pitch angle. Following a similar procedure to that for the L^*_{min} and L^*_{max} boundary conditions, 32 L^* slices through the dataset were calculated, for L^* values ranging between L^*_{min} and L^*_{max}. At each L^* slice, interpolation across energy provided values for energy channels with missing data. So that the electron flux could be interpolated to the selected start time of the model run, MagEIS and REPT data were also downloaded for the day prior to the simulation start time. The electron flux values were then interpolated to the selected start time before being converted to PSD.

The final boundary of the BAS-RBM is the E_{min} boundary. The electron energies used for the E_{min} boundary are discussed further in sections 7.4 and 7.5. The minimum energy for the calculations performed in this chapter was chosen at L^*_{max} and used to determine the corresponding value of the second invariant, J, for $\alpha_{eq} = 0^o$ electrons. The energies of the low energy boundary, then follow this line of constant J through all values of L^*. Again, 32 L^* slices through the cleaned, minute-averaged dataset are taken in regular steps between L^*_{min} and L^*_{max}. At each L^* value, the electron flux was interpolated to the appropriate energy value, given by the line of constant J. Figure 7.1 demonstrates that at each L^* slice, the data extracted has a different corresponding time array. The low energy boundary condition requires PSD values across all L^* at each time. To address this, the flux data was interpolated to the times of the $L^* = 4.0$ cut (mid-point between L^*_{min} and L^*_{max}). Lastly, the low energy boundary electron flux was converted to PSD using equation 2.1.

7.3 Observations of the Electron Flux between 21 April to 9 May 2013

We consider the period from the 21 April to the 9 May, 2013. Figure 7.2a - e shows the background corrected MagEIS flux from Van Allen Probes A and B. All data presented is from the 90^o local pitch angle bin. Additionally, the solar wind speed and z-component of the interplanetary magnetic field (B_z) are shown in panel f. The L^* values for the MagEIS measurements have been calculated using the IGRF and T89 field models (Thébault et al., 2015; Tsyganenko, 1989).

This date range includes two 1 MeV flux enhancement events, separated by a small dropout. The first 1 MeV enhancement period commences late on the 24 April following a dropout which diminished the pre-existing 1 MeV population. This enhancement includes a second stage, relating to a southward turning of B_z early on the 26 April that supplied additional low energy electrons to the radiation belts (Figure 7.2a and b). After a further dropout on 1 May, a second enhancement of the 1 MeV flux was observed. The second enhancement relates to a longer period of southward B_z and an increased low energy electron population (Figure 7.2a-c) that penetrates further into the radiation belt region. The 1 MeV flux is now more than an order of magnitude higher than the pre-event levels, with both MagEIS instruments recording a 1 MeV electron flux in excess of 10^3 $cm^{-2}s^{-1}sr^{-1}keV^{-1}$ for much of the outer radiation belt region.

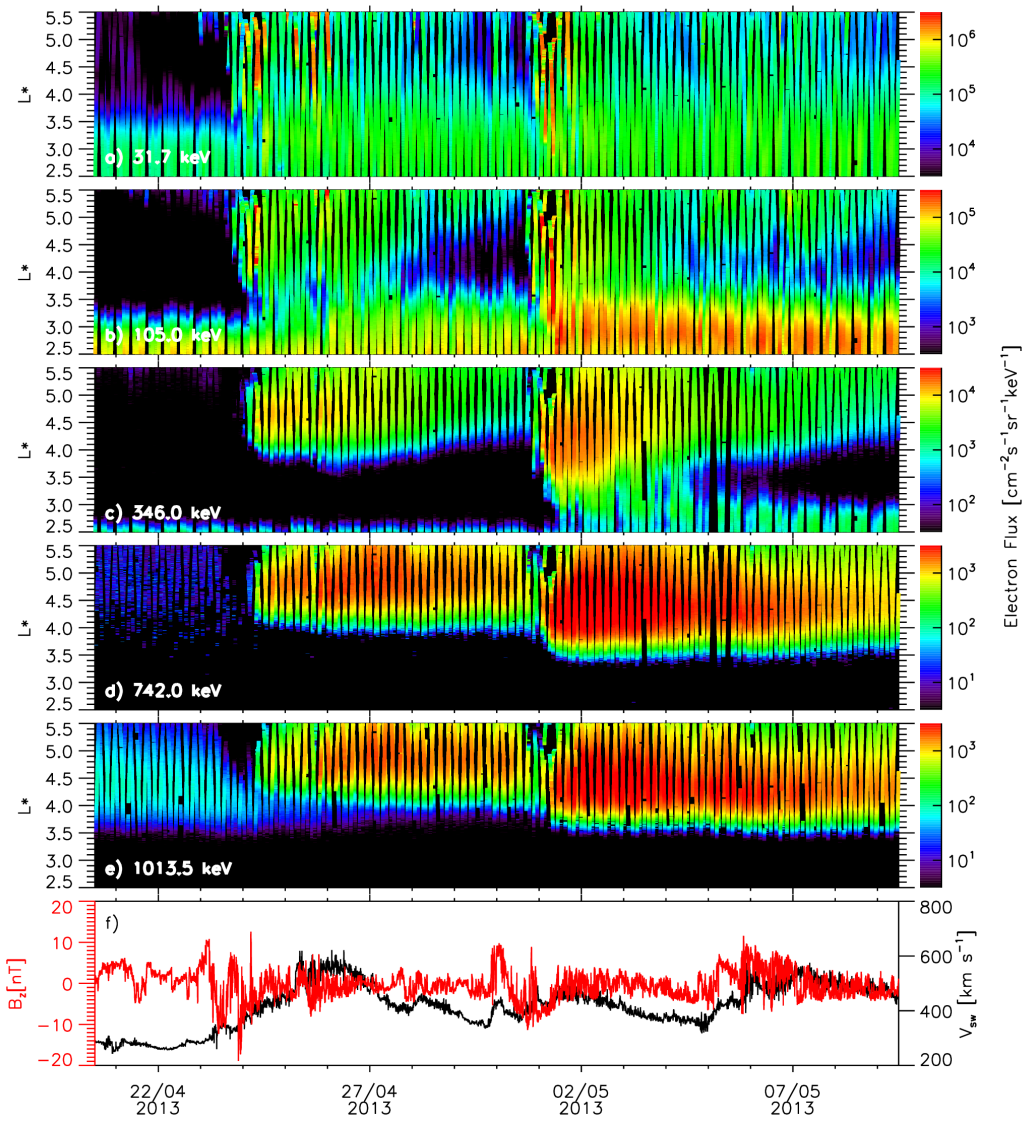

Figure 7.2 – Local perpendicular electron flux from the 31.7, 105.0, 346.0, 742.0, and 1013.5 keV channels of the MagEIS on board Van Allen Probes A and B (panels a-e) for the period from the 21 April to 9 May 2013. Solar wind speed (black line) and the z-component of the interplanetary magnetic field (red line) are shown in panel f.

7.4 Modelling the 21 April to 9 May 2013 Period

To run the BAS-RBM for the period shown in Figure 7.2 boundary conditions were created from Van Allen Probes measurements as described in section 7.2.2. A low energy boundary (LEB) condition was formulated from MagEIS observations. The minimum energy for the calculation was selected as ~161 keV at $L^* = 5.5$ (μ = 100 MeV/G for a 90^o particle in a

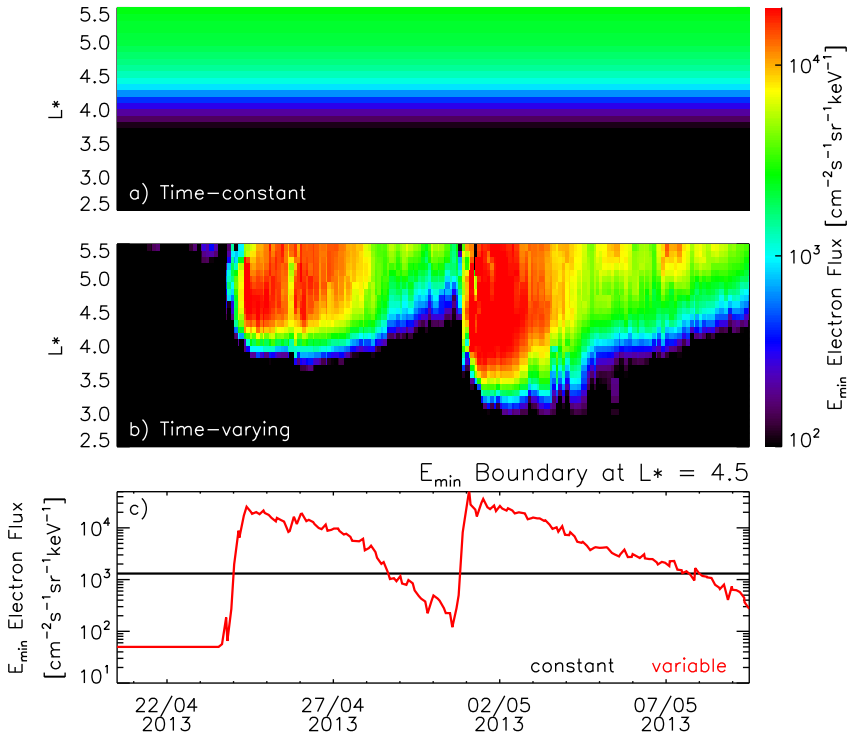

Figure 7.3 – The electron flux along the low energy boundary ($\mu_{min} = 100\ MeV/G$) of the British Antarctic Survey Radiation Belt Model using MagEIS data to supply a time-constant flux profile (panel a) and time-varying flux (panel b). The electron flux at $L^* = 4.5$ through the constant (black line) and time varying (red line) low energy boundary conditions are shown in panel c.

dipole magnetic field). Throughout the rest of the chapter, the μ value for a 90^o particle corresponding to the minimum energy chosen at $L*_{max}$ is denoted by μ_{min}.

Two different approaches were taken for calculating the LEB condition. The first involved calculating the LEB flux via the method described in section 7.2.2, then time-averaging over the period (taking the geometric mean). This provided a constant LEB condition, without seed population enhancements, and is shown in Figure 7.3a.

Secondly, we used the MagEIS data to formulate a time-dependent LEB condition at the same energies. In this instance, the procedure outlined in section 7.2.2 was again used, but the flux was not averaged over the period so that time variations were retained. The resulting time-varying LEB flux is shown in Figure 7.3b. Time variations of the electron flux on the LEB spanned more than two orders of magnitude, shown by the red line in Figure 7.3c for $L^* = 4.5$. At the start of the period, some of the MagEIS energy channels yielded missing data as the flux was below the background level. During this time we set the flux to 50 $\text{cm}^{-2}s^{-1}sr^{-1}keV^{-1}$ as a value was required for the boundary conditions.

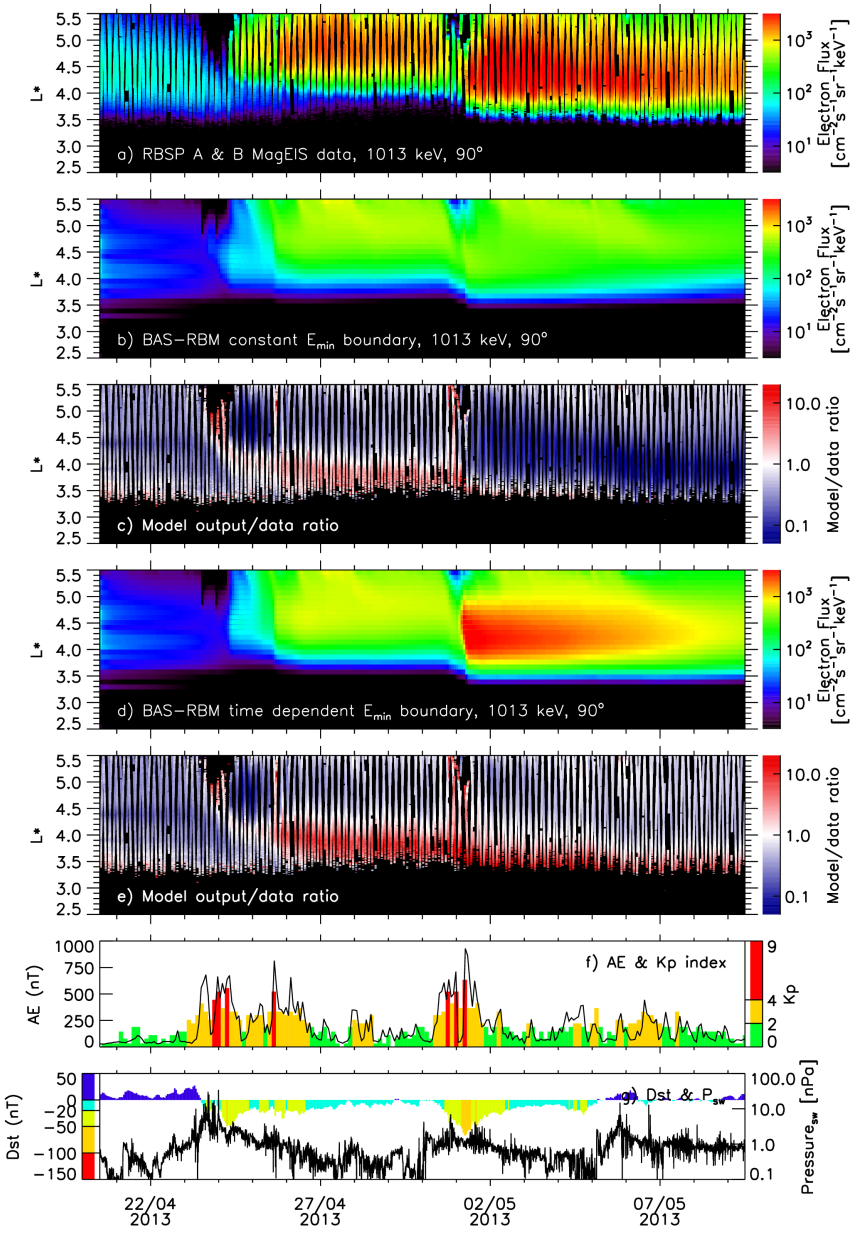

Figure 7.4 – Van Allen Probes A and B Magnetic Electron Ion Spectrometer, 90^o local pitch angle, 1013 keV electron flux observations (panel a). The 1013 keV, 90^o pitch angle flux outputted by the BAS-RBM having used the time-invariant low energy boundary condition (panel b). Ratio between the model output shown in panel b and the Van Allen Probes observations (panel c). The 1013 keV, 90^o pitch angle flux from the model using the time-varying low energy boundary condition (panel d). Ratio between the model output shown in panel d and the Van Allen Probes observations (panel e). The AE and Kp indices for the period (panel f). The Dst and Solar wind Pressure for the period (panel g).

The simulated flux at 1013.5 keV, for 90^o pitch angle, resulting from using the constant LEB condition in the BAS-RBM, is shown in Figure 7.4b. The MagEIS observed flux at this energy is also given in Figure 7.4a for a local pitch angle of 90^o (previously shown in Figure 7.2e). Both the first and second enhancements of the 1 MeV model flux are lower than observations (Figure 7.4c). Following the second enhancement event, near L^* = 4 - 5, the 1 MeV population was lower than data by up to a factor of 10. Both enhancements relate to small magnetic storms (Figure 7.4g) and the AE and Kp indices are given for reference (Figure 7.4e).

The BAS-RBM was also run using the time-varying LEB condition (Figure 7.3b), and the resulting electron flux at 1013.5 keV, 90^o pitch angle, is shown in Figure 7.4d. All the other boundary conditions and the diffusion coefficients were identical to the simulation shown in Figure 7.4b. Figure 7.4d reveals that the 1 MeV flux was larger when the time varying LEB condition was employed, particularly during the second enhancement. The ratio between the model output and the MagEIS observations (Figure 7.4e) demonstrates that this second enhancement is now closer to observations for $L^* > 4$ than in the previous model run. The region where the ratio is approximately 1 (white) varies from L^* = 4.5 to L^* = 3.5 during the period and, following the second enhancement, generally lies at a higher L^* than the simulation with a constant LEB flux.

The results presented in Figure 7.4 demonstrate that, during the second enhancement event, the rise in the low energy seed population increased the level of the 1 MeV flux. Chorus wave activity varies throughout the simulation. Increases in the seed population tend to coincide with periods of enhanced AE, and as the chorus diffusion matrix was driven by AE, enhanced chorus diffusion (Horne et al., 2013). The time varying LEB condition showed similar decay rates for both of the enhancements, and in each instance differed from the constant boundary flux by more than an order of magnitude (Figure 7.3a and b). However, there was a much greater difference between the model results for the second $\sim$1 MeV enhancement event (1 May) than the first (24 April).

7.5 Varying the Energy of the Low Energy Boundary

Some radiation belt models use time-invariant LEB conditions (Subbotin et al., 2010, 2011b; Varotsou et al., 2008). These models set the energies of LEB to low values (around 10 keV) where, during active times, the electrons are likely to be on open drift paths due to an enhanced convection electric field (Li et al., 2010; Thorne et al., 2007; Zhang et al., 2015). The assumption is then made that the number of electrons supplied by enhanced convection

and those lost on open drift paths and by precipitation ultimately balance and so the level of the flux at these energies remains relatively constant (Subbotin et al., 2011b).

When the LEB is around 10 keV the flux $\gtrsim$10 keV is determined by diffusion from the LEB and outer boundary condition. However, data shows that electrons can be injected into the radiation belt region over a range of energies by electric fields (Dai et al., 2015). Placing the LEB at a higher energy better includes electrons that are from a non-diffusive origin. Additionally, seed population electrons are largely influenced by the convection electric field and the electron flux at these energies is magnetic local time (MLT) dependent during active times (Allison et al., 2017) (see chapter 5). As 3-D radiation belt models do not include the MLT dimension, working under a drift-averaged assumption, large MLT asymmetries may introduce errors into the calculation. To avoid MLT variations, some radiation belt models set the LEB at higher energies, away from the convective energy range (Albert et al., 2009; Glauert et al., 2014a,b, 2018).

To investigate the effect of the location of the LEB, we reduce the energies of the LEB condition, setting μ_{min} = 30 MeV/G, and also explore the effect of moving the boundary up in energy, using μ_{min} = 200 MeV/G. In a dipole field, μ_{min} = 30 MeV/G corresponds to ~53 keV at L^* = 5.5, while μ_{min} = 200 MeV/G, corresponds to ~291 keV. Figure 7.5 shows the minimum energy for the model, at each L^*, for the three different values of μ_{min}. Both a constant and time-varying LEB condition were calculated for each value of μ_{min} from MagEIS observations in the manner discussed in section 7.3 and are shown in Figures 7.6 and 7.7.

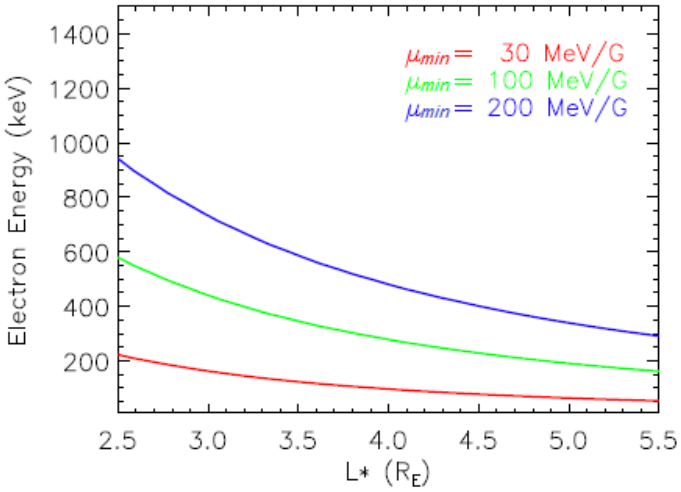

Figure 7.5 – The minimum energy at each L^* for each of the three values of μ_{min}.

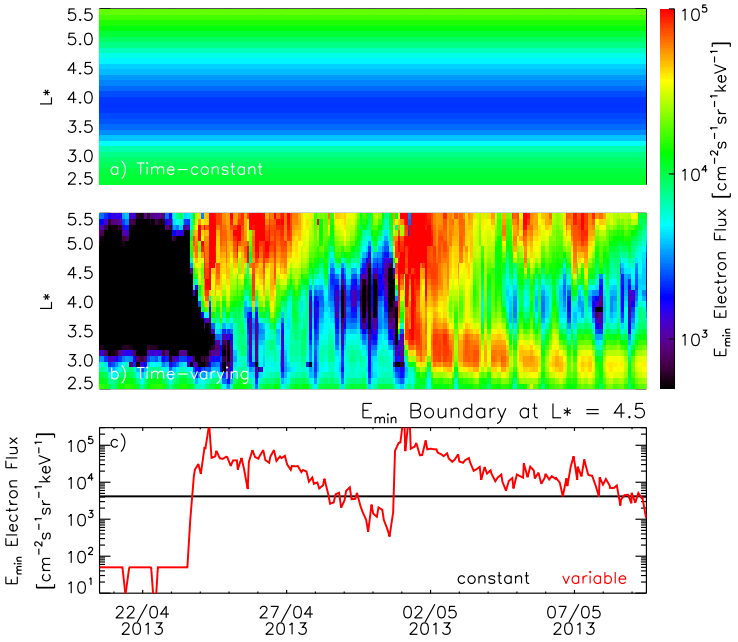

Figure 7.6 – The time-constant (panel a) and time-varying (panel b) electron flux on the low energy boundary corresponding to $\mu_{min} = 30\ MeV/G$. The flux at L^* = 4.5 through the constant (black line) and time-varying (red line) flux is shown in panel c.

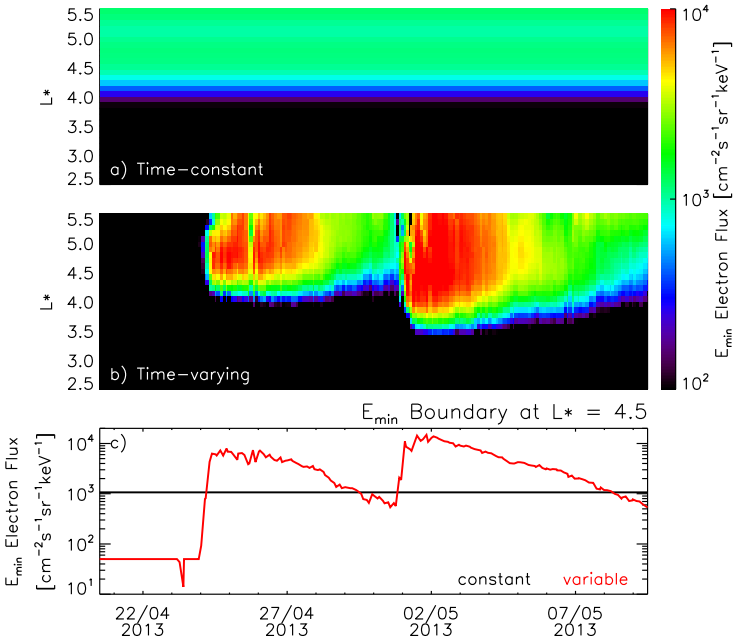

Figure 7.7 – Same as 7.6 but for the electron flux on the low energy boundary condition corresponding to $\mu_{min} = 200\ MeV/G$.

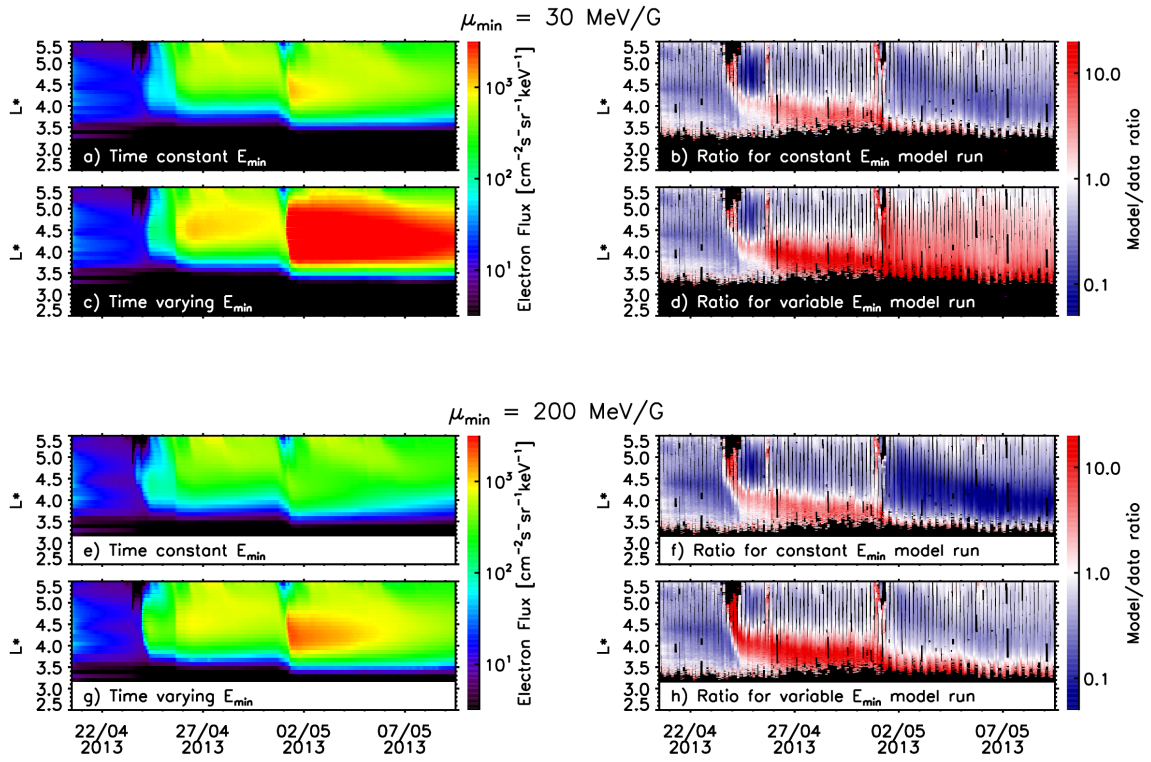

Figure 7.8 – Electron flux from the BAS Radiation Belt Model at 1013 keV, 90^o pitch angle, for time-constant low energy boundary condition at energies given by μ_{min} = 30 MeV/G (panel a) and by μ_{min} = 200 MeV/G (panel e), and for a time-varying low energy boundary condition at energies given by μ_{min} = 30 MeV/G (panel c) and by μ_{min} = 200 MeV/G (panel g). The ratios between the model outputs and the MagEIS observations are shown on the right-hand side for each of the four model runs presented.

Figure 7.8 shows the result of using lower (panels a - d) and higher energies (panels e - h) for the LEB. When using a constant LEB condition, a higher flux at 1 MeV was achieved for μ_{min} = 30 MeV/G (Figure 7.8a) than for μ_{min} = 100 MeV/G (Figure 7.4b). Comparing Figure 7.8c with Figure 7.4d indicates that the flux was also higher for the μ_{min} = 30 MeV/G time-varying LEB condition. The second 1 MeV flux enhancement, occurring on the 1 May 2013, was nearly a factor of 10 higher than the MagEIS data for $3.5 < L^* < 5$ when the μ_{min} = 30 MeV/G time-varying LEB condition was used (Figure 7.8d).

Conversely, when μ_{min} = 200 MeV/G, the 1 MeV flux was lower than the observations (Figure 7.8f and h) for $L^* > 4.5$ during the first and second enhancements. Thus, the results indicate that raising the energies of the LEB condition reduced the 1 MeV flux, contrary to what one might expect.

To see how the model results compare to the observed electron spectrum, Figure 7.9 shows the flux-energy distributions at L^* = 4.5 for selected times, from Van Allen Probe A

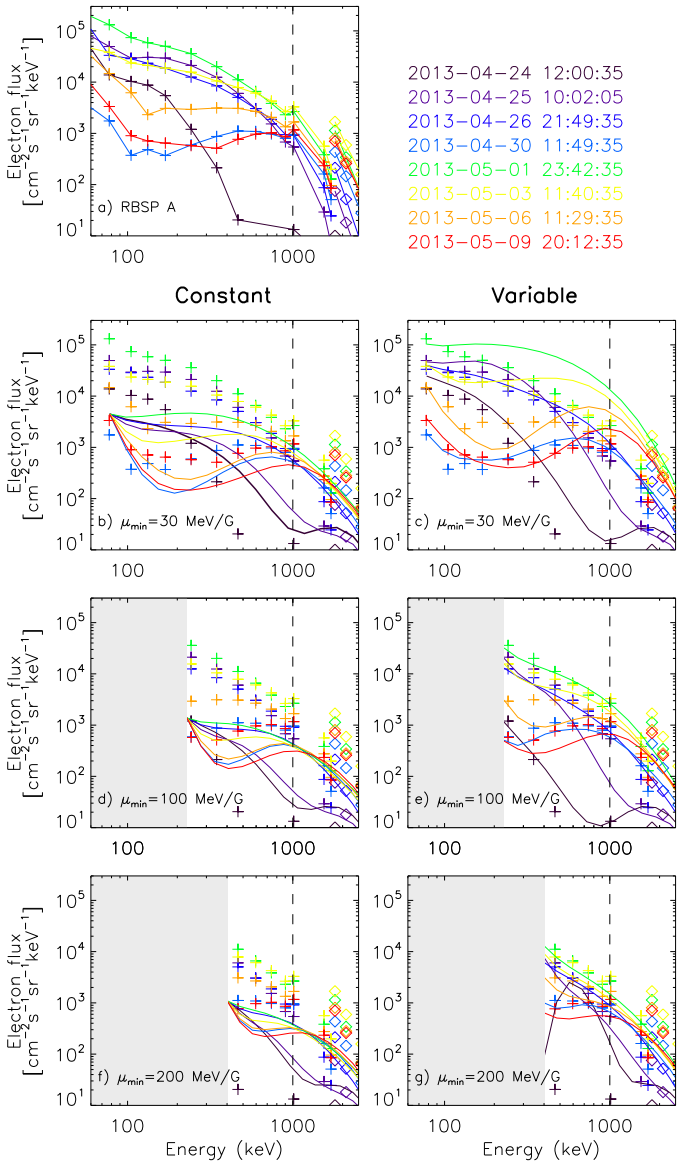

Figure 7.9 – Flux-energy distributions from selected times during the 21 April - 9 May 2013 period at L^* = 4.5. Panel a shows the MagEIS (plus symbols) and REPT (diamonds) observations from Van Allen Probe A. These symbols have been added for comparison on all of the panels shown. Additionally, for reference, a vertical dashed line marks 1 MeV. The colored lines on Panel b show the BAS-RBM output from the time-constant low energy boundary, μ_{min} = 30 MeV/G run and, panel c, the time-varying low energy boundary at the same minimum energies. Panels d and e respectively show the model outputs for the time-constant and time-varying low energy boundary conditions at energies given by μ_{min} = 100 MeV/G. Panels f and g show the model outputs for the time-constant and time-varying low energy boundary conditions at energies given by μ_{min} = 200 MeV/G.

measurements (panel a) and from the BAS-RBM using constant (panels b, d, and f) and time-varying (panels c, e, and g) LEB conditions. Measurements from the MagEIS instrument are shown as plus symbols, while REPT observations are indicated by diamonds. A slight discontinuity between the MagEIS and REPT observations can be observed, which we have not attempted to resolve, instead choosing to concentrate on the ∼1 MeV flux from MagEIS. Vertical dashed lines mark the 1 MeV location for reference.

The model results from the constant LEB condition (Figure 7.9b, d, and f) tend to be lower than the Van Allen Probe observations across a broad energy range, which ultimately affected 1 MeV enhancements. However, we note that there was better agreement when the low energy values were set by smaller μ_{min} (Figure 7.9b). For some of the selected times, a minimum can be seen near ∼200 keV in both the model flux and the Van Allen Probe A measurements. This is due mainly to loss by precipitation in this energy range (Ripoll et al., 2016).

Generally, observed flux levels were best reproduced when the time varying LEB conditions were used (Figure 7.9c, e, and g). As data is used to set the variable LEB condition, the model flux in Figures 7.9c, e, and g agrees well with observations at energies close to the respective lowest energy, which varies between the three model runs. Using the μ_{min} = 30 MeV/G time-varying LEB condition (panel c) tended to result in a higher flux during active periods than the MagEIS observations, particularly for energies >400 keV. A peak in the electron flux arises at 2013-04-24 12:00:35 for the μ_{min} = 200 MeV/G model run shown in Figure 7.9g (black curve), resulting from a decrease in the variable LEB flux. This spectral form was not reflected by the Van Allen Probe A observations and is discussed further in Section 7.8.

With the exception of periods where 's-shaped' flux-energy distributions are observed (Reeves et al., 2016; Ripoll et al., 2016), the electron flux in the radiation belts generally falls with increasing energy (Cayton et al., 1989). As a result, when the LEB is moved down in energy, the PSD on the boundary will increase. This will raise the maximum PSD that can be achieved by diffusion to higher energies and may be a reason for the higher flux at 1 MeV seen in Figures 7.8 and 7.9 when lower values of μ_{min} were employed. Another reason is that the 3D BAS-RBM does not include convection terms and therefore does not include convective loss to the magnetopause. This missing loss process will be most important for the lowest energies that are only included in the simulations with μ_{min} = 30 MeV/G. In Figure 7.9c the flux was higher than the data at 2013-05-01 23:42:35, during the second enhancement (green line), for energies $\gtrsim$90 keV. Convective loss would likely reduce the flux at the lowest energies shown here, lowering the available seed population and preventing their

acceleration to higher energies. Additionally, the model may underestimate the precipitation during this active period. It is likely that a combination of the above reasons resulted in the model flux exceeding observations for the second 1 MeV enhancement when the μ_{min} = 30 MeV/G time-varying LEB condition was used.

Another important factor is the efficiency of chorus diffusion for different electron energies. Figure 7.9 shows more temporal variability in the flux at all energies, including 1 MeV, for lower values of μ_{min}. Short lived flux enhancements that occur at ~100 keV (see Figure 7.2b) may be rapidly accelerated by chorus waves, raising the flux at 1 MeV.

7.6 Size of the Seed Population Enhancement

To understand the effects of chorus waves on the seed population in more detail, we use the 2-D BAS-RBM, neglecting radial diffusion (Horne et al., 2018). We performed an idealised study at L^* = 4.5. For the initial condition, the electron phase space density (PSD) was set to a constant value at all energies and pitch angles, except at the LEB, where PSD was set to a value a 100 times higher. Thus, the only initial energy gradient in the calculation was from the LEB condition and all subsequent PSD enhancements in the model originate from diffusing electrons from the LEB. Figures 7.11a and 7.12a show the initial PSD profile used for the model run, with the lowest energy in the calculation set to 10 keV. The chorus diffusion coefficients were held constant for the duration of the simulation and are shown in Figure 7.10, set using AE = 500 nT (Horne et al., 2013) to represent active conditions.

The resulting PSD profile after 24 hours is shown in Figure 7.11b. 10 keV electrons have been accelerated up to ~200 keV by the chorus waves. For the energy range from ~200

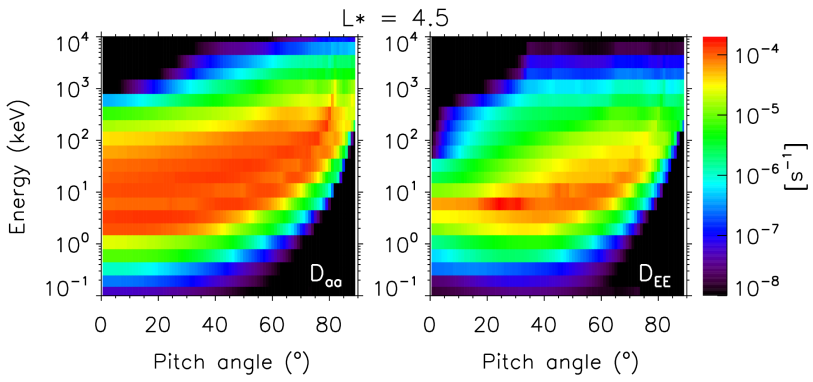

Figure 7.10 – Pitch angle ($D_{\alpha\alpha}$) and energy (D_{EE}) diffusion coefficients for L^* = 4.5, AE = 500 nT as calculated by (Horne et al., 2013).

keV to ∼900 keV, the PSD has decreased from the initial levels, forming a gap between the <200 keV and >900 keV energies. Above ∼900 keV there has been little-to-no change from the initial condition. Therefore Figure 7.11b shows that the 10 keV electrons from the LEB condition were not accelerated up to >1 MeV energies after a day of continuous chorus wave activity.

The same model setup described above (see Figure 7.12a) was run for a 30 day period and the results are shown in Figure 7.11c. Very little difference was observed between the PSD profile after 20 days (not shown) and after 30 days, implying that we are approaching a steady state solution. The PSD gap between ∼200 keV and ∼900 keV has persisted, even after 30 days, and the 10 keV electrons from the LEB condition were still not accelerated up to >1 MeV, even after a month of continuous chorus wave activity. Either the rate of loss from chorus waves in the 200 - 900 keV energy range was faster than the rate of acceleration,

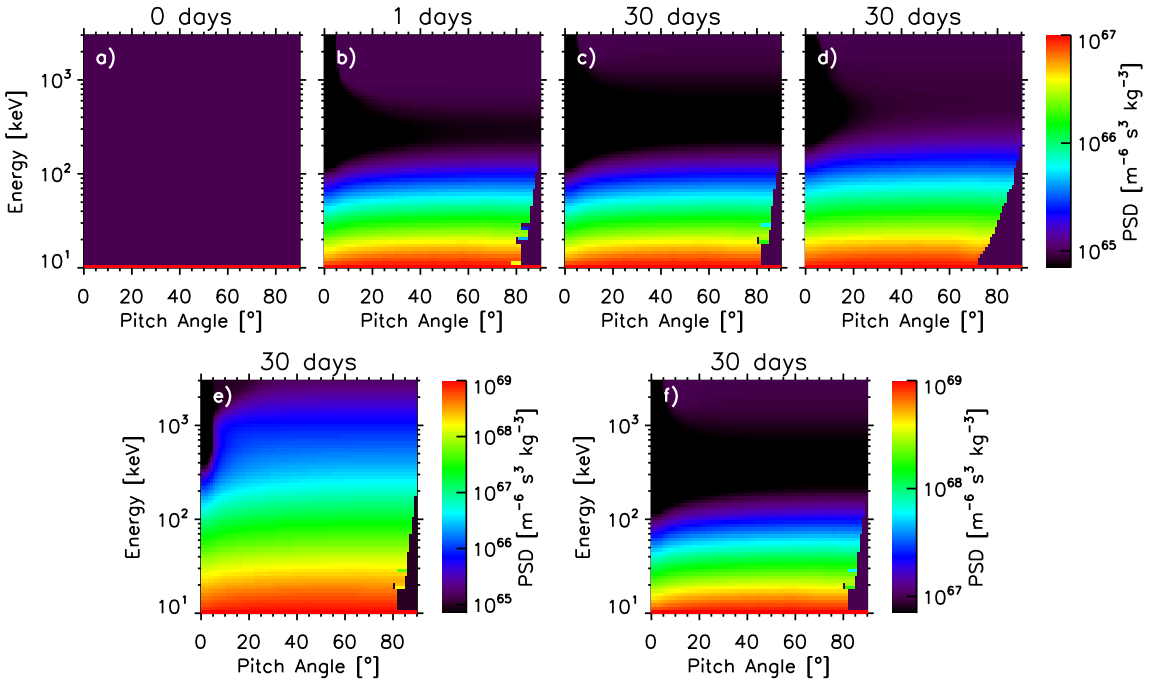

Figure 7.11 – Electron phase space density profiles resulting from idealised experiments with the 2-D BAS Radiation Belt Model. Chorus diffusion rates correspond to (b, c, e, and f) AE = 500 nT, or (d only) AE = 900 nT. Panel (a) shows the shape of the initial PSD distribution used for the model runs in (b - d). The resulting PSD is shown after (b) a day and (c) 30 days. Panel (d) shows how the initial PSD in (a) has changed after 30 days, using chorus diffusion coefficients set by a higher activity. In panels (e) and (f): the PSD on the LEB is a factor of 100 higher than in (b - d), and the 2D BAS-RBM was run for a 30 day period. The initial PSD, away from the LEB condition is a factor of 100 higher in (f) than (e).

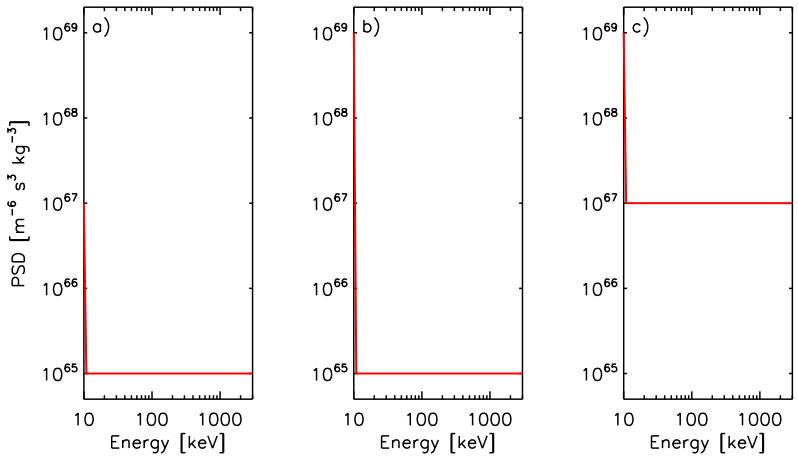

Figure 7.12 – The three different initial conditions used in Figure 7.11. The initial condition in panel (a) is used for the Figure 7.11a - d. The initial condition in panel (b) is used for Figure 7.11e and the initial condition in panel (c) for Figure 7.11f. All three initial conditions use isotropic PSD so that above profiles apply for all pitch angles.

preventing electrons from reaching >900 keV energies, or chorus diffusion was not effective up to 1 MeV for the selected activity. Examination of the chorus diffusion coefficients shows the later not to be the case (Horne et al., 2013). The chorus diffusion coefficients were increased to correspond to AE = 900 nT and the model run again for 30 days (Figure 7.11d). Even with larger chorus diffusion coefficients, the >1 MeV PSD still did not show an enhancement.

Figure 7.11e shows the result after running the 2-D BAS-RBM for 30 days with AE = 500 nT where the initial PSD profile was the same as shown in Figure 7.11a, but the PSD at the LEB was a factor of 100 higher. The new initial model setup is shown in Figure 7.12b. Now the 10 keV electrons *can* be accelerated up to >1 MeV energies by chorus waves at L^* = 4.5. In Figure 7.11f, the LEB condition was identical to that used in Figure 7.11e, but the initial PSD has been raised such that the PSD gradient at the LEB was the same as for Figure 7.11a-d (see Figure 7.12c). Once the PSD-energy gradient was reduced to previous levels, the >1 MeV electron flux did not show an enhancement after 30 days, even though the PSD level at 10 keV had not changed. It is therefore the gradient in the PSD-energy profile which is important for the >1 MeV enhancement rather than the level of the PSD on LEB. Increasing the size of PSD-energy gradients ($\frac{\partial f}{\partial E}$ in equation 2.26) increases the rate of energy diffusion, allowing energy diffusion to overcome losses and enable an increase in flux all the way up to a few MeV.

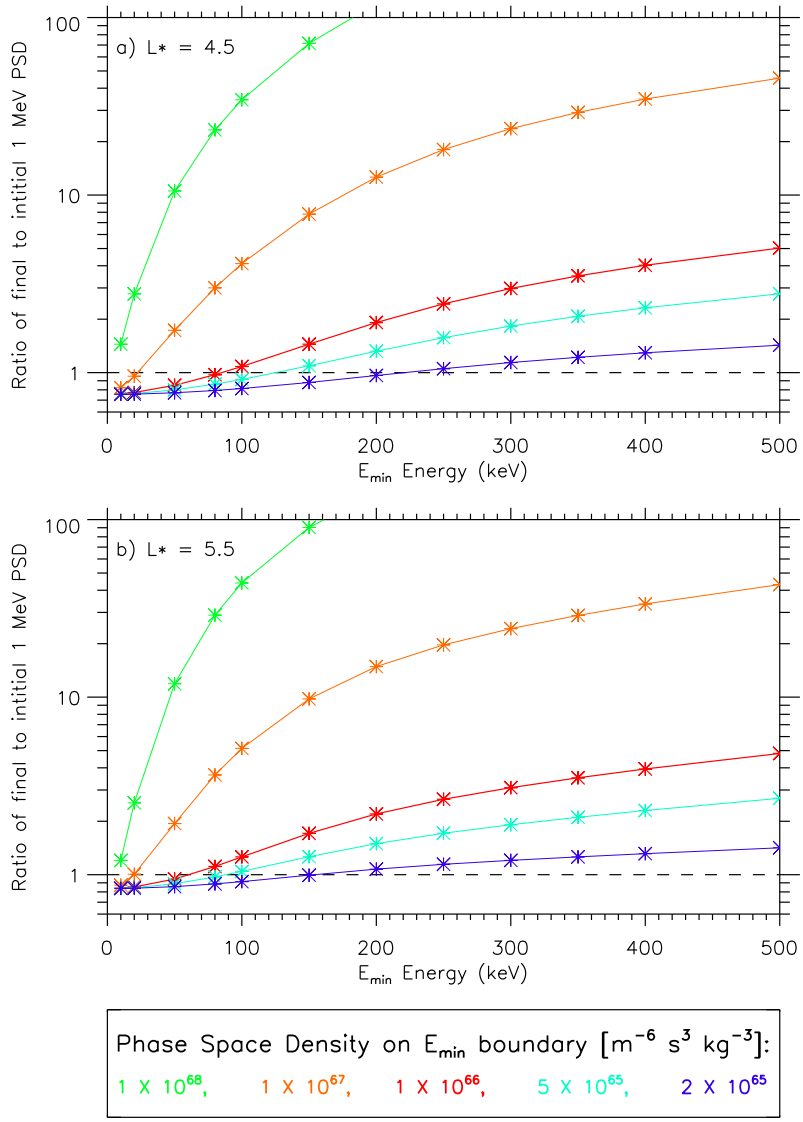

Figure 7.13 – Ratio between the final (after 30 days) and initial phase space density at 1 MeV, 90^o pitch angle plotted against the energy at which a phase space density enhancement, of various magnitudes (different colored lines), was supplied. Panel a) shows the results at L^* = 4.5 and panel b) at L^* = 5.5. A dashed line marks the ratio of one, separating the region where the final 1 MeV phase space density was enhanced from where it showed a net decrease. Away from the low energy boundary, the initial phase space density was set to 10^{65} $m^{-6}s^3kg^{-3}$ at all energies and pitch angles.

Energy diffusion by chorus waves is not effective at pitch angles near 90^o for $\leq$200 keV electrons (purple area on bottom right of Figure 7.11b-f), and as a result, the model gives large pitch angle gradients in this region. For the model results in Figure 7.11, these large negative pitch angle gradients cause diffusion towards 90^o, resulting in PSD enhancements at

high pitch angles not seen at lower energies. This is clearest in Figure 7.11e, where the PSD at 89^o is greater than initial levels for energies >200 keV, but for <200 keV, at this pitch angle the PSD has not increased from the initial condition.

Figure 7.13 considers a wider range of LEB values than Figure 7.11. Panel a shows the ratio at 1 MeV of the PSD after 30 days to the initial PSD, $\alpha = 90^o$, L^* = 4.5, for different minimum energies. For all model runs, and for the entire 30 day period, we use chorus diffusion coefficients corresponding to AE = 500 nT. A dashed line marks a ratio of 1, separating where the 1 MeV PSD has shown a net decrease after 30 days (<1) from where a net increase was observed (>1). When the LEB was set to 10 keV, an increase in the 1 MeV PSD level was only observed for a boundary PSD of 10^{68} $m^6 s^{-3} kg^{-3}$ (green curve), otherwise the ratio was less than 1. However, as the energy of the LEB condition was increased, a ratio greater than 1 could be obtained for smaller PSD values. Figure 7.13a therefore suggests that the 1 MeV population is sensitive to small PSD gradients at a few hundred keV. The electron energies that can be accelerated to 1 MeV are determined by the size of the enhancement and the resulting PSD-energy gradients.

Figure 7.13b shows the same results as Figure 7.13a, but at L^* = 5.5 instead of L^* = 4.5. Very similar trends are observed as seen in Figure 7.13a, however, for the same energy, moderately smaller PSD enhancements were required to achieve a 1 MeV enhancement. This suggests that, at larger L^*, chorus waves are better able to accelerate lower energy electrons to >1 MeV energies.

7.7 Importance of the PSD-Energy Gradients in the Radiation Belt Region

In the simulations presented in Section 7.6, there were initially no gradients in the PSD apart from at the LEB. To test the importance of initial gradients, Figure 7.14a presents two 2D BAS-RBM runs for L^* = 4.5, $\alpha = 85^o$, each starting with a different PSD distribution, one using a soft spectrum (red dotted line) and the other using a hard spectrum (blue dotted line). In both cases, the same PSD has been used on the LEB and isotropic pitch angle distributions assumed. Only chorus diffusion is included, and again, diffusion coefficients correspond to AE = 500 nT for both runs.

After an hour, the soft spectrum showed an increased PSD for energies ≤350 keV (red dashed line) while, over the same energy range, the PSD of the hard spectrum remained mostly the same as the initial configuration (blue dashed line). Following a day of chorus

activity, the soft spectrum (red thick line) showed an increased PSD for <400 keV, but slight PSD decrease at higher energies. In contrast, for the hard spectrum (blue thick line), the PSD has decreased for energies <500 keV but a small increase can be observed in the 500 keV to 1 MeV energy range. Ultimately, both starting PSD distributions evolve to the same steady state, showing the same final form after 30 days (thin red and blue line) and the 1 MeV PSD has decreased from initial levels.

For the hard spectrum, the initial gradients at ∼500 keV were such that chorus acceleration to ≥500 keV was faster than the rate of loss. However, as time passed and electrons around 500 keV were lost or accelerated, this gradient shallowed to the point that acceleration to ≥500 keV was no longer faster than the loss rate and the ∼500 keV to 1 MeV energy range ultimately experienced a net loss. Due to the initial PSD-energy gradients, the PSD profile evolved differently towards the same steady state form. In this case, whether the ∼500 keV to 1 MeV energy range showed an enhancement or a decrease depended on the initial PSD energy gradients as well as on the duration of the chorus wave activity.

Figure 7.14b again shows the evolution of both a hard and soft initial spectrum, but with larger PSD gradients than for Figure 7.14a (note different scale). The PSD profiles evolved at a faster rate than in Figure 7.14a for both initial distributions. In this case, the PSD at 1 MeV

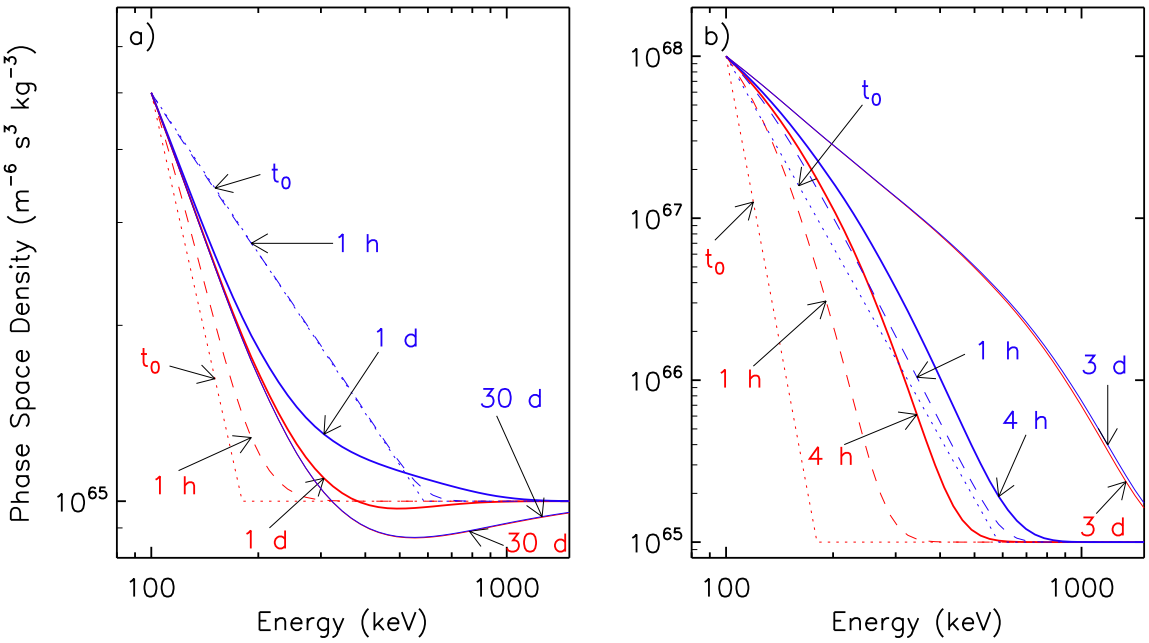

Figure 7.14 – The evolution of different phase space density distributions at $\alpha = 85^o$ in the 2-D BAS Radiation Belt Model, one shown in red the other in blue. Two different values for the low energy boundary phase space density at 100 keV were considered (panels a and b).

has increased by a factor of $\sim$7 in 3 days for both the hard and soft spectrum. The larger gradients in PSD cause the two spectra to tend to the same form more rapidly, and show similar PSD values, particularly for energies $<$800 keV, after 3 days of chorus wave activity.

7.8 Discussion

Previous work by Reeves et al. (2003) found that only about half of all storms increased the flux of relativistic electrons in the radiations belts. The remaining $\sim$50% either showed no change in the relativistic flux level, or a decrease. Local acceleration by whistler mode chorus waves is thought to be the dominant mechanism for most $>$1 MeV enhancements in the outer radiation belt region (Boyd et al., 2018). Chorus waves are known to cause both loss and acceleration (Horne et al., 2005a), and the balance between these two processes is therefore important for determining whether the relativistic electron flux will increase or decrease during a storm. The 2D BAS-RBM runs shown in Figure 7.14 demonstrated that, after one day, even with the same chorus diffusion coefficients and the same LEB condition, the phase space density of the $\sim$500 keV - 1 MeV electrons increased for the soft spectrum, but decreased for the hard spectrum. The pre-existing gradients in phase space density with energy were important for the rate of energy diffusion, and thus important to determine whether the rate of acceleration by chorus waves was faster than the rate of loss. This suggests that the state of the radiation belts prior to periods of high activity is an important factor to determine whether the relativistic flux level will be enhanced or decreased during an event.

In this chapter, we have shown a better agreement between the model and data when we include variations in the seed population (e.g. Figure 7.4). The results agree with Jaynes et al. (2015) who found that increases in both the source and seed populations were essential for $>$1 MeV flux enhancements, suggesting that a higher source population led to higher chorus wave power. However, Jaynes et al. (2015) drew their conclusions from interpreting observations, whereas here we have used a chorus wave model (Horne et al., 2013) and calculated the effect on the electron flux to show explicitly that the seed population increase was an important component leading to the second 1 MeV enhancement in the 21 April - 9 May 2013 period. Additionally, Figure 7.15 shows the 1 MeV, 90^o flux from the 3-D BAS-RBM for the studied period when the energy and pitch angle diffusion coefficients did not vary with time, instead set by the average value of AE. The left column of Figure 7.15 shows the model results using time-varying LEB conditions, while the right column shows the results using time-constant LEB conditions. Without the intensification of the chorus

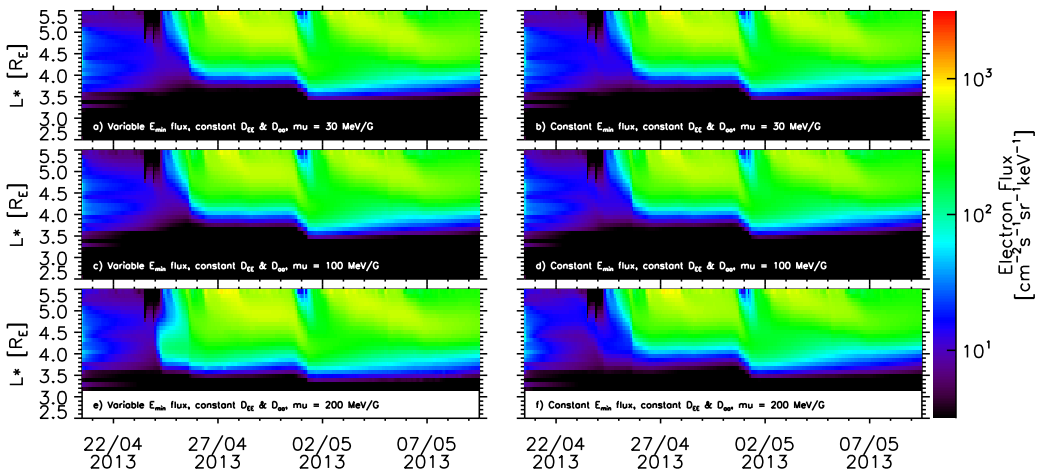

Figure 7.15 – The 1013.5 keV, 90^o electron flux from the 3-D BAS-RBM for the 21 April to 10 May 2013, using the average vale of AE for the period to set the values of $D_{\alpha\alpha}$ and D_{EE}. Panels a) and b) show the result using μ_{min} = 30 MeV/G time-varying and time-constant LEB conditions, respectively. Panels c) and d) show the same, but for μ_{min} = 100 MeV/G, as do panels e) and f) but for μ_{min} = 200 MeV/G. Note the colour scale used is the same as in Figures 7.2 and 7.4.

wave activity (captured by changes in the diffusion coefficients), the second enhancement event is again considerably lower than the Van Allen Probes observations (see Figure 7.2 or 7.4 which use the same colour scale as Figure 7.15) regardless of the LEB condition used. Figures 7.4 and 7.15 therefore show that increases in both the seed and chorus wave activity are required for the 1 MeV flux to be enhanced.

Using time-varying event-specific LEB conditions in the 3-D BAS-RBM allows the PSD on the LEB condition to decrease as well as increase. Considering Figure 7.9g, the data shows low flux over a range of energies at 2013-04-24 12:00:35 following a flux dropout (black symbols). Corresponding to this, the LEB condition was reduced, introducing positive gradients in the energy spectrum (black line). A decrease in the LEB may result in diffusion to lower energies, if chorus waves are present, reducing the PSD in the calculation. However, the agreement between model and data at subsequent times in Figure 7.9g was better than when using a constant LEB condition (Figure 7.9f). Additionally, Figures 7.4 and 7.8 show that larger 1 MeV flux values were produced when time varying LEB conditions were used, suggesting that the net effect was to increase the electron flux. It would therefore appear that possible PSD reductions only made a small contribution. This is likely because, generally, the low energy populations will decrease during quiet times, when diffusion coefficients are lower.

Whilst whistler mode chorus waves have been shown to be a particularly important acceleration mechanism (Bortnik et al., 2007; Horne and Thorne, 1998; Horne et al., 2005a,b; Summers et al., 1998; Thorne et al., 2005), other processes, such as radial diffusion, have a considerable impact on the radiation belt region (Shprits and Thorne, 2004; Su et al., 2010). The experiments with the 2-D BAS-RBM presented in Sections 7.6 and 7.7 were very idealised and provided an investigative tool in order to better understand the energy dynamics in the radiation belts, omitting radial diffusion. In reality, the standard picture is likely more of a three-step process, where the seed populations are enhanced, locally accelerated by chorus waves, and then redistributed by radial diffusion (e.g. Horne, 2007), further increasing the electron energy by inward motion (Boyd et al., 2014; Thorne et al., 2013b). As a result, radial diffusion of locally energized electrons to lower L^* values could produce >1 MeV electrons from the seed population enhancement, even if the PSD-energy gradients were not sufficient for local acceleration to >1 MeV energies from chorus waves alone.

Figures 7.4 and 7.11 demonstrated that PSD gradients introduced by enhancements in the LEB condition were important to determine whether the 1 MeV population was enhanced by chorus wave activity. We note that diffusion could drive variations in these gradients faster than the LEB condition is updated. By setting the LEB condition from observations, the update rate was limited by the orbital period of the satellite (satellites), in this case the Van Allen Probes. Future work will focus on using a data-driven LEB condition with a higher time resolution, such as those derived from low earth orbit observations (Allison et al., 2018) (see chapter 6), to better include changing PSD gradients and determine the effect on the model result.

The Van Allen Probes precess slowly in MLT, and therefore for a particular L^*, supply seed population observations localised in MLT. However, during active periods, as the dynamics of the lower energy populations are so affected by the convection electric field (Califf et al., 2017), the seed population can be highly MLT dependent (Allison et al., 2017), with higher flux in the dawn-sector than the dusk. Therefore, one would expect PSD gradients at seed population energies to also be higher on the dawn side of the Earth. Chorus waves are mainly observed in the night, dawn, and dayside MLT sectors (Meredith et al., 2012) and therefore the largest PSD gradients are likely to be present in regions of chorus wave propagation. Up-and-coming 4-D radiation belt models will allow for further exploration of MLT dependent PSD-energy gradients (Shprits et al., 2015).

7.9 Conclusions

Using the 3-D and 2-D BAS-RBM, the effect of changes in the seed population has been explored. Two enhancement events between the 21 April to 9 May 2013 period were studied using the 3-D model, where seed population enhancements were both included and excluded and the energies of the low energy boundary condition varied. Using the 2-D BAS-RBM, a number of idealised experiments were performed in order to better understand the effect of chorus waves on the seed population. The main conclusions are as follows:

1. The μ_{min} = 100 MeV/G time-varying low energy boundary condition resulted in better agreement with Van Allen Probes observations at 1 MeV than using a constant low energy boundary flux. The seed population enhancement was an important component to recreate the level of the 1 MeV following the 1 May 2013.

2. Contrary to expectation, raising the energies of the low energy boundary (μ_{min} = 200 MeV/G) led to lower flux at 1 MeV and a poorer agreement with data than using μ_{min} = 100 MeV/G. Reducing the energies of the low energy boundary (μ_{min} = 30 MeV/G) raised the flux at 1 MeV but, during active periods, produced a flux higher than observations across a broad range of energies.

3. Low energy enhancements change the PSD-energy gradients and can result in faster energy diffusion. Chorus waves cause both acceleration and loss and, at the lowest energies, there is a delicate balance between these two processes. Large enough PSD gradients in energy increase the rate of energy diffusion, and can therefore overcome the loss rate, allowing electrons to be accelerated to $\sim$1 MeV by chorus waves.

4. Using a constant low energy boundary condition and constant chorus diffusion coefficients, the PSD tended towards a steady state for either a hard or soft spectrum. However, the evolution was different, and therefore, the initial PSD-energy gradients prior to an event are very important in determining the response of the 1 MeV population.

The results presented in this chapter have highlighted the importance of gradients in the phase space density with energy. Considering the findings presented in chapter 5, these gradients may differ between the dawn and dusk MLT sectors during active times. For a more realistic analysis of radiation belt variability we should consider the different phase space density energy gradients.

Chapter 8

Summary and Further Work

8.1 Summary

Electrons covering a broad energy range are trapped on the terrestrial magnetic field, presenting a hazardous environment to satellites and humans in space. Electrons with energies of a few keV to a few hundred keV are supplied to the inner magnetosphere during active periods (Cayton et al., 1989; Kissinger et al., 2014; Li et al., 1998) and subsequently accelerated to much higher energies, forming the relativistic populations of Earth's outer radiation belt (Li et al., 2014; Thorne et al., 2013b). Relativistic electron enhancements occur via local acceleration from interactions with chorus waves (Horne and Thorne, 1998; Horne et al., 2005a; Li et al., 2014) and also by inward radial diffusion of a population at large L^* (Mann et al., 2016; Ozeke et al., 2019; Shprits et al., 2005). The occurrence of each of these processes, as well as the competition with loss mechanisms, accounts for much of the observed variability in the radiation belt electron flux during active times. Changes in the low energy seed population are also important to determine the outer radiation belt response. A number of observational studies have shown strong correlations between increases in the seed population and subsequent relativistic electron enhancements (Boyd et al., 2016; Foster et al., 2013; Jaynes et al., 2015; Li et al., 2005; Obara et al., 2000; Turner and Li, 2008), highlighting the need for further knowledge on the changes in the seed population and the effect on higher energy electron flux.

The research presented in the previous chapters explores the spatial and temporal variability of low energy electrons, and considers how changes in the flux at low energies ultimately affect the occurrence of relativistic electron enhancements. Firstly, we studied the energy dependence of the azimuthal structure of electron populations. As electron drift processes are energy dependent, different energy populations drift with different speeds and trajectories.

Crucially, at energies where the convection electric field dominates, electrons can be on open drift paths and lost to the magnetopause. As a result, asymmetries between the dawn and dusk side electron flux can exist in the radiation belt region. 3-D radiation belt models work on a drift-averaged approximation, which may not be applicable at low electron energies, where dawn - dusk flux asymmetries can occur. In chapter 5, a large dataset with an extensive L^* and MLT sampling was employed to study how the azimuthal structure of trapped electron populations changes with activity over three energy channels. 14 years of $>$30, $>$100, and $>$300 keV integral electron flux measurements from the POES constellation were ordered by MLT, L^* and by six levels of activity defined by various metrics. Significant dawn-dusk flux asymmetries were not observed for the lower levels of activity for any of the electron energy ranges considered. However, at higher activities, both the $>$30 keV and $>$100 keV flux showed an increase in the dawn sector that was not present on the dusk side, likely resulting from open drift paths driven by an enhanced convection electric field. The $>$300 keV flux also showed asymmetries for the highest two activity levels but it is unlikely that enhanced convection alone is sufficient to explain the MLT differences. For $\sim$300 keV electrons, the MLT distribution observed during active periods is likely the result of a combination of losses to the magnetopause from radial transport and magnetopause shadowing, and particle injections from diplorisation fronts.

The results from chapter 5 highlight that, during active periods, $\lesssim$300 keV electron flux measurements should only be considered representative of the MLT sector where the observation was made. However, 60% of the time, electron populations with energies $\gtrsim$30 keV can be considered to be azimuthally symmetric in the outer radiation belt as, during quieter times, the convection electric field strength is not sufficient to perturb $>$30 keV electrons onto open drift paths.

The POES dataset, used in chapter 5, provides excellent MLT and L^* resolution and covers periods back to 1998. A novel method was developed in chapter 6 to make use of this extensive radiation belt and MLT coverage for low energy boundary conditions in radiation belt models. Chaper 5 demonstrated that low energy flux enhancements can be transient and MLT-localised, therefore a dataset with a good temporal and spatial resolution is particularly useful for low energy boundary conditions. To use POES low Earth orbit measurements of integral electron flux for the low energy boundary of the radiation belt models, the low equatorial pitch angle data was first converted to omnidirectional integral flux by assuming a form for the pitch angle distribution given by L^* and Kp parametrised Van Allen Probe data. Two methods were explored for the retrieval of a differential flux distribution, using both the AE9 design model and a iterative fitting approach. Finally, the omnidirectional

differential flux spectrum was converted to 90^o directional flux using pitch angle distributions again given by parametrised Van Allen Probes measurements. The results were compared to MagEIS observations and, on average, differed by less than a factor of 4 for $L^* \gtrsim 3.7$, excluding periods of s-shaped energy spectra. Using the POES data for the low energy boundary condition of the BAS-RBM showed very similar results for June 2013 as using the Van Allen Probes data for the boundary. The developed method may be used to form realistic event specific low energy boundary conditions when Van Allen Probe data is unavailable. This would include events prior to September 2012 or, as the Van Allen Probes mission is set to end in 2020, for modelling periods after this date.

The final part of this thesis considered the effect of changes in the seed population on 1 MeV electrons in Radiation Belt Models. Despite a number of studies demonstrating correlations between the observed seed and core populations (e.g. Boyd et al., 2016; Tang et al., 2017; Turner and Li, 2008), the effect of seed population enhancements in radiation belt models had previously been limited to just two studies that provided conflicting results. Subbotin et al. (2011a) found that the flux of 1 MeV electrons from VERB-3D was relatively insensitive to the flux at low values of μ. Conversely, Tu et al. (2014) showed that an observed enhancement in the PSD at μ = 1279 MeV/G was only reproduced by the DREAM-3D model when increases in the seed population were included. Hence, in chapter 7 of this thesis, the 3D BAS-RBM was used to study two 1 MeV flux enhancements between the 21 April to 9 May 2013. Constant and time-varying low energy boundary conditions were employed and the seed population enhancement found to be an important component to recreate the observed level of the 1 MeV flux for the second enhancement, but had less of an effect for the first. Therefore, in the BAS-RBM simulations, the first enhancement reflected the results of Subbotin et al. (2011a) and the second agreed with Tu et al. (2014). Further analysis in chapter 7 used the 2-D BAS-RBM to demonstrate that the response of the 1 MeV population was dependent on the PSD-energy gradients introduced by enhancements in the seed population. Low energy electron enhancements change the PSD-energy gradients and can result in faster energy diffusion. Chorus waves cause both acceleration and loss, and for seed population energies, there is a delicate balance between these two processes. By increasing the PSD-energy gradients, the rate of loss is overcome, and electrons can be accelerated to $\sim$1 MeV by chorus waves.

Furthermore, in chapter 7 two model runs, using the same low energy boundary condition and chorus diffusion coefficients, showed different results after a day due purely to the initial PSD-energy gradients present. The PSD in the $\sim$500 keV - 1 MeV range increased for the soft spectrum and decreased for the hard spectrum. Previously, Reeves et al. (2003) found

that only ∼50% of storms increased the flux of relativistic electrons in the radiation belts and Boyd et al. (2018) demonstrates that acceleration by chorus waves is likely the dominant mechanism for most >1 MeV enhancements in the outer radiation belt region. The model results presented in chapter 7 suggest that the state of the radiation belts prior to periods of high activity can determine whether the relativistic flux level will be enhanced or decreased by chorus waves during an event. As such, pre-existing energy gradients in PSD may partially account for why not all storms increase the relativistic electron flux.

8.2 Suggestions for Further Work

The results presented on the MLT distribution of low energy electrons and the importance of PSD-energy gradients for 1 MeV flux enhancements highlight some further questions and avenues for research. Additionally, a method for obtaining the equatorial differential flux from low Earth orbit POES observations has been developed. This can be used to develop a low energy boundary condition for radiation belt models outside of the Van Allen probes era, and provides better temporal and spatial coverage than Van Allen Probes. Here, a number of additional studies that continue or expand on the research presented in this thesis are described.

Analysis of the MLT distribution of various electron populations performed in chapter 5 highlights that during periods of high activity, ∼30 keV and ∼100 keV electrons tend to be on open drift paths. However, the statistical survey only considers flux for various activity levels, and does not directly show the evolution of the MLT distribution in time. A superposed epoch analysis could be performed on the POES dataset to study time variations in the MLT structure further. As in chapter 5 the largest MLT asymmetries were observed when the AE index was used to define the levels of activity, an increase in AE by a selected amount could be used to define the zero epoch. Analysing the POES dataset in this manner should demonstrate whether the enhanced low energy populations are truly transient, or whether propagation does continue onto the dusk side as activity, and the convection electric field, dies away. If the supplied seed population is largely transient, we are left with the question of whether chorus waves accelerate this population to energies that would be on closed drift paths faster than the travel time to the magnetopause. The later could be investigated using a chorus diffusion matrix (Horne et al., 2013) and the 2-D BAS-RBM (Horne et al., 2018).

In chapter 5, magnetopause shadowing was considered as a mechanism which may result in MLT asymmetries in the >300 keV electron flux. Figure 5.11 showed a transient population outside of the last closed drift shell on the dawn side of the Earth that was not

present on the dusk side. For dusk sector MLT values, the flux remained low for all six activity levels. It is conceivable that the electron flux may show a L^* gradient in the dusk sector relating to the last closed drift shell. The POES satellites are in a polar orbit, and so measure electrons out to the last closed drift shell and beyond. The POES dusk side flux observations could therefore be used to determine the last closed drift shell value by identification of flux gradients. Further work could investigate this suggestion and potentially develop a method for L^*_{LCDS} retrieval. Recent work has highlighted the importance of the last closed drift shell value in modelling the radiation belts during storm times (Olifer et al., 2018). A last closed drift shell derived from data, as opposed to an assumed magnetic field model, would provide an L^*_{LCDS} value which could be supplied to radiation belt models to aid simulation and understanding during dropout periods.

A novel method for determining the equatorial differential flux from POES observations was presented in chapter 6. One of the benefits of using the POES data as a low energy boundary condition is that the seed population at L^* values out to the last closed drift shell can be included in the simulation. Following the approach by Glauert et al. (2014a), the PSD on the outer boundary condition (where $L^*_{max} = 10$) could be set to zero, simulating total loss to the magnetopause. By doing so, Glauert et al. (2014a) showed that 3 MeV enhancements could be achieved purely by acceleration of the $\sim$150 keV electron populations on the low energy boundary. Further work could use the POES low energy boundary condition to expand on the work of Glauert et al. (2014a), aiming to recreate the observed rebuilding of the radiation belts following a selected dropout event, purely from the acceleration of the seed population. Acceleration by radial diffusion requires a population at the edge of the outer radiation belt to be diffused inwards (Mann et al., 2016). The formation of this population from the seed population could be studied by simulating the whole of the radiation belt region. Additionally, the role of local acceleration throughout the outer belt could be considered. Modelling the creation of the radiation belts purely from acceleration of the seed population, allows our current understanding for how the radiation belts are formed to be examined. If the model result is significantly lower than observations then additional source or acceleration processes are likely.

In addition to its broad L^* range, the POES low energy boundary method provides better MLT coverage and more frequently samples across the radiation belt region than the Van Allen Probes. Horne et al. (2018) suggested that continuous substorm activity may be driven by fast solar wind streams and act to 'pump-up' the radiation belts by supplying source and seed electrons, fueling chorus waves and resulting in acceleration. During a fast solar wind stream, comparing MagEIS data when Van Allen Probes are primarily in the dusk

sector, to the POES differential flux in the dawn sector may provide an indication of whether short lived seed population enhancements are not sampled by the Van Allen Probes due to the MLT limitation and orbit period. If short lived seed population enhancements were present in the dusk side Van Allen Probes measurements, then time differences between the observations from dawn side POES and dusk side Van Allen Probes could be considered. As the results presented in chapter 7 highlight the importance of PSD-energy gradients for flux enhancements, short lived seed population increases from repeated substorm activity may be important for >1 MeV enhancements. To test this, a model run using the POES low energy boundary condition could be compared to one using the Van Allen Probes low energy boundary for a fast solar wind stream event.

Previous work by Boyd et al. (2016) showed observational evidence for a seed population PSD threshold necessary for >1 MeV enhancements. Chapter 7 demonstrates that it is the energy gradients in PSD that are crucial for 1 MeV enhancements rather than the level of the seed population itself. However, the threshold shown by Boyd et al. (2016) may suggest something about the PSD level before a core population increase. An obvious avenue for further work here is to consider the PSD-energy gradients for a number of events in a statistical sense using Van Allen Probes data. As discussed in chapter 4, the Van Allen Probes MagEIS instrument measures the differential electron flux in a number of energy channels, primarily sampling energies from ∼30 keV to 1.5 MeV. A field model could be used to convert these flux values to PSD in order to study the energy gradients present before, during, and after core population enhancements.

3-D radiation belt models, like the BAS-RBM used in this thesis, do not have a source term in the model equation. As a result, PSD is only added to the calculation via the boundary conditions. However, for the low energy boundary, this corresponds to a single energy at each L^* value. In reality, substorm injections or enhanced convection will likely lead to an increased PSD over a range of seed population energies at the same L^* rather than just at a single energy. The model relies on diffusion to transfer any enhancement at the low energy boundary to higher energies, but this will obviously be subject to a time delay and may not introduce the same PSD gradients as observed. In chapter 7 the importance of PSD gradients for radiation belt enhancements was explored. Figure 7.14 demonstrates that hard and soft energy spectra will evolve to the same steady state solution via different paths, whereby, the PSD for some energy ranges may initially increase for the hard spectrum while decreasing for the soft. Due to the constantly changing environment of the radiation belts, a steady state is unlikely, and as a result, the PSD variations will depend on the initial PSD-energy gradients. In order to correctly include those gradients, a source term is required in the model equation.

Further work could focus on studying Van Allen Probes data to look for dispersionless injections in the electron flux in order to better quantify the energy range supplied to the radiation belts. Following a statistical survey, an activity dependent parametrisation could be adopted for the energy width and shape of the source term. The effect of including a source term in the model could then be investigated for a number of events.

Appendix A

POES Trapped, Drift Loss Cone, and Bounce Loss Cone Observations

POES are low earth orbit satellites and observe electrons with low equatorial pitch angles. In this appendix we perform a pitch angle analysis of the POES data to determine whether trapped, bounce loss cone, or drift loss cone flux is observed.

Local Pitch Angle

As the POES satellites orbit around the Earth in the manner described in chapter 4, the angle between the aperture of the T0 and T90 detectors and the local magnetic field changes. As a result, the particle pitch angles measured throughout the orbit also vary and, consequently, the spacecraft can observe trapped, transient, or precipitating populations, or a mixture of all three. Additionally, Earth's magnetic field exhibits variations with magnetic longitude, and the observed particle pitch angle will vary as the POES satellite samples over different regions of the Earth.

Figure A.1 shows the local pitch angles observed by the T0 (blue) and T90 (red) detectors for different magnetic longitudes at $L^* = 4$. The centre field-of-view for each telescope is shown as a dashed black line and the respective coloured region accounts for the width of the opening angle of the detector. The black solid line marks the local loss cone pitch angle, $\alpha_{LClocal}$, calculated using the IGRF magnetic field model (Thébault et al., 2015) using:

$$\alpha_{LClocal} = \sin^{-1}\sqrt{\frac{B_{loc}}{B_{100}}}. \tag{A.1}$$

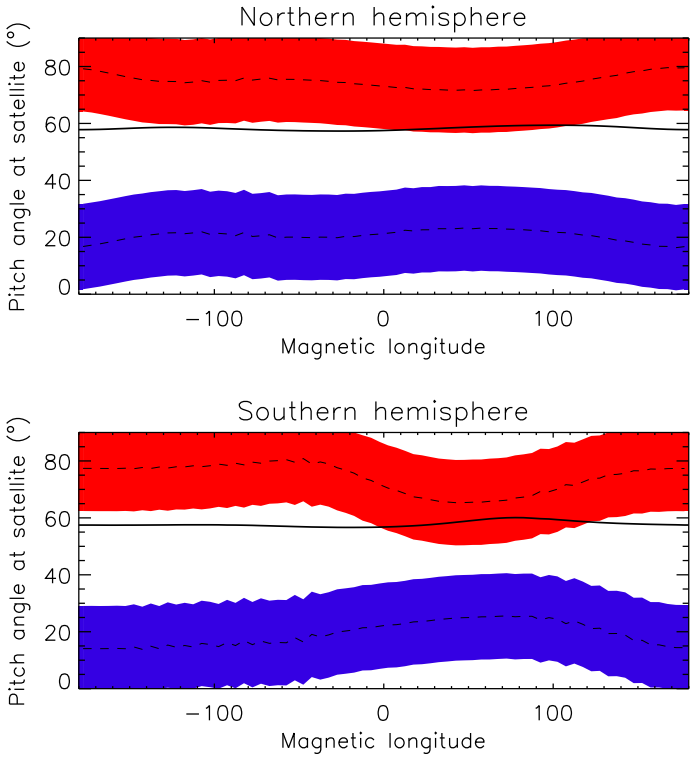

Figure A.1 – Local pitch angle range observed by the T0 detector (blue) and T90 detector (red) on the NOAA15 satellite at $L^* = 4$,for the northern (top) and southern (bottom) hemisphere. The local loss cone angle is shown as a solid black line and the centre field-of-view pitch angle for each detector shown as a dashed line. Constructed from January - April 2000 data.

Here B_{loc} is the local field strength at the satellite and B_{100} is the magnetic field strength at 100 km altitude. Below 100 km it is assumed that particles will be lost to the atmosphere. Electrons with pitch angles lower than the black line in Figure A.1 are in the local loss cone.

At all magnetic longitudes in both the northern and southern hemisphere, T0 observes electrons in the bounce loss cone. T90, on the other hand, generally observes electrons with pitch angles greater than the local loss cone. At all magnetic longitudes, the centre field-of-view pitch angle for the T90 detector is outside of the bounce loss cone in both hemispheres. However, a fraction of the T90 viewing angle does lie inside the bounce loss cone for magnetic longitudes approximately in the 0^o - 100^o range, for both the northern and southern hemisphere.

Analysis of the local pitch angle shows where the POES satellites observe electrons inside the bounce loss cone, but does not indicate whether electrons may be in the drift loss cone (see section 1.5.3.1). To determine this, the equatorial pitch angles need to be studied.

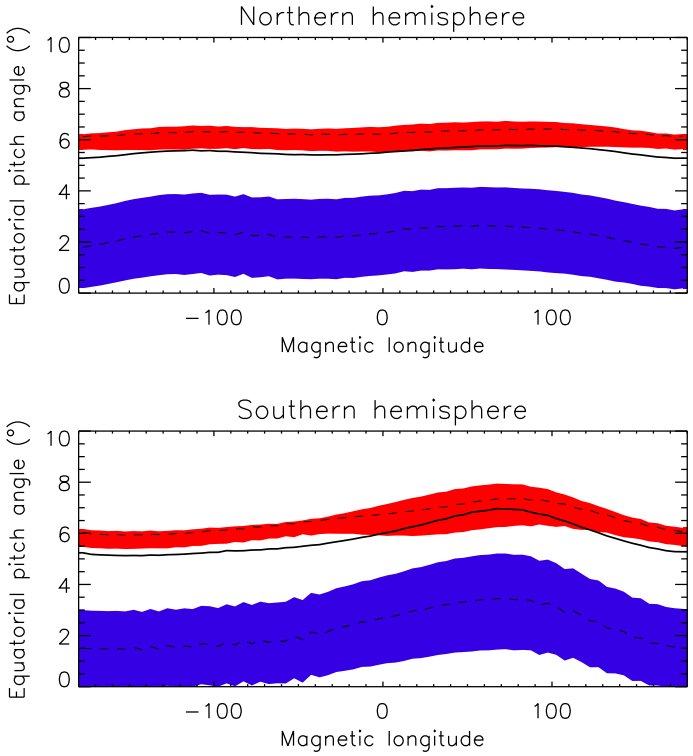

Figure A.2 – Equatorial pitch angles observed by the T0 (blue) and T90 (red) detector on the NOAA15 satellite at $L^* = 4$,for the northern (top) and southern (bottom) hemisphere. The equatorial loss cone angle is shown as a solid black line and the centre field-of-view equatorial pitch angle for each detector shown as a dashed line. Constructed from January - April 2000 data.

Equatorial Pitch Angle

Figure A.2 shows the equatorial pitch angles observed by T0 (blue) and T90 (red) for $L^* = 4$. Again, the equatorial pitch angle of the loss cone at each magnetic longitude was computed using the IGRF field (following the approach by Rodger et al. (2010a)).

Figure A.2 reiterates the information shown by Figure A.1, demonstrating that T0 observes flux entirely in the bounce loss cone and showing that part of the viewing angle of T90 is also in the bounce loss cone for $\sim 0^o$ to $\sim 100^o$ magnetic longitude. However, unlike in Figure A.1, also shown is the loss cone enlargement over the South Atlantic Anomaly (SAA) region in the southern hemisphere. As the magnetic field is weaker over this magnetic longitude range, particles which, away from the SAA, would have mirrored above the POES satellite orbit now have to penetrate down to lower altitudes in order to undergo magnetic mirroring. Consequently, POES observes electrons with larger equatorial pitch angles over this region, as shown in the southern hemisphere panel of Figure A.2.

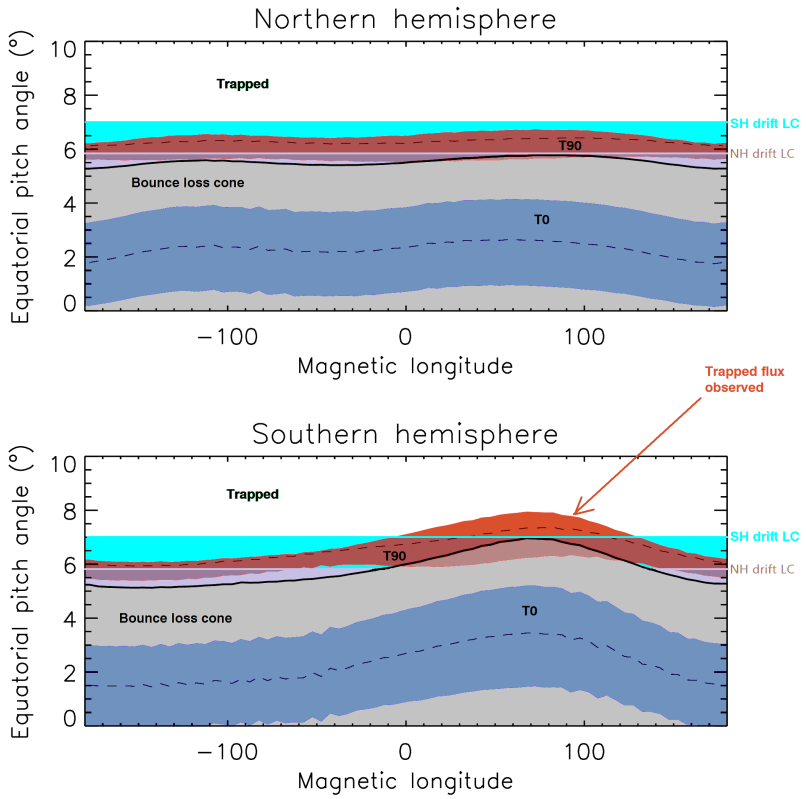

Figure A.3 – Equatorial electron pitch angles sampled by the T0 (blue) and T90 (red) detectors of NOAA15. The equatorial bounce loss cone angle is shown as a solid black line and electrons in the bounce loss cone shaded in grey. The drift loss cone angle in the northern hemisphere is marked as a lilac line (labelled NH drift LC) and electrons with pitch angles between the bounce loss cone and the northern hemisphere drift loss cone shaded in lilac. The southern hemisphere drift loss cone is shown in cyan and pitch angles between this and the northern hemisphere drift loss cone shaded in cyan. Electrons with pitch angles above the southern drift loss cone are likely stably trapped. Constructed from January - April 2000 data.

The equatorial drift loss cone angle for a particular hemisphere is the maximum equatorial bounce loss cone pitch angle across all magnetic longitudes at that L^*. Note that treating electrons with pitch angles less than this value as drift loss cone observations is only an approximation as, while at one location an electron may look to be in the drift loss cone for a particular L^*, the electron equatorial pitch angle changes throughout the drift and, over the loss region, the pitch angle may in fact be different.

The drift loss cone angle is marked on Figure A.3 as cyan for the southern hemisphere and lilac for the northern hemisphere. While a particle may not be in the drift loss cone in the hemisphere in which it is observed, it could still be in the drift loss cone for the opposite

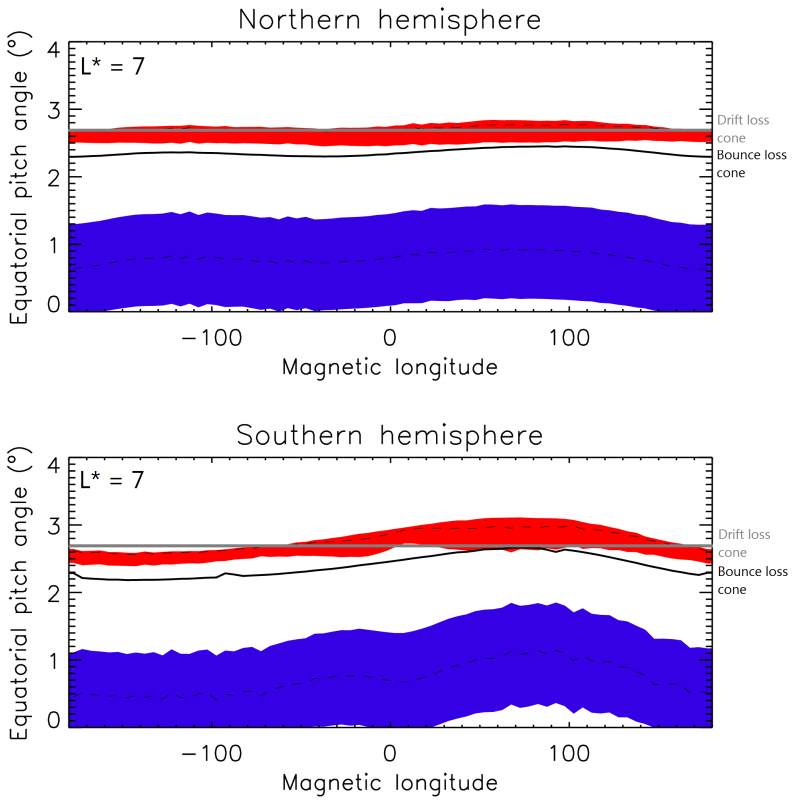

Figure A.4 – Equatorial pitch angles for the T0 (blue) and T90 (red) detectors of NOAA15 at L^* = 7 in both the Northern and Southern hemisphere. The bounce loss cone is shown as the solid black line and the drift loss cone as the grey line. Constructed from January - April 2000 data.

hemisphere as the electron bounce period is considerably less than the drift period. As such, the drift loss cone angle is defined as whichever is larger, the northern or southern hemisphere drift loss cone.

Various populations are marked in Figure A.3. Electrons with pitch angles below the thick black line (grey shaded region) are in the bounce loss cone. Above the bounce loss cone (black line), but below the northern hemisphere drift loss cone angle (lilac line), electrons are likely in the drift loss cone in the northern hemisphere. In the case shown in Figure A.3, the southern hemisphere drift loss cone angle is greater than for the northern hemisphere, and so the electrons with pitch angles less than the cyan line are inside the drift loss cone. Above the cyan line of the southern hemisphere drift loss cone, electrons are trapped (white region). Notice that at L^* = 4.0 the T90 detector of NOAA15 only observes trapped electron in the southern hemisphere over a limited longitude range, otherwise mostly sampling the drift loss cone.

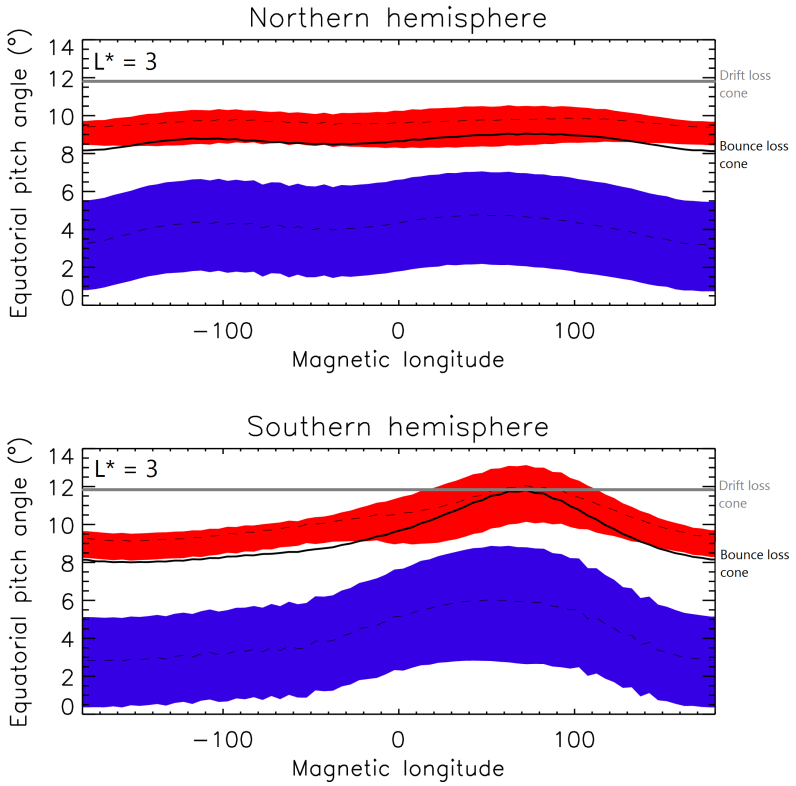

Figure A.5 – Equatorial pitch angle for the T0 (blue) and T90 (red) detectors of NOAA15 at L^* = 3 for both the Northern and Southern hemisphere. The bounce loss cone is shown as the solid black line and the drift loss cone as the grey line. Constructed from January - April 2000 data.

While the small range of magnetic longitude over which NOAA15 measures trapped electron flux[1] may look to be extremely limited at L^* = 4, when data from multiple spacecraft are combined, the POES satellites still provide very good coverage of the trapped radiation belt population. Due to the ∼100 minute orbit, each satellite samples L^* = 4 multiple times over the correct magnetic longitude range.

At different L^* values

In the previous two sections, only L^* = 4 was shown. Figure A.4 shows the equatorial pitch angles observed by NOAA15 T0 (blue) and T90 (red) for L^* = 7. At larger L^* values, the centre angle of the field-of-view T90 detector is locally closer to 90^o. Additionally, the influence of the SAA reduces at larger L^* and so the southern hemisphere drift loss cone value

[1] Very similar magnetic longitude ranges apply for the other POES satellites

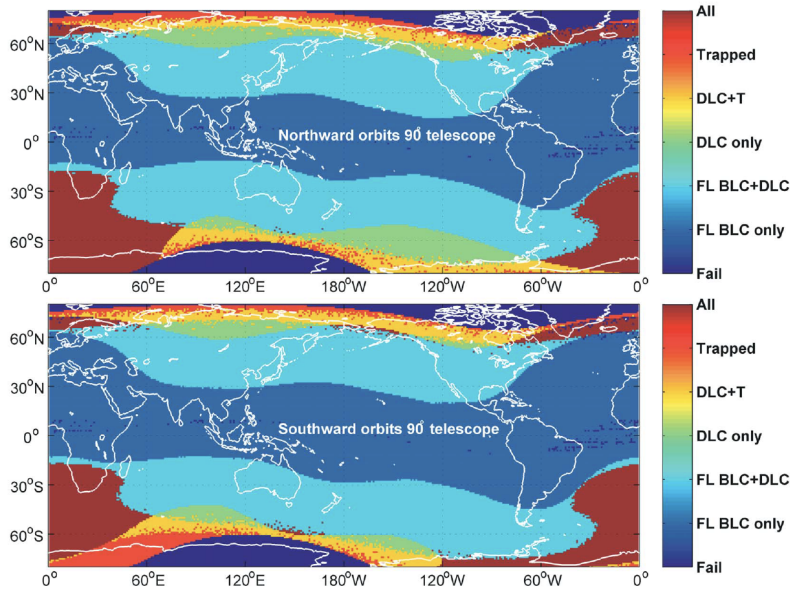

Figure A.6 – Figure from Rodger et al. (2010a). Various electron populations measured by the T90 detector on POES. Here "T" indicates trapped flux, "DLC" is drift loss cone, and "FL BLC" is field line bounce loss cone.

decreases. As a result, POES measures trapped electron populations over a broader range of magnetic longitudes, and begins to observe trapped electrons in the northern hemisphere as well as the southern. Figure A.6 by Rodger et al. (2010a), also demonstrates that at higher latitudes, more trapped electrons are observed.

At lower L^*, the opposite is true. Figure A.5 shows the NOAA15 T0 and T90 equatorial pitch angles at $L^* = 3$. At this L^*, there is a larger increase in bounce loss cone over the SAA region than shown by Figures A.2 and A.4, increasing the drift loss cone. The range of magnetic longitude over which trapped electrons are observed narrows.

For $L^* \lesssim 2.0$, T90 mostly observes electrons in the drift and bounce loss cone. However, at low latitudes, the local angle of the T0 detector is such that, over some magnetic longitudes, trapped populations are measured. This was also found by Rodger et al. (2010b), as shown in Figure A.7. T0 typically observes trapped electrons for $L^* \lesssim 1.5$ and, as a result, there is a small L^* range where the centre angle of the field-of-view for both T0 and T90 is not in the trapped pitch angle range. This accounts for the small ring of missing data between $1.5 < L^* < 2.0$ in Figure 5.3.

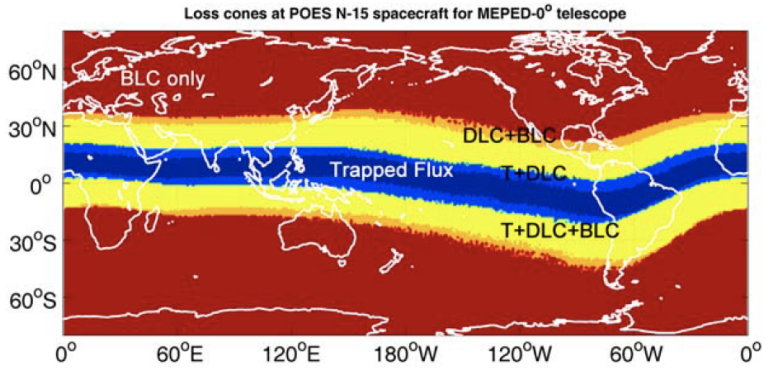

Figure A.7 – Figure from Rodger et al. (2010b). Various populations observed by the T0 detector on NOAA15. Here T indicates trapped flux, DLC is drift-loss cone, and BLC is bounce loss cone.

Data processing

As the drift loss cone angle will always be greater than or equal to the bounce loss cone, the drift loss cone angle was calculated for each L^* between L^* = 1.1 and L^* = 8.0, in steps of 0.1 L^*. The approach of Rodger et al. (2010a) was followed, using the IGRF field model. The pitch angles of every POES measurement were then compared to the drift loss cone value to determine whether the observation was trapped.

For the study in chapter 5, considering the MLT distributions of electrons at different energies, the above analysis was used to isolate measurements where the centre-field of view angle (dashed line in Figure A.2) was outside the drift loss cone. Figure A.8 shows the average of the flux measurements from NOAA15, 16, 17, 18, 19, and MetOp02 taken during 2009 for the same L^*-MLT bins used in chapter 5. The left hand column shows the averaged T90 data while the right hand column shows the average T90 and T0 measurements where the centre axis of the field-of-view lay outside the drift and bounce loss cone. The average of the trapped flux (right column) tends to be higher than the average of the unselected T90 flux, particularly in the inner belt region where we find that T90 often observes flux in the drift and bounce loss cone (see Figure A.5).

For the work presented in chapter 6, developing a method to formulate a low energy boundary condition from the POES dataset, the above analysis was used to determine the fraction of the field-of-view observing trapped flux shown in Figure 6.1. Data points where POES measured less than 20% trapped electrons were omitted, otherwise a correction was applied to account for the fact that only part of the telescope field-of-view was sampling trapped flux, yet the count measurement was divided by the full opening angle.

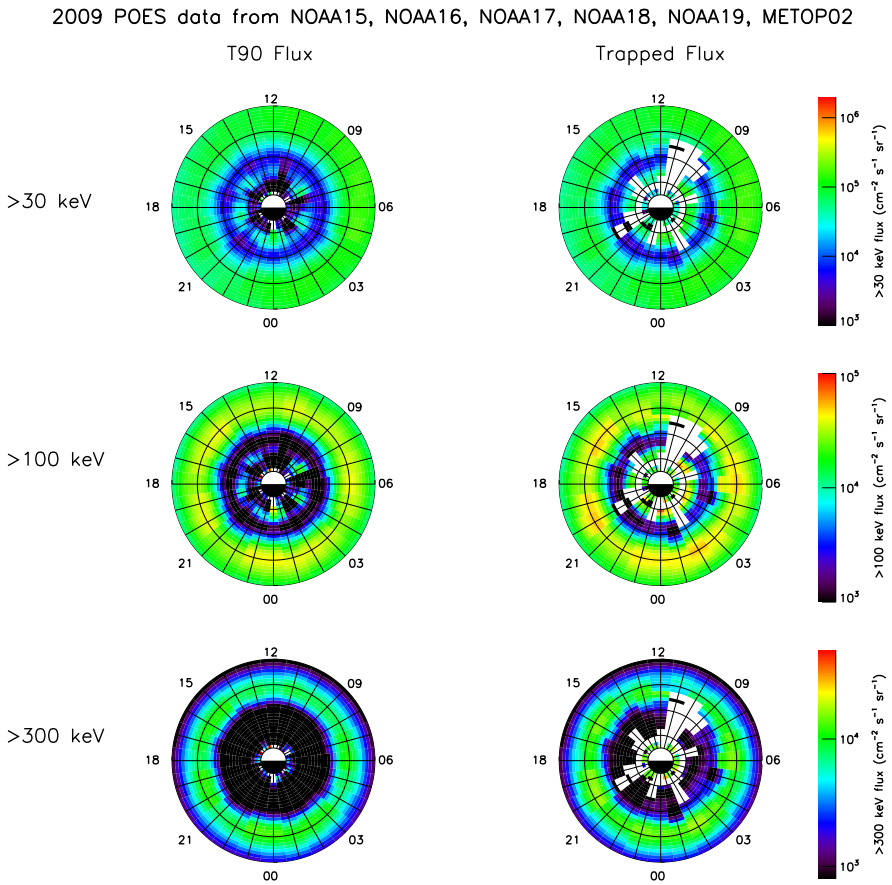

Figure A.8 – Mean T90 flux (left column) and mean of the flux measurements with the centre axis of the field-of-view outside the drift and bounce loss cones (right column) for each MLT-L^* bin. Data from NOAA15, 16, 17, 18, 19, and MetOp02 taken in 2009 has been used to construct the Figure. The plots extend out to $L^* = 8$ and markers denote the $L^* = 2$, 4, and 6 positions.

References

Abel, B. and Thorne, R. M. (1998). Electron scattering loss in Earth's inner magnetosphere: 1. Dominant physical processes. *Journal of Geophysical Research: Space Physics*, 103(A2):2385–2396. **doi:** 10.1029/97JA02919.

Akasofu, S.-I. (1964). The development of the auroral substorm. *Planetary and Space Science*, 12(4):273 – 282. **doi:** 10.1016/0032-0633(64)90151-5.

Albert, J. M. (2003). Evaluation of quasi-linear diffusion coefficients for EMIC waves in a multispecies plasma. *Journal of Geophysical Research: Space Physics*, 108(A6):1249. **doi:** 10.1029/2002JA009792.

Albert, J. M., Meredith, N. P., and Horne, R. B. (2009). Three-dimensional diffusion simulation of outer radiation belt electrons during the 9 October 1990 magnetic storm. *Journal of Geophysical Research: Space Physics*, 114(A9):A09214. **doi:** 10.1029/2009JA014336.

Albert, J. M., Starks, M. J., Horne, R. B., Meredith, N. P., and Glauert, S. A. (2017). Quasi-linear simulations of inner radiation belt electron pitch angle and energy distributions. *Geophysical Research Letters*, 43(6):2381–2388. **doi:** 10.1002/2016GL067938.

Albert, J. M. and Young, S. L. (2005). Multidimensional quasi-linear diffusion of radiation belt electrons. *Geophysical Research Letters*, 32(14):L14110. **doi:** 10.1029/2005GL023191.

Allison, H. J., Horne, R. B., Glauert, S. A., and Del Zanna, G. (2017). The magnetic local time distribution of energetic electrons in the radiation belt region. *Journal of Geophysical Research: Space Physics*, 122(8):8108–8123. **doi:** 10.1002/2017JA024084.

Allison, H. J., Horne, R. B., Glauert, S. A., and Del Zanna, G. (2018). Determination of the equatorial electron differential flux from observations at low earth orbit. *Journal of Geophysical Research: Space Physics*, 123(11):9574–9596. **doi:** 10.1029/2018JA025786.

Andre, M. (1985). Dispersion surfaces. *Journal of Plasma Physics*, 33(1):1–19. **doi:** 10.1017/S0022377800002270.

Arnoldy, R. L. and Chan, K. W. (1969). Particle substorms observed at the geostationary orbit. *Journal of Geophysical Research*, 74(21):5019–5028. **doi:** 10.1029/JA074i021p05019.

Baker, D. N., Blake, J. B., Callis, L. B., Belian, R. D., and Cayton, T. E. (1989). Relativistic electrons near geostationary orbit: Evidence for internal magnetospheric acceleration. *Geophysical Research Letters*, 16(6):559–562. **doi:** 10.1029/GL016i006p00559.

Baker, D. N., Blake, J. B., Klebesadel, R. W., and Higbie, P. R. (1986). Highly relativistic electrons in the Earth's outer magnetosphere: 1. Lifetimes and temporal history 1979–1984. *Journal of Geophysical Research: Space Physics*, 91(A4):4265–4276. **doi:** 10.1029/JA091iA04p04265.

Baker, D. N., Higbie, P. R., Belian, R. D., and Hones Jr., E. W. (1979). Do Jovian electrons influence the terrestrial outer radiation zone? *Geophysical Research Letters*, 6(6):531–534. **doi:** 10.1029/GL006i006p00531.

Baker, D. N., Jaynes, A. N., Li, X., Henderson, M. G., Kanekal, S. G., Reeves, G. D., Spence, H. E., Claudepierre, S. G., Fennell, J. F., Hudson, M. K., Thorne, R. M., Foster, J. C., Erickson, P. J., Malaspina, D. M., Wygant, J. R., Boyd, A., Kletzing, C. A., Drozdov, A., and Shprits, Y. Y. (2014). Gradual diffusion and punctuated phase space density enhancements of highly relativistic electrons: Van Allen Probes observations. *Geophysical Research Letters*, 41(5):1351–1358. **doi:** 10.1002/2013GL058942.

Baker, D. N., Kanekal, S. G., Horne, R. B., Meredith, N. P., and Glauert, S. A. (2007). Low-altitude measurements of 2 - 6 MeV electron trapping lifetimes at $1.5 < L < 2.5$. *Geophysical Research Letters*, 34(20):L20110. **doi:** 10.1029/2007GL031007.

Baker, D. N., Kanekal, S. G., Hoxie, V. C., Batiste, S., Bolton, M., Li, X., Elkington, S. R., Monk, S., Reukauf, R., Steg, S., Westfall, J., Belting, C., Bolton, B., Braun, D., Cervelli, B., Hubbell, K., Kien, M., Knappmiller, S., Wade, S., Lamprecht, B., Stevens, K., Wallace, J., Yehle, A., Spence, H. E., and Friedel, R. (2013a). The Relativistic Electron-Proton Telescope (REPT) instrument on board the Radiation Belt Storm Probes (RBSP) Spacecraft: Characterization of Earth's radiation belt high-energy particle populations. *Space Science Reviews*, 179(1):337–381. **doi:** 10.1007/s11214-012-9950-9.

Baker, D. N., Kanekal, S. G., Hoxie, V. C., Henderson, M. G., Li, X., Spence, H. E., Elkington, S. R., Friedel, R. H. W., Goldstein, J., Hudson, M. K., Reeves, G. D., Thorne, R. M., Kletzing, C. A., and Claudepierre, S. G. (2013b). A long-lived relativistic electron storage ring embedded in Earth's outer Van Allen belt. *Science*, 340(6129):186–190. **doi:** 10.1126/science.1233518.

Barker, A. B., Li, X., and Selesnick, R. S. (2005). Modeling the radiation belt electrons with radial diffusion driven by the solar wind. *Space Weather*, 3(10):S10003. **doi:** 10.1029/2004SW000118.

Bartels, J., Heck, N. H., and Johnston, H. F. (1939). The three-hour-range index measuring geomagnetic activity. *Terrestrial Magnetism and Atmospheric Electricity*, 44(4):411–454. **doi:** 10.1029/TE044i004p00411.

Bartels, J. and Veldkamp, J. (1949). International data on magnetic disturbances, first quarter, 1949. *Journal of Geophysical Research (1896-1977)*, 54(3):295–299. **doi:** 10.1029/JZ054i003p00295.

Baumjohann, W. (1993). The near-Earth plasma sheet: An AMPTE/IRM perspective. *Space Science Reviews*, 64(1):141–163. **doi:** 10.1007/BF00819660.

Baumjohann, W. and Treumann, R. A. (1996). *Basic Space Plasma Physics*. Published by Imperial College Press and distributed by World Scientific Publishing Co. **doi:** 10.1142/p015.

Bentley, S. N., Watt, C. E. J., Owens, M. J., and Rae, I. J. (2018). ULF wave activity in the magnetosphere: Resolving solar wind interdependencies to identify driving mechanisms. *Journal of Geophysical Research: Space Physics*, 123(4):2745–2771. **doi:** 10.1002/2017JA024740.

Birn, J., Thomsen, M. F., Borovsky, J. E., Reeves, G. D., McComas, D. J., Belian, R. D., and Hesse, M. (1998). Substorm electron injections: Geosynchronous observations and test particle simulations. *Journal of Geophysical Research: Space Physics*, 103(A5):9235–9248. **doi:** 10.1029/97JA02635.

Blake, J. B., Carranza, P. A., Claudepierre, S. G., Clemmons, J. H., Crain, W. R., Dotan, Y., Fennell, J. F., Fuentes, F. H., Galvan, R. M., George, J. S., Henderson, M. G., Lalic, M., Lin, A. Y., Looper, M. D., Mabry, D. J., Mazur, J. E., McCarthy, B., Nguyen, C. Q., O'Brien, T. P., Perez, M. A., Redding, M. T., Roeder, J. L., Salvaggio, D. J., Sorensen, G. A., Spence, H. E., Yi, S., and Zakrzewski, M. P. (2013). The Magnetic Electron Ion Spectrometer (MagEIS) instruments aboard the Radiation Belt Storm Probes (RBSP) spacecraft. *Space Science Reviews*, 179(1):383–421. **doi:** 10.1007/s11214-013-9991-8.

Borovsky, J. E. (1986). Magnetic pumping by magnetosonic waves in the presence of noncompressive electromagnetic fluctuations. *The Physics of Fluids*, 29(10):3245–3260. **doi:** 10.1063/1.865842.

Borovsky, J. E. and Denton, M. H. (2009). Relativistic-electron dropouts and recovery: A superposed epoch study of the magnetosphere and the solar wind. *Journal of Geophysical Research: Space Physics*, 114(A2):A02201. **doi:** 10.1029/2008JA013128.

Borovsky, J. E., Goertz, C. K., and Joyce, G. (1981). Magnetic pumping of particles in the outer Jovian magnetosphere. *Journal of Geophysical Research: Space Physics*, 86(A5):3481–3495. **doi:** 10.1029/JA086iA05p03481.

Borovsky, J. E., Horne, R. B., and Meredith, N. P. (2017). The contribution of compressional magnetic pumping to the energization of the Earth's outer electron radiation belt during high-speed stream-driven storms. *Journal of Geophysical Research: Space Physics*, 122(12):12,072–12,089. **doi:** 10.1002/2017JA024607.

Bortnik, J., Thorne, R. M., and Meredith, N. P. (2007). Modeling the propagation characteristics of chorus using CRRES suprathermal electron fluxes. *Journal of Geophysical Research: Space Physics*, 112(A8):A08204. **doi:** 10.1029/2006JA012237.

Bortnik, J., Thorne, R. M., and Meredith, N. P. (2008). The unexpected origin of plasmaspheric hiss from discrete chorus emissions. *Nature*, 452:62–66. **doi:** 10.1038/nature06741.

Bossen, M., McPherron, R. L., and Russell, C. T. (1976). A statistical study of Pc-1 magnetic pulsations at synchronous orbit. *Journal of Geophysical Research*, 81(34):6083–6091. **doi:** 10.1029/JA081i034p06083.

Bourdarie, S., Boscher, D., Beutier, T., Sauvaud, J.-A., and Blanc, M. (1997). Electron and proton radiation belt dynamic simulations during storm periods: A new asymmetric convection-diffusion model. *Journal of Geophysical Research: Space Physics*, 102(A8):17541–17552. **doi:** 10.1029/97JA01305.

Boyd, A. J., Spence, H. E., Claudepierre, S. G., Fennell, J. F., Blake, J. B., Baker, D. N., Reeves, G. D., and Turner, D. L. (2014). Quantifying the radiation belt seed population in the 17 March 2013 electron acceleration event. *Geophysical Research Letters*, 41(7):2275–2281. **doi:** 10.1002/2014GL059626.

Boyd, A. J., Spence, H. E., Huang, C.-L., Reeves, G. D., Baker, D. N., Turner, D. L., Claudepierre, S. G., Fennell, J. F., Blake, J. B., and Shprits, Y. Y. (2016). Statistical properties of the radiation belt seed population. *Journal of Geophysical Research: Space Physics*, 121(8):7636–7646. **doi:** 10.1002/2016JA022652.

Boyd, A. J., Turner, D. L., Reeves, G. D., Spence, H. E., Baker, D. N., and Blake, J. B. (2018). What causes radiation belt enhancements: A survey of the Van Allen Probes Era. *Geophysical Research Letters*, 45(11):5253–5259. **doi:** 10.1029/2018GL077699.

Brautigam, D. H. and Albert, J. M. (2000). Radial diffusion analysis of outer radiation belt electrons during the October 9, 1990, magnetic storm. *Journal of Geophysical Research: Space Physics*, 105(A1):291–309. **doi:** 10.1029/1999JA900344.

Califf, S., Li, X., Zhao, H., Kellerman, A., Sarris, T. E., Jaynes, A., and Malaspina, D. M. (2017). The role of the convection electric field in filling the slot region between the inner and outer radiation belts. *Journal of Geophysical Research: Space Physics*, 122(2):2051–2068. **doi:** 10.1002/2016JA023657.

Carpenter, D. L. and Anderson, R. R. (1992). An ISEE/whistler model of equatorial electron density in the magnetosphere. *Journal of Geophysical Research: Space Physics*, 97(A2):1097–1108. **doi:** 10.1029/91JA01548.

Case, N. A. and Wild, J. A. (2013). The location of the Earth's magnetopause: A comparison of modeled position and in situ Cluster data. *Journal of Geophysical Research: Space Physics*, 118(10):6127–6135. **doi:** 10.1002/jgra.50572.

Cayton, T. E., Belian, R. D., Gary, S. P., Fritz, T. A., and Baker, D. N. (1989). Energetic electron components at geosynchronous orbit. *Geophysical Research Letters*, 16(2):147–150. **doi:** 10.1029/GL016i002p00147.

Chapman, S. and Bartels, J. (1962). *Geomagnetism*. Number V. 1 in Geomagnetism. Clarendon Press.

Chen, L., Bortnik, J., Li, W., Thorne, R. M., and Horne, R. B. (2012a). Modeling the properties of plasmaspheric hiss: 1. Dependence on chorus wave emission. *Journal of Geophysical Research: Space Physics*, 117(A5):A05201. **doi:** 10.1029/2011JA017201.

Chen, L., Li, W., Bortnik, J., and Thorne, R. M. (2012b). Amplification of whistler-mode hiss inside the plasmasphere. *Geophysical Research Letters*, 39(8):L08111. **doi:** 10.1029/2012GL051488.

Chen, M. W. and Schulz, M. (2001). Simulations of storm time diffuse aurora with plasmasheet electrons in strong pitch angle diffusion. *Journal of Geophysical Research: Space Physics*, 106(A2):1873–1886. **doi:** 10.1029/2000JA000161.

Chen, Y., Reeves, G. D., and Friedel, R. H. W. (2007). The energization of relativistic electrons in the outer Van Allen radiation belt. *Nature Physics*, 3:614–617. **doi:** 10.1038/nphys655.

Claudepierre, S. G., Elkington, S. R., and Wiltberger, M. (2008). Solar wind driving of magnetospheric ULF waves: Pulsations driven by velocity shear at the magnetopause. *Journal of Geophysical Research: Space Physics*, 113(A5):A05218. **doi:** 10.1029/2007JA012890.

Claudepierre, S. G., O'Brien, T. P., Blake, J. B., Fennell, J. F., Roeder, J. L., Clemmons, J. H., Looper, M. D., Mazur, J. E., Mulligan, T. M., Spence, H. E., Reeves, G. D., Friedel, R. H. W., Henderson, M. G., and Larsen, B. A. (2015). A background correction algorithm for Van Allen Probes MagEIS electron flux measurements. *Journal of Geophysical Research: Space Physics*, 120(7):5703–5727. **doi:** 10.1002/2015JA021171.

Claudepierre, S. G., Wiltberger, M., Elkington, S. R., Lotko, W., and Hudson, M. K. (2009). Magnetospheric cavity modes driven by solar wind dynamic pressure fluctuations. *Geophysical Research Letters*, 36(13):L13101. **doi:** 10.1029/2009GL039045.

Cornwall, J. M. (1968). Diffusion processes influenced by conjugate-point wave phenomena. *Radio Science*, 3(7):740–744. **doi:** 10.1002/rds196837740.

Cornwall, J. M., Coroniti, F. V., and Thorne, R. M. (1970). Turbulent loss of ring current protons. *Journal of Geophysical Research*, 75(25):4699–4709. **doi:** 10.1029/JA075i025p04699.

Cravens, T. E. (1997). *Physics of Solar System Plasmas*. Cambridge Atmospheric and Space Science Series. Cambridge University Press.

Daglis, I. A., Thorne, R. M., Baumjohann, W., and Orsini, S. (1999). The terrestrial ring current: Origin, formation, and decay. *Reviews of Geophysics*, 37(4):407–438. **doi:** 10.1029/1999RG900009.

Dai, L., Wang, C., Duan, S., He, Z., Wygant, J. R., Cattell, C. A., Tao, X., Su, Z., Kletzing, C., Baker, D. N., Li, X., Malaspina, D., Blake, J. B., Fennell, J., Claudepierre, S., Turner, D. L., Reeves, G. D., Funsten, H. O., Spence, H. E., Angelopoulos, V., Fruehauff, D., Chen, L., Thaller, S., Breneman, A., and Tang, X. (2015). Near-Earth injection of MeV electrons associated with intense dipolarization electric fields: Van Allen Probes observations. *Geophysical Research Letters*, 42(15):6170–6179. **doi:** 10.1002/2015GL064955.

Davis, L. (1947). Stellar electromagnetic fields. *Phys. Rev.*, 72:632–633. **doi:** 10.1103/PhysRev.72.632.

Davis, T. N. and Sugiura, M. (1966). Auroral electrojet activity index AE and its universal time variations. *Journal of Geophysical Research (1896-1977)*, 71(3):785–801. **doi:** 10.1029/JZ071i003p00785.

DeForest, S. E. and McIlwain, C. E. (1971). Plasma clouds in the magnetosphere. *Journal of Geophysical Research (1896-1977)*, 76(16):3587–3611. **doi:** 10.1029/JA076i016p03587.

Denton, M. H. and Borovsky, J. E. (2012). Magnetosphere response to high-speed solar wind streams: A comparison of weak and strong driving and the importance of extended periods of fast solar wind. *Journal of Geophysical Research: Space Physics*, 117(A9):A00L05. **doi:** 10.1029/2011JA017124.

Dessler, A. J. and Karplus, R. (1961). Some effects of diamagnetic ring currents on Van Allen radiation. *Journal of Geophysical Research (1896-1977)*, 66(8):2289–2295. **doi:** 10.1029/JZ066i008p02289.

Dessler, A. J. and Parker, E. N. (1959). Hydromagnetic theory of geomagnetic storms. *Journal of Geophysical Research (1896-1977)*, 64(12):2239–2252. **doi:** 10.1029/JZ064i012p02239.

Dungey, J. W. (1961). Interplanetary Magnetic Field and the Auroral Zones. *Physical Review Letters*, 6:47–48. **doi:** 10.1103/PhysRevLett.6.47.

Echer, E., Gonzalez, W., and Tsurutani, B. (2011). Statistical studies of geomagnetic storms with peak Dst < -50nt from 1957 to 2008. *Journal of Atmospheric and Solar-Terrestrial Physics*, 73(11):1454 – 1459. **doi:** 10.1016/j.jastp.2011.04.021.

Elkington, S. R., Hudson, M. K., and Chan, A. A. (1999). Acceleration of relativistic electrons via drift-resonant interaction with toroidal-mode Pc-5 ULF oscillations. *Geophysical Research Letters*, 26(21):3273–3276. **doi:** 10.1029/1999GL003659.

Evans, D. S. and Greer, M. S. (2004). *Polar Orbiting Environmental Satellite Space Environment Monitor-2: Instrument descriptions and archive data documentation*. NOAA Tech. Mem. 93, version 1.4, Space Weather Prediction Cent., Boulder, Colo.

Fennell, J. F., Claudepierre, S. G., Blake, J. B., O'Brien, T. P., Clemmons, J. H., Baker, D. N., Spence, H. E., and Reeves, G. D. (2015). Van Allen Probes show that the inner radiation zone contains no MeV electrons: ECT/MagEIS data. *Geophysical Research Letters*, 42(5):1283–1289. **doi:** 10.1002/2014GL062874.

Fok, M.-C., Buzulukova, N. Y., Chen, S.-H., Glocer, A., Nagai, T., Valek, P., and Perez, J. D. (2014). The comprehensive inner magnetosphere-ionosphere model. *Journal of Geophysical Research: Space Physics*, 119(9):7522–7540. **doi:** 10.1002/2014JA020239.

Fok, M.-C., Moore, T. E., Kozyra, J. U., Ho, G. C., and Hamilton, D. C. (1995). Three-dimensional ring current decay model. *Journal of Geophysical Research: Space Physics*, 100(A6):9619–9632. **doi:** 10.1029/94JA03029.

Foster, J. C., Erickson, P. J., Baker, D. N., Claudepierre, S. G., Kletzing, C. A., Kurth, W., Reeves, G. D., Thaller, S. A., Spence, H. E., Shprits, Y. Y., and Wygant, J. R. (2013). Prompt energization of relativistic and highly relativistic electrons during a substorm interval: Van Allen Probes observations. *Geophysical Research Letters*, 41(1):20–25. **doi:** 10.1002/2013GL058438.

Foster, J. C., Wygant, J. R., Hudson, M. K., Boyd, A. J., Baker, D. N., Erickson, P. J., and Spence, H. E. (2015). Shock-induced prompt relativistic electron acceleration in the inner magnetosphere. *Journal of Geophysical Research: Space Physics*, 120(3):1661–1674. **doi:** 10.1002/2014JA020642.

Fraser, B. and Nguyen, T. (2001). Is the plasmapause a preferred source region of electromagnetic ion cyclotron waves in the magnetosphere? *Journal of Atmospheric and Solar-Terrestrial Physics*, 63(11):1225 – 1247. The Plasmasphere Revisited: A Tribute to Donald Carpenter.

Freeman Jr., J. W. (1964). The morphology of the electron distribution in the outer radiation zone and near the magnetospheric boundary as observed by Explorer 12. *Journal of Geophysical Research (1896-1977)*, 69(9):1691–1723. **doi:** 10.1029/JZ069i009p01691.

Friedel, R., Reeves, G., and Obara, T. (2002). Relativistic electron dynamics in the inner magnetosphere – a review. *Journal of Atmospheric and Solar-Terrestrial Physics*, 64(2):265 – 282. **doi:** 10.1016/S1364-6826(01)00088-8.

Friedel, R. H. W., Korth, H., Henderson, M. G., Thomsen, M. F., and Scudder, J. D. (2001). Plasma sheet access to the inner magnetosphere. *Journal of Geophysical Research: Space Physics*, 106(A4):5845–5858. **doi:** 10.1029/2000JA003011.

Fujimoto, M. and Nishida, A. (1990). Energization and anisotropization of energetic electrons in the earth's radiation belt by the recirculation process. *Journal of Geophysical Research: Space Physics*, 95(A4):4265–4270. **doi:** 10.1029/JA095iA04p04265.

Fälthammar, C.-G. (1965). Effects of time-dependent electric fields on geomagnetically trapped radiation. *Journal of Geophysical Research*, 70(11):2503–2516. **doi:** 10.1029/JZ070i011p02503.

Gannon, J. L., Li, X., and Heynderickx, D. (2007). Pitch angle distribution analysis of radiation belt electrons based on Combined Release and Radiation Effects Satellite Medium Electrons A data. *Journal of Geophysical Research: Space Physics*, 112(A5):A05212. **doi:** 10.1029/2005JA011565.

Ganushkina, N. Y., Amariutei, O. A., Shprits, Y. Y., and Liemohn, M. W. (2013). Transport of the plasma sheet electrons to the geostationary distances. *Journal of Geophysical Research: Space Physics*, 118(1):82–98. **doi:** 10.1029/2012JA017923.

Ganushkina, N. Y., Liemohn, M. W., Amariutei, O. A., and Pitchford, D. (2014). Low-energy electrons (5–50 keV) in the inner magnetosphere. *Journal of Geophysical Research: Space Physics*, 119(1):246–259. **doi:** 10.1002/2013JA019304.

Ginet, G. P., O'Brien, T. P., Huston, S. L., Johnston, W. R., Guild, T. B., Friedel, R., Lindstrom, C. D., Roth, C. J., Whelan, P., Quinn, R. A., Madden, D., Morley, S., and Su, Y.-J. (2013). AE9, AP9 and SPM: New models for specifying the trapped energetic particle and space plasma environment. *Space Science Reviews*, 179(1):579–615. **doi**: 10.1007/s11214-013-9964-y.

Glauert, S. A. and Horne, R. B. (2005). Calculation of pitch angle and energy diffusion coefficients with the PADIE code. *Journal of Geophysical Research: Space Physics*, 110(A4):A04206. **doi:** 10.1029/2004JA010851.

Glauert, S. A., Horne, R. B., and Meredith, N. P. (2014a). Simulating the Earth's radiation belts: Internal acceleration and continuous losses to the magnetopause. *Journal of Geophysical Research: Space Physics*, 119(9):7444–7463. **doi:** 10.1002/2014JA020092.

Glauert, S. A., Horne, R. B., and Meredith, N. P. (2014b). Three-dimensional electron radiation belt simulations using the BAS Radiation Belt Model with new diffusion models for chorus, plasmaspheric hiss, and lightning-generated whistlers. *Journal of Geophysical Research: Space Physics*, 119(1):268–289. **doi:** 10.1002/2013JA019281.

Glauert, S. A., Horne, R. B., and Meredith, N. P. (2018). A 30-year simulation of the outer electron radiation belt. *Space Weather*, 16(10):1498–1522. **doi:** 10.1029/2018SW001981.

Goertz, C. K. (1978). Energization of charged particles in Jupiter's outer magnetosphere. *Journal of Geophysical Research: Space Physics*, 83(A7):3145–3150. **doi:** 10.1029/JA083iA07p03145.

Green, J. C. and Kivelson, M. G. (2004). Relativistic electrons in the outer radiation belt: Differentiating between acceleration mechanisms. *Journal of Geophysical Research: Space Physics*, 109(A3):A03213. **doi:** 10.1029/2003JA010153.

Hardy, D. A., Gussenhoven, M. S., and Holeman, E. (1985). A statistical model of auroral electron precipitation. *Journal of Geophysical Research: Space Physics*, 90(A5):4229–4248. **doi:** 10.1029/JA090iA05p04229.

Hargreaves, J. (1979). *The Upper Atmosphere and Solar Terrestrial Relations: An Introduction to the Aerospace Environment*. Van Nostrand Reinhold.

Hikishima, M., Yagitani, S., Omura, Y., and Nagano, I. (2009). Coherent nonlinear scattering of energetic electrons in the process of whistler mode chorus generation. *Journal of Geophysical Research: Space Physics*, 114(A10):A10205. **doi:** 10.1029/2009JA014371.

Hill, T. (1974). Origin of the plasma sheet. *Reviews of Geophysics*, 12(3):379–388. **doi:** 10.1029/RG012i003p00379.

Höcker, A. and Kartvelishvili, V. (1996). SVD approach to data unfolding. *Nuclear Instruments and Methods in Physics Research Section A: Accelerators, Spectrometers, Detectors and Associated Equipment*, 372(3):469 – 481. **doi:** 10.1016/0168-9002(95)01478-0.

Hones, E. W. (1976). Observations in the Earth's magnetotail relating to magnetic merging. *Solar Physics*, 47(1):101–113. **doi:** 10.1007/BF00152248.

Horne, R. B. (2007). Acceleration of killer electrons. *Nature Physics*, 3:590–591. **doi:** 10.1038/nphys703.

Horne, R. B., Glauert, S. A., Meredith, N. P., Boscher, D., Maget, V., Heynderickx, D., and Pitchford, D. (2013). Space weather impacts on satellites and forecasting the Earth's electron radiation belts with SPACECAST. *Space Weather*, 11(4):169–186. **doi:** 10.1002/swe.20023.

Horne, R. B., Glauert, S. A., and Thorne, R. M. (2003). Resonant diffusion of radiation belt electrons by whistler-mode chorus. *Geophysical Research Letters*, 30(9):46. **doi:** 10.1029/2003GL016963.

Horne, R. B., Phillips, M. W., Glauert, S. A., Meredith, N. P., Hands, A. D. P., Ryden, K. A., and Li, W. (2018). Realistic worst case for a severe space weather event driven by a fast solar wind stream. *Space Weather*, 16(9):1202–1215. **doi:** 10.1029/2018SW001948.

Horne, R. B. and Thorne, R. M. (1998). Potential waves for relativistic electron scattering and stochastic acceleration during magnetic storms. *Geophysical Research Letters*, 25(15):3011–3014. **doi:** 10.1029/98GL01002.

Horne, R. B. and Thorne, R. M. (2003). Relativistic electron acceleration and precipitation during resonant interactions with whistler-mode chorus. *Geophysical Research Letters*, 30(10):34. **doi:** 10.1029/2003GL016973.

Horne, R. B., Thorne, R. M., Glauert, S. A., Albert, J. M., Meredith, N. P., and Anderson, R. R. (2005a). Timescale for radiation belt electron acceleration by whistler mode chorus waves. *Journal of Geophysical Research: Space Physics*, 110(A3):A03225. **doi:** 10.1029/2004JA010811.

Horne, R. B., Thorne, R. M., Shprits, Y. Y., Meredith, N. P., Glauert, S. A., Smith, A. J., Kanekal, S. G., Baker, D. N., Engebretson, M. J., Posch, J. L., Spasojevic, M., Inan, U. S., Pickett, J. S., and Decreau, P. M. E. (2005b). Wave acceleration of electrons in the Van Allen radiation belts. *Nature*, 437(7056):227–230. **doi:** 10.1038/nature03939.

Hudson, M., Jaynes, A., Kress, B., Li, Z., Patel, M., Shen, X.-C., Thaller, S., Wiltberger, M., and Wygant, J. (2017). Simulated prompt acceleration of multi-MeV electrons by the 17 March 2015 interplanetary shock. *Journal of Geophysical Research: Space Physics*, 122(10):10,036–10,046. **doi:** 10.1002/2017JA024445.

Hutchinson, J. A., Wright, D. M., and Milan, S. E. (2011). Geomagnetic storms over the last solar cycle: A superposed epoch analysis. *Journal of Geophysical Research: Space Physics*, 116(A9):A09211. **doi:** 10.1029/2011JA016463.

Hwang, J. A., Lee, D.-Y., Lyons, L. R., Smith, A. J., Zou, S., Min, K. W., Kim, K.-H., Moon, Y.-J., and Park, Y. D. (2007). Statistical significance of association between whistler-mode chorus enhancements and enhanced convection periods during high-speed streams. *Journal of Geophysical Research: Space Physics*, 112(A9):A09213. **doi:** 10.1029/2007JA012388.

Iles, R. H. A., Meredith, N. P., Fazakerley, A. N., and Horne, R. B. (2006). Phase space density analysis of the outer radiation belt energetic electron dynamics. *Journal of Geophysical Research: Space Physics*, 111(A3):A03204. **doi:** 10.1029/2005JA011206.

Ingraham, J. C., Cayton, T. E., Belian, R. D., Christensen, R. A., Friedel, R. H. W., Meier, M. M., Reeves, G. D., and Tuszewski, M. (2001). Substorm injection of relativistic electrons to geosynchronous orbit during the great magnetic storm of March 24, 1991. *Journal of Geophysical Research: Space Physics*, 106(A11):25759–25776. **doi:** 10.1029/2000JA000458.

Jacobs, J. A., Kato, Y., Matsushita, S., and Troitskaya, V. A. (1964). Classification of Geomagnetic Micropulsations. *Geophysical Journal International*, 8(3):341–342. **doi:** 10.1111/j.1365-246X.1964.tb06301.x.

Jaynes, A. N., Baker, D. N., Singer, H. J., Rodriguez, J. V., Loto'aniu, T. M., Ali, A. F., Elkington, S. R., Li, X., Kanekal, S. G., Claudepierre, S. G., Fennell, J. F., Li, W., Thorne, R. M., Kletzing, C. A., Spence, H. E., and Reeves, G. D. (2015). Source and seed populations for relativistic electrons: Their roles in radiation belt changes. *Journal of Geophysical Research: Space Physics*, 120(9):7240–7254. **doi:** 10.1002/2015JA021234.

Jordanova, V. K., Kistler, L. M., Kozyra, J. U., Khazanov, G. V., and Nagy, A. F. (1996). Collisional losses of ring current ions. *Journal of Geophysical Research: Space Physics*, 101(A1):111–126. **doi:** 10.1029/95JA02000.

Kavanagh, L. D., Freeman, J. W., and Chen, A. J. (1968). Plasma flow in the magnetosphere. *Journal of Geophysical Research*, 73(17):5511–5519. **doi:** 10.1029/JA073i017p05511.

Kellerman, A. C. and Shprits, Y. Y. (2012). On the influence of solar wind conditions on the outer-electron radiation belt. *Journal of Geophysical Research: Space Physics*, 117(A5):A05217. **doi:** 10.1029/2011JA017253.

Kennel, C. F. and Petschek, H. E. (1966). Limit on stably trapped particle fluxes. *Journal of Geophysical Research (1896-1977)*, 71(1):1–28. **doi:** 10.1029/JZ071i001p00001.

Kersten, T., Horne, R. B., Glauert, S. A., Meredith, N. P., Fraser, B. J., and Grew, R. S. (2014). Electron losses from the radiation belts caused by EMIC waves. *Journal of Geophysical Research: Space Physics*, 119(11):8820–8837. **doi:** 10.1002/2014JA020366.

Kim, H.-J. and Chan, A. A. (1997). Fully adiabatic changes in storm time relativistic electron fluxes. *Journal of Geophysical Research: Space Physics*, 102(A10):22107–22116. **doi:** 10.1029/97JA01814.

Kim, K.-C. and Shprits, Y. (2013). Long-term relativistic radiation belt electron responses to GEM magnetic storms. *Journal of Atmospheric and Solar-Terrestrial Physics*, 100–101:59 – 67. **doi:** 10.1016/j.jastp.2013.04.007.

Kim, K.-C., Shprits, Y., Subbotin, D., and Ni, B. (2011). Understanding the dynamic evolution of the relativistic electron slot region including radial and pitch angle diffusion. *Journal of Geophysical Research: Space Physics*, 116(A10):A10214. **doi:** 10.1029/2011JA016684.

Kissinger, J., Kepko, L., Baker, D. N., Kanekal, S., Li, W., McPherron, R. L., and Angelopoulos, V. (2014). The importance of storm time steady magnetospheric convection in determining the final relativistic electron flux level. *Journal of Geophysical Research: Space Physics*, 119(9):7433–7443. **doi:** 10.1002/2014JA019948.

Kivelson, M. and Russell, C. (1995). *Introduction to Space Physics*. Cambridge atmospheric and space science series. Cambridge University Press.

Kivelson, M. G. (1976). Magnetospheric electric fields and their variation with geomagnetic activity. *Reviews of Geophysics*, 14(2):189–197. **doi:** 10.1029/RG014i002p00189.

Koller, J., Reeves, G. D., and Friedel, R. H. W. (2009). LANL* V1.0: A radiation belt drift shell model suitable for real-time and reanalysis applications. *Geoscientific Model Development*, 2(2):113–122. **doi:** 10.5194/gmd-2-113-2009.

Korth, H., Thomsen, M. F., Borovsky, J. E., and McComas, D. J. (1999). Plasma sheet access to geosynchronous orbit. *Journal of Geophysical Research: Space Physics*, 104(A11):25047–25061. **doi:** 10.1029/1999JA900292.

Kronberg, E. A., Grigorenko, E. E., Turner, D. L., Daly, P. W., Khotyaintsev, Y., and Kozak, L. (2017). Comparing and contrasting dispersionless injections at geosynchronous orbit during a substorm event. *Journal of Geophysical Research: Space Physics*, 122(3):3055–3072. **doi:** 10.1002/2016JA023551.

Lam, M. M., Horne, R. B., Meredith, N. P., Glauert, S. A., Moffat-Griffin, T., and Green, J. C. (2010). Origin of energetic electron precipitation >30 keV into the atmosphere. *Journal of Geophysical Research: Space Physics*, 115(A4):A00F08. **doi:** 10.1029/2009JA014619.

Lejosne, S., Boscher, D., Maget, V., and Rolland, G. (2012). Bounce-averaged approach to radial diffusion modeling: From a new derivation of the instantaneous rate of change of the third adiabatic invariant to the characterization of the radial diffusion process. *Journal of Geophysical Research: Space Physics*, 117(A8):A08231. **doi:** 10.1029/2012JA018011.

Lenchek, A. M., Singer, S. F., and Wentworth, R. C. (1961). Geomagnetically trapped electrons from cosmic ray albedo neutrons. *Journal of Geophysical Research*, 66(12):4027–4046. **doi:** 10.1029/JZ066i012p04027.

Li, W., Ma, Q., Thorne, R. M., Bortnik, J., Kletzing, C. A., Kurth, W. S., Hospodarsky, G. B., and Nishimura, Y. (2015). Statistical properties of plasmaspheric hiss derived from Van Allen Probes data and their effects on radiation belt electron dynamics. *Journal of Geophysical Research: Space Physics*, 120(5):3393–3405. **doi:** 10.1002/2015JA021048.

Li, W., Thorne, R. M., Angelopoulos, V., Bonnell, J. W., McFadden, J. P., Carlson, C. W., LeContel, O., Roux, A., Glassmeier, K. H., and Auster, H. U. (2009). Evaluation of whistler-mode chorus intensification on the nightside during an injection event observed on the THEMIS spacecraft. *Journal of Geophysical Research: Space Physics*, 114(A1):A00C14. **doi:** 10.1029/2008JA013554.

Li, W., Thorne, R. M., Bortnik, J., Nishimura, Y., Angelopoulos, V., Chen, L., McFadden, J. P., and Bonnell, J. W. (2010). Global distributions of suprathermal electrons observed on THEMIS and potential mechanisms for access into the plasmasphere. *Journal of Geophysical Research: Space Physics*, 115(A12):A00J10. **doi:** 10.1029/2010JA015687.

Li, W., Thorne, R. M., Ma, Q., Ni, B., Bortnik, J., Baker, D. N., Spence, H. E., Reeves, G. D., Kanekal, S. G., Green, J. C., Kletzing, C. A., Kurth, W. S., Hospodarsky, G. B., Blake, J. B., Fennell, J. F., and Claudepierre, S. G. (2014). Radiation belt electron acceleration by chorus waves during the 17 March 2013 storm. *Journal of Geophysical Research: Space Physics*, 119(6):4681–4693. **doi:** 10.1002/2014JA019945.

Li, X., Baker, D. N., Kanekal, S. G., Looper, M., and Temerin, M. (2001). Long term measurements of radiation belts by SAMPEX and their variations. *Geophysical Research Letters*, 28(20):3827–3830. **doi:** 10.1029/2001GL013586.

Li, X., Baker, D. N., Temerin, M., Reeves, G., Friedel, R., and Shen, C. (2005). Energetic electrons, 50 keV to 6 MeV, at geosynchronous orbit: Their responses to solar wind variations. *Space Weather*, 3(4):S04001. **doi:** 10.1029/2004SW000105.

Li, X., Baker, D. N., Temerin, M., Reeves, G. D., and Belian, R. D. (1998). Simulation of dispersionless injections and drift echoes of energetic electrons associated with substorms. *Geophysical Research Letters*, 25(20):3763–3766. **doi:** 10.1029/1998GL900001.

Li, X., Roth, I., Temerin, M., Wygant, J. R., Hudson, M. K., and Blake, J. B. (1993). Simulation of the prompt energization and transport of radiation belt particles during the March 24, 1991 SSC. *Geophysical Research Letters*, 20(22):2423–2426. **doi:** 10.1029/93GL02701.

Liu, S., Chen, M. W., Lyons, L. R., Korth, H., Albert, J. M., Roeder, J. L., Anderson, P. C., and Thomsen, M. F. (2003). Contribution of convective transport to stormtime ring current electron injection. *Journal of Geophysical Research: Space Physics*, 108(A10):SMP 7. **doi:** 10.1029/2003JA010004.

Liu, S., Yan, Q., Yang, C., Zhou, Q., He, Z., He, Y., Gao, Z., and Xiao, F. (2018). Quantifying extremely rapid flux enhancements of radiation belt relativistic electrons associated with radial diffusion. *Geophysical Research Letters*, 45(3):1262–1270. **doi:** 10.1002/2017GL076513.

Liu, W. L., Li, X., Sarris, T., Cully, C., Ergun, R., Angelopoulos, V., Larson, D., Keiling, A., Glassmeier, K. H., and Auster, H. U. (2009). Observation and modeling of the injection observed by THEMIS and LANL satellites during the 23 March 2007 substorm event. *Journal of Geophysical Research: Space Physics*, 114(A1):A00C18. **doi:** 10.1029/2008JA013498.

Liu, W. W., Rostoker, G., and Baker, D. N. (1999). Internal acceleration of relativistic electrons by large-amplitude ULF pulsations. *Journal of Geophysical Research: Space Physics*, 104(A8):17391–17407. **doi:** 10.1029/1999JA900168.

Lyons, L. and Williams, D. (1984). *Quantitative Aspects of Magnetospheric Physics*. Geophysics and Astrophysics Monographs. Springer Netherlands.

Lyons, L. R. and Thorne, R. M. (1973). Equilibrium structure of radiation belt electrons. *Journal of Geophysical Research*, 78(13):2142–2149. **doi:** 10.1029/JA078i013p02142.

Lyons, L. R., Thorne, R. M., and Kennel, C. F. (1972). Pitch-angle diffusion of radiation belt electrons within the plasmasphere. *Journal of Geophysical Research (1896-1977)*, 77(19):3455–3474. **doi:** 10.1029/JA077i019p03455.

Ma, Q., Li, W., Thorne, R. M., Ni, B., Kletzing, C. A., Kurth, W. S., Hospodarsky, G. B., Reeves, G. D., Henderson, M. G., Spence, H. E., Baker, D. N., Blake, J. B., Fennell, J. F., Claudepierre, S. G., and Angelopoulos, V. (2015). Modeling inward diffusion and slow decay of energetic electrons in the Earth's outer radiation belt. *Geophysical Research Letters*, 42(4):987–995. **doi:** 10.1002/2014GL062977.

Mann, I., O'Brien, T., and Milling, D. (2004). Correlations between ULF wave power, solar wind speed, and relativistic electron flux in the magnetosphere: solar cycle dependence. *Journal of Atmospheric and Solar-Terrestrial Physics*, 66(2):187 – 198. **doi:** 10.1016/j.jastp.2003.10.002.

Mann, I. R., Ozeke, L. G., Murphy, K. R., Claudepierre, S. G., Turner, D. L., Baker, D. N., Rae, I. J., Kale, A., Milling, D. K., Boyd, A. J., Spence, H. E., Reeves, G. D., Singer, H. J., Dimitrakoudis, S., Daglis, I. A., and Honary, F. (2016). Explaining the dynamics of the ultra-relativistic third Van Allen radiation belt. *Nature Physics*, 12:978 – 983. **doi:** 10.1038/nphys3799.

Mauk, B. H., Fox, N. J., Kanekal, S. G., Kessel, R. L., Sibeck, D. G., and Ukhorskiy, A. (2013). Science objectives and rationale for the Radiation Belt Storm Probes Mission. *Space Science Reviews*, 179(1):3–27. **doi:** 10.1007/s11214-012-9908-y.

Maus, S. (2017). A corotation electric field model of the earth derived from swarm satellite magnetic field measurements. *Journal of Geophysical Research: Space Physics*, 122(8):8733–8754. **doi:** 10.1002/2017JA024221.

Maynard, N. C. and Chen, A. J. (1975). Isolated cold plasma regions: Observations and their relation to possible production mechanisms. *Journal of Geophysical Research*, 80(7):1009–1013. **doi:** 10.1029/JA080i007p01009.

McAdams, K. L. and Reeves, G. D. (2001). Non-adiabatic response of relativistic radiation belt electrons to GEM magnetic storms. *Geophysical Research Letters*, 28(9):1879–1882. **doi:** 10.1029/2000GL011998.

McGreevy, R. L. (2001). Reverse Monte Carlo modelling. *Journal of Physics: Condensed Matter*, 13(46):R877–R913. **doi:** 0953-8984/13/i=46/a=201.

McGreevy, R. L. and Pusztai, L. (1988). Reverse Monte Carlo simulation: A new technique for the determination of disordered structures. *Molecular Simulation*, 1(6):359–367. **doi:** 10.1080/08927028808080958.

McIlwain, C. E. (1961). Coordinates for mapping the distribution of magnetically trapped particles. *Journal of Geophysical Research (1896-1977)*, 66(11):3681–3691. **doi:** 10.1029/JZ066i011p03681.

McPherron, R. L., Russell, C. T., and Aubry, M. P. (1973). Satellite studies of magnetospheric substorms on August 15, 1968: 9. Phenomenological model for substorms. *Journal of Geophysical Research*, 78(16):3131–3149. **doi:** 10.1029/JA078i016p03131.

Meredith, N. P., Cain, M., Horne, R. B., Thorne, R. M., Summers, D., and Anderson, R. R. (2003a). Evidence for chorus-driven electron acceleration to relativistic energies from a survey of geomagnetically disturbed periods. *Journal of Geophysical Research: Space Physics*, 108(A6):SMP 15. **doi:** 10.1029/2002JA009764.

Meredith, N. P., Horne, R. B., and Anderson, R. R. (2001). Substorm dependence of chorus amplitudes: Implications for the acceleration of electrons to relativistic energies. *Journal of Geophysical Research: Space Physics*, 106(A7):13165–13178. **doi:** 10.1029/2000JA900156.

Meredith, N. P., Horne, R. B., Clilverd, M. A., Horsfall, D., Thorne, R. M., and Anderson, R. R. (2006a). Origins of plasmaspheric hiss. *Journal of Geophysical Research: Space Physics*, 111(A9):A09217. **doi:** 10.1029/2006JA011707.

Meredith, N. P., Horne, R. B., Glauert, S. A., and Anderson, R. R. (2007). Slot region electron loss timescales due to plasmaspheric hiss and lightning-generated whistlers. *Journal of Geophysical Research: Space Physics*, 112(A8):A08214. **doi:** 10.1029/2007JA012413.

Meredith, N. P., Horne, R. B., Glauert, S. A., Baker, D. N., Kanekal, S. G., and Albert, J. M. (2009). Relativistic electron loss timescales in the slot region. *Journal of Geophysical Research: Space Physics*, 114(A3):A03222. **doi:** 10.1029/2008JA013889.

Meredith, N. P., Horne, R. B., Glauert, S. A., Thorne, R. M., Summers, D., Albert, J. M., and Anderson, R. R. (2006b). Energetic outer zone electron loss timescales during low geomagnetic activity. *Journal of Geophysical Research: Space Physics*, 111(A5):A05212. **doi:** 10.1029/2005JA011516.

Meredith, N. P., Horne, R. B., Isles, J. D., and Green, J. C. (2016). Extreme energetic electron fluxes in low earth orbit: Analysis of poes E > 30, E > 100, and E > 300 kev electrons. *Space Weather*, 14(2):136–150. **doi:** 10.1002/2015SW001348.

Meredith, N. P., Horne, R. B., Kersten, T., Fraser, B. J., and Grew, R. S. (2014). Global morphology and spectral properties of EMIC waves derived from CRRES observations. *Journal of Geophysical Research: Space Physics*, 119(7):5328–5342. **doi:** 10.1002/2014JA020064.

Meredith, N. P., Horne, R. B., Kersten, T., Li, W., Bortnik, J., Sicard, A., and Yearby, K. H. (2018). Global model of plasmaspheric hiss from multiple satellite observations. *Journal of Geophysical Research: Space Physics*, 123(6):4526–4541. **doi:** 10.1029/2018JA025226.

Meredith, N. P., Horne, R. B., Sandberg, I., Papadimitriou, C., and Evans, H. D. R. (2017). Extreme relativistic electron fluxes in the Earth's outer radiation belt: Analysis of INTEGRAL IREM data. *Space Weather*, 15(7):917–933. **doi:** 10.1002/2017SW001651.

Meredith, N. P., Horne, R. B., Sicard-Piet, A., Boscher, D., Yearby, K. H., Li, W., and Thorne, R. M. (2012). Global model of lower band and upper band chorus from multiple satellite observations. *Journal of Geophysical Research: Space Physics*, 117(A10):A10225. **doi:** 10.1029/2012JA017978.

Meredith, N. P., Horne, R. B., Summers, D., Thorne, R. M., Iles, R. H. A., Heynderickx, D., and Anderson, R. R. (2002). Evidence for acceleration of outer zone electrons to relativistic energies by whistler mode chorus. *Annales Geophysicae*, 20(7):967–979. **doi:** 10.5194/angeo-20-967-2002.

Meredith, N. P., Horne, R. B., Thorne, R. M., Summers, D., and Anderson, R. R. (2004). Substorm dependence of plasmaspheric hiss. *Journal of Geophysical Research: Space Physics*, 109(A6):A06209. **doi:** 10.1029/2004JA010387.

Meredith, N. P., Thorne, R. M., Horne, R. B., Summers, D., Fraser, B. J., and Anderson, R. R. (2003b). Statistical analysis of relativistic electron energies for cyclotron resonance with EMIC waves observed on CRRES. *Journal of Geophysical Research: Space Physics*, 108(A6):SMP 17. **doi:** 10.1029/2002JA009700.

Miyoshi, Y., Morioka, A., Misawa, H., Obara, T., Nagai, T., and Kasahara, Y. (2003). Rebuilding process of the outer radiation belt during the 3 November 1993 magnetic storm: NOAA and Exos-D observations. *Journal of Geophysical Research: Space Physics*, 108(A1):SMP 3. **doi:** 10.1029/2001JA007542.

Miyoshi, Y. S., Jordanova, V. K., Morioka, A., Thomsen, M. F., Reeves, G. D., Evans, D. S., and Green, J. C. (2006). Observations and modeling of energetic electron dynamics during the October 2001 storm. *Journal of Geophysical Research: Space Physics*, 111(A11):A11S02. **doi:** 10.1029/2005JA011351.

Morley, S. K., Friedel, R. H. W., Spanswick, E. L., Reeves, G. D., Steinberg, J. T., Koller, J., Cayton, T., and Noveroske, E. (2010). Dropouts of the outer electron radiation belt in response to solar wind stream interfaces: global positioning system observations. *Proceedings of the Royal Society A: Mathematical, Physical and Engineering Sciences*, 466(2123):3329–3350. **doi:** 10.1098/rspa.2010.0078.

Mozer, F. S. (1971). Power spectra of the magnetospheric electric field. *Journal of Geophysical Research*, 76(16):3651–3667. **doi:** 10.1029/JA076i016p03651.

Ni, B., Bortnik, J., Thorne, R. M., Ma, Q., and Chen, L. (2013). Resonant scattering and resultant pitch angle evolution of relativistic electrons by plasmaspheric hiss. *Journal of Geophysical Research: Space Physics*, 118(12):7740–7751. **doi:** 10.1002/2013JA019260.

Ni, B., Thorne, R. M., Shprits, Y. Y., and Bortnik, J. (2008). Resonant scattering of plasma sheet electrons by whistler-mode chorus: Contribution to diffuse auroral precipitation. *Geophysical Research Letters*, 35(11):L11106. **doi:** 10.1029/2008GL034032.

Ni, B., Zou, Z., Gu, X., Zhou, C., Thorne, R. M., Bortnik, J., Shi, R., Zhao, Z., Baker, D. N., Kanekal, S. G., Spence, H. E., Reeves, G. D., and Li, X. (2015). Variability of the pitch angle distribution of radiation belt ultrarelativistic electrons during and following intense geomagnetic storms: Van Allen Probes observations. *Journal of Geophysical Research: Space Physics*, 120(6):4863–4876. **doi:** 10.1002/2015JA021065.

Ni, B., Zou, Z., Li, X., Bortnik, J., Xie, L., and Gu, X. (2016). Occurrence characteristics of outer zone relativistic electron butterfly distribution: A survey of Van Allen Probes REPT measurements. *Geophysical Research Letters*, 43(11):5644–5652. **doi:** 10.1002/2016GL069350.

Nishimura, Y., Bortnik, J., Li, W., Thorne, R. M., Lyons, L. R., Angelopoulos, V., Mende, S. B., Bonnell, J. W., Le Contel, O., Cully, C., Ergun, R., and Auster, U. (2010). Identifying the driver of pulsating aurora. *Science*, 330(6000):81–84. **doi:** 10.1126/science.1193186.

Nosé, M., Keika, K., Kletzing, C. A., Spence, H. E., Smith, C. W., MacDowall, R. J., Reeves, G. D., Larsen, B. A., and Mitchell, D. G. (2016). Van Allen Probes observations of magnetic field dipolarization and its associated O+ flux variations in the inner magnetosphere at L $<$ 6.6. *Journal of Geophysical Research: Space Physics*, 121(8):7572–7589. **doi:** 10.1002/2016JA022549.

Obara, T., Nagatsuma, T., Den, M., Miyoshi, Y., and Morioka, A. (2000). Main-phase creation of "seed" electrons in the outer radiation belt. *Earth, Planets and Space*, 52(1):41–47. **doi:** 10.1186/BF03351612.

O'Brien, T. P., McPherron, R. L., Sornette, D., Reeves, G. D., Friedel, R., and Singer, H. J. (2001). Which magnetic storms produce relativistic electrons at geosynchronous orbit? *Journal of Geophysical Research: Space Physics*, 106(A8):15533–15544. **doi:** 10.1029/2001JA000052.

Olifer, L., Mann, I. R., Morley, S. K., Ozeke, L. G., and Choi, D. (2018). On the role of last closed drift shell dynamics in driving fast losses and van allen radiation belt extinction. *Journal of Geophysical Research: Space Physics*, 123(5):3692–3703. **doi:** 10.1029/2018JA025190.

Omura, Y., Furuya, N., and Summers, D. (2007). Relativistic turning acceleration of resonant electrons by coherent whistler mode waves in a dipole magnetic field. *Journal of Geophysical Research: Space Physics*, 112(A6):A06236. **doi:** 10.1029/2006JA012243.

Omura, Y., Katoh, Y., and Summers, D. (2008). Theory and simulation of the generation of whistler-mode chorus. *Journal of Geophysical Research: Space Physics*, 113(A4):A04223. **doi:** 10.1029/2007JA012622.

Onsager, T. G., Rostoker, G., Kim, H.-J., Reeves, G. D., Obara, T., Singer, H. J., and Smithtro, C. (2002). Radiation belt electron flux dropouts: Local time, radial, and particle-energy dependence. *Journal of Geophysical Research: Space Physics*, 107(A11):SMP 21. **doi:** 10.1029/2001JA000187.

Ozeke, L. G., Mann, I. R., Claudepierre, S. G., Henderson, M., Morley, S. K., Murphy, K. R., Olifer, L., Spence, H. E., and Baker, D. N. (2019). The March 2015 superstorm revisited: Phase space density profiles and fast ULF wave diffusive transport. *Journal of Geophysical Research: Space Physics*, 124(2):1143–1156. **doi:** 10.1029/2018JA026326.

Ozeke, L. G., Mann, I. R., Murphy, K. R., Jonathan Rae, I., and Milling, D. K. (2014). Analytic expressions for ULF wave radiation belt radial diffusion coefficients. *Journal of Geophysical Research: Space Physics*, 119(3):1587–1605. **doi:** 10.1002/2013JA019204.

Ozeke, L. G., Mann, I. R., Murphy, K. R., Rae, I. J., Milling, D. K., Elkington, S. R., Chan, A. A., and Singer, H. J. (2012). ULF wave derived radiation belt radial diffusion coefficients. *Journal of Geophysical Research: Space Physics*, 117(A4). **doi:** 10.1029/2011JA017463.

Pande, B., Pande, S., Chandra, R., and Mathpal, M. C. (2018). Solar flares, CMEs and solar energetic particle events during solar cycle 24. *Advances in Space Research*, 61(2):777 – 785. **doi:** 10.1016/j.asr.2017.11.025.

Park, C. G. (1974). Some features of plasma distribution in the plasmasphere deduced from Antarctic whistlers. *Journal of Geophysical Research*, 79(1):169–173. **doi:** 10.1029/JA079i001p00169.

Peck, E. D., Randall, C. E., Green, J. C., Rodriguez, J. V., and Rodger, C. J. (2015). POES MEPED differential flux retrievals and electron channel contamination correction. *Journal of Geophysical Research: Space Physics*, 120(6):4596–4612. **doi:** 10.1002/2014JA020817.

Pfitzer, K. A. and Winckler, J. R. (1968). Experimental observation of a large addition to the electron inner radiation belt after a solar flare event. *Journal of Geophysical Research (1896-1977)*, 73(17):5792–5797. **doi:** 10.1029/JA073i017p05792.

Qin, M., Hudson, M., Millan, R., Woodger, L., and Shekhar, S. (2018). Statistical investigation of the efficiency of EMIC waves in precipitating relativistic electrons. *Journal of Geophysical Research: Space Physics*, 123(8):6223–6230. **doi:** 10.1029/2018JA025419.

Reeves, G. D. (1998). Relativistic electrons and magnetic storms: 1992–1995. *Geophysical Research Letters*, 25(11):1817–1820. **doi:** 10.1029/98GL01398.

Reeves, G. D., Friedel, R. H. W., Larsen, B. A., Skoug, R. M., Funsten, H. O., Claudepierre, S. G., Fennell, J. F., Turner, D. L., Denton, M. H., Spence, H. E., Blake, J. B., and Baker, D. N. (2016). Energy-dependent dynamics of keV to MeV electrons in the inner zone, outer zone, and slot regions. *Journal of Geophysical Research: Space Physics*, 121(1):397–412. **doi:** 10.1002/2015JA021569.

Reeves, G. D., McAdams, K. L., Friedel, R. H. W., and O'Brien, T. P. (2003). Acceleration and loss of relativistic electrons during geomagnetic storms. *Geophysical Research Letters*, 30(10):36. **doi:** 10.1029/2002GL016513.

Reeves, G. D., Spence, H. E., Henderson, M. G., Morley, S. K., Friedel, R. H. W., Funsten, H. O., Baker, D. N., Kanekal, S. G., Blake, J. B., Fennell, J. F., Claudepierre, S. G., Thorne, R. M., Turner, D. L., Kletzing, C. A., Kurth, W. S., Larsen, B. A., and Niehof, J. T. (2013). Electron acceleration in the heart of the Van Allen radiation belts. *Science*, 341(6149):991–994. **doi:** 10.1126/science.1237743.

Richard, R. L., El-Alaoui, M., Ashour-Abdalla, M., and Walker, R. J. (2002). Interplanetary magnetic field control of the entry of solar energetic particles into the magnetosphere. *Journal of Geophysical Research: Space Physics*, 107(A8):SSH 7. **doi:** 10.1029/2001JA000099.

Ripoll, J.-F., Loridan, V., Denton, M. H., Cunningham, G., Reeves, G., Santolík, O., Fennell, J., Turner, D. L., Drozdov, A. Y., Cervantes Villa, J. S., Shprits, Y. Y., Thaller, S. A., Kurth, W. S., Kletzing, C. A., Henderson, M. G., and Ukhorskiy, A. Y. (2018). Observations and Fokker-Planck simulations of the L-shell, energy, and pitch-angle structure of Earth's electron radiation belts during quiet times. *Journal of Geophysical Research: Space Physics*, 124(2):1125–1142. **doi:** 10.1029/2018JA026111.

Ripoll, J.-F., Reeves, G. D., Cunningham, G. S., Loridan, V., Denton, M., Santolík, O., Kurth, W. S., Kletzing, C. A., Turner, D. L., Henderson, M. G., and Ukhorskiy, A. Y. (2016). Reproducing the observed energy-dependent structure of Earth's electron radiation belts during storm recovery with an event-specific diffusion model. *Geophysical Research Letters*, 43(11):5616–5625. **doi:** 10.1002/2016GL068869.

Ripoll, J.-F., Santolik, O., Reeves, G. D., Kurth, W. S., Denton, M. H., Loridan, V., Thaller, S. A., Kletzing, C. A., and Turner, D. L. (2017). Effects of whistler mode hiss waves in March 2013. *Journal of Geophysical Research: Space Physics*, 122(7):7433–7462. **doi:** 10.1002/2017JA024139.

Rodger, C. J., Carson, B. R., Cummer, S. A., Gamble, R. J., Clilverd, M. A., Green, J. C., Sauvaud, J.-A., Parrot, M., and Berthelier, J.-J. (2010a). Contrasting the efficiency of radiation belt losses caused by ducted and nonducted whistler-mode waves from ground-based transmitters. *Journal of Geophysical Research: Space Physics*, 115(A12):A12208. **doi:** 10.1029/2010JA015880.

Rodger, C. J., Clilverd, M. A., Green, J. C., and Lam, M. M. (2010b). Use of POES SEM-2 observations to examine radiation belt dynamics and energetic electron precipitation into the atmosphere. *Journal of Geophysical Research: Space Physics*, 115(A4):A04202. **doi:** 10.1029/2008JA014023.

Roederer, J. G. (1970). *Dynamics of Geomagnetically Trapped Radiation*, volume 2. Springer-Verlag Berlin Heidelberg, New York, 1 edition.

Roederer, J. G. and Zhang, H. (2014). *Dynamics of Magnetically Trapped Particles*, volume 403 of *Astrophysics and Space Science Library*. Springer-Verlag Berlin Heidelberg, 2 edition.

Rosen, A., Sonett, C. P., Coleman, P. J., and McIlwain, C. E. (1959). Ionizing radiation at altitudes of 3,500 to 36,000 kilometers Pioneer I. *Journal of Geophysical Research*, 64(7):709–712. **doi:** 10.1029/JZ064i007p00709.

Sandberg, I., Daglis, I. A., Anastasiadis, A., Buhler, P., Nieminen, P., and Evans, H. (2012). Unfolding and validation of SREM fluxes. *IEEE Trans. Nucl. Sci.*, 59:1105–1112. **doi:** 10.1109/TNS.2012.2187216.

Sarris, T. E., Li, X., Tsaggas, N., and Paschalidis, N. (2002). Modeling energetic particle injections in dynamic pulse fields with varying propagation speeds. *Journal of Geophysical Research: Space Physics*, 107(A3):SMP 1. **doi:** 10.1029/2001JA900166.

Sauvaud, J.-A. and Winckler, J. (1980). Dynamics of plasma, energetic particles, and fields near synchronous orbit in the nighttime sector during magnetospheric substorms. *Journal of Geophysical Research: Space Physics*, 85(A5):2043–2056. **doi:** 10.1029/JA085iA05p02043.

Schiller, Q., Li, X., Blum, L., Tu, W., Turner, D. L., and Blake, J. B. (2014). A nonstorm time enhancement of relativistic electrons in the outer radiation belt. *Geophysical Research Letters*, 41(1):7–12. **doi:** 10.1002/2013GL058485.

Schulz, M. and Lanzerotti, L. (1974). *Particle Diffusion in the Radiation Belts*. Physics and Chemistry in Space. Springer Berlin Heidelberg.

Sckopke, N. (1966). A general relation between the energy of trapped particles and the disturbance field near the earth. *Journal of Geophysical Research (1896-1977)*, 71(13):3125–3130. **doi:** 10.1029/JZ071i013p03125.

Selesnick, R. S., Baker, D. N., Jaynes, A. N., Li, X., Kanekal, S. G., Hudson, M. K., and Kress, B. T. (2014). Observations of the inner radiation belt: CRAND and trapped solar protons. *Journal of Geophysical Research: Space Physics*, 119(8):6541–6552. **doi:** 10.1002/2014JA020188.

Selesnick, R. S. and Blake, J. B. (2000). On the source location of radiation belt relativistic electrons. *Journal of Geophysical Research: Space Physics*, 105(A2):2607–2624. **doi:** 10.1029/1999JA900445.

Selesnick, R. S., Looper, M. D., and Mewaldt, R. A. (2007). A theoretical model of the inner proton radiation belt. *Space Weather*, 5(4):S04003. **doi:** 10.1029/2006SW000275.

Sergeev, V. A., Bösinger, T., Belian, R. D., Reeves, G. D., and Cayton, T. E. (1992). Drifting holes in the energetic electron flux at geosynchronous orbit following substorm onset. *Journal of Geophysical Research: Space Physics*, 97(A5):6541–6548. **doi:** 10.1029/92JA00182.

Sergeev, V. A., Nikolaev, A. V., Kubyshkina, M. V., Tsyganenko, N. A., Singer, H. J., Rodriguez, J. V., Angelopoulos, V., Nakamura, R., Milan, S. E., Coxon, J. C., Anderson, B. J., and Korth, H. (2014). Event study combining magnetospheric and ionospheric perspectives of the substorm current wedge modeling. *Journal of Geophysical Research: Space Physics*, 119(12):9714–9728. **doi:** 10.1002/2014JA020522.

Sergeev, V. A., Pellinen, R. J., and Pulkkinen, T. I. (1996). Steady magnetospheric convection: A review of recent results. *Space Science Reviews*, 75(3):551–604. **doi:** 10.1007/BF00833344.

Sergeev, V. A., Shukhtina, M. A., Rasinkangas, R., Korth, A., Reeves, G. D., Singer, H. J., Thomsen, M. F., and Vagina, L. I. (1998). Event study of deep energetic particle injections during substorm. *Journal of Geophysical Research: Space Physics*, 103(A5):9217–9234. **doi:** 10.1029/97JA03686.

Sheldon, R. B., Spence, H. E., Sullivan, J. D., Fritz, T. A., and Chen, J. (1998). The discovery of trapped energetic electrons in the outer cusp. *Geophysical Research Letters*, 25(11):1825–1828. **doi:** 10.1029/98GL01399.

Shi, R., Summers, D., Ni, B., Fennell, J. F., Blake, J. B., Spence, H. E., and Reeves, G. D. (2016). Survey of radiation belt energetic electron pitch angle distributions based on the Van Allen Probes MagEIS measurements. *Journal of Geophysical Research: Space Physics*, 121(2):1078–1090. **doi:** 10.1002/2015JA021724.

Shprits, Y., Subbotin, D., Ni, B., Horne, R., Baker, D., and Cruce, P. (2011). Profound change of the near-Earth radiation environment caused by solar superstorms. *Space Weather*, 9(8):S08007. **doi:** 10.1029/2011SW000662.

Shprits, Y. Y., Elkington, S. R., Meredith, N. P., and Subbotin, D. A. (2008a). Review of modeling of losses and sources of relativistic electrons in the outer radiation belt I: Radial transport. *Journal of Atmospheric and Solar-Terrestrial Physics*, 70(14):1679 – 1693. **doi:** 10.1016/j.jastp.2008.06.008.

Shprits, Y. Y., Kellerman, A. C., Drozdov, A. Y., Spence, H. E., Reeves, G. D., and Baker, D. N. (2015). Combined convective and diffusive simulations: VERB-4D comparison with 17 March 2013 Van Allen Probes observations. *Geophysical Research Letters*, 42(22):9600–9608. **doi:** 10.1002/2015GL065230.

Shprits, Y. Y., Subbotin, D., Drozdov, A., Usanova, M. E., Kellerman, A., Orlova, K., Baker, D. N., Turner, D. L., and Kim, K.-C. (2013). Unusual stable trapping of the ultrarelativistic electrons in the van allen radiation belts. *Nature Physics*, 9:699 – 703. **doi:** 10.1038/nphys2760.

Shprits, Y. Y., Subbotin, D. A., Meredith, N. P., and Elkington, S. R. (2008b). Review of modeling of losses and sources of relativistic electrons in the outer radiation belt II: Local acceleration and loss. *Journal of Atmospheric and Solar-Terrestrial Physics*, 70(14):1694 – 1713. **doi:** 10.1016/j.jastp.2008.06.014.

Shprits, Y. Y. and Thorne, R. M. (2004). Time dependent radial diffusion modeling of relativistic electrons with realistic loss rates. *Geophysical Research Letters*, 31(8):L08805. **doi:** 10.1029/2004GL019591.

Shprits, Y. Y., Thorne, R. M., Friedel, R., Reeves, G. D., Fennell, J., Baker, D. N., and Kanekal, S. G. (2006a). Outward radial diffusion driven by losses at magnetopause. *Journal of Geophysical Research: Space Physics*, 111(A11):A11214. **doi:** 10.1029/2006JA011657.

Shprits, Y. Y., Thorne, R. M., Horne, R. B., Glauert, S. A., Cartwright, M., Russell, C. T., Baker, D. N., and Kanekal, S. G. (2006b). Acceleration mechanism responsible for the formation of the new radiation belt during the 2003 Halloween solar storm. *Geophysical Research Letters*, 33(5):L05104. **doi:** 10.1029/2005GL024256.

Shprits, Y. Y., Thorne, R. M., Reeves, G. D., and Friedel, R. (2005). Radial diffusion modeling with empirical lifetimes: Comparison with CRRES observations. *Annales Geophysicae*, 23(4):1467–1471. **doi:** 10.5194/angeo-23-1467-2005.

Shue, J.-H., Song, P., Russell, C. T., Steinberg, J. T., Chao, J. K., Zastenker, G., Vaisberg, O. L., Kokubun, S., Singer, H. J., Detman, T. R., and Kawano, H. (1998). Magnetopause location under extreme solar wind conditions. *Journal of Geophysical Research: Space Physics*, 103(A8):17691–17700. **doi:** 10.1029/98JA01103.

Sigsbee, K., Menietti, J. D., Santolík, O., and Pickett, J. S. (2010). Locations of chorus emissions observed by the polar plasma wave instrument. *Journal of Geophysical Research: Space Physics*, 115(A6):A00F12. **doi:** 10.1029/2009JA014579.

Spence, H. E., Reeves, G. D., Baker, D. N., Blake, J. B., Bolton, M., Bourdarie, S., Chan, A. A., Claudepierre, S. G., Clemmons, J. H., Cravens, J. P., Elkington, S. R., Fennell, J. F., Friedel, R. H. W., Funsten, H. O., Goldstein, J., Green, J. C., Guthrie, A., Henderson, M. G., Horne, R. B., Hudson, M. K., Jahn, J.-M., Jordanova, V. K., Kanekal, S. G., Klatt, B. W., Larsen, B. A., Li, X., MacDonald, E. A., Mann, I. R., Niehof, J., O'Brien, T. P., Onsager, T. G., Salvaggio, D., Skoug, R. M., Smith, S. S., Suther, L. L., Thomsen, M. F., and Thorne, R. M. (2013). Science goals and overview of the Radiation Belt Storm Probes (RBSP) Energetic Particle, Composition, and Thermal Plasma (ECT) suite on NASA's Van Allen Probes mission. *Space Science Reviews*, 179(1):311–336. **doi:** 10.1007/s11214-013-0007-5.

Stix, T. (1962). *The Theory of Plasma Waves*. McGraw-Hill.

Störmer, C. (1955). *The Polar Aurora*. Clarendon Press.

Su, Z., Xiao, F., Zheng, H., and Wang, S. (2010). STEERB: A three-dimensional code for storm-time evolution of electron radiation belt. *Journal of Geophysical Research: Space Physics*, 115(A9):A09208. **doi:** 10.1029/2009JA015210.

Su, Z., Zhu, H., Xiao, F., Zong, Q. G., Zhou, X. Z., Zheng, H., Wang, Y., Wang, S., Hao, Y. X., Gao, Z., He, Z., Baker, D. N., Spence, H. E., Reeves, G. D., Blake, J. B., and Wygant, J. R. (2015). Ultra-low-frequency wave-driven diffusion of radiation belt relativistic electrons. *Nature Communications*, 6:10096. **doi:** 10.1038/ncomms10096.

Subbotin, D., Shprits, Y., and Ni, B. (2010). Three-dimensional VERB radiation belt simulations including mixed diffusion. *Journal of Geophysical Research: Space Physics*, 115(A3):A03205. **doi:** 10.1029/2009JA015070.

Subbotin, D. A. and Shprits, Y. Y. (2009). Three-dimensional modeling of the radiation belts using the Versatile Electron Radiation Belt (VERB) code. *Space Weather*, 7(10):S10001. **doi:** 10.1029/2008SW000452.

Subbotin, D. A., Shprits, Y. Y., Gkioulidou, M., Lyons, L. R., Ni, B., Merkin, V. G., Toffoletto, F. R., Thorne, R. M., Horne, R., and Hudson, M. K. (2011a). Simulation of the acceleration of relativistic electrons in the inner magnetosphere using RCM-VERB coupled codes. *Journal of Geophysical Research: Space Physics*, 116(A8):A08211. **doi:** 10.1029/2010JA016350.

Subbotin, D. A., Shprits, Y. Y., and Ni, B. (2011b). Long-term radiation belt simulation with the VERB 3-D code: Comparison with CRRES observations. *Journal of Geophysical Research: Space Physics*, 116(A12):A12210. **doi:** 10.1029/2011JA017019.

Sugiura, M. (1964). Hourly values of equatorial Dst for the IGY. *Ann. Int. Geophys. Yr.*, Vol: 35. **doi:** 19650020355.

Sugiura, M. and Poros, D. J. (1971). Hourly values of equatorial Dst for the years 1957 to 1970. *Report of Goddard Space Flight Centre*. **doi:** X-645-7i-278.

Sugiura, M., Skillman, T. L., Ledley, B. G., and Heppner, J. P. (1968). Propagation of the sudden commencement of July 8, 1966, to the magnetotail. *Journal of Geophysical Research*, 73(21):6699–6709. **doi:** 10.1029/JA073i021p06699.

Summers, D., Ni, B., Meredith, N. P., Horne, R. B., Thorne, R. M., Moldwin, M. B., and Anderson, R. R. (2008). Electron scattering by whistler-mode ELF hiss in plasmaspheric plumes. *Journal of Geophysical Research: Space Physics*, 113(A4):A04219. **doi:** 10.1029/2007JA012678.

Summers, D. and Thorne, R. M. (2003). Relativistic electron pitch-angle scattering by electromagnetic ion cyclotron waves during geomagnetic storms. *Journal of Geophysical Research: Space Physics*, 108(A4):SMP 2. **doi:** 10.1029/2002JA009489.

Summers, D., Thorne, R. M., and Xiao, F. (1998). Relativistic theory of wave-particle resonant diffusion with application to electron acceleration in the magnetosphere. *Journal of Geophysical Research: Space Physics*, 103(A9):20487–20500. **doi:** 10.1029/98JA01740.

Tang, C. L., Wang, Y. X., Ni, B., Zhang, J.-C., Reeves, G. D., Su, Z. P., Baker, D. N., Spence, H. E., Funsten, H. O., and Blake, J. B. (2017). Radiation belt seed population and its association with the relativistic electron dynamics: A statistical study. *Journal of Geophysical Research: Space Physics*, 122(5):5261–5276. **doi:** 10.1002/2017JA023905.

Tang, C. L., Xie, X. J., Ni, B., Su, Z. P., Reeves, G. D., Zhang, J.-C., Baker, D. N., Spence, H. E., Funsten, H. O., Blake, J. B., Wygant, J. R., and Dai, G. Y. (2018). Rapid enhancements of the seed populations in the heart of the Earth's outer radiation belt: A multicase study. *Journal of Geophysical Research: Space Physics*, 123(6):4895–4907. **doi:** 10.1029/2017JA025142.

Tang, C. L., Zhang, J.-C., Reeves, G. D., Su, Z. P., Baker, D. N., Spence, H. E., Funsten, H. O., Blake, J. B., and Wygant, J. R. (2016). Prompt enhancement of the Earth's outer radiation belt due to substorm electron injections. *Journal of Geophysical Research: Space Physics*, 121(12):11,826–11,838. **doi:** 10.1002/2016JA023550.

Tao, X., Albert, J. M., and Chan, A. A. (2009). Numerical modeling of multidimensional diffusion in the radiation belts using layer methods. *Journal of Geophysical Research: Space Physics*, 114(A2):A02215. **doi:** 10.1029/2008JA013826.

Tao, X., Chan, A. A., Albert, J. M., and Miller, J. A. (2008). Stochastic modeling of multidimensional diffusion in the radiation belts. *Journal of Geophysical Research: Space Physics*, 113(A7):A07212. **doi:** 10.1029/2007JA012985.

Thébault, E., Finlay, C. C., Beggan, C. D., Alken, P., Aubert, J., Barrois, O., Bertrand, F., Bondar, T., Boness, A., Brocco, L., Canet, E., Chambodut, A., Chulliat, A., Coïsson, P., Civet, F., Du, A., Fournier, A., Fratter, I., Gillet, N., Hamilton, B., Hamoudi, M., Hulot, G., Jager, T., Korte, M., Kuang, W., Lalanne, X., Langlais, B., Léger, J.-M., Lesur, V., Lowes, F. J., Macmillan, S., Mandea, M., Manoj, C., Maus, S., Olsen, N., Petrov, V., Ridley, V., Rother, M., Sabaka, T. J., Saturnino, D., Schachtschneider, R., Sirol, O., Tangborn, A., Thomson, A., Tøffner-Clausen, L., Vigneron, P., Wardinski, I., and Zvereva, T. (2015). International Geomagnetic Reference Field: the 12th generation. *Earth, Planets and Space*, 67(1):79. **doi:** 10.1186/s40623-015-0228-9.

Thorne, R. M. (2010). Radiation belt dynamics: The importance of wave-particle interactions. *Geophysical Research Letters*, 37(22):L22107. **doi:** 10.1029/2010GL044990.

Thorne, R. M., Li, W., Ni, B., Ma, Q., Bortnik, J., Baker, D. N., Spence, H. E., Reeves, G. D., Henderson, M. G., Kletzing, C. A., Kurth, W. S., Hospodarsky, G. B., Turner, D., and Angelopoulos, V. (2013a). Evolution and slow decay of an unusual narrow ring of relativistic electrons near $L^* \sim 3.2$ following the September 2012 magnetic storm. *Geophysical Research Letters*, 40(14):3507–3511. **doi:** 10.1002/grl.50627.

Thorne, R. M., Li, W., Ni, B., Ma, Q., Bortnik, J., Chen, L., Baker, D. N., Spence, H. E., Reeves, G. D., Henderson, M. G., Kletzing, C. A., Kurth, W. S., Hospodarsky, G. B., Blake, J. B., Fennell, J. F., Claudepierre, S. G., and Kanekal, S. G. (2013b). Rapid local acceleration of relativistic radiation-belt electrons by magnetospheric chorus. *Nature*, 504:411–414. **doi:** 10.1038/nature12889.

Thorne, R. M., O'Brien, T. P., Shprits, Y. Y., Summers, D., and Horne, R. B. (2005). Timescale for MeV electron microburst loss during geomagnetic storms. *Journal of Geophysical Research: Space Physics*, 110(A9):A09202. **doi:** 10.1029/2004JA010882.

Thorne, R. M., Shprits, Y. Y., Meredith, N. P., Horne, R. B., Li, W., and Lyons, L. R. (2007). Refilling of the slot region between the inner and outer electron radiation belts during geomagnetic storms. *Journal of Geophysical Research: Space Physics*, 112(A6):A06203. **doi:** 10.1029/2006JA012176.

Thorne, R. M., Smith, E. J., Burton, R. K., and Holzer, R. E. (1973). Plasmaspheric hiss. *Journal of Geophysical Research (1896-1977)*, 78(10):1581–1596. **doi:** 10.1029/JA078i010p01581.

Toffoletto, F., Sazykin, S., Spiro, R., and Wolf, R. (2003). Inner magnetospheric modeling with the Rice Convection Model. *Space Science Reviews*, 107(1):175–196. **doi:** 10.1023/A:1025532008047.

Tsurutani, B. T. and Smith, E. J. (1974). Postmidnight chorus: A substorm phenomenon. *Journal of Geophysical Research*, 79(1):118–127. **doi:** 10.1029/JA079i001p00118.

Tsyganenko, N. (1989). A magnetospheric magnetic field model with a warped tail current sheet. *Planetary and Space Science*, 37(1):5 – 20. **doi:** 10.1016/0032-0633(89)90066-4.

Tsyganenko, N. A. (1995). Modeling the Earth's magnetospheric magnetic field confined within a realistic magnetopause. *Journal of Geophysical Research: Space Physics*, 100(A4):5599–5612. **doi:** 10.1029/94JA03193.

Tu, W., Cunningham, G. S., Chen, Y., Henderson, M. G., Camporeale, E., and Reeves, G. D. (2013). Modeling radiation belt electron dynamics during GEM challenge intervals with the DREAM3D diffusion model. *Journal of Geophysical Research: Space Physics*, 118(10):6197–6211. **doi:** 10.1002/jgra.50560.

Tu, W., Cunningham, G. S., Chen, Y., Morley, S. K., Reeves, G. D., Blake, J. B., Baker, D. N., and Spence, H. (2014). Event-specific chorus wave and electron seed population models in DREAM3D using the Van Allen Probes. *Geophysical Research Letters*, 41(5):1359–1366. **doi:** 10.1002/2013GL058819.

Turner, D. L., Angelopoulos, V., Li, W., Bortnik, J., Ni, B., Ma, Q., Thorne, R. M., Morley, S. K., Henderson, M. G., Reeves, G. D., Usanova, M., Mann, I. R., Claudepierre, S. G., Blake, J. B., Baker, D. N., Huang, C.-L., Spence, H., Kurth, W., Kletzing, C., and Rodriguez, J. V. (2014). Competing source and loss mechanisms due to wave-particle interactions in Earth's outer radiation belt during the 30 September to 3 October 2012 geomagnetic storm. *Journal of Geophysical Research: Space Physics*, 119(3):1960–1979. **doi:** 10.1002/2014JA019770.

Turner, D. L., Angelopoulos, V., Li, W., Hartinger, M. D., Usanova, M., Mann, I. R., Bortnik, J., and Shprits, Y. (2013). On the storm-time evolution of relativistic electron phase space density in Earth's outer radiation belt. *Journal of Geophysical Research: Space Physics*, 118(5):2196–2212. **doi:** 10.1002/jgra.50151.

Turner, D. L., Fennell, J. F., Blake, J. B., Claudepierre, S. G., Clemmons, J. H., Jaynes, A. N., Leonard, T., Baker, D. N., Cohen, I. J., Gkioulidou, M., Ukhorskiy, A. Y., Mauk, B. H., Gabrielse, C., Angelopoulos, V., Strangeway, R. J., Kletzing, C. A., Le Contel, O., Spence, H. E., Torbert, R. B., Burch, J. L., and Reeves, G. D. (2017). Multipoint observations of energetic particle injections and substorm activity during a conjunction between Magnetospheric Multiscale (MMS) and Van Allen Probes. *Journal of Geophysical Research: Space Physics*, 122(11):11,481–11,504. **doi:** 10.1002/2017JA024554.

Turner, D. L. and Li, X. (2008). Quantitative forecast of relativistic electron flux at geosynchronous orbit based on low-energy electron flux. *Space Weather*, 6(5):S05005. **doi:** 10.1029/2007SW000354.

Turner, D. L., Shprits, Y., Hartinger, M., and Angelopoulos, V. (2012). Explaining sudden losses of outer radiation belt electrons during geomagnetic storms. *Nature Physics*, 8(3):208–212. **doi:** 10.1038/nphys2185.

Ukhorskiy, A. Y., Anderson, B. J., Takahashi, K., and Tsyganenko, N. A. (2006). Impact of ULF oscillations in solar wind dynamic pressure on the outer radiation belt electrons. *Geophysical Research Letters*, 33(6):L06111. **doi:** 10.1029/2005GL024380.

Ukhorskiy, A. Y. and Sitnov, M. I. (2013). Dynamics of radiation belt particles. *Space Science Reviews*, 179(1):545–578. **doi:** 10.1007/s11214-012-9938-5.

Usanova, M. E., Drozdov, A., Orlova, K., Mann, I. R., Shprits, Y., Robertson, M. T., Turner, D. L., Milling, D. K., Kale, A., Baker, D. N., Thaller, S. A., Reeves, G. D., Spence, H. E., Kletzing, C., and Wygant, J. (2014). Effect of EMIC waves on relativistic and ultrarelativistic electron populations: Ground-based and Van Allen Probes observations. *Geophysical Research Letters*, 41(5):1375–1381. **doi:** 10.1002/2013GL059024.

Vampola, A. (1997). Outer zone energetic electron environment update. In *Conference on the High Energy Radiation Background in Space. Workshop Record*, pages 128–136. IEEE. **doi:** 10.1109/CHERBS.1997.660263.

Van Allen, J. A. (1957). Direct detection of auroral radiation with rocket equipment. *Proceedings of the National Academy of Sciences of the United States of America*, 43(1):57–62. **doi:** 00278424.

Van Allen, J. A. (1958). Observation of high intensity radiation by satellites 1958 α and γ. *Journal of Jet Propulsion*, 28(9):588–592. **doi:** 10.2514/8.7396.

Van Allen, J. A. (1959a). The geomagnetically trapped corpuscular radiation. *Journal of Geophysical Research*, 64(11):1683–1689. **doi:** 10.1029/JZ064i011p01683.

Van Allen, J. A. (1959b). Radiation belts around the Earth. *Scientific American*, 200(3):39–47.

Van Allen, J. A. and Frank, L. A. (1959a). Radiation Around the Earth to a Radial Distance of 107,400 km. *Nature*, 183:430–434. **doi:** 10.1038/183430a0.

Van Allen, J. A. and Frank, L. A. (1959b). Radiation measurements to 658,300 km with Pioneer IV. *Nature*, 184:219–224. **doi:** 10.1038/184219a0.

Van Allen, J. A., McIlwain, C. E., and Ludwig, G. H. (1959). Radiation observations with satellite 1958 ε. *Journal of Geophysical Research*, 64(3):271–286. **doi:** 10.1029/JZ064i003p00271.

Varotsou, A., Boscher, D., Bourdarie, S., Horne, R. B., Glauert, S. A., and Meredith, N. P. (2005). Simulation of the outer radiation belt electrons near geosynchronous orbit including both radial diffusion and resonant interaction with whistler-mode chorus waves. *Geophysical Research Letters*, 32(19):L19106. **doi:** 10.1029/2005GL023282.

Varotsou, A., Boscher, D., Bourdarie, S., Horne, R. B., Meredith, N. P., Glauert, S. A., and Friedel, R. H. (2008). Three-dimensional test simulations of the outer radiation belt electron dynamics including electron-chorus resonant interactions. *Journal of Geophysical Research: Space Physics*, 113(A12):A12212. **doi:** 10.1029/2007JA012862.

Walt, M. (1994). *Introduction to geomagnetically trapped radiation*, volume 10 of *Cambridge Atmospheric and Space Science Series*. Cambridge University Press.

Wang, C., Ma, Q., Tao, X., Zhang, Y., Teng, S., Albert, J. M., Chan, A. A., Li, W., Ni, B., Lu, Q., and Wang, S. (2017). Modeling radiation belt dynamics using a 3-D layer method code. *Journal of Geophysical Research: Space Physics*, 122(8):8642–8658. **doi:** 10.1002/2017JA024143.

Williams, D. J. (1987). Ring current and radiation belts. *Reviews of Geophysics*, 25(3):570–578. **doi:** 10.1029/RG025i003p00570.

Xiang, Z., Tu, W., Li, X., Ni, B., Morley, S. K., and Baker, D. N. (2017). Understanding the mechanisms of radiation belt dropouts observed by Van Allen Probes. *Journal of Geophysical Research: Space Physics*, 122(10):9858–9879. **doi:** 10.1002/2017JA024487.

Xiang, Z., Tu, W., Ni, B., Henderson, M. G., and Cao, X. (2018). A statistical survey of radiation belt dropouts observed by Van Allen Probes. *Geophysical Research Letters*, 45(16):8035–8043. **doi:** 10.1029/2018GL078907.

Yando, K., Millan, R. M., Green, J. C., and Evans, D. S. (2011). A Monte Carlo simulation of the NOAA POES Medium Energy Proton and Electron Detector instrument. *Journal of Geophysical Research: Space Physics*, 116(A10):A10231. **doi:** 10.1029/2011JA016671.

Zaharia, S., Cheng, C. Z., and Johnson, J. R. (2000). Particle transport and energization associated with substorms. *Journal of Geophysical Research: Space Physics*, 105(A8):18741–18752. **doi:** 10.1029/1999JA000407.

Zhang, D., Cao, J. B., Wei, X. H., and Li, L. Y. (2015). New technique to calculate electron Alfvén layer and its application in interpreting geosynchronous access of PS energetic electrons. *Journal of Geophysical Research: Space Physics*, 120(3):1675–1683. **doi:** 10.1002/2014JA020670.

Zhang, J.-C., Wolf, R. A., Spiro, R. W., Erickson, G. M., Sazykin, S., Toffoletto, F. R., and Yang, J. (2009). Rice Convection Model simulation of the substorm-associated injection of an observed plasma bubble into the inner magnetosphere: 2. Simulation results. *Journal of Geophysical Research: Space Physics*, 114(A8):A08219. **doi:** 10.1029/2009JA014131.

Zhao, H., Friedel, R. H. W., Chen, Y., Reeves, G. D., Baker, D. N., Li, X., Jaynes, A. N., Kanekal, S. G., Claudepierre, S. G., Fennell, J. F., Blake, J. B., and Spence, H. E. (2018). An empirical model of radiation belt electron pitch angle distributions based on Van Allen Probes measurements. *Journal of Geophysical Research: Space Physics*, 123(5):3493–3511. **doi:** 10.1029/2018JA025277.

Zhao, H. and Li, X. (2013). Inward shift of outer radiation belt electrons as a function of Dst index and the influence of the solar wind on electron injections into the slot region. *Journal of Geophysical Research: Space Physics*, 118(2):756–764. **doi:** 10.1029/2012JA018179.

Zhao, H., Li, X., Blake, J. B., Fennell, J. F., Claudepierre, S. G., Baker, D. N., Jaynes, A. N., and Malaspina, D. M. (2014a). Characteristics of pitch angle distributions of hundreds of keV electrons in the slot region and inner radiation belt. *Journal of Geophysical Research: Space Physics*, 119(12):9543–9557. **doi:** 10.1002/2014JA020386.

Zhao, H., Li, X., Blake, J. B., Fennell, J. F., Claudepierre, S. G., Baker, D. N., Jaynes, A. N., Malaspina, D. M., and Kanekal, S. G. (2014b). Peculiar pitch angle distribution of relativistic electrons in the inner radiation belt and slot region. *Geophysical Research Letters*, 41(7):2250–2257. **doi:** 10.1002/2014GL059725.